Mineral Mediated Catalysis of Fatty Acids

BENJAMIN SMITH

Mineral Mediated Catalysis of Fatty Acids

Benjamin Smith

A thesis submitted for the degree of Doctor of Philosophy

Department of Chemistry

Durham University

2014

Abstract

In order to reduce reliance on fossil oil, and it's associated problems, there is a need to develop new platform chemicals, fuels and products, in a sustainable way, from biomass. In this thesis the catalytic upgrading of fatty acids, derived from the lipid fraction of biomass, through deoxygenation reactions is studied.

Chapter 1 reviews the general area of catalytic upgrading of biomass into biofuels and bioproducts. The history and motivation for alternative sources of fuels and materials are introduced, followed by a summary of the reaction processes currently utilised for biofuels and bioproducts production. It is shown that the demand for alternative fuel sources initially led to the mass commercial production of ethanol, *via* fermentation of sugars, and biodiesel, through *trans*-esterification of lipids present in vegetable and algal oils. A selection of the catalysts and mechanisms for *trans*-esterification reactions is reviewed and, following an outline of the fuel properties and processes, an evaluation of "green diesel" production is given, whereby fatty acids are converted directly into hydrocarbons through decarboxylation reactions. This review culminates in an analysis of alternative conversion of fatty acids into long chain ketone bioproducts, namely ketonic decarboxylation, which details the catalysts and processes involved to date.

Chapter 2 describes the analytical methods utilised in this thesis to investigate heterogeneous catalysis of biomass conversion, along with the relevant background theory and describes the type of data that can be obtained using the techniques. The techniques include powder X-ray diffraction, thermogravimetric analysis, scanning electron microscopy, inductively coupled plasma optical emission spectroscopy, surface area analysis, Hammett basicity, elemental analysis, Fourier-transform infra-red spectroscopy and gas chromatography.

Chapter 3 introduces a class of materials known as layered double hydroxides (LDHs) of general formula $M^{z+}_{1-x}M^{3+}_{x}(OH)_2]^{q+}(X^{n-})_{q/n}\cdot yH_2O$. The ease with which these mixed oxide materials may be prepared offers significant scope for the variation of the metal cations; the M^{2+}:M^{3+} ratio (denoted R-value); the counter anion(s); and crystal morphology. These LDHs consist of positively charged layers, with negatively charged counter-anions and water residing in the interlayer. A review of the commonly used synthesis methods for LDHs is given, along with the advantages and disadvantages associated with each method. Following this, the synthesis of the Mg-Al LDHs and their calcined counterparts, mixed metal oxides (MMOs) (for R-values 1-6) *via* a readily scalable co-precipitation (CoP) and a more environmentally-friendly co-hydration (CoH)

route is described. A range of techniques, outlined in chapter 2, are utilised to study the LDH and MMO crystal and chemical structures, surface topography, surface area, pore volume and relative basicities. The crystal structures of two of the CoP-LDHs were refined to the 3R-polytype using DICVOL,[1] however the other LDHs were not significantly ordered and could not be refined. Upon calcination from LDHs to MMOs, the interlayer counter-anions and water are lost, along with the layered structure, leading to a commensurate increase in surface area and pore volume.

In chapter 4, investigations undertaken to deoxygenate stearic acid, a free fatty acid model biomass compound, are described. As a catalyst, 5 % Pd/C was used, adapting a method found in the literature.[2] These reactions were undertaken at 230 °C, with decarboxylation of stearic acid producing straight-chain *n*-heptadecane at up to 58 % conversion by gas chromatography analysis. However, in this study, issues arose due to catalyst instability and an ensuing loss of catalyst activity was observed.

In chapters 5 and 6, to increase catalyst stability and recyclability, while also reducing costs relative to the Pd/C catalyst used in chapter 4, (due to the use of precious metals), LDHs and their calcined derivatives, MMOs, were utilised for deoxygenation of the model stearic acid biomass. Thermal reactions of stearic acid controls, without catalyst, were not observed to occur, however, stearic acid conversions between 83-97 % at 250 °C were observed to occur with both LDH and MMO catalysts. However, unlike the Pd/C reaction, no decarboxylated product was evidenced and, instead, a waxy solid formed, which was subsequently analysed and found to be the ketonic decarboxylation product, stearone. A protocol was developed to separate the stearone from the catalyst. Gas chromatography analysis showed the LDH and MMO materials catalysed the conversion of stearic acid to a similar degree, allowing for the error within the extraction and analysis processes employed. The reasons for similarity in reactivity are discussed, and it is suggested that an intermediate state of catalyst is present in the reactor.

Comparing synthesis methods, the CoH materials were as effective as their CoP counterparts, despite the presence of $Mg(OH)_2$ secondary-phases. Within the LDH phases, an indication of catalytic dependence on pore size was also recorded, with the smaller pore-sized materials leading to lower conversions of stearic acid, resulting from the bulky size and required head alignment of the long-chain fatty acid molecules. In terms of control reactions, calcined MgO led to 90 % conversion of stearic acid to stearone, however very little reaction occurred with uncalcined MgO (0.5 %) and zero reaction with the acidic Al_2O_3 (both uncalcined and calcined). Hence activated MgO is also an effective catalyst for ketonic decarboxylation.

Chapter 7 summarises the results and discussion given within this thesis, highlighting the milestones achieved such as the first ketonic decarboxylation reactions involving MMO catalysts and concluding that LDHs and MMOs catalyse the conversion of stearic acid *via* ketonic decarboxylation of free fatty acids to high value ketones, to a similar degree, within the associated errors. In addition the LDH synthesis method employed does not play a significant role in the degree of catalysis, resulting in the recommendation that the more environmentally-friendly co-hydration synthesis method should be employed for the catalyst involved in the conversion of stearic acid derived from biomass. The MMO catalysts were found to behave akin to the calcined MgO material during the ketonic decarboxylation of stearic acid, while the catalytic reactions involving LDH catalysts were potentially involving the interaction of their interlayer anions and cations. Finally, a summary of additional work for further developing this process is discussed.

Contents

List of figures and tables

List of abbreviations

Adip	adipic acid
bbl	barrels
BET	Brunauer-Emmett-Teller
BJH	Barrett-Joyner-Halenda
BSTFA	N,O-Bis(trimethylsilyl)trifluoroacetamide
CoH	co-hydration
CoH-LDH	co-hydrated layered double hydroxide
CoH-MMO	co-hydrated mixed metal oxide
CoP	co-precipitation
CoP-LDH	co-precipitated layered double hydroxide
CoP-MMO	co-precipitated mixed metal oxide
DCP-AES	direct current plasma atomic emission spectroscopy
DFT	density functional theory
DRIFTS	diffuse reflectance infrared Fourier transform spectroscopy
EDX	energy dispersive X-ray
EPSRC	Engineering and Physical Sciences Research Council
EU	European Union
FAEE	fatty acid ethyl ester
FAME	fatty acid methyl ester
FEG	field emission gun
FFAs	free fatty acids
FID	flame ionisation detector
FTIR	Fourier transfom infra-red
FWHM	full-width half-maximum
GC	gas chromatography
GC-MS	gas chromatography-mass spectrometry
HVO	heavy vacuum oil
ICP-OES	inductively coupled plasma optical emission spectroscopy
IR	infra-red
LCA	life cycle analysis
LDHs	layered double hydroxides
MBOH	2-methyl-3butyn-2-ol
MMOs	mixed metal oxides
MS	mass spectrometer
NAs	naphthenic acids
NMR	nuclear magnetic resonance
PXRD	powder x-ray diffraction
SEM	scanning electron microscopy
SVO	straight vegetable oil
TA	terephthalic acid
TAN	total acidity number
TCD	thermal conductivity detector
TGA	thermogravimetric analysis
TGA-MS	thermogravimetric analysis- mass spectrometry
THF	tetrahydrofuran
TOF	time of flight
TPD	temperature programmed desorption
TR-SD	simulated-distillation gas chromatography column
UK	United Kingdom
US	United States

USA	United States of America
XRD	X-ray diffraction

Declaration

The work described in this thesis was carried out in the Department of Chemistry, Durham University between May 2008 and August 2011. All of this work is my own unless specifically stated otherwise. No part of this work has previously been submitted for a degree at this or any other institution.

Statement of Copyright

Acknowledgements

Firstly, thank you to my supervisor Dr Chris Greenwell for his constant advice, support, guidance, encouragement and enthusiasm throughout. Many thanks also to Chris for giving me the opportunity to attend and present at multiple conferences across the globe.

Secondly, many thanks to my co-supervisor Prof. Andy Whiting for his continued assistance and for the practical support of access to instruments and lab space within the Whiting lab. I would also like to thank Dr Phil Dyer for his wisdom, support and thought-provoking discussions throughout the latter half of this project. The Engineering and Physical Sciences Research Council (EPSRC) and KiOR (www.kior.com) are thanked for funding.

The following deserve a special mention for their assistance with various experimental techniques; Dr Li Li, Dr Louise Gildea, Mr Dave Hunter, Mr Leon Bowen, Mr Scott Kimmins, Dr Hayley Charville and Dr Chris Ottley. I would also like to thank those within the Durham University Chromatography, XRD, TGA, Microanalysis, Mass Spectrometry and NMR facilities.

I am eternally grateful to the members of the Greenwell and Whiting groups for making the Chemistry Department such an enjoyable and dynamic place to come to work every day.

A special thank you to Professor Judith Howard for her years of ongoing support, for originally inviting me to the PhD Project Open Evening in 2008 and especially for introducing me to Chris.

Last but not least, heartfelt thanks to my family for their relentless support, encouragement and above all for their patience and proof-reading.

For the Smiths

1 Catalytic upgrading of biomass into valuable bio-products

1.1 Introduction

The discovery and use of fossil-based hydrocarbons has transformed the economies and infrastructure of societies and nations. Until recently, the cost of oil had decreased, so supplies were readily available and inexpensive; no longer was it the rich-few who could afford to use this energy source and the technology required to access it. However with the consumption of crude oil increasing by around 1 million barrels (bbl) of oil daily,[3] and known reserves estimated to last only another 120 years,[4] prices have rapidly escalated over the last decade. In 2011, globally, 83.6 million barrels of oil were produced daily at an average cost of £72 ($111) per barrel, which equates to a market of £6 billion/day for 509759 TJ of equivalent energy.[4] Owing to crude oil being a finite resource there is a pressing need to develop alternative fuels and products that are compatible with existing technology, rather than develop wholly new materials that require the costly and time-consuming complete replacement of current infrastructure.[5] Alongside the challenge of sourcing alternative-to-fossil materials, are the issues of the production processes required for these and the manufacturing-sustainability.[6] Within this context, the processes and catalysts utilised to produce alternative materials and feedstocks also need to be environmentally friendly, as well as the final products.[7, 8] The energy required for a chemical reaction can be reduced through use of specific catalysts, which provide alternative, lower energy, reaction pathways. The energetic advantages of using an effective catalyst in a chemical process are illustrated using the generic catalysed-reaction energy-profile shown in Figure 1.1.

1.1.1 Alternative feedstock sources for chemicals - history and motivation

The use of bio-products and biofuels are by no means a modern idea, with over a century ago, Rudolph Diesel inventing an engine which initially ran on peanut oil.[9] It was not until many years later that crude oil-based diesel, being at the time cheaper, became the preferred alternative. Biofuels have historically been used in times of shortage, for example during periods of conflict and

civil unrest. During the first half of the 20th century a great deal of research was carried out into renewable and bio-based materials, these studies were collectively known as "chemurgy".[10] In the past, ethanol was blended with petrol, however as bio-based materials and their associated processes were more expensive than their fossil counterparts, this was not pursued on a large commercial scale. In more recent times, the cost to the environment has also been taken into consideration, as well as the short- and long- term availability of feedstocks.

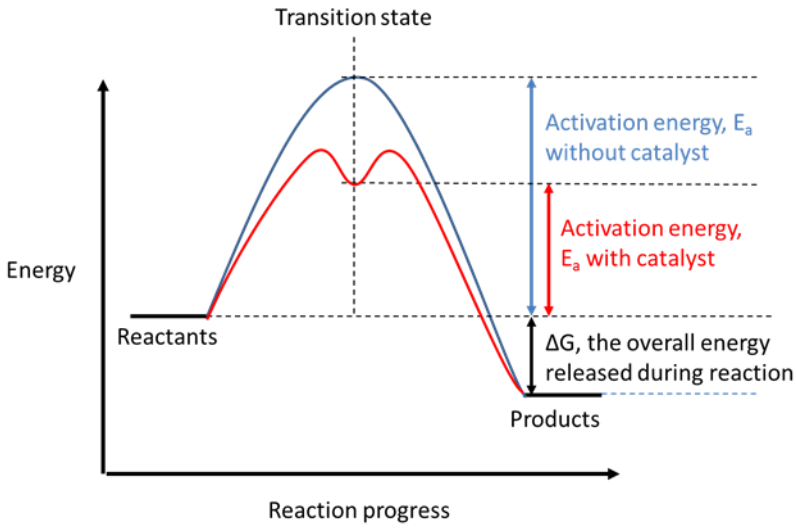

Figure 1.1 Generic energy-profile for a reaction involving conversion of reactants to products, showing the lower activation energy, E_a, required for the catalysed reaction over the uncatalysed reaction, due to the lower-energy transition state involved.

Currently, industry and transport infrastructure across the developed world are inherently based on fossil fuels derived from crude oil. Crude oil is becoming a costly and increasingly unsustainable source of energy, which is linked to the phenomenon of global warming, where carbon dioxide acts as a ''greenhouse gas'' in the atmosphere, raising global temperatures.[11] For example, globally, 2005 was the warmest year on record, to then, throughout all 12 months.[12] Rising levels of greenhouse gases have equated to a 30 % increase in radiative forcing (the difference between radiant energy received by Earth and radiant energy exiting Earth) since 1990.[13] There is an increasingly recognised need to slow down this warming trend for the wellbeing of future generations, and to reduce the warming effects on Earth.[14]

Using natural, biological resources, solar energy can be captured by plants, *via* photosynthesis, to convert atmospheric carbon dioxide to biomass, from which biofuels and bio-products can be produced. These sources are regarded as ‘‘environmentally friendly’’ since they are carbon neutral - ‘‘recycling’’ carbon dioxide from the atmosphere, rather than releasing long-term entrapped carbon as occurs with fossil fuel combustion. Although plants are not as efficient at converting light as photovoltaic solar cells, their cost of production is significantly less and, unlike photovoltaic electricity, they can be converted into feedstocks that are compatible with a petrochemical based society. To put this into numerical context with existing petrochemical expenditure, 31 billion bbl of oil was produced in 2011, with consumption per region shown in Figure 1.2.

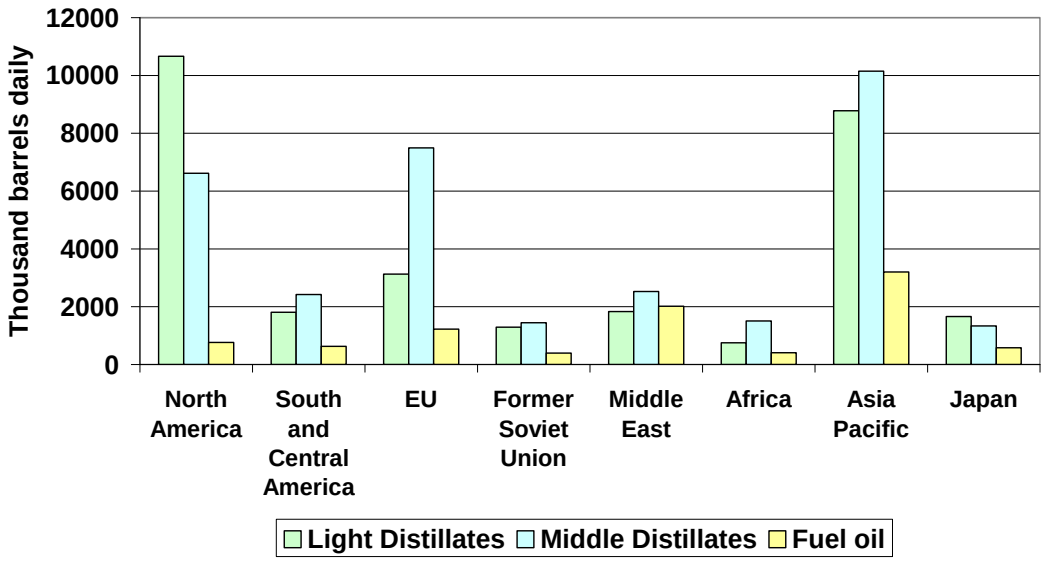

Figure 1.2 Daily world barrels of oil consumed by distillate fraction per region in 2011. Data taken from the BP statistical review of world energy 2012.[4]

Recently there has been a push towards growing biomass for biofuels and bio-products across the world. There are various reasons for this, not least the potential for perceived ‘‘reduction’’ of greenhouse gas emissions and sustainability.[15] Biofuels are also lower in sulphur content compared to their fossil counterparts.[16] However, recently biofuels have received much negative press with studies suggesting that many of them, rather than being carbon neutral, may in

fact lead to greater carbon dioxide and other greenhouse gas emissions, due to changing land use during their production.[17, 18] Conversely, other research has shown that certain biofuel sources can be described as carbon negative in that they lock up more carbon dioxide than is released during their production.[19] Clearly, the type of biomass used as a resource is an important consideration. There is also ever increasing concern about the use of agricultural land for chemical/energy generation, rather than food production, for an increasing world population.[20] As a potential solution to this issue, the use of algae (aquatic photosynthetic microbes) as a bioenergy resource has been suggested since algae does not compete with food for land use or water resources, have highly efficient yields of oil compounds and it is estimated that such biofuels can be produced for around $50 bbl,[21] with a whole range of high value co-products also delivered such as pigments, health foods and nutraceuticals.[22]

Legislation is also a driver of bio-product manufacture. The European Union (EU) set a target of 5.75 % biofuel content in its member states' fuels by the close of 2010, and also recommended that emissions were monitored on non-adapted vehicles.[23] The United Kingdom (UK) government set its own biofuel target of 5 % by volume of total road transport fuel sales by 2010, however it is only achieved 3 % by the period 2012-2013.[24] The total estimated amount of UK agricultural land was 17272000 hectares in 2005, of which 10 % was available for biofuel growth without adversely affecting food supplies (based on grassland less than 5 years old). To reach the UK target of 5 % by 2010 1200000 hectares of land were required, which was achievable, whereas the EU target of 5.75 % would have required 1750000 hectares which was greater than that currently available.[25] Countries producing their own bio-products would have reduced reliance on other states to provide crude oil, resulting in supply security. Reliance on other nations for supplies can increase international tensions, and drive up prices through speculation owing to uncertainty of supply. Bio-product manufacture can also lead to increased support and employment for rural communities.[20]

The world production of biofuels was estimated to be 69 billion litres of fossil based equivalent in 2011.[4] The transport sector, including aviation, produces about one quarter of the UK's total carbon emissions.[26] Road transport contributes 85 % of this, with passenger cars accounting for approximately half of all carbon emitted by the transport sector. The use of bio-products has previously been limited due to the high cost of production relative to fossil-based sources. This is partly due to high feedstock costs, though with rising crude oil prices, biofuels are becoming an increasingly viable alternative. To mitigate the cost of production the concept of a biorefinery has been developed, where the losses from one product (e.g. biofuels) can be offset by the gains of high-value lower-volume co-products, for use in the cosmetics industry for example.[27] This diversification principle could also help to reduce waste in production since a greater proportion of the biomass would be utilised, if whole biomass is not converted to fuel. For instance, glycerol is the main byproduct of current biodiesel manufacturing processes. If suitable processes/conversions of glycerol could make it into a useful commodity, then it would cease to be just a byproduct, resulting in reduced overall production costs for biodiesel. Example processes include steam-reforming of glycerol to form hydrogen,[28] and pyrolysis of glycerol to produce syngas, methane and ethane.[29] Also, glycerol can be used to produce 1,3-propanediol which is a precursor for fibre synthesis, usually obtained from petrochemical origins.[30] With the projected increase in market demand for bio-based materials, conventional infrastructure would need to be transformed and as such, some areas such as the seaports of Antwerp and Rotterdam have already made changes to their infrastructure producing "bio-hubs" to cope with this expected expansion.[31]

An alternative path to refining parts of biomass not suitable for fuel conversion is to modify the organism such that more parts can be converted to fuel. Savage *et al*. recently looked at how synthetic biology can help the production of modern biofuels. With the current methods of ethanol production, a great deal of plant biomass (cellulose) is not utilized during refining. Engineered plants could be used to overcome this, previously resistant to fermentation, utilising new chemical processes and enzymes to break down carbohydrate sources. Novel fatty acid synthases could be

produced to build up fatty acid groups via addition of $-COCH_3$ to a chain until the required length is obtained.[32]

The remainder of this chapter will focus on reviewing the existing literature for converting the lipid and fatty acid fractions of biomass feedstock to oxygenated fuels, deoxygenated fuels and deoxygenated products.

1.1.2 Current transport biofuel sources

Biofuels can be produced from a wide variety of biomass sources, with bioethanol and biodiesel being the main biofuels currently in commercial production (Figure 1.3).

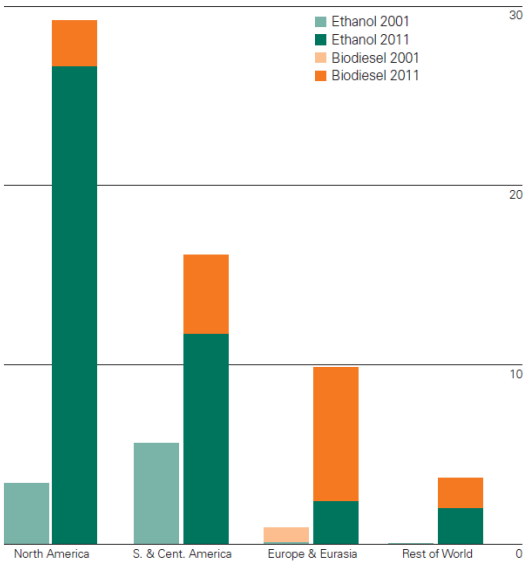

Figure 1.3 Ethanol and biodiesel production in 2001 and 2011, measured in tonnes of oil equivalent x 10^6. 1 tonne of oil = 1165 litres of oil. Taken from the BP statistical review of world energy 2012[4]

First generation biofuels are those fuels derived from existing food-based crops. Producing these fuels leads to competition between food and fuel crops for arable land.[33] With nearly 870 million people classed as undernourished worldwide between 2010-2012, this is a source of potential concern.[34] First generation biofuel crops are: sugar crops for bioethanol, such as sugar cane and sugar beets; starch crops for bioethanol, such as corn and wheat; oilseed crops for biodiesel, such as rapeseed, soybeans and palm. It has been estimated that biofuels such as ethanol and biodiesel yield 25 % and 93 % more energy than the energy required in their production,

respectively, along with 12 % and 41 % reductions in greenhouse gases released during their use, respectively.[35] However, if all current USA corn and soybean farmland were used to produce ethanol and biodiesel it would only satisfy 6 % of the USA's petrol and 12% of USA's diesel domestic requirements.[35] Another key problem is that these crops are also required for food production. Large quantities of fertilisers are needed, which have environmental impacts in their own right. As biofuels become more utilised, further sources of biomass are required, such as Switchgrass,[36] which can grow in less productive farming environments and with lower inputs required, e.g. fertiliser.

Efforts have been made to yield the maximum amount of energy from biomass sources, rather than just using the accessible oils, and thus reducing waste. Singh et al. have demonstrated the use of not only the oils of Jatropha curcas to produce biodiesel, but also the use of seed husks, seed shell and oilcake, resulting in a 300 % increase in the amount of energy released, compared to using just the oil for biodiesel alone.[37] This is an important issue which must be addressed during biofuel production to ensure that all resources are used effectively, since there is limited land set-aside for bioenergy production, the process efficiency is of the utmost importance.

There is an emerging interest in use of advanced biofuels derived from non-food based crops, consisting of cellulosic biomass made up of cellulose, hemicellulose and lignin.[38] The sources of these include Switchgrass, Miscanthus, Willow and also crop residues. These specific energy-crops do not compete with land explicitly destined for food crops and can be grown in low quality environments. The main challenge with advanced biofuels is that the initial capital investment costs are a great deal higher than for first generation biofuels, which can be processed *via* more conventional methods.[39]

1.1.2.1 Carbohydrate derived products – ethanol

Ethanol produced by fermentation of carbohydrates can be used as a petrol (gasoline) substitute or can be blended with it. A problem with ethanol as a fuel is that it absorbs water, making it difficult

to store and transport before use. Ethanol also has a relatively low energy density compared to petrol and efforts have been made to produce branched higher carbon number alcohols, with higher energy density, using the microorganism Escherichia coli[40] Presently, bioethanol production equates to 86 % of the total world biofuel production, having nearly doubled in output in the years 2002-2007.[9]

Table 1.1Conversions for the measurement of oil. [a] varies slightly according to oil source and density.

Quantity	Equivalence
Barrel	1
Litre	159
Imperial gallon	35
US gallon	42
Metric tonnes	~0.139[a]

In 2005, Brazil was producing 282 000 bbl of ethanol a day from sugarcane,[41] and the United States of America (USA) was producing 260 000 bbl a day from corn (see oil conversion Table 1.1 for alternative units), although corn requires increased inputs of fertiliser (compared to sugarcane) and a greater amount of biomass feedstock per bbl.[42] Achieving this output required 3.5 % of the total USA water consumption.[43] In view of water and fertiliser requirements, some countries are beginning to change the energy crops they grow.[44] It has been found that wheat, grown in Europe during winter, was more energy efficient when fertilizer was used, with at least 5 times as much energy returned than used during the fertiliser's own production, packaging, transport and spreading energies combined.[45] Contrary to this, it has been suggested that there may be an increase in nitrous oxide emissions overall, due to the increased use of fertilisers required to grow crops in the, sometimes, poorer environments.[46] Clearly, for any biomass to bio-product process, a full life cycle analysis must be considered before production proceeds.[7]

1.1.2.2 Lipid derived products – biodiesel

Lipids produced by biomass can be upgraded and used as a replacement for diesel-type fuel. An advantage of biodiesel over fossil diesel is that it is extremely low in sulphur content, thus during combustion there is a reduction in the amount of SO_X produced, which is an acid rain forming species and leads to other sulphur-based pollutants. The performance of a range of vegetable oil-based fuels in internal combustion engines has been reviewed by Ramadhas *et al.*, with overall results comparable to fossil-based diesel.[47] Use of straight vegetable oil (SVO) can cause engine problems in the long term and viscosity problems in colder climates unless engine modifications are made to preheat the fuel.[48] Biodiesel tends to have greater viscosity compared to fossil diesel due to the increased polar interactions between fatty acid esters arising from the increased oxygen content, though biodiesel is lower in viscosity than SVO. Biodiesel can be blended with fossil diesel to lower the viscosity of the biodiesel, since the polar ester–ester interactions will be in lower concentration. Blending bio- and fossil-fuels can lead to extended crude oil based fuel supplies.

Table 1.2 Potential oil feedstock yields of various crops. [a] 70% oil (by wt) in biomass [b] 30% oil (by wt) in biomass.[49]

Crop	Oil Yield (Litres/hectare)
Corn	172
Soybean	446
Canola	1190
Jatropha	1892
Coconut	2689
Palm Oil	5950
Microalgae [a]	136,900
Microalgae [b]	58,700

Microalgae are a promising source of biomass for biofuel production, since the growth rates and oil yields can be very high with certain species containing over 80 % oils based on dry weight (Table 1.2).[50] It has been estimated that it would take 61 % of arable farming land in the USA to meet domestic fuel requirements using first generation biomass, but only 3 % of the same area for microalgae, which grow extremely rapidly (many species doubling in mass in less than 24 h). Crucially, algae can be grown in photobioreactors (Figure 1.4), as well as open systems, yielding

biomass crop continuously year round. The oil fraction can be extracted using a solvent such as hexane, with the remaining protein and carbohydrate biomass being digested under anaerobic conditions to make methane, or used as animal feed. *Trans*-esterification of the oils is then used to produce biodiesel (Section 1.3).[49] Use of microalgae is currently on a relatively small scale, compared to the use of sugar cane and soybeans, but microalgae have the potential to provide biofuels and various other bio-products that do not compete with domestic food crops in the long run.

Figure 1.4 Tubular photobioreactor for algae production. Taken from Greenwell *et al.*[51]

1.2 Triglycerides and free fatty acids derived from biomass

Crude vegetable/algae oils consist of mainly triglycerides, which are glycerol molecules esterified with three fatty acids (Figure 1.5). The three fatty acids can all be the same, two the same or all different, with the most common carbon chain lengths being evenly numbered and containing either 16, 18 or 20 carbon atoms.[52] Various mixtures of triglycerides have been characterised, depending on the oil feedstock used. Long chain free fatty acids (FFAs) may also be present in the oils, which may also be saturated or unsaturated.

The choice of oil feedstock plays an important role in the overall cost of the finished product since it constitutes up to 60–75 % of the process costs.[53] Feedstocks are generally area specific, for example soybean oil in the USA and rapeseed oil in Europe. The oils vary in their physical properties such as density, viscosity and cold flow as chain length and degree of saturation of constituent fatty acids alters, with higher quality feedstocks leading to more desirable fuel properties.[54]

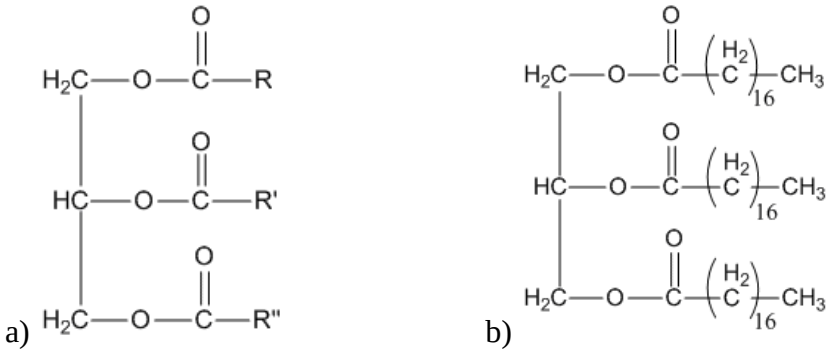

Figure 1.5 a) Schematic to show the structure of a triglyceride molecule which is a glycerol molecule esterified with three fatty acids, of which R, R' and R'' may all be the same, two the same or all different; b) the triglyceride of stearic acid (octadecanoic acid).

1.3 Catalytic upgrading of triglycerides: trans-esterification

Biodiesel is a term used to describe "a fuel comprised of monoalkyl esters of long-chain fatty acids that are derived from vegetable oils or animal fats",[55] although some believe it should be used in a more general nature to describe "a diesel fuel that originates from renewable raw materials".[56] Irrespective of the definition, biodiesel can be used as a direct replacement for fossil diesel, though it is an oxygenated fuel rather than being entirely a hydrocarbon like its fossil counterpart. Fatty acid methyl ester (FAME) or fatty acid ethyl ester (FAEE) products may be used directly as biodiesel or be blended with fossil-based diesel and some modifications may be required for engines to run at over 10 % biodiesel content. This is since biodiesel has slightly different properties compared to fossil diesel, with some of these being given in Table 1.3. The energy density for biodiesel is 14 % lower than that of fossil-diesel and also the lowest temperature at which a fuel will flow through a standard filter in a specified time (cold filter plugging point) is

higher, being at -5 °C compared to -17 °C, leading to problems in colder climates where fuel lines may need to be heated. Other issues with oxygenated fuels include that they are hygroscopic absorbing water molecules and attack rubber seals on older engines, which may need to be replaced. However one advantage is that biodiesel exhibits enhanced lubricity over fossil diesel.

Table 1.3 Comparison of fossil fuels and oxygenated biofuels. [a] GHG = greenhouse gas [57]

Fuel	Energy per kg (MJ/kg)	Cold filter plugging point (°C/F)	Flash point (°C/F)	Typical net GHG[a] (g CO2/ MJ final energy)
Gasoline	42.9	-	<-40/<-40	12.5
Ethanol (sugarcane, Brazil)	26.8	-	5 /41 (fuel grade 95% ethanol)	-60.9 (with bagasse used as fuel)
Diesel	43.0	-17/1	>55/>131	14.2
Biodiesel (soy)	36.8	-5.6/22	>130/>266	-50.7, -45.4 (using glycerol as chemical, animal feed)

One of the methods used commercially to produce biodiesel is *trans*-esterification, shown schematically in Figure 1.6, where triglycerides present in vegetable oils are esterified, usually with methanol (methanolysis), to yield the corresponding methyl esters and glycerol. *Trans*-esterification is required to remove the glycerol backbone that links the three long-chain fatty acid ester groups in triglycerides and replace them with mono-alkyl ester groups, thus significantly enhancing the properties of the material towards those of fossil diesel. Glycerol, resulting from *trans*-esterification, may be sold as a by-product to help make the process more economically viable. *Trans*-esterification is usually performed in the presence of a catalyst (acidic or basic, homogeneous or heterogeneous), although it may also be driven by undertaking the reaction under supercritical conditions.[58]

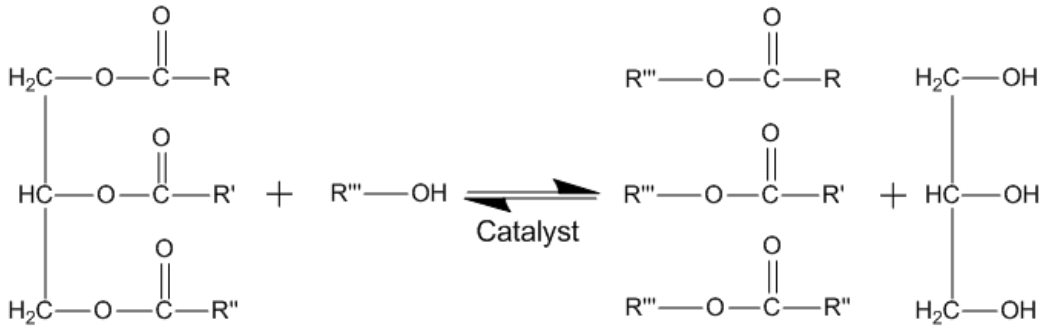

Figure 1.6 *Trans*-esterification of a triglyceride. Methanol is normally the alcohol used, together with an acid or base catalyst. This is a three step reaction, proceeding via the tri-,di- and monoglycerides to the alkyl esters which can be used as biodiesel. The by-product glycerol can also be sold to recuperate production costs.

A wide range of catalysts and reaction conditions have been trialled for *trans*-esterification and an overview of some of these is shown in Table 1.4. Many of these reactions are acid- and base-catalysed *trans*-esterification reactions, with their respective generic mechanisms being shown in Figure 1.7. In the acid catalysed *trans*-esterification, the carbonyl oxygen is initially protonated and the electron pair from the C-O π bond is transferred back to the oxygen atom, forming a secondary carbocation. The carbocation then undergoes nucleophilic attack from the lone pair on an oxygen atom in an alcohol molecule, with cleavage, and subsequent protonation of the original ester alcohol to yield the *trans*-esterified product. In triglycerides there are three alcohol ester groups, which are removed in turn following this same mechanistic pathway, forming glycerol. In base-catalysed *trans*-esterification, the base first removes a proton from an alcohol molecule, with the resulting anion nucleophile then attacking the carbon atom of a carbonyl group, followed by elimination of the one of the glycerol alcohol groups. The departing alkoxide is protonated as an alcohol leaves the *trans*-esterified molecule. Base catalysts have been found to be have more than 4000 times higher rates than acid catalysts for *trans*-esterification catalysis.[59]

Table 1.4 Selected reactions for *trans*-esterification of biomass lipid to biofuel conversion.

Author	Year	Catalyst	Reaction Conditions	Product	Reported yields %
Vicente[60]	2004	NaOH	65 °C, 6:1 methanol:oil. 1% catalyst (wt.%) t = 4 h.	FAME	87

Vicente[60]	2004	KOH	66 °C, 6:1 methanol:oil. 1% catalyst (wt.%) t = 4 h.	FAME	92
Vicente[60]	2004	sodium methoxide	67 °C, 6:1 methanol:oil. 1% catalyst (wt.%) t = 4 h.	FAME	99
Vicente[60]	2004	potassium, methoxide	68 °C, 6:1 methanol:oil. 1% catalyst (wt.%) t = 4 h.	FAME	99
Miao[61]	2006	H_2SO_4	30 °C, 56:1 molar ratio of methanol to oil, 100% catalyst (based on oil weight), t = 4h.	FAME	>60%
Zafiropoulos[62]	2007	sodium methoxide	50 °C, 3:1 methanol:oil, 0.3 wt% catalyst, t = 2 h.	FAME	99
Cantrell [63]	2005	MgAl Layered double hydroxide	60 °C, 30:1 molar ratio of methanol to oil,0.05g calcined catalyst, t = 3 h.	Methyl butanoate	75
Macala[64]	2008	MgAl Layered double hydroxide with Fe 10%	80 °C, 6:1 methanol:oil, 1% calcined catalyst (wt.%) t = 1 h.	*Trans*-esterified soybean oil	38
Bo [65]	2007	KF/Al_2O_3 0.331 (wt/wt)	65 °C, 12:1 methanol:oil, 4% calcined catalyst (wt.%), t = 3 h.	FAME	>90
Li [66]	2007	Eu_2O_3/Al_2O_3 with Eu 0.45–9.00 wt%.	70 °C, 6:1 methanol:oil, 4% calcined catalyst (wt.%), t = 8 h.	FAME	63
Bokade [67]	2007	TPA/K-10 (dodecatungestophosphoric acid)	170 °C, 5:1 methanol:oil, 10% TPA/K-10catalyst (wt.%), t = 8 h.	FAME	84
Azcan[68]	2008	KOH	50 °C, 6:1 methanol:oil, 1% catalyst (wt.%), microwave heating, t = 5 min.	FAME	94
Azcan[68]	2008	NaOH	40 °C , 6:1 methanol:oil, 1% catalyst (wt.%), microwave heating t = 3 min.	FAME	93
Barakos[69]	2008	MgAl-CO_3 layered double hydroxide	200 °C, 6:1 methanol:oil, 1% catalyst (wt.%), high initial FFA content, t = 3 h.	FAME	99 (final FFA < 1 %)
Kouzu[70]	2008	CaO	Reflux, 12:1 methanol:oil, 14 mmol catalyst, t = 1 h.	FAME	93

Garcia [71]	2008	S–ZrO_2	120 °C, 20:1 methanol:oil, 5% catalyst (wt.%), t = 1 h.	FAME	99
Saydut[72]	2008	sodium hydroxide	60 °C, 6:1 methanol:oil, 0.5% catalyst (wt.%), t = 2 h.	FAME	74
da Silva [73]	2008	Co(II) ions adsorbed in chitosan	70 °C, 6:1 methanol:oil, 2% catalyst (wt.%), t = 3 h, pH 8.5.	FAME	94

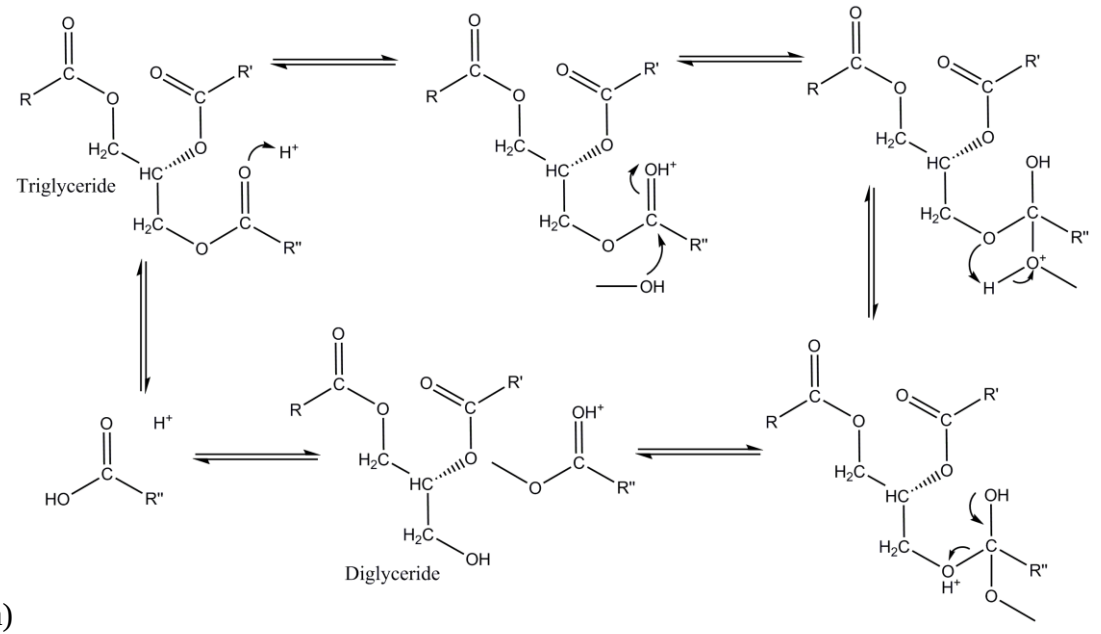

(a)

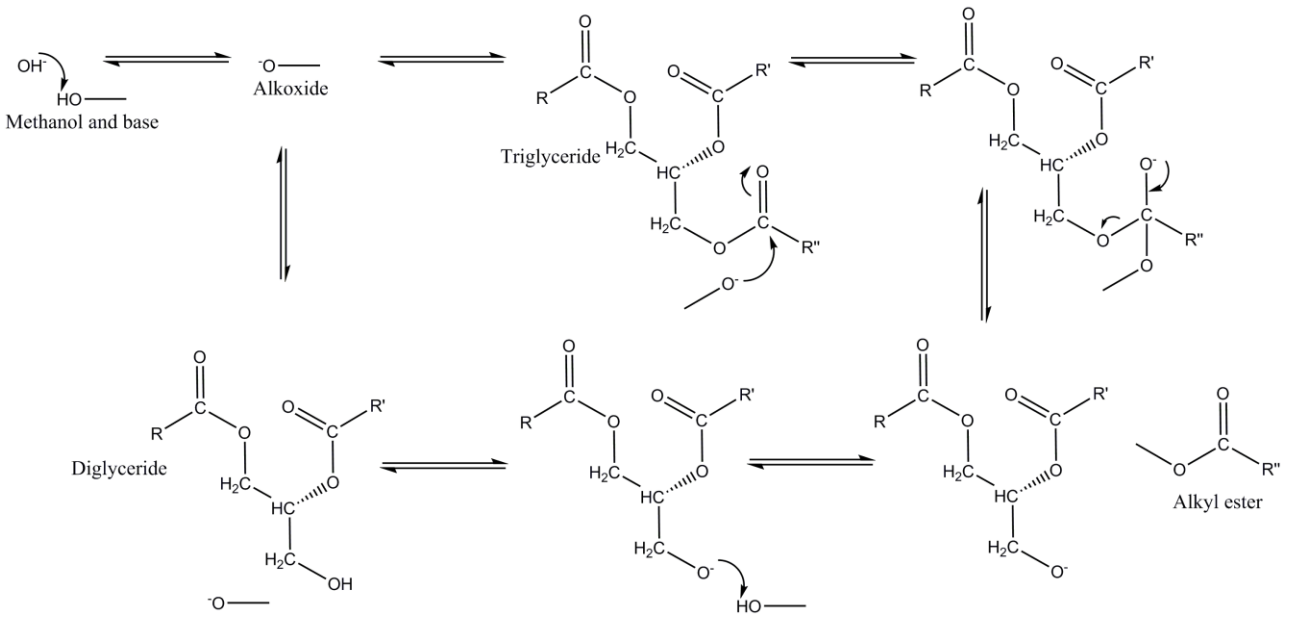

(b)

Figure 1.7 Schematic of mechanisms for *trans*-esterification of triglycerides using a) acid and b) base catalysts.

To make a true biofuel all sources of raw materials need to be derived from biomass. The methanol used in *trans*-esterification processes is usually produced from fossil fuel sources. However, impure methanol may be produced from wood gasification, which can then be used in the synthesis of biodiesel. For FAEE biodiesel, ethanol can be produced *via* fermentation of sugars.

1.3.1 Homogeneous catalysis for biodiesel production

Homogeneous (same phase) acid or base catalysis has the advantage of the catalyst being in the same phase, and in constant contact with the reaction mixture, leading to increased rates, but it suffers from the requirement of a neutralisation step to remove the catalyst, and thus potential loss of raw material and increased processing steps.

1.3.1.1 Homogeneous *trans*-esterification catalysts

Using microalgal oil from *C. protothecoides*, Miao and Wu used acid catalysed *trans*-esterification to produce biodiesel, with methanol and sulphuric acid (preliminary tests suggested that an alkali catalyst was not suitable possibly due to the high acid value of the microalgal oil which would neutralise a base catalyst).[61] The best combination the authors found was with 100 % catalyst (based on oil weight), 56 : 1 molar ratio of methanol to oil, 30 °C and a reaction time of 4 h.

Vicente *et al*. have compared the four most common homogeneous catalysts for *trans*-esterification – sodium hydroxide, potassium hydroxide, sodium methoxide and potassium methoxide.[60] At 65 °C, 6 : 1 methanol : sunflower oil ratio, sodium methoxide was found to lead to the largest yield with 99.3 % with 99.7 % biodiesel purity. The remaining catalysts were found to be in the yield order: potassium methoxide (98.5 %), potassium hydroxide (91.7 %), sodium hydroxide (86.7 %). The order is in agreement with *trans*-esterification of used frying oils with sodium methoxide (89 %) giving higher yields than both potassium hydroxide and sodium hydroxide.[74]

1.3.1.2 Soap formation in homogeneous catalysis

As discussed earlier, plant and algal oils can contain high amounts of FFAs.[49] If these are not pre-treated (esterified) then they can react with homogeneous base catalysts during *trans*-esterification and form the corresponding soaps, leading to separation problems downstream in the production process.[75] Lower grade feedstocks may decrease the cost of biodiesel production, but they generally contain greater numbers of FFAs.[76] FFAs may also be formed from water reacting to hydrolyse FAME (Figure 1.8). Greases (yellow and brown) are relatively inexpensive feedstocks for biodiesel but are high in FFA content, making it a challenge to *trans*-esterify *via* base catalysed reactions without some form of pre-treatment. The pre-treatment stage usually requires a homogeneous acid-catalyst which must be further neutralised before esterification, again increasing the cost of preparation. Zafiropoulos *et al*. investigated the use of immobilised diphenylammonium heterogeneous catalysts to successfully pre-treat greases with a FFA content decreased from 11 % to around 1 %.[62] Following pre-treatment, base catalysed *trans*-esterification with sodium methoxide catalyst and methanol at 50 °C for 2 h, gave up to 99 % yield of FAME. Base catalysed pre-treatment can also be used.[77]

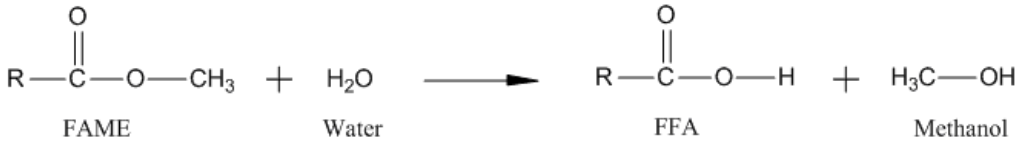

Figure 1.8 Schematic showing formation of free fatty acids from hydrolysis of fatty acid methyl esters.

1.3.2 Heterogeneous catalysis for biodiesel production

Efficient heterogeneous catalysts offer economic benefits in producing biofuels since, unlike homogeneous catalysts, they are easily separated after *trans*-esterification, and so can be readily recycled, lowering production costs. However this is offset against problems owing to the reaction being dependent on diffusion of reactants to surface/active site.

1.3.2.1 Heterogeneous *trans*-esterification catalysts

Layered double hydroxides (LDHs) are a promising group of compounds which comprise of positively charged layered materials with charge balancing anions within the interlayer region (See chapter 3). A wide range of anions may be intercalated including organic ions. For example Choudary *et al*. incorporated *tert*-butoxide, which was found to catalyse a wide range of *trans*-esterification reactions,[78] including the production of emulsifiers for food products.[79] LDH materials with hydrotalcite composition ($[Mg_{(1-x)}Al_x(OH)_2]^{x+}(CO_3)_{x/n}^{2-}$ over the range x = 0.25–0.55) can be formed by co-precipitation of soluble metal salts.[63] These solid base materials can have their properties tuned according to the anion intercalated into the layers and the Mg : Al ratio. The co-precipitation method may be alkali free, leading to no alkaline contaminant in the catalyst. Using LDHs, Cantrell *et al*. carried out *trans*-esterification in a stirred batch reactor for 3 h at 60 °C with 0.05 g MMO, with glyceryl tributyrate, methanol and hexyl ether, and the reaction was periodically sampled with gas chromatography (GC).[63] Glyceryl tributyrate was converted into methylbutanoate *via* di- and monoglycerides. Hydrotalcite, with a Mg : Al ratio of 2.93 : 1, led to the highest conversion, which the authors attributed to increased intralayer electron density (and associated basicity) with increasing Mg content. Both Mg^{2+} and Al^{3+} can be completely or partially substituted in the layered structure by other bivalent or trivalent metal ions, respectively.

Calcination of LDH materials leads to the formation of mixed metal oxides (MMOs), which are usually more basic catalysts than the corresponding parent layered samples.[80] In a further recent study, calcined LDH samples doped with various metal ions to replace Al^{3+}, were tested for biodiesel production.[64] 10 % Gallium dopants led to an increase to around 80 % conversion, at 60 °C, of triacetin to the corresponding methyl esters. The use of an Fe based dopant at 5 % and 10 % led to even greater activity with >95 % yield after 40 min at 60 °C, as compared to 1.0 % weight of dopant. The surface area for this catalyst was found to be ~50 % greater than the uncalcined MgAl hydrotalcite, which is typical of hydrotalcite-like or LDH materials. The mixed oxides that derive from calcination of LDHs at temperatures between *ca*. 400–550 °C, exhibit significantly higher

surface area (ca. 200–300m^2 g^{-1}) compared to the parent LDH samples (*ca*. 50–100 m^2 g^{-1}). Upon regeneration, through rehydration, the catalyst was extracted and re-calcined, giving only 50 % of the initial activity of the original catalyst, with further regeneration yielding similar results.

LDHs can become contaminated with sodium base used in their synthesis. This is normally removed by washing at the end of their preparation, however if left entrained can enhance MMO activity. In a study by Cross *et al*.,[81] MMOs were produced from LDHs subjected to varying degrees of washings, leading to intrinsic sodium contaminant. There was a direct correlation found between the amount of sodium contained in the samples and catalyst activity for *trans*-esterification, with conversion being considerably enhanced with high sodium content. Sodium was also found to leach from LDH samples containing 2.1 % Na by weight, thereby possibly acting as a homogeneous catalyst.

A solid-base catalyst KF/Al_2O_3 has been utilised for the conversion of palm oil to alkyl esters by Bo *et al*.[65] The catalyst was prepared *via* impregnation of KF to give a supported catalyst on Al_2O_3. This was then dried and calcined at 600 °C. The *trans*-esterification was carried out at atmospheric pressure and with an optimum temperature of 65 °C; above this the volatility of methanol became an issue, leading to a decrease in the methanol : oil ratio from the desired 12 : 1. A catalyst ratio of KF : Al_2O_3 0.331 (wt/wt) using 4 % catalyst (wt) over 4 h was found to lead to triglyceride production of over 90 %. Interestingly, calcination of the catalyst at 600 °C led to a new phase of K_3AlF_6 as characterised by X-ray diffraction (XRD) and Thermogravimetric Analysis (TGA).

A superbase (as denoted by the Hammett scale[82, 83]) was prepared by calcination of $Eu(NO_3)_3/Al_2O_3$ for 2 h at 300 °C, 2 h at 550 °C and 8 h at 900 °C forming Eu_2O_3/Al_2O_3 with an optimal Eu content of >6.75 %.[66] This was used to *trans*-esterify soybean oil in a fixed bed reactor at atmospheric pressure. Again the reaction temperature was optimal at around 70 °C due to the volatility of methanol. Water was removed from the oil and methanol to prevent reaction with the catalyst. No reaction was observed for the first 30 min, as monitored by GC, with a steady increase

in rate from 2 h and a final conversion of 63 % at 8 h. The methanol : oil ratio was ≥4 for the greatest conversion, although continually increasing the methanol ratio can lead to separation problems from the prepared methyl esters, so a value of 5–6 was proposed. After 40 h of use, catalyst activity had decreased, leading only to around 35 % conversion, thought to be due to water and FFAs. After each subsequent regeneration the catalyst had lost surface area and its associated activity had decreased.[66]

Some potential oils for biodiesel production such as deep frying oils are high in FFA content, making them unsuitable for base catalysed *trans*-esterification (section 1.3.1.2). In these cases a heterogeneous acid catalyst is preferred. Sulphated zirconia catalyst ($S–ZrO_2$) has been found to catalyse soybean oil to biodiesel with 98.6 % FAME yield.[71] Unfortunately the catalyst is deactivated rapidly. Zinc stearate immobilised on silica gel was found to convert waste cooking oil of 15 % FFA to 98 % FAME with no loss of activity after four catalytic cycles, though the reaction temperature was relatively high at 200 °C.[84] Carbohydrate-derived heterogeneous acid catalysts have been shown to *trans*-esterify oils with up to 27.8 wt % FFA content to 92 % FAME after 8 h.[85] These catalysts were found to be exceptionally stable in that they were still around 93 % active after 50 successive uses.

The alcohol used in *trans*-esterification may lead to fuels with differing properties. Usually methanol is the alcohol of choice, but Bokade *et al*. varied the alcohol used from methanol to *n*-octanol over 10 wt % of catalyst TPA/K-10.[67] The reported percentage conversions were methanol (84 %), ethanol (80 %), *n*-propanol (76 %) and *n*-octanol (72 %) showing a decrease in oil conversion, possibly due to the increasing number of carbon atoms leading to a lower rate of reaction. This means less efficiency in the process and so greater costs incurred in the resulting fuel product.

1.3.2.2 Novel energy sources (microwaves) for *trans*-esterification

Trans-esterification rates may also be increased using microwave heating. Using a potassium hydroxide catalyst and methanol to *trans*-esterify rapeseed oil, *trans*-esterification has been optimised at a temperature of 60 °C and a reaction time of 5 min.[68] This is significantly quicker than previously reported reactions, without microwaves, with a biodiesel yield of 93.7 % and a purity of 97.8 % (greater than the required 96.5 % set out in EN 14214 – Automotive fuels – Fatty acid methyl esters (FAME) for diesel engines – Requirements and test methods).[86] Using the same microwave methods, sodium hydroxide performed best at 40 °C for 3 min with a FAME yield of 90.9 % and purity of 93.7 %.

1.3.3 Life cycle analysis of biodiesel production

A life cycle analysis (LCA) simulation of four *trans*-esterification plants for biodiesel production was carried out using the industrial process modelling and simulation program Aspen HYSYS (HYprotech SYStem).[59] HYSYS allows the user to design reactor systems and chemical processes, which, through using libraries including chemical, thermodynamic and economic data, enables the simulation of overall costs, efficiencies, waste streams and energy balances for an entire industry process. The four *trans*-esterification processes experimented with in HYSYS were: (i) pre-treated, alkali catalysed (using H_2SO_4/NaOH); (ii) homogenous acid catalysed (using H_2SO_4); (iii) heterogeneous acid catalysed (using SnO); and (iv) supercritical conditions (at 200 bar, 350 °C). Each process simulated aimed to convert waste Canola vegetable oil, simulated as triolein and 5 % oleic acid (present as FFA) to methyl oleate. The ester conversion was 99.9% for (i), (ii) and (iv), with process (iii) being slightly lower at 98.65 % conversion, with purities of 99 % achieved. Pilot plants capable of 8000 tonnes/year biodiesel production and with 330 days operation/year with no water impurities in the feedstock were simulated. Capital investment costs were greatest for the supercritical process at (US dollars) $2.15 million, with the order (iv) > (ii) > (i) > (iii) being at

$0.63 million. Incorporating all the running costs for a year and a corporate tax of 50 %, each plant was evaluated for its net annual after-tax profit. The percentage profits were process: (i) -22.2 %; (ii) -8.71 %; (iii) 58.76 %; and (iv) -0.90 %. This indicates that using a heterogeneous acid catalyst could lead to a plant which is sustainable without any government-based subsidies. Plant (iii) also had the lowest start-up capital investment. The economics of the four plants were based on biodiesel valued at a typical $600/tonne. Heterogeneous base catalysis requires a more expensive catalyst and incurs liquid waste disposal costs leading to a net loss. Homogeneous catalysis required a great deal of methanol whereas the supercritical conditions in (iv) incurred increased high pressure costs. This leads to the conclusion that the use of heterogeneous acid catalysts is a promising area of research for biodiesel production *via trans*-esterification due to its low start-up capital investment and relatively higher (positive) percentage profit. This is in contrast to the use of base catalysts, which have been found to have more than 4000 times a higher rate for *trans*-esterification catalysis than acid catalysts.[87]

1.4 Catalytic upgrading of free fatty acids: decarboxylation

Petroleum hydrocarbons are believed to have formed in nature, through the decarboxylation of fatty acids, potentially in the presence of natural clay catalysts present in fossil oil source rocks.[88] If the biofuels can also be deoxygenated, then biomass derived fuels can be produced which could be used as a direct replacement for fossil sourced hydrocarbons. Such fuels have been termed 'green diesel'.[89] This is an emerging area, with deoxygenation usually being performed *via* decarboxylation/hydrogenation reactions. Figure 1.9 shows a schematic of the decarboxylation of stearic acid.

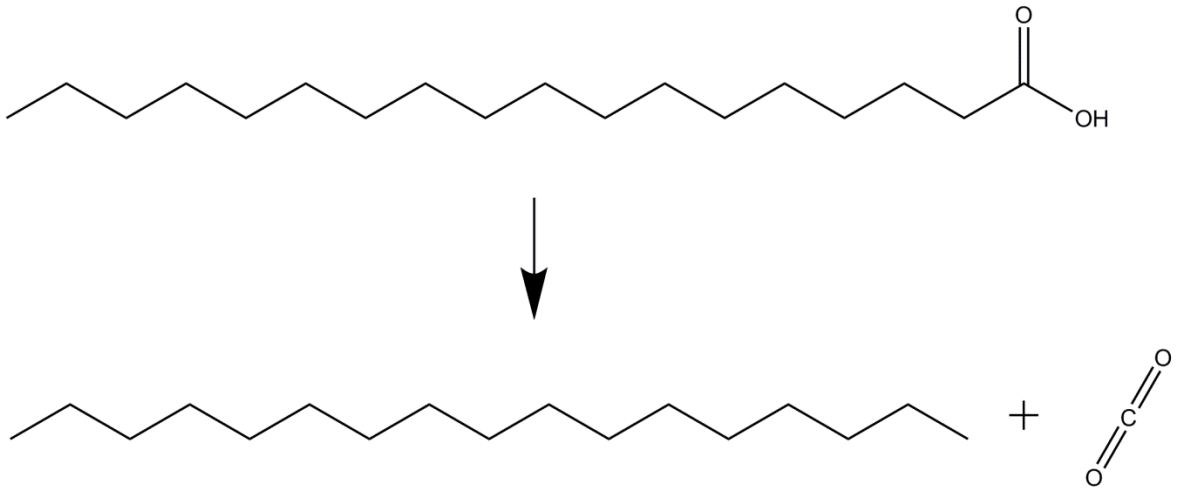

Figure 1.9 Schematic to show decarboxylation of stearic acid, producing straight chain hydrocarbon *n*-heptadecane through the removal of CO_2.

Early studies into mineral decarboxylation by various workers, including Almon and Johns,[90] were conducted to understand fossil oil formation. The decarboxylation of fatty acids during fossil fuel formation appeared to be *via* a free-radical mechanism, with increased reaction rates when free-radical initiators are present, such as H_2O_2, and decreased rates in the presence of oxygen, a free-radical inhibitor. The presence of H_2O_2 led to a 43 % increase in reaction rate ($K = 7.84 \times 10^{-6} sec^{-1}$). In the presence of O_2 this led to a 41 % decrease in rate (with $K = 3.23 \times 10^{-6} sec^{-1}$). The presence of water was found to lead to different product distributions compared to the anhydrous reaction. However, in recent studies, Geatches *et al*., *via* computational simulation, believe the results are not due to a radical reaction, but *via* a substitution in the clay sheet, which attracts a counter-ion that donates an electron to the reactant-clay system,[91] with reaction proceeding by means of an alcohol intermediate to the alkane.

Pyrolysis, where biomass is heated in an inert atmosphere, is the normal method for deoxygenating vegetable feedstocks,[92] using zeolite catalysts,[93] but this can lead to a lower energy fuel. Bertram published work using a homogeneous catalyst over selenium to decarboxylate stearic acid to heptadecane in 1936.[94] Recently, using a commercial activated carbon supported catalyst, *n*-heptadecane was found to be the main product when the model compounds stearic acid, ethyl stearate and tristearin were deoxygenated.[2] The decarboxylation of stearic acid resulted in

production of heptadecenes, which then decreased over the reaction time, suggesting that they were intermediates. At 300 °C and at a pressure of 17 bar, stearic acid was found to have a higher percentage conversion with a reaction atmosphere of 5 % hydrogen and 95 % argon (by volume) when compared to reaction atmospheres of both 100 % helium and 100 % hydrogen. Ethyl stearate was found to convert into stearic acid before decarboxylating to *n*-heptadecane, best achieved in a similar reaction atmosphere of 5 % hydrogen and 95 % argon (by volume), although selectivity to *n*-heptadecane decreased on going from 300–360 °C whilst aromatics started to be produced instead, which are unsuitable in diesel fuel. The reaction kinetics for ethyl stearate and stearic acid decarboxylation over palladium/carbon (Pd/C) catalyst have been studied.[95] With ethyl stearate the rate of reaction increased from 300–360 °C, with an activation energy of 57.3 kJ mol^{-1} from first order kinetics (K - 6.27 x 10-^{12} min^{-1} at 300 °C). For the major intermediate product, stearic acid, the reaction order is almost zero, with the Pd/C catalyst deactivated at high concentrations of stearic acid.

Further studies into heterogeneous decarboxylation were carried out by Snare *et al.*[96] The uncatalysed reaction was performed first and found to only lead to a < 5 % conversion. Similarly, using direct current plasma atomic emission spectroscopy (DCP-AES) with a Pd/C catalyst it was proved that the reaction was indeed heterogeneous and not homogeneous by catalyst leaching. A range of catalysts were tested, supported on carbon and metal oxides (Ir, Mo, Ni, Os, Pd, Pt, Rh and Ru) as well as a Raney nickel catalyst. Side reactions were observed over 6 h of reaction (300 °C, 6 bar, helium) such as isomerisation, dehydrogenation, aromatics and shorter hydrocarbons by cracking). The initial rate was greatest for 5 % Pd/C (1.9 mmol s^{-1} g_{met}^{-1}) with carbon supported catalysts in general leading to higher rates, possibly due to catalyst structure. It was found that some side products produced using Ru/C and Rh/C catalysts were selective towards unsaturated side products, which could have led to their deactivation. 5 % Pd/C was found to be the preferred catalyst for decarboxylation of stearic acid, with Pt/C giving best performance for decarbonylation,

followed by Ni, Rh, Ir, Ru and Os. Additional work with unsaturated renewables also led to diesel-like hydrocarbons.[97]

Further work with Pd supported on Sibunit (a porous carbon–carbon composite material with a high mesopore volume) as a catalyst, using dodecane, at a pressure of 17 bar helium was carried out.[98] This process was trialled in a semi-batch reactor with 300 ml volume. Using 4 wt % catalyst, stearic acid was deoxygenated with increasing initial reaction rate and decreasing time for 100 % conversion as temperature increased from 270 °C to 300 °C to 330 °C. At 270 °C it was found that there was a lag time of 60 min before stearic acid conversion progressed.

Green diesel has been produced by catalytic saturation, hydrodeoxygenation, decarboxylation and hydroisomerisation reactions.[89] Using hydrogen at around 1.5–3.8 % in the reactor produced green diesel yields between 88–99 % depending on the catalyst used. The resulting product was comparable in its properties to ultra-low sulphur diesel, and superior to oxygenated biodiesel. Production from palm oil is estimated as feasible at a crude oil price of $52 bbl and soybean oil at $67 bbl. In the study green diesels were found to have positively higher net energy balances than fossil diesel and biodiesel, which translates to lower fossil fuel inputs during their production. Green diesel production also leads to considerably lower greenhouse gas emissions per energy equivalent compared to fossil-diesel, being slightly less than comparable amounts of biodiesel. These results suggest that green diesel is a superior bio-based energy source, in terms of sustainability, compared to oxygenated biodiesel. A summary of some of the decarboxylation reactions trialled is shown in Table 1.5.

Decarboxylation is also of interest in improving fossil oil properties. The value of crude oils is often reduced if there is a high total acidity number (TAN) due to the presence of naphthenic acids (NAs). These acidic compounds lead to increased corrosion of pipelines and refinery equipment. Decarboxylation catalysts, which have been developed to remove these NAs, leading to a higher quality oil, could also be used for deoxygenating biomass to produce green diesel. In a study by Goddard,[99] aimed at reducing TAN in crude oils, various routes for decarboxylation were

tried. It was found that MgO was effective for converting NAs at 250 °C with some CO_2 production, suggesting decarboxylation was one of the methods of conversion. It was thought that since the relative CO_2 yield was lower than acid conversion, some of the acid may have been neutralised by MgO or that stable metal carbonates were formed. Further studies revealed that at 20 % (wt %) MgO loading the CO_2 yield and acid conversion increased linearly up to 250 °C. Also, whilst increasing catalyst loading at 250 °C, 20 % (wt%) MgO was found to be the saturation point for CO_2 yield and acid conversion. Other carboxylic acid types including succinnic acid and cyclohexane carboxylic acid were trialled with MgO and measured for their CO_2 production. CO_2 was detected in their reactions, suggesting that decarboxylation occurs irrespective of acid structure. When small amounts of Ni and Cu were added these showed enhanced decarboxylation which was not seen when these were added to other oxides. MgO was found to play a role in the adsorption and decarboxylation of NAs, however ketonic decarboxylation was also occurring, leading to the lower observed levels of CO_2 than that of the respective acid conversions (*vide infra*).

In summary, green diesel, produced by catalysed decarboxylation of fatty acids, is a promising biofuel since it is fully compatible with existing fossil-diesel infrastructure and also has reduced levels of sulphur in comparison to fossil diesel. However, greater research and investment in green diesel is required before full scale production can be attained.

1.5 Catalytic upgrading of free fatty acids: ketonic decarboxylation

An interesting reaction for producing bio-products is ketonic decarboxylation, where free fatty acids are reacted together to form a long-chain ketone, with the loss of CO_2 and H_2O in the reaction (Figure 1.10). FFAs are a constituent of biomass and can also be derived from the hydrolysis of triglycerides. This is a clean reaction, producing the desired ketone, water and CO_2 (which may subsequently be captured[100]), resulting in a fossil-free feedstock, with varying carbon chain length.

Table 1.5 Summary of decarboxylation reactions for conversion of fatty acids.

Author	Year	Catalyst	Feedstock	Reaction conditions[a]	Main product	Yields / %
Bertram [94]	1936	selenium	stearic acid	325 °C, 28 % catalyst (wt%), t = 900 mins.	*n*-heptadecane	50
Almon [90]	1975	Ca-montmorillonite	behenic acid	250 °C excess water.	*n*-heneicosane	-
Kubickova[2]	2005	activated carbon supported palladium (5 wt%, Aldrich)	stearic acid	300 °C, 17 bar H_2 (5 vol%) + Ar (95 vol%), 4% catalyst.	*n*-heptadecane	62
Snare [96]	2006	Pd/C	stearic acid	300 °C, 6 bar He, 1 g catalyst t = 360 mins.	*n*-heptadecane	100
Lestari [98]	2008	Pd/C (Sibunit)	stearic acid	330 °C, 17 bar He, 4% catalyst (wt%) t = 20 min.	*n*-heptadecane	100
Liu [101]	2009	Ni–Mo/SiO_2	Jatropha oil	350 °C, 45 bar, H_2 flow.	C_{11}-C_{20} hydrocarbons	83
Fu [102]	2010	5% Pt/C	palmitic acid	370 °C, hydrothermal water, 400% catalyst (wt%), t = 160 mins,	pentadecane	76
Mikulec[103]	2010	NiMo/g–Al_2O_3	rapeseed oil	340 °C, 30 bar, H_2 flow.	hydrocarbons	92.9
Morgan [104]	2010	20% Ni/C	soybean oil	350 °C, 6.9 bar Ar, 1% catalyst (wt%)	C_8-C_{17} hydrocarbons	92

Ketonic decarboxylation is a reaction that has been studied since the 19th century[105] and interest has increased during the 21st century in using ketonic decarboxylation for conversion of biomass feedstock.[106] Currently ketones are produced industrially by means of oxidation of fossil-based hydrocarbons.[107] Ketones that are produced from the ketonic decarboxylation of free fatty acids provide a sustainable bio-based product. Long chain ketones may then be used in lubricants or diesel fuels, or they can be further upgraded into hydrocarbons and hydroxyalkylenes by cracking/hydrotreatment. An alternative set of compounds, which may be further synthesised from long-chain ketones are gemini surfactants.[108] These compounds exhibit greater surface-activity than standard surfactants, with much lower critical miscellar concentrations of around 10-1000 fold. Using mixed chain length organic acids in ketonic decarboxylation reactions, it is possible to generate a wide variety of organic chain lengths.

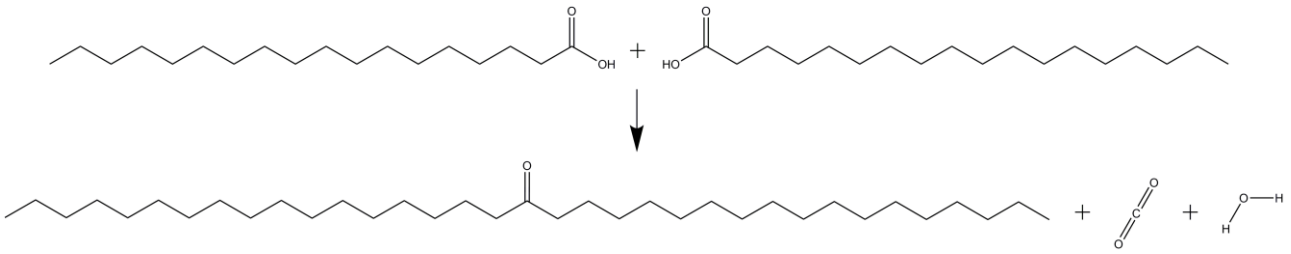

Figure 1.10 Schematic to show ketonic decarboxylation of stearic acid forming stearone, with removal of CO_2 and H_2O.

Basic oxide catalysts, which can abstract protons, have mainly been studied for ketonic decarboxylation and a selection of these reactions are shown in Table 1.6. Heterogeneous MMO materials have been used for the catalysis of acetic acid to acetone with up to 89 % yield, however the chain length of this acid is significantly shorter than those typical of FFAs. Lauric acid, as used by Corma *et al*.,[109] is more representative of the FFA compounds found in biomass. This study utilised basic MgO which led to 97 % yield of laurone. Klimkiewicz *et al*.,[110, 111] used an interesting methodology to convert methyl esters found in rape oil to ketones, using metal oxides at 385-390 °C. Methanol, was used to reduce catalysts in the first study,[111] and as a solvent in the second study,[110] was deemed to be present as an inert species, however when it was substituted with *n*-hexane, conversion declined considerably and cracking reactions were predominant. As can be seen, ketonic decarboxylation reactions require high driving temperatures, which can raise questions about the suitability of this as a sustainable process.

Renz,[112] studying the mechanism for ketonic decarboxylation, suggested that it occurs in a concerted fashion involving nucleophilic attack (Figure 1.11). For the dicarboxylic acid, adipic acid, one of the acid groups is first deprotonated by a base. Following this, elimination of carbon dioxide occurs and the consequential carbanion attacks the second carboxylic acid group simultaneously. This forms a ketone hydrate, which then decomposes into the desired ketone and hydroxide. The hydroxide then either deprotonates further carboxylic acid groups or regenerates the catalytic base.

Table 1.6 Summary of selected ketonic decarboxylation reactions for conversion of fatty acids and esters.

Author	Year	Feedstock	Catalyst	Reaction conditions	Main product	Yields / %
Miller [113]	1950	trimethylacetic acid	aerogel thoria catalyst	490 °C	t-butyl isobutyl ketone	15
Glinski[114]	1995	acetic acid	CeO_2\SiO_2	400 °C 20% catalyst (wt%)	acetone	97
Das [115]	2000	Acetic acid	Calcined Mg4:Al1 layered double hydroxide	350 °C	acetone	87
Das [116]	2000	acetic acid	Calcined Zn3:Al1 layered double hydroxide	425 °C	acetone	89
Klimkiewicz[111]	2001	Rape oil methyl esters	Fe, Si, Cr, K oxides 100:2:1:0.1 reduced in methanol	390 °C	Mainly stearone	56
Klimkiewicz [110]	2001	Rape oil methyl esters and methanol	Sn, Ce, Rh, oxides 90:9:1	385°C	Mainly stearone	63
Renz[117]	2004	adipic acid	$Ba(OH)_2$	350 °C, 5% catalyst	cyclopentanone	90
Nagashima[118]	2005	propanoic acid	CeO_2–MnO_2	350 °C, 10% catalyst (mol%)	3-pentanone	72
Corma [109]	2008	lauric acid	MgO	400 °C	laurone	97
Deng [119]	2009	acetic acid	CeO_2/ 3% K_2O/TiO_2	350 °C	acetone	99

For reactions involving two different carboxylic acids, isotopic labelling with ^{14}C has shown that the acid group which results in an alkyl group that can more readily stabilise a partial negative charge is the one that is released as the CO_2 molecule. The mechanism suggested by Renz also confirms why acids which do not contain α-hydrogens can also undergo ketonic decarboxylation.[120]

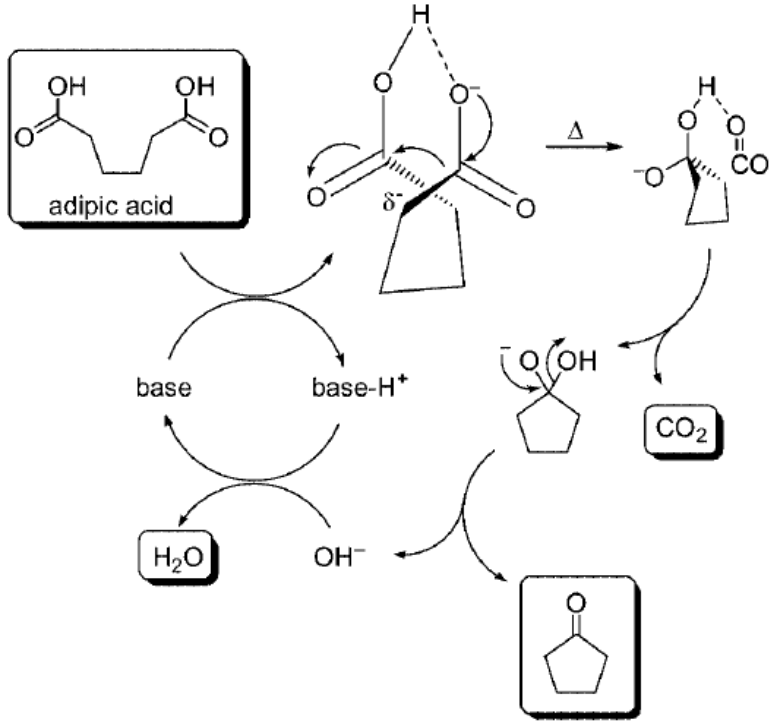

Figure 1.11 Concerted ketonic decarboxylation mechanism proposed by Renz involving nucleophilic attack on the non-dissociated carboxylic acid by the dissociated carboxylic acid. Shown for adipic acid. Taken from Renz.[112]

Through flow reactions and GC-MS studies, the Goddard research group looking into NA removal from poor quality crude oils,[99] realised that the CO_2 yields obtained from these reactions were lower than their respective acid conversions (section 4.1.2). This was determined to be because ketonic decarboxylation was occurring where RCOR' (R and R' correspond to various alkyl groups) was being produced and only one equivalent of CO_2 per two acid molecules, rather than the expected two for decarboxylation. Using transition state studies for ketonic decarboxylation, the authors suggested that one acid molecule is deprotonated and adsorbed onto the surface, then a second free acid molecule reacts with this in a 6-membered ring transition state (Figure 1.12). Following this, CO_2 and H_2O are released. MgO, being a strong heterogeneous base, was found to effectively catalyse this reaction at temperatures below that of the thermal reaction. It was also found that by using mixed acid cyclic feedstocks, different groups for R and R' could be combined in the ketone, leading to desirable products/chain lengths, which could then be used or reacted.

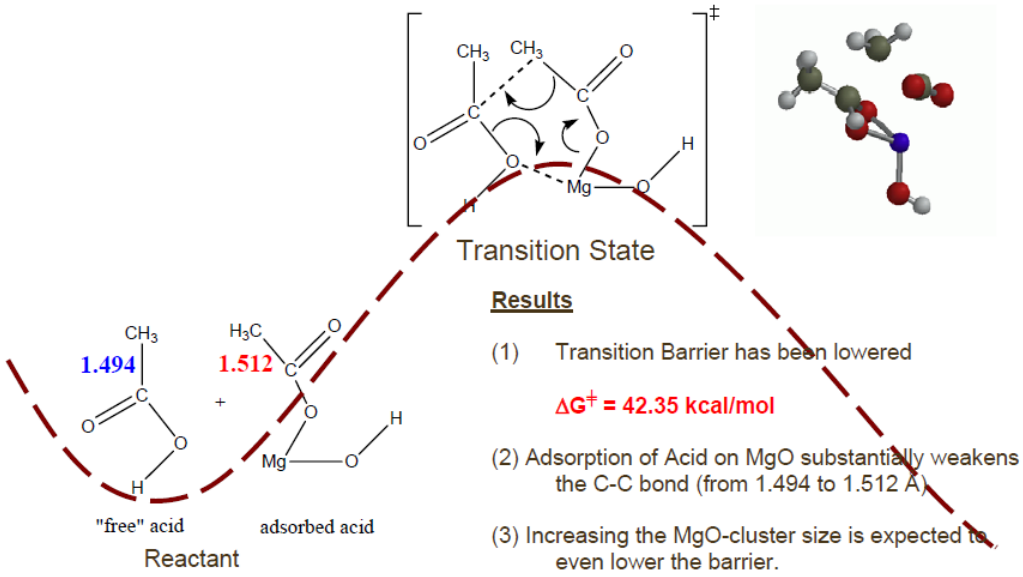

Figure 1.12 Proposed ketonic decarboxylation transition state, based on computer simulation studies, taken from Zhang *et al.*[99]

1.6 Summary and Conclusions

Fossil hydrocarbons are a required commodity in the world today, but their sources will eventually be exhausted, owing, inexorably, to demand exceeding production. Thus, there is a need to develop renewable replacements, which, ideally can be used with existing infrastructure. Products derived from biomass present a sustainable alternative, but they in turn have their own advantages and disadvantages. With the current issues of rising carbon dioxide levels and associated global warming, on an environmental scale, the cycling of carbon from the atmosphere into biomass and then returning to the atmosphere upon combustion, which has no net gain effect, is of great importance.

First generation biofuels are currently in commercial production, utilising energy from food-based crops, either by fermenting sugar to form bioethanol or extracting oils for conversion to biodiesel. There are ethical issues with using bio-products whose feedstocks are food derived or that take up land required for food crops or rainforests. Alongside this there is a need to develop next generation biofuels to meet biofuel targets.[121] Extracting energy from the whole crop, for example including the stalks of biomass, is also required, thus potentially leading to the highest

levels of efficiency and sustainability. Algae are a promising source of oils for upgrading to a range of products as a biorefinery. They are capable of doubling their mass multiple times per day, they photosynthesise more efficiently than terrestrial crops and they take up far less land to produce comparable amounts of lipids. Life cycle analysis of any process is critical to ensure economic feasibility.

Biodiesel is an oxygenated fuel and there is a need to develop decarboxylation processes over the current *trans*-esterification processes to produce deoxygenated fuel, the so-called green diesel. Green diesel can be used as a fully compatible direct replacement for diesel as it is comprised of hydrocarbons, produced by deoxygenating fatty acids. Green diesel has more negative CO_2 footprint than biodiesel, and can be produced at a cost comparable to biodiesel, but it requires different reaction conditions. Similar catalysts used in the green diesel process can also be used to upgrade poor quality crude oil which contains naphthenic acids, thereby increasing useable crude oil supplies. Related processes and catalysts can be used to produce other chemicals required by society, for example fatty acids can be converted into long-chain ketones which can then be further upgraded to gemini surfactants.

Breakthroughs in heterogeneous catalysis for decarboxylation and ketonic decarboxylation reactions that allow the use of existing petrochemical processing and refining infrastructure, and produce a product that is compatible with the existing technology, are likely to make bio-products a viable alternative source in the future.

1.7 Aims of thesis

Sustainable bio-based model fatty acid feedstocks are examined as a feedstock for reactions in this thesis, involving non-precious metal based catalysts. The catalysts selected were LDHs and their calcined counterparts, MMOs. These comprise a family of heterogeneous catalysts whose composition, morphology and basicity can be readily tuned to catalyse a variety of reactions.[122] As it has been pointed out, when producing an environmentally friendly and sustainable product it is

also of importance to use a correspondingly green process.[7] The traditional preparation method for LDHs - co-precipitation - requires large amounts of alkali base and also produces a highly basic supernatant which must be disposed of post-reaction. Greenwell *et al*.[123] have recently prepared LDHs *via* an environmentally friendly co-hydration route from metal oxide and organic acid pre-cursors.

In an attempt to synthesise valuable bio-products, LDHs and MMOs were trialled, for the decarboxylation reaction of stearic acid. This reaction is akin to the possible production of crude oil in clay-catalysed systems.[90] However ketonic decarboxylation was found to be the dominant reaction with these catalysts leading to long-chain ketones. It is hypothesised that LDHs/MMOs, bearing sites of low basicity (OH^-), medium-strong Lewis base O^{2-}-M^{n+} pairs and strong basic sites relating to secluded O^{2-} ions, will result in high catalytic activity to the desired decarboxylated products.

2 Analytical methods used in the study of heterogeneous catalysis for biomass conversion

2.1 Introduction

In this thesis layered double hydroxides (LDHs), and their calcined counterparts, mixed metal oxides, MMOs, will be prepared and used as catalysts for decarboxylation and ketonic decarboxylation reactions of stearic acid. Layered double hydroxides are based on the structure of naturally-occurring Hydrotalcite, which has the general formula $(Mg_6Al_2(OH)_{16}CO_3{\cdot}4H_2O)$[80]. In addition to natural LDHs, a range of synthetic LDH compounds with multiple synthesis variables including: choice of metal cation variety; M^{2+}:M^{3+} ratio (denoted R-value); choice of counter anion(s); and crystal morphology (Figure 2.1) can be prepared. The LDHs all have a positively charged layer structure, along with charge balancing anions and water residing in the interlayer.[124]

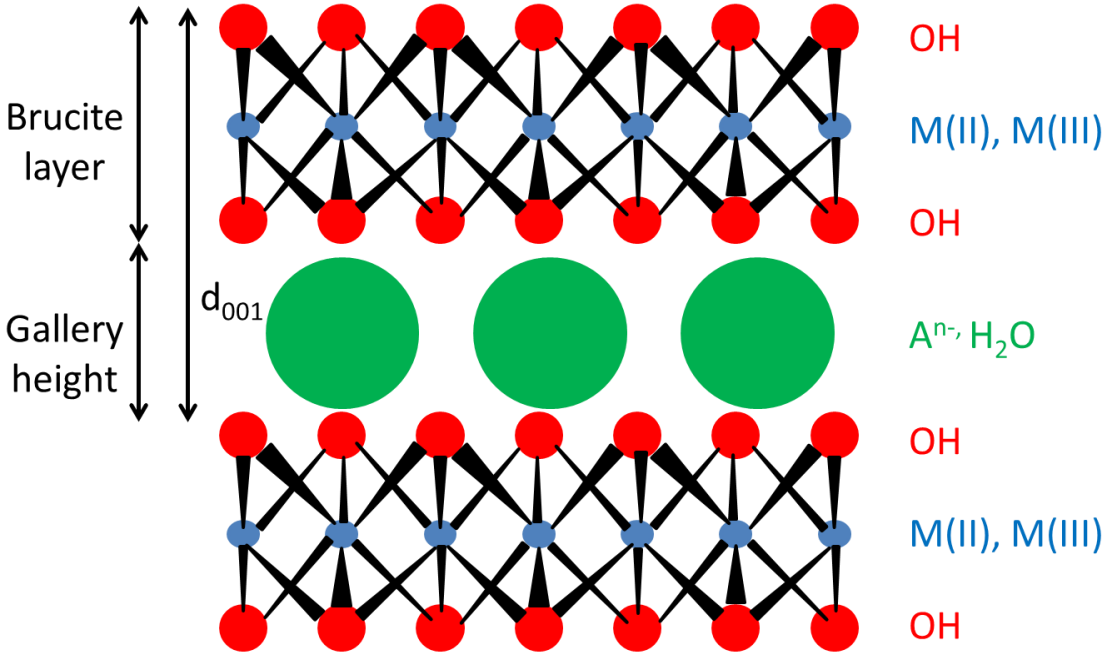

Figure 2.1 Schematic illustrating a typical layered double hydroxide structure, where M^{II} and M^{III} ions are coordinated in an octahedral fashion to OH groups in brucite-like layers, along with charge balancing counter-anions and water residing in the corresponding interlayer galleries.

Synthetic LDHs are invariably polycrystalline, however naturally-occurring LDHs can be crystalline with regular repeating layer units such as the 3-layer repeat rhombohedral (3*R*-polytype)[125] form and 2-layer repeat hexagonal (2*H*-polytype)[126] form (Figure 2.2). The rhombohedral form is more common naturally than the hexagonal form, though some crystals contain both forms, for example pyroaurite.[127] Aspects relating to LDH preparation and crystal structure will be discussed and described in Chapter 3.

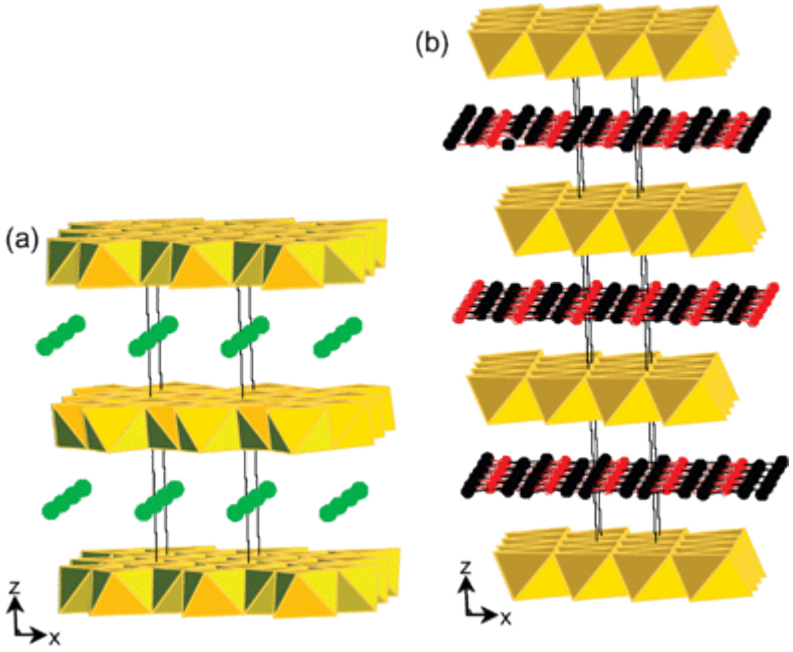

Figure 2.2 a) Schematics illustrating the 2-layer repeat hexagonal and b) 3-layer rhombohedral forms of layered double hydroxides. Taken from Khan and O'Hare.[127]

2.2 Structure determination of layered double hydroxides

Owing to the fact that LDH materials are polycrystalline, where they contain many microscopic crystallites rather than a periodically ordered single crystal, it is not possible to fully determine their structure by single crystal x-ray diffraction. As such, LDHs are a challenging group of materials to analyse, because they cannot be analysed by one single process alone.

Poly-crystallinity in LDHs arises due to a number of factors, such as water content in the interlayer being affected by atmospheric humidity, the effects of temperature and that the water molecules are in a continuously fluctuating hydrogen bonding network.[127] There is rarely long range order in the interlayer gallery and anion content may be inhomogeneous due to competing

carbonate impurities forming, owing to the carbonate anion's high affinity for the interlayer. Also, Al_2O_3 impurities may be present on LDH surfaces from synthesis of the MgAl-LDHs, that are undetected by powder x-ray diffraction (PXRD), but which may be detected by other methods such as X-ray fluorescence or chemical analysis.[128] Generally, LDH layers stack with regular interlayer distances, however they may be stacked in different orientations leading to various polytypes including hexagonal and rhombohedral.[126] Stacking faults can arise from interstratification (varying water/anion content in successive interlayers) and interlayer disorder, meaning that the superposition can be mis-oriented and exhibit turbostratic disorder, where basal planes are randomly orientated and misaligned, about the c-axis.[80, 129]

These are among some of the factors which contribute to the complexity of solving the structure of LDHs. Thus multiple methods need to be employed in a logical manner to determine the LDH structure based on the collective partial nature of the information that can be obtained from each.

2.2.1 Powder X-Ray diffraction

X-Ray diffraction is the most commonly used analytical technique for gaining structural information about crystalline and polycrystalline, but not amorphous, materials. When an X-ray is incident on, and interacts with, an atom's electrons Rayleigh scattering occurs. In a crystalline structure, the regular repeat distance between atoms is in the angstrom region, similar to the wavelength (λ) of X-rays and thus their electron clouds can be used as a diffraction grating for Rayleigh scattering of a monochromatic source. Bragg's law is defined in **(1)** where d_{hkl} is the distance between two adjacent parallel planes and θ is the Bragg angle between the incident wave and the atomic planes. When the increased path length of diffracted incident waves (Figure 2.3) is equal to a multiple of the X-ray's wavelength, λ, then constructive interference will occur, whereas when this is not the case then destructive interference will occur, with the overall result of these reflections leading to a diffraction pattern. When the diffracted X-rays interfere constructively, then

Braggs' Law is been satisfied, whereas if the diffracted X-rays interfere destructively then Braggs' Law is not been satisfied.

$$n\lambda = 2d_{hkl} \sin\theta \quad \textbf{(1)}$$

If a sample is crystalline and single crystals can be grown then single crystal X-ray diffraction may be employed to determine the samples exact crystal structure (excluding hydrogen atoms, which are approximated). During single crystal X-ray diffraction, a sample is placed in a monochromatic X-ray beam and oriented through multiple angles in 3-dimensional space to obtain the full diffraction pattern, enabling structure determination. For an ideal polycrystalline material, every orientation of the crystal will be present equally in a sample and so full 3-dimensional data collection is not possible as there is a loss in reciprocal space from 3-dimensional to 1-dimensional. Consequently, powder X-ray diffraction is utilised to record diffraction patterns for polycrystalline materials that can be then refined using methods such as Rietveld refinement,[130] which uses a least squares approach, to identify the crystal structure. Some polycrystalline materials, which have crystals with large aspect ratios, where one dimension is significantly larger than the other dimensions, may lead to a preferred orientation in powder samples due to the crystallite anisotropy. This subsequently broadens the peaks in the diffraction pattern and without rectification, will prevent accurate analysis of crystallite size.[131] A transmission-mode diffraction analysis may be able to overcome this, as described below. When X-rays are incident on a sample with only some crystals aligned in the correct orientation then cones of diffracted rays are produced. Using a detector perpendicular to the incident X-ray beam can detect these cones and build up a more detailed diffraction pattern in 3-D, rather than reflection mode which only orientates within a single plane at varying angles (Figure 2.4), however data collection time is much greater.

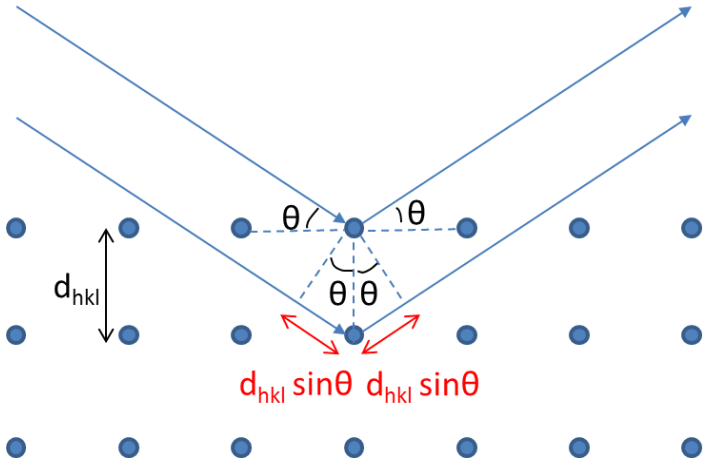

Figure 2.3 Schematic illustrating monochromatic rays incident on adjacent parallel planes at an incident angle θ having a difference in path length equal to $2d_{hkl}$ sinθ.

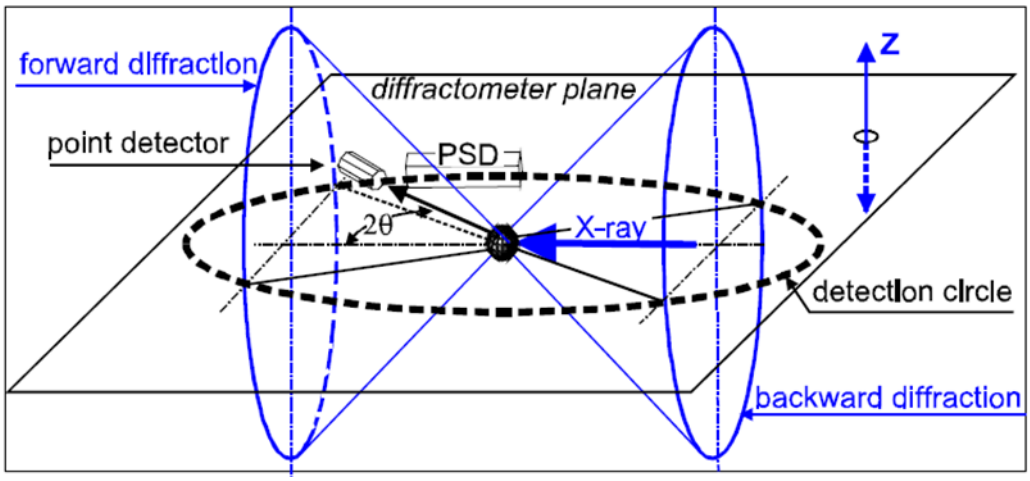

Figure 2.4 Comparison of conventional (black) and transmission (blue) x-ray diffraction. In conventional XRD reflection mode is used with the X-ray beam and detector orientated in a diffractometer plane, whereas in transmission XRD a detector is used which can detect in the z-plane. Taken from He *et al.*.[132]

Naturally occurring LDHs can be ordered enough to form single crystals,[133] however synthetic LDHs are invariably polycrystalline and thus powder X-ray diffraction must be employed rather than single crystal X-ray diffraction. The instruments used in this X-ray diffraction analysis, diffractometers, can be used in reflection and transmission modes. The X-ray diffraction in this thesis only uses the more common reflection mode. This work was carried out using an instrument at the Department of Chemistry, University of Cambridge.

Dried LDH (in an oven at 80 °C overnight and re-equilibrated in atmosphere) and calcined MMO (at 500 °C for 3 hours) materials described herein were finely ground with an agate pestle

and mortar, and then pressed onto a ground glass sample holder. Following this preparation the materials were characterised by powder X-ray diffraction (PXRD) using a Philips X'pert PW3710 diffractometer with Cu Kα radiation (λ = 1.5418 Å) at 15 °C. Cu Kβ radiation was removed through the use of a Ni filter. Diffraction patterns were acquired using a 2θ range of 3.00 to 80.00 degrees in 0.02 degree increments, with each step being held for 20.00 seconds. The divergence slit, which removes X-rays with large divergence angles, was fixed at 0.5 º and the anti-scatter slit, which is to ensure that only X-rays corresponding to the divergence slit arrive at the detector, was fixed at 1 º. The X'Pert HighScore Plus software package[134] was used to interpret the XRD data collected and indexing was attempted using the DICVOL automatic indexing algorithm,[1] with the data obtained shown in Appendix 1 and Appendix 2. The DICVOL method locates the unit cell parameters from the radial *d*-spacing by searching solutions in the parameter space for crystal systems of decreasing symmetry order. DICVOL indexing was carried out first through a search and match from the obtained peak list for each sample, then refining this cell, which was limited to rhombohedral/hexagonal systems. Despite the disordered nature of LDHs, various information can be obtained from the PXRD pattern, notably the cell parameters. The *c* parameter can be used to give the interlayer spacing and the *a* parameter can be used to find the divalent/trivalent cation ratio (*vide infra*). Both parameters are unaffected by stacking disorder, however the *a* parameter is indirectly connected with the stacking disorder since it accounts for the Al^{3+} substitution in the LDH lattice, which can contribute to lack of order in the stacking. LDHs are of hexagonal/rhombohedral symmetry where the *a* parameter equals the *b* parameter. This determination allows the cell to be defined. A typical LDH PXRD pattern is shown in Figure 2.5.

For rhombohedral systems the *c* parameter can be calculated from the (00l) reflections (Figure 2.6a) using equation **(2)**. The interlayer spacing is equal to one third of this value when taking into consideration a three-layer repeat. The thickness of one hydroxide layer is 4.8 Å, thus subtracting this from the interlayer spacing, the gallery height can be determined.

The lattice parameter a_0 can be determined using the (110) reflection (equation **(3))** (Figure 2.6b), found around 60 ° 2θ for Cu Kα radiation (equating to ~3 Å), since it is related to the average cation-cation distance for the hydroxide layer in LDHs. Equation **(3)** is derived from the fact that rhombohedral lattices can be split up into equilateral triangles, as shown in Figure 2.7, with lengths which are equal to the unit cell *a* parameter, being bisected by the d_{110} plane, giving the average cation-cation distance.

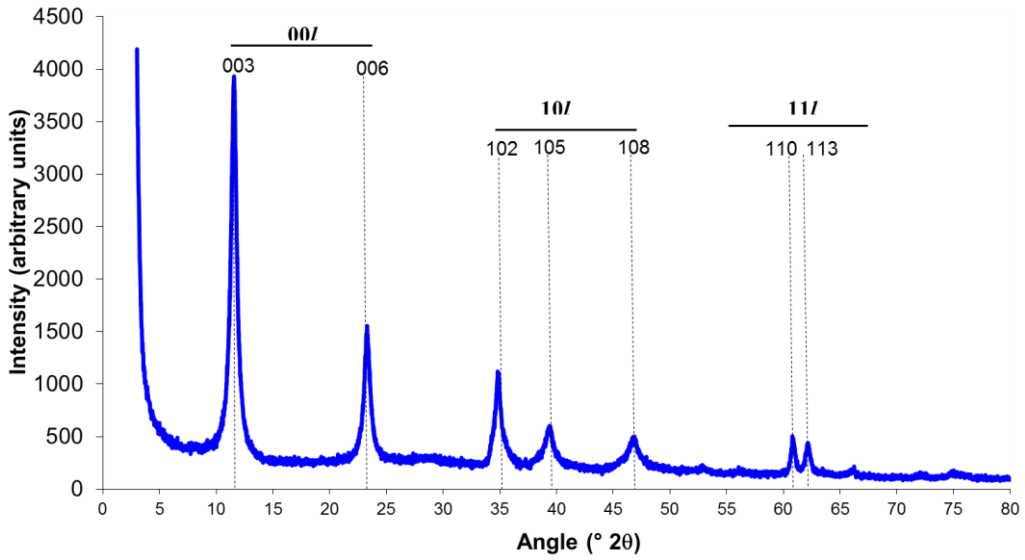

Figure 2.5 Powder X-ray diffraction pattern of $MgAl(CO_3)$ layered double hydroxide of Mg:Al 2:1, prepared by co-precipitation as described in section 3, illustrating the characteristic peaks of LDHs.

$$c = \frac{\mathrm{n}d_{(00n)} + 2\mathrm{n}d_{(002n)}}{2} \qquad \textbf{(2)}$$

$$a_0 = 2d_{(110)} \qquad \textbf{(3)}$$

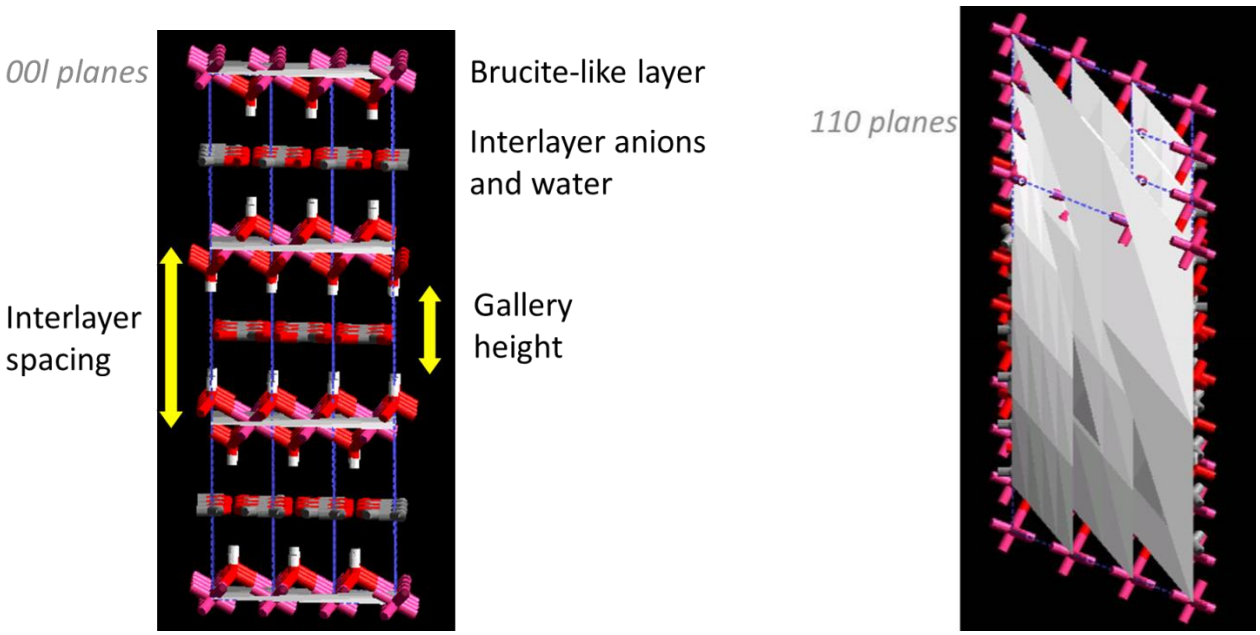

a) b)

Figure 2.6 a) 003 and b) 110 planes shown in silver for a layered double hydroxide 3R polytype.[133] Colour scheme: M(II) and M(III) ions purple; oxygen red; hydrogen white; carbon grey.

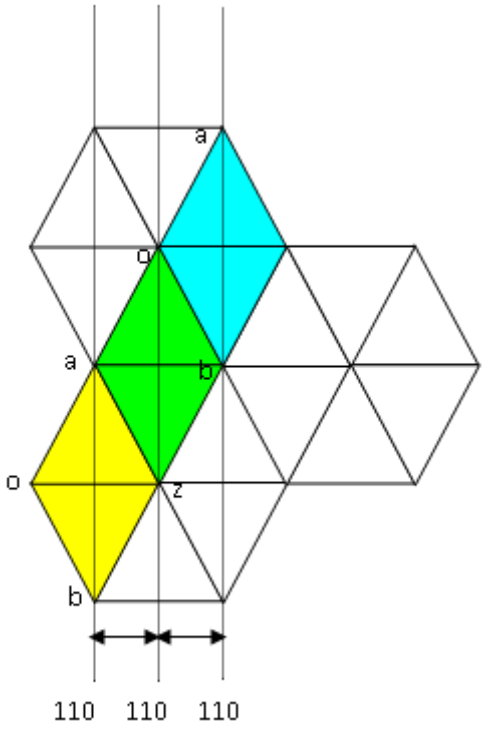

Figure 2.7 Schematic of a repeating rhombohedral unit cell. Splitting the yellow rhombohedron into equilateral triangles gives the relationship oa=az=oz. The new length oz is bisected by the 110 plane and so, through symmetry, leads to the relationship $a=2d_{110}$.

As M^{3+} exhibits a different cation radius to M^{2+} this results in a different cation-cation distance. Through empirical measurement of the range of cation ratios M^{2+}:M^{3+} a ratio relationship has been proposed by Kaneyoshi and Jones[135] (equation **(4)**) which can be utilised for nitrate and carbonate containing LDHs.

$$a(\text{Å}) = 3.1203 - 0.2346x \quad \textbf{(4)}$$

$$\text{Where } x = \frac{\text{Al}}{\text{Mg} + \text{Al}}$$

The crystallite size in the *a* and *c* directions can be determined from the Scherrer equation **(5)**. K is a constant (~1) which varies with the breadth taking method, λ is the incident wavelength of X-rays, β_{hkl} is full width at half maximum height (FWHM) for a specific peak and θ_{hkl} is the reflection angle at the specific peak centre. The Scherrer equation is only applicable to nano-scale particles and gives a lower limit for crystallite size. It follows that large line broadening occurs for small crystallites, but further line broadening in LDHs is uneven due to anisotropic bonding from structural disorder and preferred orientation during sample preparation.

$$L_{hkl} = \frac{K\lambda}{\beta_{hkl}.\cos\theta_{hkl}} \quad \textbf{(5)}$$

As LDHs can form different polytypes by stacking in a variety of ways, the *h*0*l* and 0*kl* reflections can be broadened. Polytypes do not affect the 00*l* or *hk*0 peaks since they are related to the cationic sheet and interlayer spacing. Turbostratic disorder, where basal planes are randomly orientated and misaligned, along the *c*-axis, can affect the 113 and 0*kl* reflections to a certain degree.[136] 00*l* peaks can also be broadened by interstratification where there is an irregular repeat of two different interlayers.

Impurities and by-products present from synthesis may also identified by PXRD to confirm if the LDH is a pure-phase. MgO or similar compounds may be present and identified, however amorphous aluminium oxides will not be observed in the PXRD as it has no atoms with regular spacing to diffract X-rays in such a way that a pattern forms.

2.2.2 Thermogravimetric analyses

Thermogravimetric analyses (TGA) involve a sample being heated in an atmosphere, typically an inert gas, and associated weight losses recorded as a function of temperature. Weight losses can be attributed to desorption, dehydration and decomposition though weight gains may be attributed to, for example, oxidation if a non-inert atmosphere is employed. TGA can also be combined with a mass spectrometer (MS) leading to TGA-MS analysis so gases can be identified during weight loss. In TGA-MS the inert gas is used as a carrier gas to transport any evolved gases through the instrument.

For LDHs, prominent weight loss regions during TGA are:[137-139]

a) Up to 100 °C leads to loss of adsorbed surface water
b) 100-250 °C leads to loss of interlayer water
c) >250 °C leads to organic interlayer species decomposition and CO_2 evolution
d) 400-600 °C M^{2+}/M^{3+} layer dehydroxylation.

Often the latter two steps (c) and d)) overlap.[138]

For the work reported here, TGA was performed using a Perkin Elmer Pyris 1 instrument. Samples were heated from room temperature to 1000 °C in a Nitrogen atmosphere at flow rate of 20 ml/min and a heating rate of 10 °C / min and cooled back to room temperature at a rate of 10 °C / min, with mass changes for the various LDH materials being monitored throughout. TGA-mass spectrometry was also used to examine the evolution of CO_2 and H_2O as a function of temperature. TGA was carried out by the thermal analysis service within the Chemistry Department, Durham University.

2.2.3 Scanning electron microscopy

The wavelength of light limits optical microscopy to around 0.2 micrometres before diffraction effects occur, so electromagnetic wavelengths shorter than this are required for surface image and topography on a nanometre scale. Electrons exhibit a de Broglie wavelength, owing to the wave-

particle duality of matter, which is much shorter than that of light (400 – 700 nm) and so leads to images with high resolution. In scanning electron microscopy (SEM) a beam of electrons is directed onto a sample to produce an image of its surface at very high magnification (greater than 500 000) times (Figure 2.8), although individual atoms themselves cannot be seen. The wavelength of light limits optical microscopy to around 0.2 micrometres before diffraction effects occur, so electromagnetic wavelengths shorter than this are required for surface imaging and topography analysis on a nanometre scale. Electrons exhibit a de Broglie wavelength, owing to the wave-particle duality of matter, which is much shorter than that of light (400 – 700 nm) and so leads to images with high resolution.

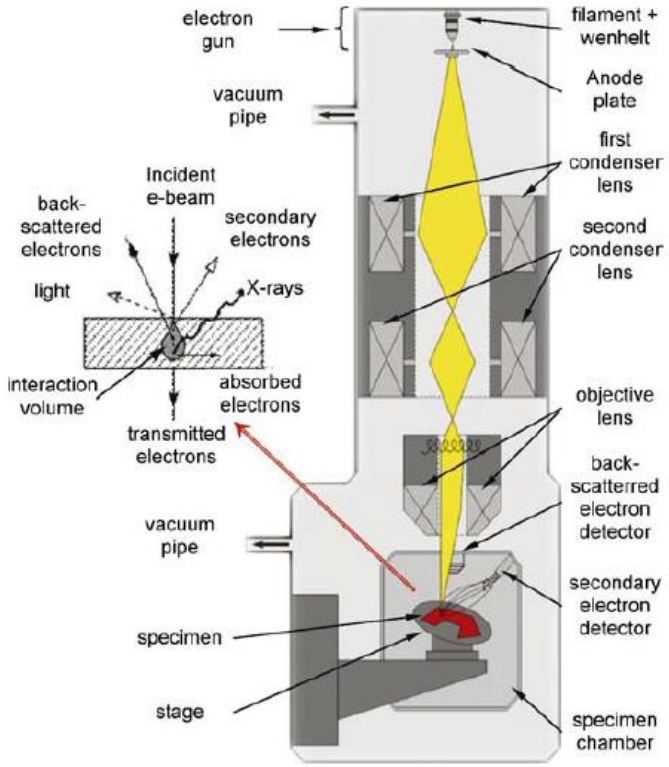

Figure 2.8 Schematic of a typical scanning electron microscope, with the electron beam show in yellow and sample in red. Taken from Sutton *et al*..[140]

SEM was used to study the surface topography of LDHs during the work undertaken in this thesis and to determine sample crystallite size. Figure 2.9 shows a scanning electron micrograph of a representative LDH sample (as prepared in Section 3), and allows sub-micron resolution images to understand morphological differences in LDHs. Energy dispersive X-ray (EDX) spectroscopy was used for quantitative and qualitative elemental analysis. This work was carried out with the

assistance of Mr Leon Bowen, Department of Physics, Durham University. A Hitachi SU70 (SEM) with a Schottky Field Emission Gun (FEG) was used to produce high resolution surface images. This type of FEG has a thermionic emitter utilising a tungsten tip coated with zirconium oxide, which has greater electrical conductivity at higher temperatures, which leads to a lower surface barrier when in a high electric field. Thermionic emitters usually employ a filament, commonly of tungsten, which is heated to over 1000 K in a vacuum. Due to the large amounts of thermal energy generated, the electrons have greater energies than the work function of the metal, W, and leave the filament. With a Schottky FEG comprising a sharp tip rather than a filament, this results in a more intense beam of electrons with greater electron brightness. Brightness refers to the number of electrons directed at a certain area per second. Also, with FEG the energies of electrons are more coherent leading to increased signal to noise ratio. The beam undergoes acceleration as it passes through a high potential difference, then is focused by electromagnetic lenses in a vacuum chamber onto the surface of the material being studied. Secondary electrons are then emitted by the coated sample and scattered to a detector, from which the image can be constructed.

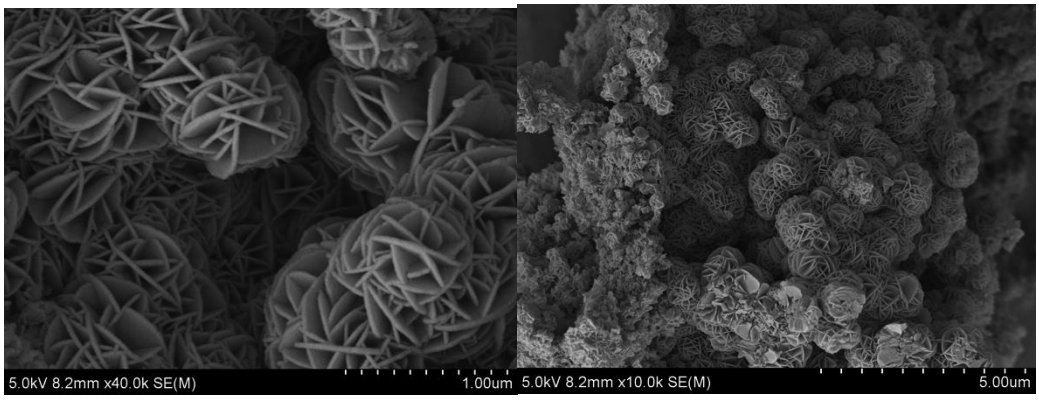

Figure 2.9 Scanning electron micrograph of $MgAl(CO_3)$ layered double hydroxide of Mg:Al 3:1, prepared by co-precipitation, as described in Section 3. The LDH particles are composed of *rose des sables* structures, with inter-crystal growth.

For samples analysed in this thesis, where only imaging was required, a cotton bud was used to sprinkle LDH/MMO sample onto a double-sided sticky carbon pad mounted on an aluminium stub.

The sample was then coated with a 15 nm thick layer of Pt using a Cressington 328 UHR sputtering system.

For SEM-EDX sample preparation, where elemental analysis was needed, a cotton bud was used to sprinkle a LDH/MMO sample into a mould, which was filled with epoxy resin and catalyst mixture in the ratio 5:1 then left to harden. The resulting epoxy was then subject to grinding and polishing to expose the solid sample, which was then coated in 40 nm of carbon. This sample was then mounted on an aluminium stub.

2.2.3.1 Element quantification by scanning electron microscope energy dispersive X-ray spectroscopy

For quantitative and qualitative analysis of element composition of the samples, SEM-EDX was used. This technique involves high energy electrons being focused onto a sample, causing secondary electrons to be expelled from the atoms, leaving electron holes. The atom shifts from the ground state to an excited state, but then proceeds to return to the ground state. This results in an electron from a higher energy level filling the electron hole and the energy difference between the higher and lower shell is then emitted as radiation. If this involves an inner energy level, it results in the energy being in the form of a secondary x-ray. As each atom has a discrete set of energy levels between which electrons can transfer, this results in characteristic wavelengths of x-ray being emitted for each atom.

$$C_{spec} = \frac{N_{spec}}{N_{std}} C_{std} = kC_{std} \quad \textbf{(6)}$$

For quantitative data the number and energy of X-rays can then be measured relative to a standard. For this work a pure cobalt standard was used to calibrate the in-built virtual standards of the instrument. The number of counts from a specimen, N_{spec}, is compared to the number of counts for a standard, N_{std}, (both minus the background count) in a specified time, then multiplied by the

concentration of the standard, C_{std} **(6)**. ZAF corrections are then applied for: atomic number correction (Z) of atomic stopping power and backscatter terms; absorption (A) of X-rays by the atom; and X-ray induced excitation fluorescence (F) effects prior to obtaining the composition.[141] Thus a percentage of elements can be determined for a sample, either at a specific point or over areas of the sample. A typical SEM-EDX analysis is shown in Figure 2.10.

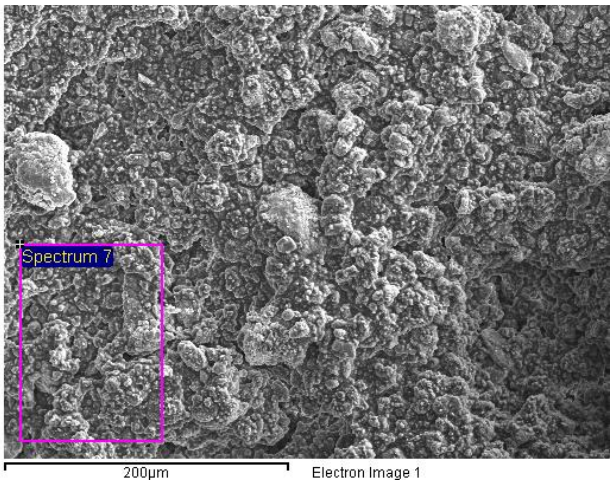

a)

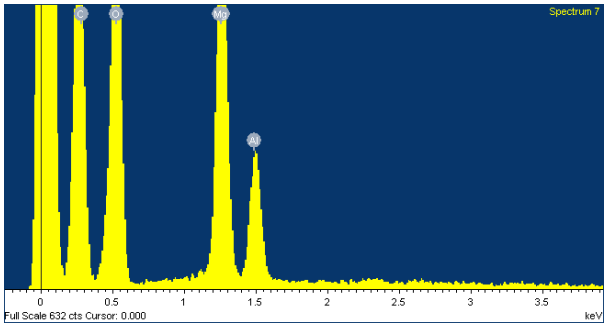

b)

Figure 2.10 Typical analysis using scanning electron microscope energy dispersive X-ray spectroscopy showing a) $MgAl(CO_3)$-layered double hydroxide of Mg:Al 3:1, prepared by co-precipitation as described in section 3, with area of analysis marked and b) EDX analysis element plot.

2.2.4 Inductively coupled plasma optical emission spectroscopy

Inductively coupled plasma optical emission spectroscopy (ICP-OES) is comprised of two parts. The plasma is created using a coil with a current of varying frequency, which in turn creates a varying magnetic field. This creates charged particles in a rarefied gas (such as argon), which flows in a rotationally symmetric pattern towards the magnetic field, resulting in inelastic collisions with

neutral atoms creating a plasma of around 7000 k. A peristaltic pump is then used to pass the sample into a nebuliser, prior to it being injected directly into the plasma and colliding with ions and electrons, breaking down into charged ions and atoms. These atoms constantly lose electrons, form ions, and then reform as atoms again, emitting characteristic wavelengths during this process.

The materials in this thesis were analysed using a Perkin Elmer Optima 3300RL instrument, which was calibrated with Mg/Al standards (2 ppm, 5 ppm, 10 ppm) made from Romil 1000 ppm stock solutions. Multiple wavelengths (aluminium: 396.193 nm, 308.215 nm, 394.401 nm, 237.313 nm; magnesium: 285.213 nm, 279.077 nm, 280.271 nm, 279.552 nm) were measured to confirm that these were interference/error-free and the standards were analysed every ten samples to confirm instrument calibration (Table 2.1). 0.1 g of each sample to be analysed was dissolved in 2.5 ml concentrated HNO_3 for 24 hours and then diluted 100-fold with high purity water prior to analysis.

Table 2.1 Standards analysed every ten samples to reconfirm ICP-OES instrument calibration, showing the calculated ppm values for each solution according to the elemental characteristic wavelengths. Figures in parenthesis are the standard deviation.

Element	Wavelength (nm)	Stock solution X ppm			
		2 (ppm)	5 (ppm)	10 (ppm)	2 (ppm)
Al	396.153	2.0470 (0.0160)	5.3780 (0.0188)	10.4000 (0.0300)	2.0720 (0.0164)
	308.215	2.0700 (0.0158)	5.2950 (0.0248)	10.2200 (0.0632)	2.0860 (0.0150)
	394.401	2.0700 (0.0096)	5.2790 (0.0424)	10.2400 (0.0616)	2.0830 (0.0238)
	237.313	2.0660 (0.0297)	5.2860 (0.0425)	10.2300 (0.0803)	2.0860 (0.0462)
Mg	285.213	2.0220 (0.0153)	5.5830 (0.0251)	10.1300 (0.0310)	2.0400 (0.0154)
	279.077	2.0230 (0.0280)	5.5330 (0.0441)	10.0600 (0.0722)	2.0410 (0.0199)
	280.271	2.0200 (0.0212)	5.5590 (0.0294)	10.1000 (0.0289)	2.0380 (0.0107)
	279.553	2.0270 (0.0233)	5.5870 (0.0298)	10.1000 (0.0293)	2.0450 (0.0113)

2.2.5 Surface area analysis

Exploiting the phenomenon of adsorption, surface area analysis can be carried out. Surface adsorption is where atoms adhere to a sample, most commonly gas atom substrate adsorbing onto a solid adsorbate, due to chemisorption (covalent/ionic bonding) or physisorption (van-der-Waals bonding). As the gas atoms are accommodated, this leads to a reduction in pressure. The surface area analysis instrument measures changes in pressure from which it computes the volume of gas adsorbed. According to Brunauer-Emmett-Teller (BET) theory the specific surface area can be determined by altering the pressure of a system and creating an isotherm of gas adsorption.[142] BET theory was developed as a multilayered variant of Langmuir theory,[142] the latter stating that the adsorbate only contains a monolayer of adsorbed atoms at equivalent adsorption sites. In the BET equation **(7)** V is the adsorbed gas quantity, V_m is the adsorbed monolayer gas quantity, p is the equilibrium pressure of adsorbates at the adsorption temperature, P_0 is the saturation pressure of adsorbates at the adsorption temperature and c is the BET constant. A plot of $1/(V[(P_0/P)]–1)$ against P/P_0 (called a BET plot) enables V_m and c to be calculated, which can be further used to determine the specific surface area, S_{BET} **(8)**, where $S_{BET,\ total}$ **(9)** is the total surface area , N is Avogadros number, s is the adsorption cross-section of the adsorbing species and *a* is the mass of adsorbate.[143]

$$\frac{1}{V[\frac{P_0}{P}-1]} = \frac{1}{V_m c} + \frac{(c-1)\frac{P}{P_0}}{V_m c} \quad \textbf{(7)}$$

$$S_{BET} = \frac{S_{BET,total}}{a} \quad \textbf{(8)}$$

$$S_{BET,total} = \frac{(V_m N s)}{V} \quad \textbf{(9)}$$

BET theory has some disadvantages due to the assumptions it encompasses, which are not entirely valid for all, for example, the adsorbate surface is not always energetically homogeneous, which

results in deviations at low pressure.[144] Similarly, it is also assumed that monolayer coverage occurs before multilayer coverage, which is not always the case in microporous solids where capillary condensation occurs readily in pores before monolayer coverage, leading to an unrealistically high surface area measurement.[145]

The various types of physisorptions obtained from surface area analysis are shown in Figure 2.11. Type I isotherms result from microporous solids with small external surfaces. Type II are observed with non-porous/macroporous materials. Type III are a rare case and caused by adsorbent-adsorbent interactions, for example with Br_2 adsorption on silica gel.[146] Type I-II adsorptions are reversible. In contrast, type IV isotherms exhibit a hysteresis loop due to capillary condensation in mesopores. Point B in Type II and Type IV isotherms indicates where the monolayer adsorption is complete and from where multilayer adsorption commences. Type V isotherms are rare and are related to Type III, but occur with certain porous materials, *e.g.* phosphorous on NaX.[146] Type VI isotherms show multilayer adsorption on a uniform non-porous surface.[143]

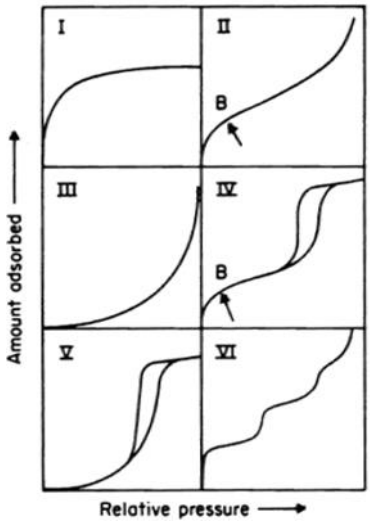

Figure 2.11 Type I-VI gas physisorption isotherms obtained from surface analysis, as identified by IUPAC. Taken from Sing *et al.*.[143]

The method of Barrett-Joyner-Halenda (BJH)[147] is a procedure for calculating pore size distributions from experimental isotherms using the Kelvin equation **(10)**, but applying the fact that there will already be condensed multilayers on the pore walls which must be added to this value

(11). The Kelvin equation **(10)** predicts for a particularly-sized cylindrical pore, the specific pressure at which adsorbed gas will condense and evaporate, where r_k is the mean radius of curvature of the liquid meniscus, γ is the liquid surface tension and θ represents the contact angle between solid and condensed phases. To calculate the actual radius of the pore, the statistical layer adsorption thickness for each experimental P/P_0 value must first be calculated by comparing the isotherm obtained for the sample to that of N_2 adsorption on a non-porous reference sample of similar surface characteristics, obtaining the increased thickness (t) of the layers. Using this value the actual pore size (r_p) can be calculated **(11)**. Upon desorption for some materials a "spike" is sometimes observed in the pore width results after the end point of hysteresis has been reached. This is due to a large release of the adsorbed gas at the end of hysteresis and should be omitted when calculating the average pore width.[148]

$$\ln \frac{P}{P_0} = -\frac{2\gamma V_m}{r_k RT}\cos\theta \qquad \textbf{(10)}$$

$$\text{where } r_k(\text{Å}) = \frac{4.15}{\log(\frac{P_0}{P})}$$

$$r_p = r_k + t \qquad \textbf{(11)}$$

Specific surface area, pore volume and average pore size measurements were performed in this thesis by N_2 adsorption and desorption at –196 °C, using a Micromeritics ASAP 2020 system. For each sample analysed, 0.5 g of finely ground sample was placed in a pre-weighed analysis tube (m_1) which was connected with a de-gas port and heated at 80 °C (LDH) or 200 °C (MMO) for 4 h under a vacuum of 200 µm Hg to remove any volatile materials adsorbed on the surface. After this, the sample was cooled to room temperature and then the tube with degased sample was re-weighed (m_2), with the accurate mass of the sample being the mass difference (m_2 - m_1). An isothermal jacket was placed over the tube and it was connected to an analysis port, cooled under liquid N_2 and degassed. The sample then underwent nitrogen adsorption/desorption at various pressures.

2.2.6 Estimation of basicity

LDHs prepared *via* co-precipitation and co-hydration and their calcined MMO derivatives were analysed semi-quantitatively for basicity with the assistance of Dr Louise Gildea using appropriate solutions of the Hammett base indicators: bromothymol blue (pH range 6.0 – 7.6), *m*-cresol purple (pH range 7.6 – 9.2), phenolphthalein (pH range 8.0 – 10.0) and indigo carmine (pH range 11.5 – 13.0) (Table 2.2). according to a previously-reported protocol.[122] These indicators can probe the lateral crystal faces and outer crystal surfaces of the insoluble LDH materials, where catalysis is believed to occur, measuring the strength of basic sites present, with often more than one type of basic site strength being found to exist in any given sample.[149] However it must be noted that there may be entrained acid or base resulting from LDH synthesis which may affect these results.[81] Similarly, the solvent may be interacting with the indicators. Jinesh *et al.*, using Hammett base indicators, found that carbonate-containing LDHs had $15 > pK_a > 11$.[150] Similarly, Chisem and co-workers found a $pK_a > 12$ for both pre- and post-calcined LDHs heated at 400 °C for 2 hours.[151] Other studies have found calcined Mg-AL carbonate LDHs to have basicity in the region $11 > pK_a > 9.9$, with pK_a as high as 12.2 for rehydrated samples.[152] Xie *et al.* found basic sites in the range of $9.8 > pK_a > 7.2$ and $15.0 > pK_a > 9.3$ to exist in calcined carbonate LDHs of R-value 2-4.[149] In summary, a range of different pKa values have been obtained in the literature for LDHs which demonstrates the tunability of their catalytic applications depending on their starting materials and synthesis methods.

Table 2.2 Hammett indicators used to probe basicity in this thesis.[82]

Indicator	pK_a range	Colour in acid	Colour in base
Bromothymol blue	6.0 - 7.6	yellow	blue
M-cresol purple	7.6 - 9.2	yellow	purple
Phenolphthalein	8.0 – 10.0	colourless	magenta
Indigo carmine	11.5 – 13.0	blue	yellow

Limitations associated with the use of Hammett base indicators for measurements of basicity with insoluble LDHs and MMOs include that the testing requires visual inspection of colour changes, which may be weak and unreliable. Thus, these semi-quantitative results are now more often looked at in conjunction with quantitative tests such as CO_2 titration and temperature programmed desorption (TPD)[153].

Adapting a method used by Brito *et al.*[154], 5 mg of the solid sample to be analysed was first added to a test tube, followed by 2.5 mg indicator and 2.5 ml methanol. The test tube was then sealed and left for 5 minutes before being placed in a sonicator for 1 hour to equilibriate. After 1 hour the colour of the solution was noted. Each indicator was added in succession to test tubes containing separate samples of each solid until there were no further colour changes associated with increasing basicity.

2.2.7 Elemental analysis

C, H and N analysis on the LDH samples prepared in this thesis was carried out by the Microanalysis service within the Chemistry Department, Durham University. Approximately 3 mg of sample was placed in a tin capsule which is exposed to a high oxygen environment at 950 °C using an Exeter analytical CE-440 elemental analyser. This leads to combustion of the sample and tin oxide formation, which elevates the internal temperatures to over 1800 °C and forms CO_2, H_2O, N_2 and NO_x. NO_x is then reduced to nitrogen and the sample passes over a thermal conductivity detector (TCD) allowing calculation of the percentage composition in the solid sample.

2.2.8 Fourier transform infra-red spectroscopy

Fourier transfom infra-red (FTIR) spectroscopy can be used to explore the absorption of specific wavelengths in the infra-red region of the electromagnetic spectra (400 – 4000 cm^{-1}) by functional groups within a molecule. Absorption of these wavelengths occurs, for atoms where a change in dipole moment can occur, when they equal the resonant frequencies of their natural bending and

stretching vibrational modes. These can then be used in structure determination, allowing the changes in the cationic sheets associated with changing M^{2+} and varying the M^{2+} content which in turn also affects OH^- and H_2O adsorption bands.[155] FTIR is mainly used to determine the functional groups present in organic molecules with characteristic frequencies absorbed and can thus be used to study LDH interlayer anions[156]. Impurities of the M^{2+} and M^{3+} metal hydroxides such as brucite and gibbsite, with their strong adsorption bands at ~3700 cm^{-1} due to OH^- can also be detected *via* this method.[157] A typical infra-red spectra of MgAl–carbonate LDH before and after thermal activation is show in Figure 2.12, with loss of carbonate (1300-1550 cm^{-1}) and hydrogen bonding OH groups (3300 cm^{-1}) upon decomposition to a MMO.[158]

Within this thesis FTIR was used on pre- and post-calcined samples to check for the decomposition of LDHs to form MMOs through removal of carbonate, which is FTIR-active and thus should not appear in the MMO spectra. FTIR spectra were recorded from 1000 to 4000 cm^{-1} on a Perkin Elmer 1600 Series instrument with 8 cm^{-1} resolution over 16 scans.

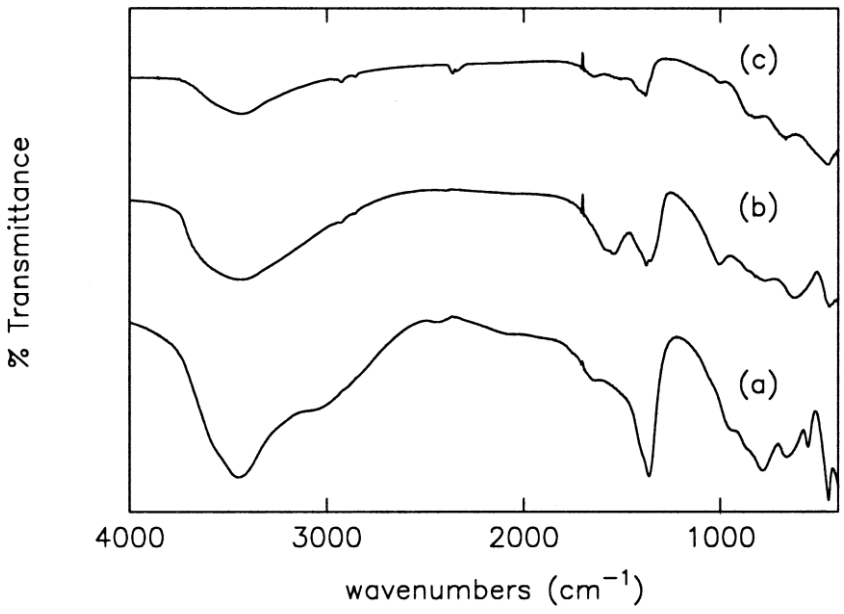

Figure 2.12 A typical infra-red spectra of MgAl–carbonate LDH a) before and after thermal activation at b) 483 K and c) 823 K. Taken from Kagunya *et al*. Characteristic carbonate symmetric and anti-symmetric stretching vibrational modes are in the region 1300-1500 cm^{-1}, along with polymeric hydrogen-bonding at 3300 cm^{-1}.

2.3 Analysis of organic liquid reaction products in this thesis

Owing to the complexity of possible products and co-products resulting from catalytic reaction trials within this thesis, complimentary analysis methods are required. Therefore a combination of gas chromatography and mass spectrometry is utilised to qualitatively and quantitatively evaluate the organic solid and liquid phase components.

2.3.1 Gas chromatography

Gas chromatography (GC) is a technique used for both qualitative and quantitative analysis of mixtures that have boiling points typically below 300°C and that do not decompose upon vapourisation. GC can be used to check, for example, components in a mixture, purity of a sample and completeness of a reaction. If components to be separated are in liquid or solid phase at room temperature, then these must be dissolved in a solvent and both solvent and sample vapourised in the gas chromatograph (GC), whereas gaseous samples do not require this step. In the work described in this thesis, gaseous samples were not analysed so only solid and liquid analysis will be described. A solid or liquid sample to be analysed is prepared at a known dilution in a solvent, often with a reference standard, which does not interact with the system. A small volume of this sample (typically 5 μl) is injected manually or automatically by an autosampler into the GC injector, which is commonly a split/splitless type. In this chamber the sample is vapourised without undergoing decomposition and a carrier gas such as helium carries some, or all, of the sample onto the column. For very dilute solutions the injector is set to splitless mode where 100 % of the sample transfers onto the column, whereas for high concentrations the split mode is used where only a portion of the sample is carried onto the column and the rest goes to vent. The components then flow through a narrow column, which contains a stationary phase that is chosen for, and used to, separate specific components in the mixture. Capillary columns (which can be several tens of meters long) are coated with the stationary phase and as the components travel along it some are

more strongly adsorbed than others (due to polarity, for example) thus leading to separation. Separation is also affected by temperature, the higher the temperature of a column the faster the analytes will flow through it. The GC column is housed in an oven and during a typical GC analysis the temperature may be constant (isothermal) or ramped up to speed up elution time on the column and/or held to separate components, eluting very close to each other. Following this, the sample passes through a detector, which, in this work, was a flame ionisation detector (FID). These detectors are ideal for analysis of organic molecules and have high sensitivity. In a FID, hydrogen is combusted in air to create a high temperature flame, with electrodes either side of it. As organic sample passes through the flame it is pyrolysed, creating cations and electrons, which creates an electric current between the electrodes and is recorded as an electronic signal. The time taken from injection to detection is known as the retention time and using reference standards the material can be identified. Calibration curves of known concentrations must be constructed to perform quantitative analysis of a mixture. A schematic illustrating the processes involved in gas chromatography is shown in Figure 2.13.

2.3.1.1 Analysis of liquid reaction products by gas chromatography

The samples were analysed with a gas chromatograph (GC, HP 5890 Series II) equipped with a nonpolar column (VF-5MS, with dimensions 30 m x 0.25 mm x 0.25 μl) and a flame ionisation detector (FID). Each sample was injected (5 μl) into the GC with helium as the carrier gas at pressure of 2.07 bar. The injector and detector temperatures were 250 and 275 °C respectively. The GC was kept at 200 °C throughout the whole run. Chemical standards of n-heptadecane (99 %), eicosane (99 %), stearic acid (97 %) (including the silylating agents pyridine [analytical grade] and BSTFA [98^{+} %]) and the solvent dodecane (99 %) were purchased. Quantitative calculations were performed using the internal standard (eicosane) method to produce calibration curves for the reactants stearic acid and the product n-heptadecane. Data analysis and peak integration were performed by Clarity software.[159]

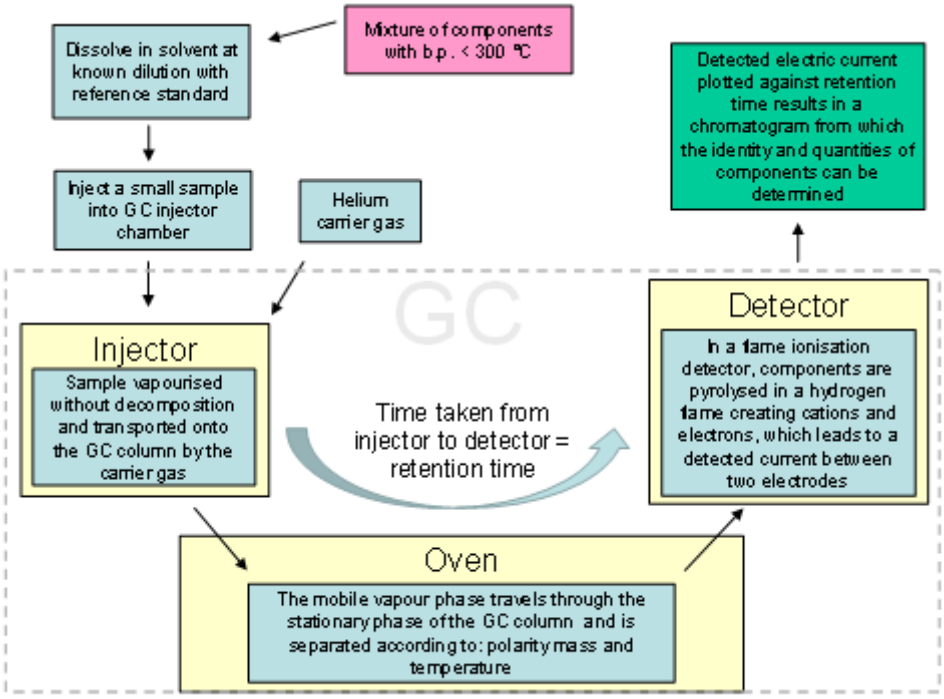

Figure 2.13 Schematic illustrating the processes involved in gas chromatography.

2.3.1.2 Analysis of Solid Reaction Products by Gas Chromatography

The solid samples produced were analysed after Soxhlet extraction using ethanol at reflux. Solid product calibration samples were analysed with a gas chromatograph (GC, HP 5890 Series II) equipped with a Thermo Scientific Trace-simulated distillation capillary column (length 10 m, ID 0.53 mm and film thickness 2.65 µm) and a flame ionisation detector (FID). The injector and detector temperatures were 250 and 350 °C respectively. Each sample was injected (5 µl) into the GC with helium as the carrier gas at pressure of 2.07 bar. The GC temperature program was based on ASTM D6584 10ae1 Standard Test Method for Determination of Total Monoglyceride, Total Diglyceride, Total Triglyceride, and Free and Total Glycerin in B-100 Biodiesel Methyl Esters by Gas Chromatography.[160] The GC was held at 50 °C for 1 min, then ramped at 15 °C /min up to 180 °C, followed by ramping at 7 °C /min up to 230 °C, then increasing up to 350 °C at 10 °C /min where it was held for 5 mins. Chemical standards of eicosane (99 %), stearic acid (97 %) (including

the silylating agents pyridine [analytical grade] and BSTFA [98^{+} %]), stearone [95 %] and the solvent tetrahydrofuran (THF) were purchased. Quantitative analysis to produce calibration curves were performed using the methods described in section 5.2.4. Data analysis and peak integration were performed using Clarity software.[159]

2.3.2 Mass spectrometry

Mass spectrometry is a technique which analyses a sample and produces a spectra based on the mass/charge ratio. Samples are admitted to the mass spectrometer and ionised, typically by bombardment with electrons. The ions then pass through a mass-to-charge analyser which, if the ions all have the same charge, separates them according to their mass. Time of flight (TOF) analysers make use of an electric field for this purpose, where lighter ions pass through to the detector first, whereas quadrupole analysers use an oscillating electric field to create an oscillating mass-selective filter. A detector is then utilised to detect electric current produced or charge induced when the analyte reaches it.[161]

Mass spectrometry was performed by the Durham University Chemistry Department Mass Spectrometry Service. Soxhlet extracted solids were analysed using a Xevo QToF mass spectrometer (Waters Ltd, UK) equipped with an Agilent 7890 GC (Agilent Technologies UK Ltd, UK) and an atmospheric solids analysis probe (ASAP) solid handling sample introduction port. Solid samples were introduced into the spectrometer from a heated melting point tube (ramp from 100 °C to 600 °C over several minutes), previously dipped into neat sample. Mass spectrometry data were processed using MassLynx 4.1[162]. Exact mass measurements were recorded using a lock-mass correction to provide < 3 mDa precision.

2.4 Combined analysis of layered double hydroxides and catalysis

The techniques outlined in this chapter offer complimentary data to each other, therefore, these techniques must be utilised in combination in order to gather accurate data on the systems involved.

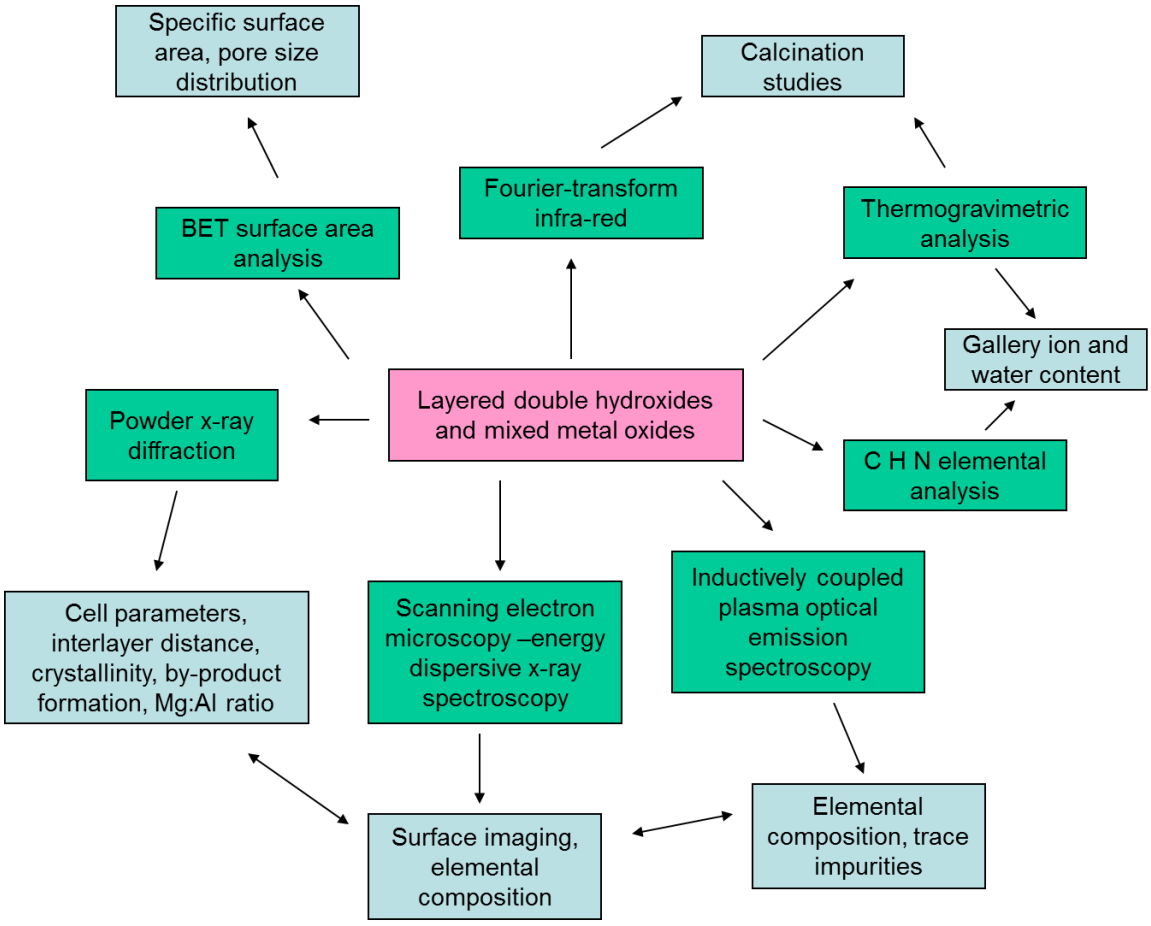

Figure 2.14 Schematic illustrating the techniques utilised in this thesis for analysis of LDHs and MMOs.

An overview schematic for the analysis of the LDH and MMO samples is shown in Figure 2.14. For the inorganic components PXRD was used to measure the various cell parameters of the LDH, interlayer distance and crystallinity. The formation of crystalline by-products can be determined and the Mg:Al ratio for the sample determined, both from XRD and ICP-OES. Following this, SEM can be used for surface imaging and elemental composition of specific sites and areas to complement the data from PXRD and ICP-OES. The latter technique can also be used to detect for trace impurities in the materials. TGA and elemental analysis can be used in conjunction to determine the gallery ion and water contents. BET studies can give information on

the specific surface area and pore size distribution, which are important when studying active sites for catalysis. Finally MMOs, a noted difficult group to study due to their rapid reaction with oxygen and moisture from the air post-calcination, however TGA can be used to study the calcination reaction and FTIR can further check for decomposition of hydroxyl groups, bonded water and interlayer anions from the LDH parent material.

An overview schematic for the liquid and wax sample analysis is shown in Figure 2.15. For the organic components GC analysis is the major tool for catalytic reaction data, post-reaction, however this relies upon reference standards being available for both quantitative and qualitative analysis. Mass spectrometry, or other structure probing techniques, must be utilised for unexpected or unknown reaction products to initially determine their structure. Following from this, GC standards may then be sought to allow full quantitative and qualitative analysis of reaction products to be undertaken.

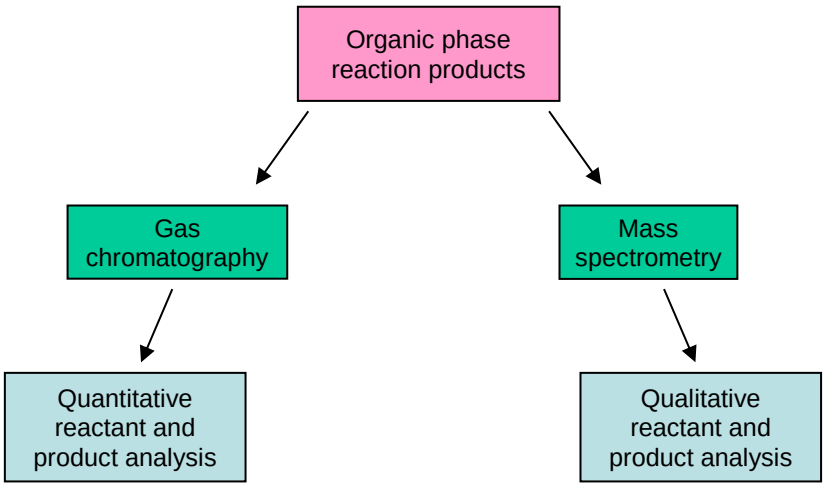

Figure 2.15 Schematic illustrating the techniques utilised in this thesis for liquid and wax phase analysis

2.5 Analysis of error

There exists the potential for error in all analytical techniques. For each described here, calibrations will be carried out in replicates, along with calibration checks performed during analysis to ensure consistency and minimise error, as well as carrying out replicates on the samples being analysed.

2.6 Uncertainty in characterisation methodology

Within this body of work there exists the potential for errors incurred from the methods involved both experimentally and analytically. LDH samples were prepared in bulk for this thesis, with samples produced in duplicate to ensure consistency. A number of areas of LDH and MMO structure chemistry are challenging to characterise with only a limited amount of information being realised. A characterisation strategy has been outlined above, however this may have its own limitations as to the real structures and properties of the materials involved.

A small number of LDH/MMO materials may be of low crystallinity resulting PXRD patterns with broad reflections being obtained, which may not refine to give cell parameters. Following this, these materials would then have to be assigned according to prior literature, leading to uncertainty in their determination. In addition the interlayer for LDHs cannot readily be probed for most anions, with only information on gallery height being obtained from the PXRD pattern.

In the calcining of LDHs to MMOs, variables include temperature, atmosphere and time of reaction, leading to complications between inter-study comparisons. There may be further effects of calcination conditions impacting on certain analysis methods more than others resulting in misrepresentation. The exact surface/structure of MMOs is hard to establish due to it being notoriously difficult to study, and with MMOs readily hydrating to LDHs this further hinders study.

Errors may be incurred in BET theory since it assumes that the adsorbate surface is homogeneous, the heat of adsorption is also assumed to be the same from the 2nd layer upwards and any intra-layer interactions between adsorbed molecules are disregarded, however these assumptions are not always true. Also, the BJH method for measuring pore size assumes that the pores are cylindrical, which is not always true for all surfaces and edges in the LDH structure.

Hammett base indicators require visual inspection of colour changes for measurements of basicity, which may be subtle and difficult to quantify. With the Hammett indicators being tested in a polar solvent,[154] and the possibility of methoxide ions being formed then these may also be interacting in the system. Thus the semi-quantitative Hammett indicator results could be looked at

in conjunction with quantitative tests such as CO_2 titration and temperature programmed desorption (TPD), though the information from these techniques is still limited in that they will not probe the LDH interlayer.

To account for these errors, analyses were recorded in duplicate and, where possible, complimentary data was sought between techniques to confirm the data obtained. Analyses were also compared and contrasted to literature studies for similar materials to qualitatively and quantitatively ascertain the suitableness of the obtained data, resulting in further analysis or techniques if large discrepancies occurred.

3 Synthesis and characterisation of Mg-Al layered double hydroxides and mixed metal oxides

3.1 Review of layered double hydroxide synthesis methods

Layered double hydroxides (LDHs) ($Mg_6Al_2(OH)_{16}CO_3 \cdot 4H_2O$) are a diverse set of materials containing multiple cations of varying valencies, along with hydroxide groups and also anions, located within the interlayer.[80] With such a wide range of materials possible there exist a multitude of synthetic methods by which these materials may be prepared. Some of the more commonly encountered methods in the literature will be reviewed in the following section 3.1, along with the preparation methods utilised within this thesis (section 3.2) and subsequent material analysis (section 3.4).

3.1.1 Layered double hydroxide synthesis *via* co-precipitation

The most commonly encountered method in the literature for synthesising LDHs is *via* co-precipitation, an approach that can be further sub-classified according to whether the reaction is undertaken at constant pH,[135] or at variable pH method, as both studied by Crepaldi.[163] Co-precipitated LDHs may be prepared with the anion of interest, (direct synthesis) or with a labile anion to be replaced subsequently in anion exchange synthesis.

Co-precipitation of metal salts takes place under conditions of supersaturation. Initially, a solute is dissolved in a solution at a higher concentration than is normally possible at equilibrium. Crystallisation of a super-saturated solution may be brought about by changes in temperature, pH, addition of co-solvent or application of pressure, each of which result in crystal nucleation, which in turn, triggers subsequent growth into crystals. Carrying out co-precipitation to form LDHs at conditions of low supersaturation leads to more crystalline products than those obtained at high supersaturation, since the rate of crystal growth is greater than the rate of crystal nucleation for the latter.[164]

The constant pH co-precipitation method at low supersaturation has been found to lead to LDHs of higher crystallinity compared to the variable pH method, since the crystals are formed under similar conditions throughout the entire precipitation rather than varying conditions, which would lead to formation of a heterogeneous product.[163] In addition this method yields highly reproducible and reliable results.[135, 165]

In constant pH co-precipitation, stoichiometric solutions of soluble salts of M^{2+} and M^{3+} are precipitated into a solution containing the desired counter-anion. The reaction mixture is maintained at constant pH by the simultaneous addition of base such as $NaOH_{(aq)}$, either manually or *via* automatic titration. Under high supersaturation conditions the reaction metal solutions are added over a much shorter time period. After precipitation the solutions undergo Ostwald ripening,[166] where smaller particles that are less energetically favourable, redissolve in solution and deposit onto the surfaces of larger particles that are more energetically favourable.[167] This leads to increased particle size homogeneity. The co-precipitation method has been further modified by the use of microwave irradiation during the ageing step, leading to smaller, homogeneous particle sizes, in shorter reaction times.[168] Following synthesis, the co-precipitated products are then filtered, washed with copious amounts of hot water and then dried in an oven.

Co-precipitation is generally only possible over an M^{2+}:M^{3+} range of 2-4. Electrostatic repulsion occurs for ratios lower than this as M^{3+} must occupy adjacent sites.[80] If M^{2+}:M^{3+} <2 then this would require M^{III}-O-M^{III} connections, which have been argued to be unfavourable due to charge repulsion, something referred to as the cation avoidance rule.[169] In addition, high M^{2+}:M^{3+} ratios have been suggested to lead to a high-density of Mg-octahedral sites, which act as nucleation sites for the formation of $Mg(OH)_2$.[80] M^{2+}:M^{3+} ratios outside of the 2-4 range have been reported, though the resulting homogeneity of the LDH sample can come into question.[170]

An alternative method of co-precipitation was developed by Zhao *et al.*, whereby a colloid mill was used for initial mixing and nucleation of reactants at 3000 rpm under high pressure, intensive vibration and hydraulic shear forces.[171] An advantage of this method is that the mixing

step is complete in 2 minutes which is subsequently followed by a separate ageing step at 100 °C, resulting in small crystallites of lower aspect ratio and a narrower particle size distribution than those produced in the much slower conventional co-precipitation.

The constant-pH co-precipitation method, however, is not perfect for an industrial scale-up due to a variety of reasons:

- High pH supernatants are created at the end of the process, as the stability range of product requires pH ~10, mainly due to the required filtering and washing to remove counter-anions.
- An inert atmosphere is required to prevent inclusion of carbonate ions within the interlayer, resulting from atmospheric carbon dioxide, which readily enters solution at high pH,[a] [164]
- Competing effects can occur between the desired counter anion and the competing metal salt counter-anions, present in high concentrations in the synthesis. This leads to the requirement of up to a 20-fold excess (relative to needed for charge balancing) of the desired counter anion during direct synthesis, further increasing costs.[164]
- Generally, low mass/charge anions are difficult to intercalate. This necessitates other synthetic methodologies.[172]

Another method of co-precipitation from a homogeneous solution employs the two-step thermally-induced hydrolysis of urea (equation**(12)**), which leads to a solution pH of around 9, precipitating metal hydroxides.[124] An advantage of this synthesis method is that it also avoids the use of alkaline metals which may become entrained in the final LDH product. The urea co-precipitation method is predominantly used for the synthesis of LDHs with counter-anions of high charge density. The rate constant for urea hydrolysis increases 200-fold when the temperature of solution is increased from 60-100 °C and rates of reaction can be controlled. For Mg:Al ratios 2:1 and 10 times excess urea:Al at 90 °C, this method gave LDHs with very good crystallinity after ageing for 48 h, with 90 % of particles formed were found to have a diameter between 0.5 – 10

[a] Carbonate ions have a very high affinity for the LDH interlayer. If carbonate is not the desired counter-anion then co-precipitations must be carried out under inert atmosphere to avoid incorporation of this resulting from the absorption of atmospheric carbon dioxide.

μm.[124] Microwave-hydrothermal treatment has been used to reduce reaction times considerably for the thermally induced hydrolysis of urea method, from that of conventional-hydrothermal treatment.[173]

$$CO(NH_2)_2 \rightarrow NH_4CNO \quad \textbf{(12)}$$

$$NH_4CNO + 2H_2O \rightarrow (NH_4)_2CO_3$$

3.1.2 Hydrothermal LDH synthesis

Larger anionic molecules of low-charge density can be directly incorporated into LDHs by using hydrothermal methods, where co-precipitation syntheses have proved unsuccessful.[172] This approach is especially useful for organic anions, such as deoxycholate that have a very low affinity for the interlayer and are thus typically precluded in co-precipitation synthesis. Ogawa and Asai were able to incorporate deoxycholate into LDH-type materials, using brucite and gibbsite (insoluble at room temperature), by combining the three materials in a sealed Teflon-lined autoclave, along with water, and heating at 150 °C for 24 h under autogeneous pressure.[172]

Greenwell *et al.* used hydrothermal methods to effectively intercalate terephthalic acid (TA) into the interlayer of an MgAl-LDH. This methodology resulted in an LDH-type material with smaller particle size distribution, lower defects and a high degree of crystallinity in comparison to materials obtained from other LDH synthesis methods, something that can clearly be observed in Figure 3.1.[174] The average crystal size obtained from the hydrothermal method (1 μm) is clearly smaller compared to the other methods, but has a higher degree of structural integrity. A large excess of TA was not required in this method unlike the (stoichiometric) co-precipitation method, which required 20-fold excess to avoid incorporation of nitrate anions.[174] Hydrothermal methods can also be employed for LDHs produced by other techniques to improve crystallinity, however this is generally for low charge to mass ratio ions.

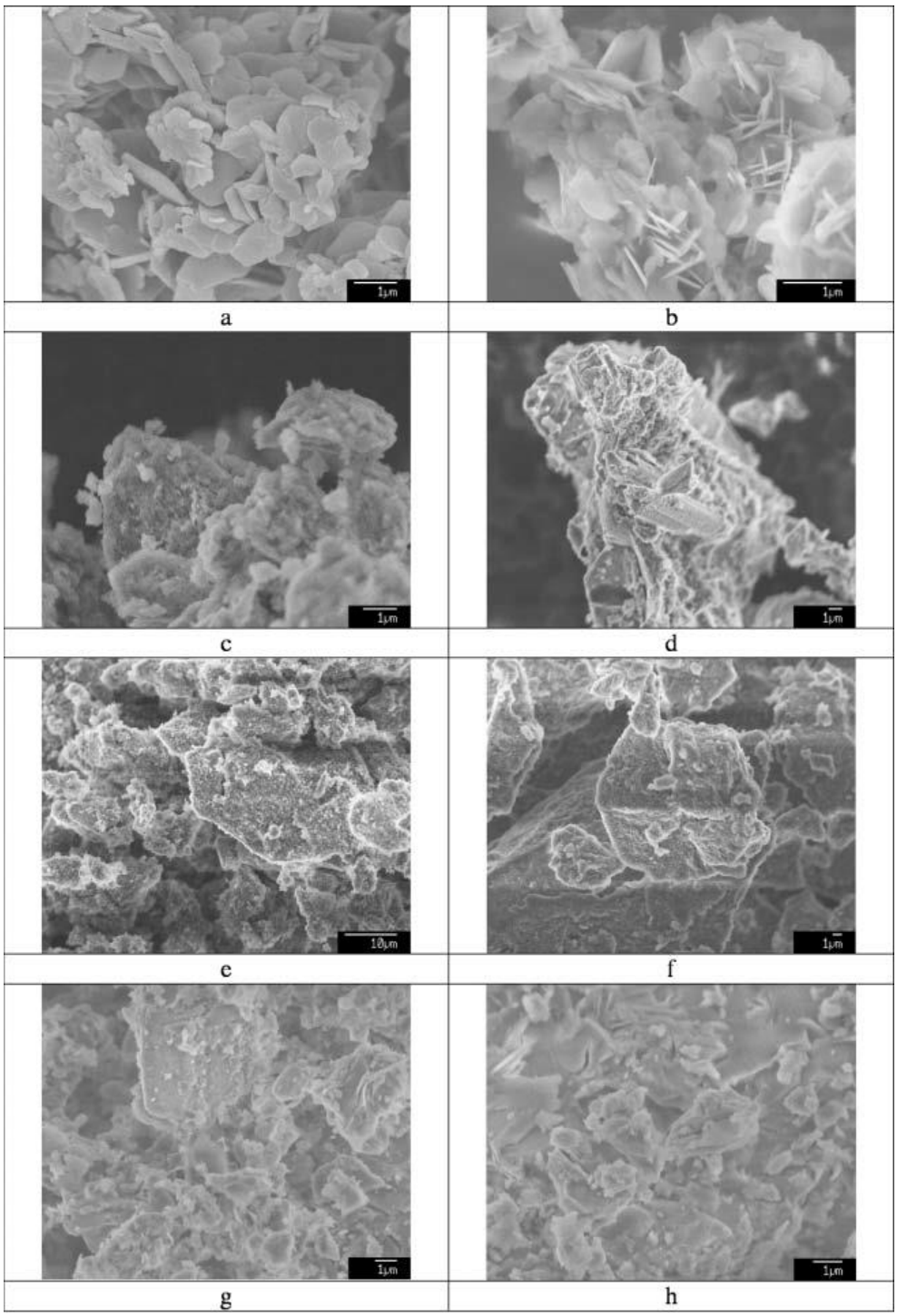

Figure 3.1 Scanning electron micrographs of Mg-Al terephthalates a) R2 and b) R5 prepared from the metal hydroxides using a hydrothermal technique; c) R2 and d) R5 prepared by the direct synthesis co-precipitation method; e) R2 and f) R5 prepared by a sol–gel method; g) R2 and h) R5 prepared by an urea hydrolysis method. The hydrothermal method leads to crystals of smaller particle size distribution and average crystal size, with less surface defects. Image taken from Greenwell *et al.*[174]

3.1.3 Layered double hydroxide synthesis *via* co-hydration

An alternative, environmentally-friendly, method of producing LDHs with organic interlayer anions (as opposed to inorganic interlayer anions), namely organo-LDHs, has been suggested by Greenwell

et al., namely *via* a co-hydration route.[123] In this method the metal oxides are co-hydrated in water, and the organic acid-derived counter-anion is believed to be incorporated into the interlayer through an insertion mechanism, with the pH being kept low so atmospheric CO_2 does not dissolve in the solution forming carbonate-LDHs.[123] The main advantage of this method is that the use of bases such as $NaOH_{(aq)}$ and $KOH_{(aq)}$ used in standard co-precipitation methods is avoided and their respective counter-cations do not need to be washed from the final product. This then avoids the need for disposal of the high pH, basic, co-produced supernatants. Another advantage for industrial scale-up of this method is that Mg and Al oxides are used since they are cheap, readily available and easily hydrate to their corresponding hydroxides in aqueous solution.

In the co-hydration LDH synthesis method a stoichiometric ratio of $MgO:Al_2O_3$ is dispersed in stirred deionised water pre-heated at 60 °C to give a 1 weight % slurry, followed by, after 10 min, the addition of a dicarboxylic acid such as adipic acid. The M^{3+}:acid molar ratio is 1.2 and an inert atmosphere is not required. LDHs of R-value 1 were observed to be phase-pure by PXRD, however SEM-EDX showed amorphous alumina was present, resulting from this being an unfavourable ratio for LDHs,[123] whereby Al^{3+} ions would necessarily have to be located next to each other in the structure. Contrarily, LDHs prepared with greater than 2:1 Mg:Al precursor ratios, all had SEM-EDX measured ratios in the range 2-3, along with poorly crystalline brucite phases present. It was suggested that this was due to either R-value 2 being the more thermodynamically favoured LDH or that with increasing basic MgO quantities, the higher pH slurries involved resulted in $Mg(OH)_2$ formation being favoured and formed in addition.

3.1.4 Secondary layered double hydroxide synthesis methods

3.1.4.1 Layered double hydroxide synthesis *via* ion exchange

Anionic exchange is possible within the interlayer of an LDH that possesses a weakly interacting interlayer anion such as nitrate.[164] This is achieved by suspending the parent LDH in a solution

containing the desired counter-anion of higher interlayer affinity. Thermodynamics control the ion exchange and depend on electrostatic interactions between the positively LDH charged layers and the anions and to a lesser extent, the corresponding changes in hydration energies of the LDHs.[175]

Ion exchange may be carried out in aqueous medium favouring inorganic anions, or an organic solvent which promotes exchange with organic ions.[176] An advantage of this amenable preparation method is the vast range of ion-exchange reactions available, which can lead to successive expansions of the interlayer, not otherwise possible in a single step. For example, a sulphate-containing LDH can be exchanged with dodecyl sulphate to expand the interlayer, increasing the interlayer separation from 11.1 Å to 26.2 Å allowing further exchange,[177] as exemplified by the work of Tseng *et al.* who were subsequently able to intercalate buckminsterfullerene.[178]

3.1.4.2 Rehydration of calcined layered double hydroxides

Subjecting LDHs to calcination at up to 550 °C leads to the removal of interlayer water, interlayer anions and hydroxyl groups, resulting in a collapse of the interlayer to form a highly-basic homogeneous mixed-metal oxide (MMO).[80] Calcination of Mg/Al LDHs to temperatures of around 450-550 °C has been observed to lead to 30 % of the Al^{3+} ions changing from adopting octahedral to tetrahedral coordination in the resulting MMO.[179]

Following calcination to MMOs at temperatures between 450-550 °C, LDHs can be readily reconstructed by rehydration, yielding similar structures to the parent-LDH, a process that has been dubbed the "memory effect".[180] However since some of the Al^{3+} remains in tetrahedral coordination, as observed by solid-state NMR, then this produces and inhomogeneous LDH.[181] Aqueous solutions containing the desired anions are required for the rehydration, along with water reconstructing the hydroxyl layers and the anions plus water intercalating into the interlayer.[182] Advantageously, the anions are incorporated into the LDH structure without competing with the undesired counter-ions present from the original LDH synthesis method, although an inert

atmosphere is still required to prevent inclusion of carbonate ions. Rehydrated LDHs have been prepared with guests such as peptides and amino acids,[183] surfactants,[184] and organic chromophores.[185]

3.2 Layered double hydroxide synthesis methods employed in this thesis

In this chapter MgAl-LDHs will be synthesised using two methods: the co-precipitation method using magnesium nitrate and aluminium nitrate in the presence of sodium bicarbonate at constant pH 10 and the co-hydration method as demonstrated by Greenwell *et al*.[123] These materials will be characterised using various experimental techniques, such as PXRD and ICP, and then compared to each other prior to their calcination to yield MMOs which will similarly be analysed, compared and contrasted.

3.2.1 Nomenclature of samples prepared

The LDH and MMO materials prepared in this thesis are described by:

a) Initially their method of preparation – CoP for co-precipitation and CoH for co-hydration;

b) Whether they are in the LDH form or have been calcined to give the MMO form;

c) Mg:Al stoichiometry during preparation, also known as the R-value.

Thus, by way of example, a mixed metal oxide produced *via* co-hydration with an R-value of 2 would be denoted as CoH-MMO-2. A list of samples prepared, their preparation method and target compounds are shown in Table 3.1.

Table 3.1 Sample ID, synthesis method and target compounds of the materials synthesised in this thesis, where OA represents the organic acid adipate dianion.

Sample ID	Synthesis method	Target compound
CoP-LDH1	Co-precipitation	$([Mg_{0.5}Al_{0.5}(OH)_2](CO_3)_{0.25}.yH_2O$
CoP-LDH2	Co-precipitation	$([Mg_{0.66}Al_{0.33}(OH)_2](CO_3)_{0.165}.yH_2O$
CoP-LDH3	Co-precipitation	$([Mg_{0.75}Al_{0.25}(OH)_2](CO_3)_{0.125}.yH_2O$
CoP-LDH4	Co-precipitation	$([Mg_{0.8}Al_{0.2}(OH)_2](CO_3)_{0.1}.yH_2O$
CoP-LDH5	Co-precipitation	$([Mg_{0.83}Al_{0.17}(OH)_2](CO_3)_{0.09}.yH_2O$
CoP-LDH6	Co-precipitation	$([Mg_{0.86}Al_{0.14}(OH)_2](CO_3)_{0.07}.yH_2O$
CoH-LDH1	Co-hydration	$[Mg_{0.5}Al_{0.5}(OH)_2](OA)_{0.25}.yH_2O$
CoH-LDH2	Co-hydration	$[Mg_{0.66}Al_{0.33}(OH)_2](OA)_{0.165}.yH_2O$
CoH-LDH3	Co-hydration	$[Mg_{0.75}Al_{0.25}(OH)_2](OA)_{0.125}.yH_2O$
CoH-LDH4	Co-hydration	$[Mg_{0.8}Al_{0.2}(OH)_2](OA)_{0.1}.yH_2O$
CoH-LDH5	Co-hydration	$[Mg_{0.83}Al_{0.17}(OH)_2](OA)_{0.09}.yH_2O$
CoH-LDH6	Co-hydration	$[Mg_{0.86}Al_{0.14}(OH)_2](OA)_{0.07}.yH_2O$
CoP-MMO-1	Co-precipitation, calcination	$[Mg_{0.5}Al_{0.5}O_{1.25}]$
CoP-MMO-2	Co-precipitation, calcination	$[Mg_{0.66}Al_{0.33}O_{1.17}]$
CoP-MMO-3	Co-precipitation, calcination	$[Mg_{0.75}Al_{0.25}O_{1.13}]$
CoP-MMO-4	Co-precipitation, calcination	$[Mg_{0.8}Al_{0.2}O_{1.1}]$
CoP-MMO-5	Co-precipitation, calcination	$[Mg_{0.8}Al_{0.17}O_{1.08}]$
CoP-MMO-6	Co-precipitation, calcination	$[Mg_{0.86}Al_{0.14}O_{1.07}]$
CoH-MMO-1	Co-hydration, calcination	$[Mg_{0.5}Al_{0.5}O_{1.25}]$
CoH-MMO-2	Co-hydration, calcination	$[Mg_{0.66}Al_{0.33}O_{1.17}]$
CoH-MMO-3	Co-hydration, calcination	$[Mg_{0.75}Al_{0.25}O_{1.13}]$
CoH-MMO-4	Co-hydration, calcination	$[Mg_{0.8}Al_{0.2}O_{1.1}]$
CoH-MMO-5	Co-hydration, calcination	$[Mg_{0.8}Al_{0.17}O_{1.08}]$
CoH-MMO-6	Co-hydration, calcination	$[Mg_{0.86}Al_{0.14}O_{1.07}]$

3.2.2 Synthesis of layered double hydroxides via co-precipitation

The carbonate LDH samples prepared were composed of the theoretical formula $[Mg^{2+}_{1-x}Al^{3+}_{x}(OH)_2]^{x+}(CO_3^{2-})_{x/2}.yH_2O$. Co-precipitated LDHs were prepared using stoichiometric ratios of Mg/Al (denoted R-value) to give R-values of 1-6. Reagents were used as supplied: magnesium nitrate hexahydrate (Sigma-Aldrich, ACS 99 %), aluminium nitrate nonahydrate (Sigma-Aldrich,

ACS 98 %), deionised water (Purelab 7000, 18.2 MΩ), sodium bicarbonate (Sigma-Aldrich, ACS 99.7 %), $NaOH_{(aq)}$ (Fisher Scientific, AR).

An example preparation for R-value 2 is given below, for exact masses of each chemical used in each R-value preparation see Table 3.2. For synthesis of the target compound $([Mg_{0.66}Al_{0.33}(OH)_2](CO_3)_{0.165}.yH_2O$ (R-value 2), magnesium nitrate hexahydrate, $Mg(NO_3)_2.6H_2O$ a colourless crystalline solid (2.3120g, 9.0 mmol) and aluminium nitrate nonahydrate, $Al(NO_3)_3.9H_2O$ a colourless crystalline solid, (1.6880g, 4.5 mmol) were readily dissolved in 100 ml deionised water. This metal nitrate solution was then added drop wise over a period of 1 hour to a stirred 100 ml excess (CO_3^{2-} : Al^{3+} = 10:1) sodium bicarbonate (3.770g, 44.9 mmol) solution at 65 °C. Instantaneous precipitation of a white solid was observed. Simultaneous addition of 1.5 mol dm^{-3} $NaOH_{(aq)}$ was used to maintain pH 10 ± 0.1, measured using a Jenway 3510 pH meter. The resulting reaction mixture, a white suspension, was then aged *in situ* at 65 °C for 5 hours, while stirring. After aging, the suspension was filtered under vacuum and the white crystalline solid product was washed on a Buchner vacuum funnel with 1 L of hot deionised water to remove any remaining Na^+ ions. The white powder product sample was then dried overnight under air in an oven at 80 °C until there was no further mass loss.

Table 3.2 Masses, moles and ratios of the reactants used for each R-value LDH co-precipitation preparation.

Sample	Mass / concentration per 100 mL solution (g / m mol dm^{-3})			Ratio	
	$Mg(NO_3)_2.6H_2O$	$Al(NO_3)_3.9H_2O$	$NaHCO_3$	Mg:Al	CO_3^{2-}:Al
CoP-LDH1	1.6240, 6.3	2.3760, 6.3	5.320, 63.3	1	10
CoP-LDH2	2.3120, 9.0	1.6880, 4.5	3.770, 44.9	2	10
CoP-LDH3	2.6884, 10.5	1.3112, 3.5	2.930, 34.9	3	10
CoP-LDH4	2.9290, 11.4	1.0712,2.9	2.400, 28.6	4	10
CoP-LDH5	3.0944, 12.1	0.9056, 2.4	2.028, 24.1	5	10
CoP-LDH6	3.2152, 12.5	0.7844, 2.1	1.756, 20.9	6	10

The powder was finely ground using an agate pestle and mortar prior to analysis and use in catalysis (Chapter 5). Samples were analysed using powder X-ray diffraction, thermogravimetric

analysis, scanning electron microscopy, inductively coupled plasma optical emission spectroscopy, surface area analysis, Hammett basicity measurements, elemental analysis and Fourier transform infra-red spectroscopy (Section 2.2).

3.2.3 Synthesis of layered double hydroxides by co-hydration

Co-hydrated LDHs were prepared following a synthesis method developed by Greenwell *et al.*,[123] composed of the theoretical formula $[Mg^{2+}_{1-x}Al^{3+}_{x}(OH)_2]^{x+}(OA)_{x/2}.yH_2O$, where OA represents the adipate dianion. Co-hydrated LDHs were prepared using stoichiometric ratios of Mg/Al to give R-values of 1-6, and adipic acid (Figure 3.2), which was previously used by Greenwell[123] to generate the required counter anions. Reagents were used as supplied: CP5 aluminium oxide (BASF), adipic acid (Sigma, 99 %), magnesium oxide (Sigma-Aldrich, ACS 98 %) and deionised water (Purelab 7000, 18.2 MΩ). In this current procedure CP5 aluminium oxide (BASF, CP = catalyst precursor particle size 5 μm, 6.7 % mass loss on ignition) was used instead of the CP3 (Alcoa, catalyst precursor particle size 3 μm, 5.8 % mass loss on ignition) stated in the article due to CP3 grade no longer being available from the supplier. The CP5 aluminium oxide will therefore require a longer hydration time in comparison to that described by Greenwell,[123] owing to the hydration time for larger alumina particles increasing with their lower surface area per unit weight.[186]

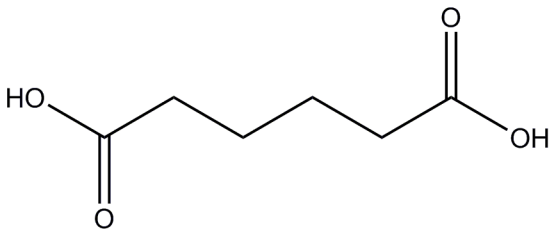

Figure 3.2 Structure of adipic acid, used in the preparation of LDHs *via* co-hydration in this thesis.

An example preparation for R-value 2 is given below, for exact masses of each chemical used in each R-value preparation see Table 3.3). For synthesis of the target compound $[Mg_{0.66}Al_{0.33}(OH)_2](OA)_{0.165}.yH_2O$ (R-value 2), aluminium oxide (1.0100g, 19.8 mmol), a white powder, was added to 250 mL of deionised water at 65 °C followed by adipic acid (1.737g, 16.9

mmol), a white crystalline solid, after 10 minutes and finally magnesium oxide (1.4900g, 37.0 mmol), a white powder, after a further 50 minutes to give an overall 1% slurry weight based on the metal oxides. The reaction mixture was then covered to prevent water loss and aged at 65 °C for 5 hours, while stirring, producing an LDH product which was filtered under vacuum. The white powder sample was then dried overnight under air in an oven at 80 °C until there was no further mass loss, followed by fine grinding using an agate pestle and mortar prior to analysis and use in catalysis (Chapter 5). Samples were analysed using powder X-ray diffraction, thermogravimetric analysis, scanning electron microscopy, inductively coupled plasma optical emission spectroscopy, surface area analysis, Hammett basicity measurements, elemental analysis and Fourier transform infra-red spectroscopy (Section 2.2).

Table 3.3 Masses, moles and ratios of the reactants used for each R-value LDH co-hydration preparation.

Sample	Mass per 100 mL solution, concentration (g, m mol dm^{-3})			Ratio	
	MgO	Al_2O_3	Adipic acid	Mg/Al	COO^-:Al
CoH-LDH1	1.0610, 26.3	1.4386, 28.2	2.474, 16.9	1	1.2
CoH-LDH2	1.4900, 37.0	1.0100, 19.8	1.737, 11.9	2	1.2
CoH-LDH3	1.7220, 42.7	0.7775, 15.3	1.337, 9.2	3	1.2
CoH-LDH4	1.8993, 47.1	0.6006, 11.8	1.033, 7.1	4	1.2
CoH-LDH5	1.9952, 49.5	0.5047, 9.9	0.868, 5.9	5	1.2
CoH-LDH6	2.0647, 51.2	0.4353, 8.5	0.749, 5.1	6	1.2

3.3 Preparation of mixed metal oxides from layered double hydroxides

Following the preparation of LDHs by co-precipitation and co-hydration, these were subsequently calcined to produce mixed metal oxides (MMOs). Calcination at 500 °C results in the decomposition of the LDH through the loss of surface water, intercalated anions and water, and dehydroxylation of the hydroxide layers. Following the collapse of the layered structure, the formed materials are highly-basic homogeneous MMOs.

MMO materials (CoP-MMO and CoH-MMO) were prepared by calcining the white powder parent-LDH (CoP-LDH1 to CoP-LDH6 and CoH-LDH1 to CoH-LDH6) of each material immediately prior to their analysis and further use. For each sample, 1 g of LDH was ground in an

agate pestle and mortar and then placed in a high-temperature-silica crucible in an oven at room temperature and then heated at a rate of 16 °C/min to 500 °C, where the sample was then held for 3 hours in air.[187] The crucible containing the sample was removed from the oven at 500 °C and placed in a desiccator under vacuum, containing anhydrous cobalt chloride desiccant, to cool over 30 mins before the resulting white powder was analysed and further used in catalysis reactions (Chapter 6). Samples were analysed using powder X-ray diffraction, inductively coupled plasma optical emission spectroscopy, surface area analysis, Hammett basicity measurements, elemental analysis and Fourier transform infra-red spectroscopy (Section 2.2).

3.4 Results and discussion

LDHs have been prepared according to two different synthesis methods and the resulting materials transformed into the corresponding MMOs by calcination. Prior to use in catalytic reactions the structure and composition of these LDH and MMO materials is characterised and reported.

3.4.1 Layered double hydroxides prepared by co-precipitation

3.4.1.1 Structure of the layered double hydroxide crystals

The PXRD patterns of LDHs synthesised by co-precipitation (CoP-LDH 1 to CoP-LDH6) are shown in Figure 3.3. For each material of a specific R-value prepared, characteristic LDH patterns were observed with distinctive LDH basal reflections (00*l*) being present at low 2θ angles, indicative of a layered structure, along with broader reflections in the (*11l*) and (*10l*) regions. An impurity phase corresponding to gibbsite is observed for CoP-LDH1, and an additional impurity is also detected in CoP-LDH6 attributed to magnesium hydroxy carbonate.[188]

After smoothing the diffraction pattern data for CoP-LDH1 to CoP-LDH6, followed by subtracting the background, attempts were made to index the PXRD data using the DICVOL automatic indexing algorithm (Section 2.2.1).[1] CoP-LDH2 and CoP-LDH4 were both successfully

indexed as 3R rhombohedral polytypes (Appendix 1 and Appendix 2). The refinements for CoP-LDH2 and CoP-LDH4 are in line with the single crystal refinements for hydrotalcite carried out by Allman and Jepsen.[189] The other CoP-LDHs unfortunately do not show patterns with strong enough reflections to fully index. Previously refined synthetic CO_3^{2-} containing LDHs have all been shown to be of the 3R polytype,[137] so following from this it is assumed that the remaining CoP-LDH can be indexed similarly.

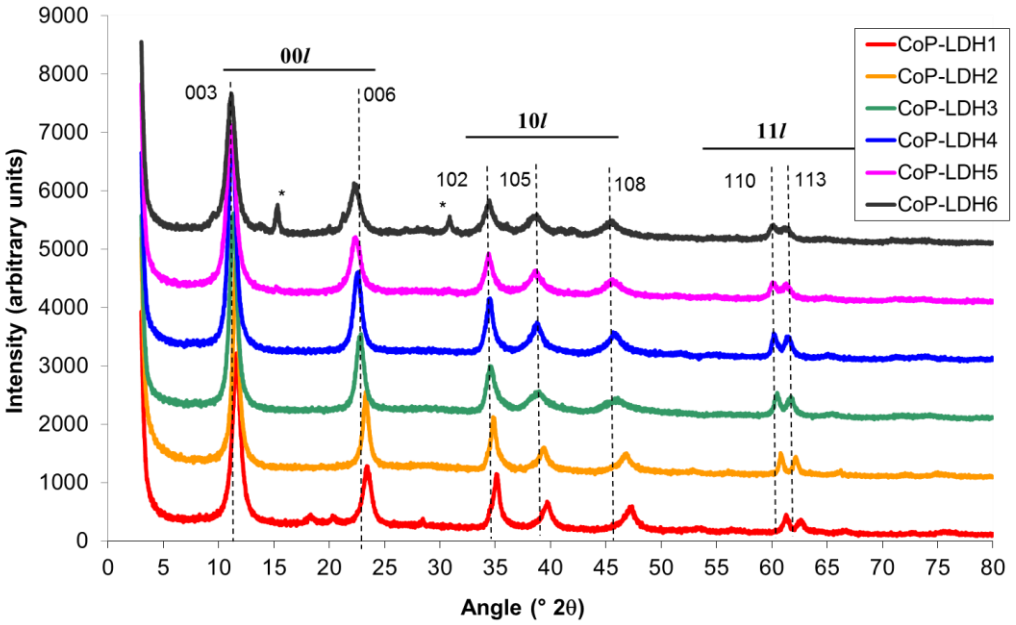

Figure 3.3 PXRD patterns for Mg_xAl – carbonate LDHs synthesised by co-precipitation, with X = 1-6. * denotes impurity. The vertical lines show the corresponding hkl reflections obtained and how these vary with the value of X.

A summary of the PXRD data for the CoP-LDH samples is shown in Table 3.4. The average cation-cation distance in the layer, a_0, calculated from the distinct d_{110} peak (see Section 2.2.1), gives very similar values for all of the prepared CoP-LDHs and lie between 3.02-3.08 Å. This value can then be used to calculate the percentage of Al in the sample using the equation **(4)** put forward by Kaneyoshi and Jones,[135] giving good correlation for CoP-LDH2 to CoP-LDH5, which only vary from the expected values by up to 1.6 %. CoP-LDH1 and CoP-LDH6 vary by 9.3 % and 3.7 %, respectively, from the expected percentages. These values can be similarly determined for *b*, since $a = b$ in hexagonal systems. Co-precipitation is reported as generally only being possible over an M^{2+}:M^{3+} range of 2-4.[80]

The *c* parameter, corresponding to a three-layer repeat, can be calculated from the d_{003} and d_{006} reflections and from this, the interlayer spacing, c_0, which is equal to one-third of this value. According to Bookin and Drits,[126] and Constantino and Pinnavaia,[187] carbonate-containing LDHs have a c_0 of 7.6 and 7.7 Å, which is in agreement with the values determined for CoP-LDH1 and CoP-LDH2 at 7.61 Å and 7.65 Å respectively. The value of c_0 increased with R-value up to 7.94 Å for both CoP-LDH 5 and CoP-LDH6. As Mg:Al ratio (R-value) increases, the cationic charge of the hydroxide layer reduces, hence this leads to less affinity for interlayer anions and also less interlayer anions overall. Thus these 2 factors may be competing in an increase and decrease, respectively, of the value of c_0 as the Mg:Al ratio increases, with the lower anion affinity leading to the greater effect. Subtracting the thickness of one LDH metal hydroxide layer (which are 4.8 Å thick) gives a gallery height of around 3 Å (see Figure 2.2).[80] The average crystallite size has also been calculated in the *a* and *c* directions using the Scherrer equation,[190] (see equation **(5)**). CoP-LDH1 has an average crystal size of 2.07 nm in the *a* direction, with the average crystal size of CoP-LDH2 being higher at 3.86 nm. The remaining CoP-LDHs then follow a general decrease down to 1.59 nm for CoP-LDH6, (excepting CoP-LDH4 which is slightly higher than that for CoP-LDH3).

These calculated average crystal sizes, however, are smaller than the crystal sizes determined from SEM imaging of the same samples; SEM images for CoP-LDH1 to COP-LDH6 are shown in Figure 3.4, and highlight a *rose des sables* structure typical of LDHs.[137] These images are of varying magnifications due to the effects of charging hindering the analysis, with the highest resolution images possible for a particular sample being shown. Electron charging is due to non-conductive samples, which are being irradiated with electrons, building up a negative charge which results in intense white areas being present on the image produced. To circumvent this, samples are coated in carbon, however with the non-conductive LDHs, charging still occurs. The crystallite size can be estimated from the micrographs to be of the order of 200 nm for CoP-LDH3, with similar

values for the other co-precipitated samples. These crystallite sizes are in a similar range to those calculated using the Scherrer equation **(5)** for the *c*-direction (91 – 221 nm).

ICP-OES data of the various LDH materials (Table 3.5) shows that, generally, Mg:Al ratios increased, as the expected Mg:Al ratios increased (i.e. Mg:Al 1-6), although, with the exception of CoP-LDH1, the ICP-OES Mg:Al values were all underestimating Mg by of 10-20 %. For Mg-Al carbonate LDHs prepared by co-precipitation at pH 8, it is proposed that only Mg:Al ratios in the range 1.0-3.0 are possible,[137] however the data obtained here suggests R-value 1.0-6.0 are feasible, although these LDHs are prepared at pH 10, which will enhance the formation. In comparison, the Mg:Al content from analysis of the d110 peak (section 2.2.1) show much less variation (except for CoP-LDH1). This would suggest that some amorphous alumina has formed which is interspersed throughout the LDH product.

SEM-EDX was used to obtain bulk Mg:Al ratios for particles, with the results being shown in Table 3.5. Analysis on a number of individual areas in CoP-LDH1 showed 4 different material types: LDHs of R-value 3.1, 0.3, MgO and Al_2O_3. This SEM-EDX analysis at a microscale confirms the presence of amorphous alumina and hence why the PXRD data for the LDH indicated less Al was present than expected on the basis of R-value. However, the ICP-OES Mg:Al value for the bulk R1 material was still 1. As such, a second sample of CoP-LDH1, which was not washed with hot deionised water during filtration was also sampled. Again, SEM-EDX showed this contained LDH material of R-value 3.1, along with the desired R-value 1.1 material, however Na_2O was also found to be present. This suggests that if effective washing is not carried out then residual sodium compounds will invariably remain in the sample.[81] Using SEM-EDX, CoP-LDH2 was found to have an Mg:Al-value higher than that obtained by ICP-OES, suggesting amorphous MgO may be present. CoP-LDH3 to CoP-LDH5 all contained material of R-value 3.1 by SEM-EDX, suggesting they have similar structures within the proposed optimal range of 1.0-3.0.[137] A second area of CoP-LDH4 was also analysed, which, however had R-value 8.8 suggesting a second phase is present and that these samples are not very homogeneous at SEM-EDX level.

Table 3.4 Parameters extracted from the PXRD patterns for CoP-LDH1 to CoP-LDH6. [a] calculated by subtracting 4.8 Å (the width of one brucite layer) from one third of the value of the *c* parameter. Estimated standard deviations shown in brackets.

Sample	d_{003} (Å)	d_{006} (Å)	d_{110} (Å)	*a* (Å)	*c* (Å)	c_0 (Å)	Gallery height (Å) [a]	Average crystal size *c* (nm)	Average crystal size *a* (nm)	Calculated Al (%)	Theoretical / ideal Al (%)
CoP-LDH1	7.63	3.80	1.51	3.02 (0.15)	22.84 (1.14)	7.61 (0.38)	2.81 (0.14)	119 (6)	227 (11)	40.7 (2.0)	50.0
CoP-LDH2	7.65	3.82	1.52	3.05 (0.15)	22.94 (1.14)	7.65 (0.38)	2.85 (0.14)	221 (11)	255 (13)	31.9 (1.6)	33.3
CoP-LDH3	7.81	3.90	1.53	3.06 (0.15)	23.42 (1.17)	7.81 (0.39)	3.01 (0.15)	129 (6)	198 (10)	25.1 (1.3)	25.0
CoP-LDH4	7.88	3.95	1.54	3.07 (0.15)	23.65 (1.18)	7.88 (0.39)	3.08 (0.15)	133 (7)	254 (13)	20.2 (1.0)	20.0
CoP-LDH5	7.94	3.97	1.54	3.08 (0.15)	23.83 (1.19)	7.94 (0.40)	3.14 (0.16)	114 (6)	168 (8)	18.3 (0.9)	16.7
CoP-LDH6	7.95	3.97	1.54	3.08 (0.15)	23.82 (1.19)	7.94 (0.40)	3.14 (0.16)	91 (5)	161 (8)	18.0 (0.9)	14.3

Table 3.5 Expected and actual, ICP-OES and SEM-EDX Mg:Al data for CoP-LDH1 to CoP-LDH6, prepared by co-precipitation, with errors given in parentheses.

Sample	Ratio of Mg:Al		SEM-EDX Main phase	SEM-EDX Other components	
	Expected	ICP-OES (±0.03)			
CoP-LDH1	1.0	1.0	3.11 (0.04)	0.32 (0.06)	MgO Al_2O_3
CoP-LDH2	2.0	1.7	2.71 (0.10)		
CoP-LDH3	3.0	2.7	3.08 (0.17)		
CoP-LDH4	4.0	3.3	3.07 (0.02)	8.77 (1.56)	
CoP-LDH5	5.0	4.0	3.12 (0.19)		
CoP-LDH6	6.0	5.2	Not recorded		
CoP-LDH1 unwashed	1.0	-	1.07 (0.04)	3.13 (0.07)	Na_2O

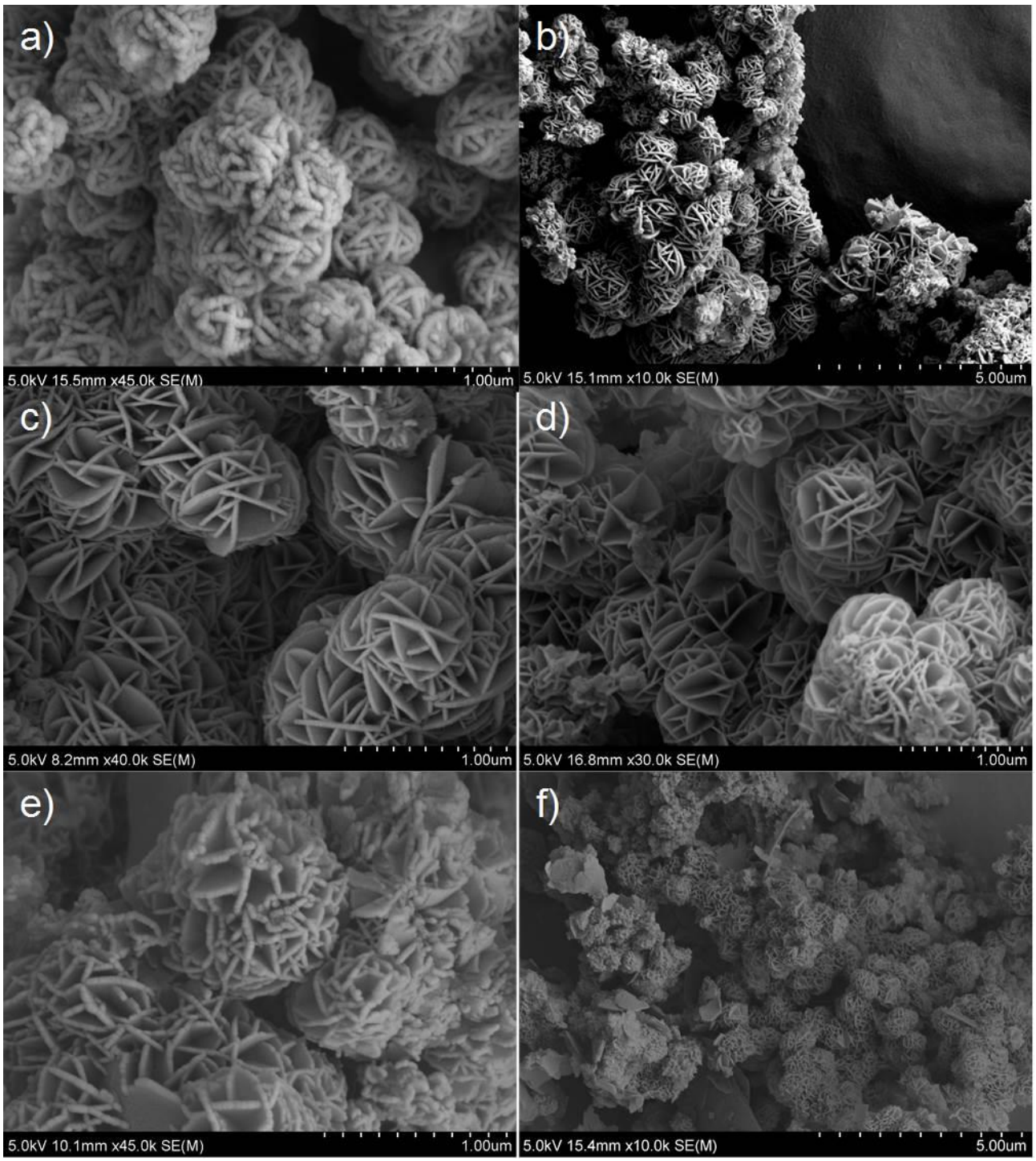

Figure 3.4 Scanning electron micrographs of a) CoP-LDH1, b) CoP-LDH2, c) CoP-LDH3, d) CoP-LDH4 e) CoP-LDH5 and f) CoP-LDH6. The samples all exhibit a *rose des sables* structure, typical for an LDH, with inter-growth between crystallite plates and the crystallite size for each sample being ~200 nm.

From the IR spectral analyses presented in Figure 3.5, the co-precipitated LDH samples show some of the characteristic carbonate symmetric and anti-symmetric stretching vibrational modes in the region 1300-1500 cm^{-1}, as expected.[191] The intensity of carbonate stretches decrease as Mg:Al ratio increases since less charge balancing carbonate anions are intercalated, however,

CoP-LDH6 does exhibit an unexpected increase in carbonate stretching intensity over the other co-precipitated samples.

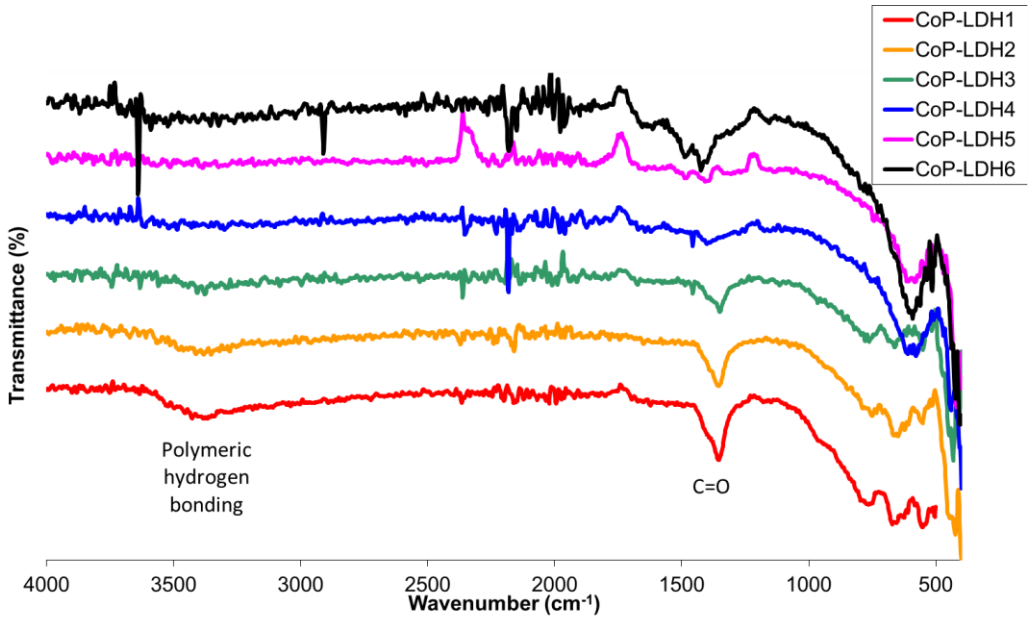

Figure 3.5 FTIR spectra of synthesised LDHs prepared using the co-precipitation method.

The presence of polymeric hydrogen-bonding (shifted to 3300 cm^{-1}) is evident in CoP-LDH1 to CoP-LDH3, however not CoP-LDH4 to CoP-LDH6 suggesting less water is present in the interlayer. Or another possibility is that since the interlayer spacing is larger for CoP-LDH4, this is too large for the H-bonding to form in a polymeric fashion.

Thermal analysis *via* TGA of the CoP-LDHs showed the expected distinct mass losses: a) evolution of water initially from loss of intercalated interlayer water; b) carbon dioxide arising from interlayer carbonate decomposition, along with dehydroxylation of the hydroxide layers; upon calcination from room temperature to 500 °C (Figure 3.6).[192] TGA data for water loss, in conjunction with the determination of the percentages of C and H *via* elemental analysis allowed the determination of possible sample compositions (Table 3.6). The Mg:Al ratio determined from ICP was used to determine the amount of OH^- and interlayer CO_3^{2-} counter anion in the LDH structure. With the calculated OH^- and CO_3^{2-} values fixed, the percentage of water was then varied to determine possible compositions when the percentage of H_2O, C and H were individually

matched to the actual experimental TGA data. However, it was not possible to match all variables simultaneously, which may be due to the percentage attributed to H_2O in TGA being over/underestimated due to adsorbed surface water and/or overlapping of the loss of interlayer water with interlayer carbonate loss. Another possible reason for less elemental hydrogen being observed in elemental analysis than the corresponding elemental hydrogen from water/hydroxyl loss in TGA is that, prior to combustion, the elemental analysis sample is kept in a pure oxygen stream and this may result in dehydration of the sample prior to analysis and so less observed percentage hydrogen.

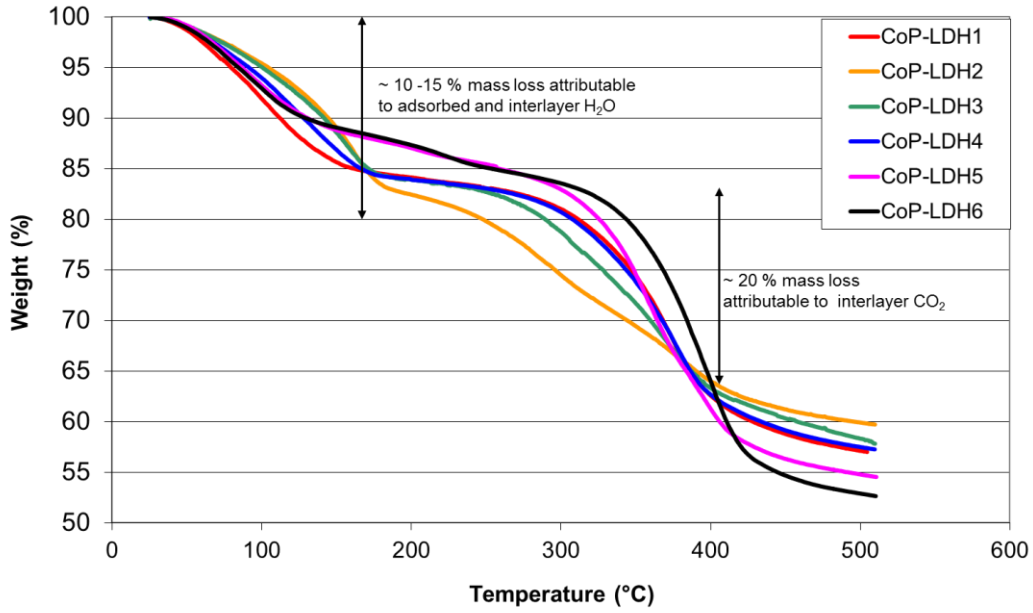

Figure 3.6 Thermogravimetric analyses (TGA) profiles of CoP-LDH1 to CoP-LDH6 samples, showing the mass loss against temperature..

3.4.1.2 Catalyst properties of the layered double hydroxides

Nitrogen adsorption/desorption isotherms for the co-precipitated LDHs are shown in Figure 3.7a. All samples exhibit type IV isotherms characteristic of mesoporous materials (see Section 2.2.5). In each case, the hysteresis loop is narrow, with almost parallel adsorption and desorption branches, something that is indicative of pores with regular geometry, while the steep desorption behaviour indicates that the pore size distribution is narrow for CoP-LDH2 to CoP-LDH6 (Figure 3.7b).[143]

Table 3.6 Analytical data and possible calculated chemical formulae for co-precipitated LDHs. Analytical data: [a] from TGA analysis; [b] from elemental analysis.

Sample	H_2O (%)	C (%)	H (%)
CoP-LDH1 - analytical data	13.41[a]	5.07[b]	4.20[b]
$[Mg_{1.0}Al(OH)_{4.0}](CO_3)_{0.50}.1.28H_2O$	13.41	3.48	3.84
$[Mg_{1.0}Al(OH)_{4.0}](CO_3)_{0.50}.1.78H_2O$	17.67	3.31	4.20
CoP-LDH2 - analytical data	16.31[a]	2.38[b]	3.86[b]
$[Mg_{1.7}Al(OH)_{5.4}](CO_3)_{0.50}.2.06H_2O$	16.31	2.64	4.22
$[Mg_{1.7}Al(OH)_{5.4}](CO_3)_{0.50}.3.45H_2O$	24.62	2.38	4.91
$[Mg_{1.7}Al(OH)_{5.4}](CO_3)_{0.50}.1.44H_2O$	11.98	2.78	3.86
CoP-LDH3 - analytical data	14.90[a]	2.37[b]	3.80[b]
$[Mg_{2.7}Al(OH)_{7.4}](CO_3)_{0.50}.2.41H_2O$	14.90	2.06	4.22
$[Mg_{2.7}Al(OH)_{7.4}](CO_3)_{0.50}.0.28H_2O$	1.98	2.37	3.16
$[Mg_{2.7}Al(OH)_{7.4}](CO_3)_{0.50}.1.49H_2O$	9.75	2.18	3.80
CoP-LDH4 - analytical data	15.33[a]	2.47[b]	3.84[b]
$[Mg_{3.3}Al(OH)_{8.6}](CO_3)_{0.50}.2.85H_2O$	15.33	1.79	4.30
$[Mg_{3.3}Al(OH)_{8.6}](CO_3)_{0.50}.1.67H_2O$	9.61	1.91	3.84
CoP-LDH5 - analytical data	9.83[a]	2.85[b]	3.78[b]
$[Mg_{4.0}Al(OH)_{10.0}](CO_3)_{0.50}.1.96H_2O$	9.83	1.67	3.90
$[Mg_{4.0}Al(OH)_{10.0}](CO_3)_{0.50}.1.63H_2O$	8.31	1.70	3.78
CoP-LDH6 - analytical data	9.66[a]	4.13[b]	3.52[b]
$[Mg_{5.2}Al(OH)_{12.4}](CO_3)_{0.50}.2.34H_2O$	9.65	1.38	3.94
$[Mg_{5.2}Al(OH)_{12.4}](CO_3)_{0.50}.1.00H_2O$	4.35	1.46	3.52

The BET analysis showed the surface area of the CoP-LDH decreased with increasing Mg:Al ratio for CoP-LDH1 (115 m^2/g), CoP-LDH2 (91 m^2/g) to CoP-LDH3 (82 m^2/g) (Table 3.7), values that are in line with the typical 100 m^2/g cited for hydrotalcites.[122] In contrast, the surface areas for CoP-LDH4 to CoP-LDH6 were significantly lower (17-39 m^2/g), however this is not uncommon, with an increase in surface area being found for these three samples, with increasing Mg-Al ratio.[193] The average pore sizes were found to generally increase with decreasing Al-content over the range ~3 to ~22 nm. The pore volume was greatest for CoP-LDH3 at 0.42 cm^3/g, with average pore width increasing from CoP-LDH1 to CoP-LDH2 and being very similar for CoP-LDH4 to CoP-LDH6. LDHs are deemed microporous solids with interlayer spacings of typically in the range 1-2 nm being reported,[194], far smaller than the average pore sizes established here, which are considered mesoporous.[143] The average pore size results for the co-precipitated LDHs are

presumably due to inter-particle voids rather than internal porosity of the interlayer nanostructure, since only the external surface is probed,[137] so the adsorption isotherms need to be treated with this in mind. Overall it can be seen for CoP-LDH1 to CoP-LDH6 that, as the surface area decreases, the pore volume increases. The surface area and average pore size follow this general pattern for CoP-LDH1 to CoP-LDH3, however for CoP-LDH4 to CoP-LDH5 as the surface area increases the average pore size decreases marginally and from CoP-LDH5 to CoP-LDH6 increases by approximately 10 %. The values obtained from surface area measurements did not show any correlation with the average crystal sizes obtained from the Scherrer equation (equation **(5)**), presumably due to the multiple variables that can affect the line broadening used to calculate this value (*vide supra*). Ageing of LDH samples at elevated temperatures during preparation has been shown to lead to lower measured surface areas in prior studies,[137] and here all of the CoP-LDH samples prepared in this study were aged for five hours at 65 °C. However, the samples prepared for the work described in this thesis were washed with 1 L of hot deionised water to remove remaining Na^+ ions, and this step may have had an effect on particle size and surface properties. It has been previously observed that as ageing temperature increases so does the particle size.[177, 195]

The CoP-LDH materials were analysed semi-quantitatively for basicity, with the assistance of Dr Louise Gildea, using appropriate solutions of the Hammett base indicators: bromothymol blue (pK_a range 6.0 – 7.6), *m*-cresol purple (pK_a range 7.6 – 9.2), phenolphthalein (pK_a range 8.0 – 10.0) and indigo carmine (pK_a range 11.5 – 13.0).[122] These indicators can probe the lateral crystal faces and outer crystal surfaces, where catalysis is believed to occur in LDHs, measuring the strength of basic sites present, with often more than one type of site found to exist.[149] Hammett basicity (Table 3.7) was measured as between pK_a 7.6-9.0 for CoP-LDH1 and CoP-LDH3, lower than all the other CoP-LDH, which were in the 9.0-10.0 range. The higher measured basicity values for CoP-LDH4 to CoP-LDH6 may be attributed to the fact that as the Mg:Al ratio increases then the composition tends toward larger domains of highly basic $Mg(OH)_2$ as the Al content reduces. Jinesh *et al.*, using Hammett base indicators, found that carbonate-containing LDHs had $11 < pK_a < 15$,[150] higher than

those observed in this present study ($7.6 < pK_a < 10.0$). This is possibly due to subtly differing testing methods used by Jinesh *et al.*,[150] who assessed Hammett basicity using different indicators and also titrated the final solutions against 0.02 M benzoic acid in dry methanol.

Similar to surface area analysis with BET, the Hammett base measurements only probe external crystal surfaces and do not probe the interlayer surfaces of the LDH. The LDH layers are strongly bound together by electrostatics, with carbonate anions already occupying the interlayer space, prohibiting access of the bulky indicator molecules. Hammett basicity tests are carried out under different conditions to those the catalysts are often used at, and so are often deemed to be inapplicable methods of distinction of actual catalytic performance.[196, 197]

In summary, carbonate containing LDHs have been prepared by co-precipitation under conditions of low-supersaturation at constant pH, with Mg/Al ratios of 1-6. Crystallographic parameters, and possible chemical compositions have been elucidated as well as properties relating to the bulk materials such as surface area and external maximum basicity. The crystal structures, TGA and elemental compositions for a series of co-precipitated Mg-Al carbonate LDHs shows general agreement with literature data. The percentage of Al calculated from PXRD data[135] showed CoP-LDH4 to CoP-LDH6 to all have similar values between 18-20 % rather than the 14-20 % they should span. These three materials also showed very similar bulk properties of pore volume, pore width, surface area and Hammett basicity in comparison to CoP-LDH1 to CoP-LDH3. However, ICP-OES, SEM-EDX, TGA and elemental analysis did not show such discernable trends between CoP-LDH1 to CoP-LDH3 in comparison with CoP-LDH4 to CoP-LDH6.

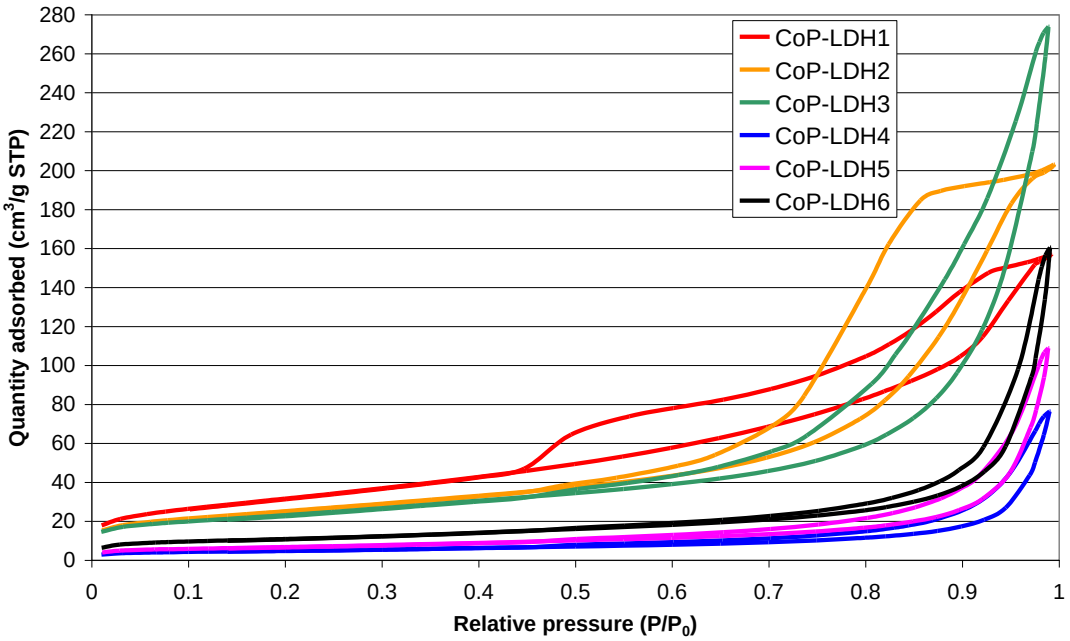

a)

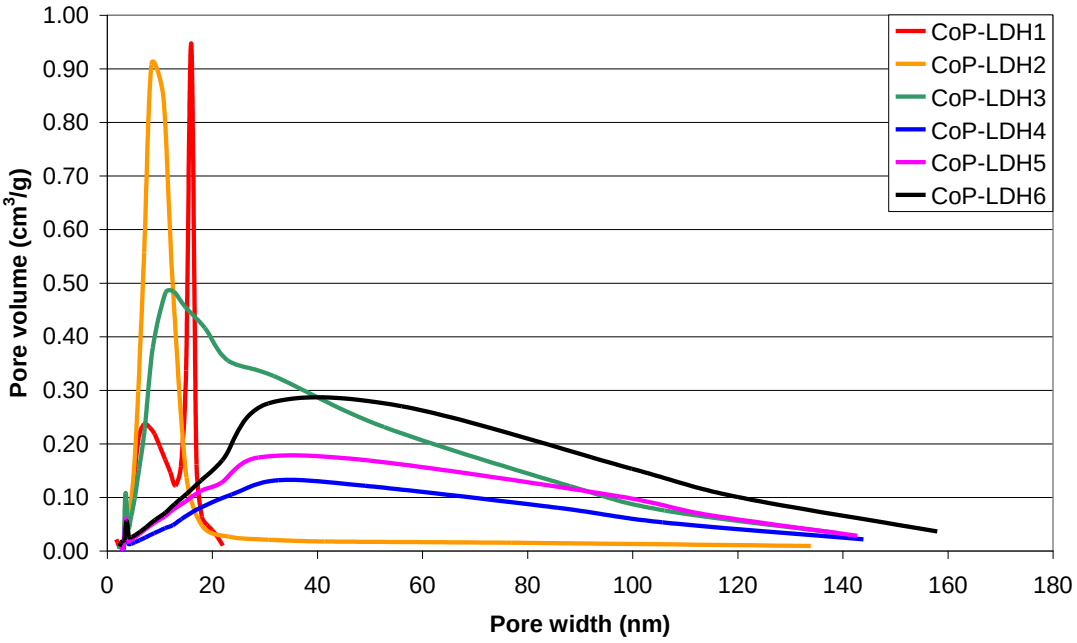

b)

Figure 3.7 a) Nitrogen adsorption/desorption isotherms showing typical hysteresis behaviour of type IV mesoporous solids and b) associated pore width distributions for CoP-LDH1 to CoP-LDH6.

Table 3.7 Nitrogen adsorption analysis and Hammett basicity data for CoP-LDH1 to CoP-LDH6. Surface area standard deviations shown in brackets.

Sample	surface area (m^2/g)	pore volume (cm^3/g)	average pore size (nm)	Hammett Basicity (pK_a)
CoP-LDH1	115.1841 (0.5242)	0.25	3.1	7.6-9.0
CoP-LDH2	90.6542 (0.1754)	0.32	8.7	9.0-10.0
CoP-LDH3	82.3775 (0.1007)	0.42	14.4	7.6-9.0
CoP-LDH4	17.1988 (0.0388)	0.12	20.5	9.0-10.0
CoP-LDH5	24.0750 (0.0257)	0.17	20.2	9.0-10.0
CoP-LDH6	38.5149 (0.1106)	0.25	22.3	9.0-10.0

3.4.2 Layered double hydroxides prepared by co-hydration

3.4.2.1 Structure of the layered double hydroxide crystals

The PXRD patterns of the LDHs synthesised by co-hydration (CoH-LDH 1 to CoH-LDH6) are shown in Figure 3.8. For CoH-LDH2 to CoH-LDH6 characteristic LDH patterns have been recorded with distinctive LDH basal reflections (00*l*) being present at low 2θ angles, indicative of a layered structure, along with broader reflections in the (*11l*) and (*10l*) regions, suggesting lower crystallinity.[129, 198] However, these samples all show varying levels of impurity as previously reported by Greenwell *et al.*,[123] with significant quantities of brucite ($Mg(OH)_2$) being detected for materials with Mg:Al > 2, on the basis of relative peak intensity within the PXRD patterns in Figure 3.11. The PXRD analysis also suggests there is a degree of unreacted MgO present in CoH-LDH4, CoH-LDH2 and CoH-LDH6. As observed here, Greenwell also reported that the LDHs containing adipate as the charge-balancing interlayer anion showed expanded phases (at 6° 2θ) for CoH-LDH2 and CoH-LDH3, where the adipate anion is perpendicular to the plane, and collapsed phases present (at 12 ° 2θ) for CoH-LDH4 to CoH-LDH6, where the adipate anion is parallel to the plane.

In the present work, unlike Greenwell however, synthesis of CoH-LDH1 was unsuccessful, with the PXRD analysis not showing any reflections corresponding to LDH. Owing to the

amorphous nature of the PXRD pattern, CoH-LDH1 was believed to be mainly composed of alumina.[169] In this case, the Mg-containing components used in the preparation of this material could possibly have reacted to form soluble Mg adipate and, hence, been lost in the supernatant following washing and filtration. The reason for the difference to the report of Greenwell *et al.*, where successfully synthesised LDHs of R-value 1 are described,[123] may in addition, possibly arise owing to the alumina used here being of larger particle size and thus possibly, in retrospect, requiring far longer reaction time.

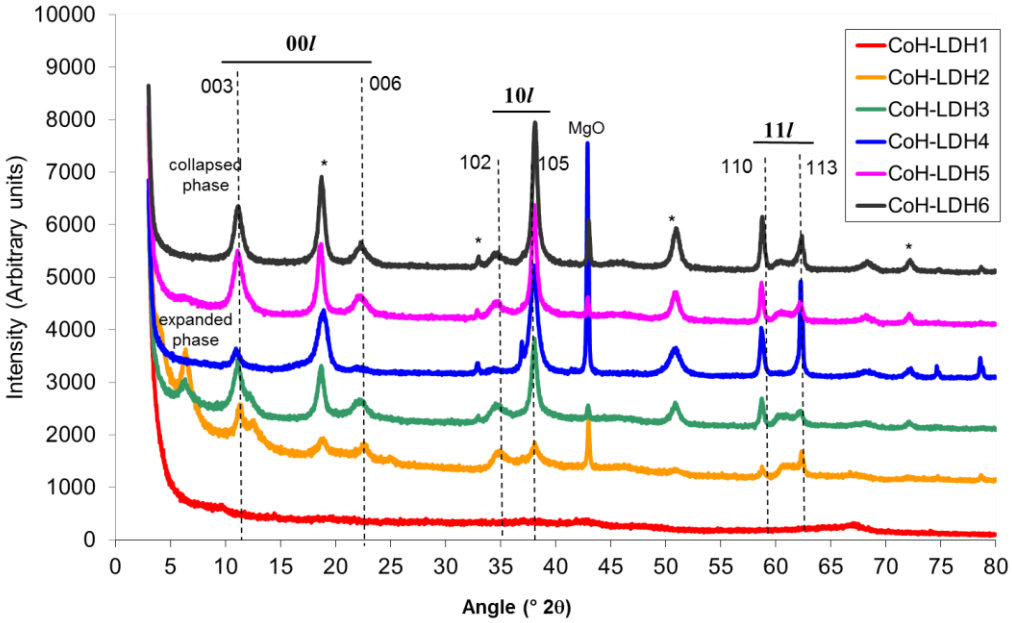

Figure 3.8: PXRD patterns for the prepared LDHs synthesised by co-hydration. * shows the brucite impurities.

Attempts were made to index the PXRD data collected for CoH-LDH2 to CoH-LDH6 using the DICVOL automatic indexing algorithm (Section 2.2.1),[1] however these proved unsuccessful. As CoP-LDH2 and CoP-LDH4 were both successfully indexed as 3R rhombohedral polytypes, it is assumed from these results that the CoH-LDH can be indexed similarly, but the PXRD patterns in these systems did not contain sufficient reflections to allow successful indexing. A summary of the PXRD data for the CoH-LDH samples is shown in Table 3.8. The average cation-cation distance within a layer, a_0, calculated from the distinct d_{110} peak, gives the same value for all CoH-LDH, 3.14 Å. This value cannot be used to calculate the percentage of Al in these systems using the equation put forward by Kaneyoshi and Jones,[135], equation **(4)**, as the correlation fit is dependent on

the counter-anion involved being either carbonate or nitrate, rather than the adipate used here. The *c* parameter, corresponding to a 3 layer repeat, can be calculated from the d_{003} and d_{006} reflections and from this the interlayer spacing, $c_{0,}$ which was between 7.83-8.09 Å for CoH-LDH2 to CoH-LDH6. Subtracting the thickness of one brucite-like layer gives the gallery height, around 3.03-3.29 Å, greater than the corresponding gallery height of 2.81-3.14 Å for the CoP-LDHs, owing to the size of the intercalated adipate dianion. Using an axial length of the adipate anion of 7.432 Å obtained from the literature,[199] the angle of tilt of the adipate anions in the interlayer, relative to the plane of the LDH sheet, was calculated as being between 24-26 °. The average crystallite size has also been calculated, using the Scherrer equation, in the *a* and *c* directions with the results being in a similar region to those of the co-precipitated LDHs (see section 3.4.1).

ICP-OES data showed general correlation with the expected Mg:Al ratio on the basis of R-value, with the exception of CoH-LDH5, which had a lower ratio than CoH-LDH4 (Table 3.9). SEM-EDX was used to obtain Mg:Al ratios across the samples at a microscale, with the results shown in Table 3.9. This also showed a general correlation with the expected Mg:Al ratio, although again, with the exception of CoH-LDH5, which has a significantly lower ratio, below that even of CoH-LDH3, suggesting this sample to be impure and that some amorphous alumina has formed, which is interspersed throughout the LDH product and, owing to its amorphous nature, is not observed in the PXRD spectra.

CoH-LDH2 to CoH-LDH6 samples, with adipate ions in the interlayer, are carbonate free according to the FTIR spectra in Figure 3.9 with no corresponding stretches observed at 672 cm^{-1} and 873 cm^{-1}.[137] This is in agreement with the work of Greenwell et al.,[123] who developed the co-hydration method as a carbonate free way to prepare LDH. CoH-LDH1 shows the characteristic carbonyl symmetric and anti-symmetric stretching vibrational modes in the region 1300-1500 cm^{-1}. However, as detailed above, CoH-LDH1 is not an LDH since it only contains aluminium by elemental analysis. When comparing the FTIR spectra recorded in this project with the literature, it was found that no C-H stretch was present, as expected for adipate at around 2950 cm^{-1}. Also no

Table 3.8 Parameters from the PXRD analysis of CoH-LDH1 to CoH-LDH6. [a] calculated by subtracting 4.8 Å (the width of one brucite layer) from one third of the value of the *c* parameter. Estimated standard deviations shown in brackets.

Sample	d_{003} (Å)	d_{006} (Å)	d_{110} (Å)	*a* (Å)	*c* (Å)	c_0 (Å)	Gallery height (Å)	Adipate tilt angle (°)	Average crystal size *c* (nm)	Average crystal size *a* (nm)
CoH-LDH1	-	-	-	-	-	-	-	-	-	-
CoH-LDH2	13.8 (expanded), 7.82 (collapsed)	3.93	1.57	3.14 (0.16)	23.50 (1.18)	7.83 (0.39)	3.03 (0.15)	24.1	140 (7)	312 (16)
CoH-LDH3	14.0 (expanded), 7.97 (collapsed)	3.99	1.57	3.14 (0.16)	23.93 (1.20)	7.98 (0.40)	3.18 (0.16)	25.3	102 (5)	301 (15)
CoH-LDH4	8.05	4.06	1.57	3.14 (0.16)	24.26 (1.21)	8.09 (0.40)	3.29 (0.16)	26.3	138 (7)	289 (14)
CoH-LDH5	7.95	4.02	1.57	3.14 (0.16)	23.98 (1.20)	7.99 (0.40)	3.19 (0.16)	25.4	116 (6)	387 (19)
CoH-LDH6	7.94	3.98	1.57	3.14 (0.16)	23.86 (1.19)	7.95 (0.40)	3.15 (0.16)	25.1	189 (9)	337 (17)

Table 3.9 Expected and actual, ICP-OES and SEM-EDX bulk Mg:Al values obtained for LDHs prepared by co-hydration, with the error shown in parentheses for SEM-EDX.

Sample	Mg:Al ratio		
	Expected	ICP-OES	SEM-EDX
CoH-LDH1	1.0	100 % Al	Not recorded
CoH-LDH2	2.0	1.3	0.68 (0.14)
CoH-LDH3	3.0	2.3	1.83 (0.26)
CoH-LDH4	4.0	3.7	4.03 (1.63)
CoH-LDH5	5.0	3.2	1.62 (0.43)
CoH-LDH6	6.0	5.0	6.72 (3.49)

OH structure resulting from brucite is observed for higher R-values,[123] suggesting more scans or alternative IR techniques may be required to observe these.

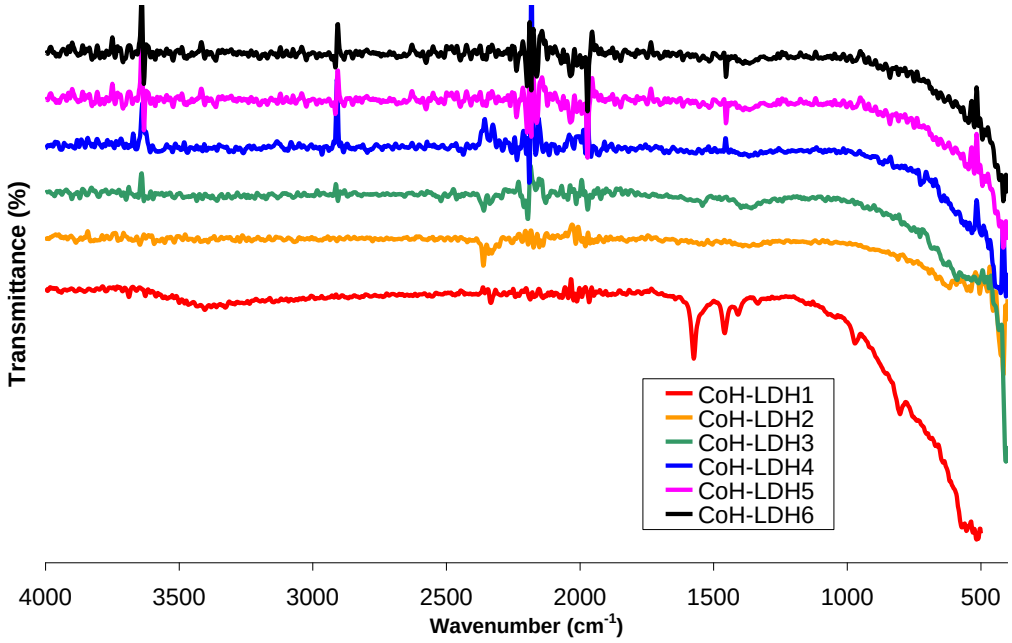

Figure 3.9 FTIR spectra of the synthesised layered double hydroxides prepared using the co-hydration method.

Thermal analysis *via* TGA of the CoH-LDHs showed the expected distinct mass losses associated with evolution of water, initially from loss of intercalated interlayer water and then from dehydroxylation of the hydroxide layers, and later from adipic acid decomposition upon calcination from room temperature to 500 °C (Figure 3.10), further confirming successful intercalation of the adipate anion.[192] TGA data for water loss, in conjunction with elemental analysis of C and H content, allowed the calculation of potential sample compositions (Table 3.10). The Mg:Al ratio determined from ICP was used to determine the amount of OH^- in the LDH structure. With these values fixed the percentages of water, carbonate, hydroxide and adipate were varied to determine possible compositions when the percentage of H_2O, C and H were matched in a pairwise way. No carbonate was seen to be present from the corresponding PXRD spectra and so any impurity may be due to incorporation of the hydroxide anion. It was not possible to match the C, H and H_2O simultaneously to be in agreement with the experimental data, something that may be due to the percentage attributed to H_2O in the TGA data being over/underestimated due to adsorbed surface

water and/or overlapping of the loss of interlayer water with interlayer anion loss. Another possible reason for less hydrogen being observed in elemental analysis than calculated is that, prior to combustion, the elemental analysis sample is kept in a pure oxygen stream and this may result in dehydration of the sample.

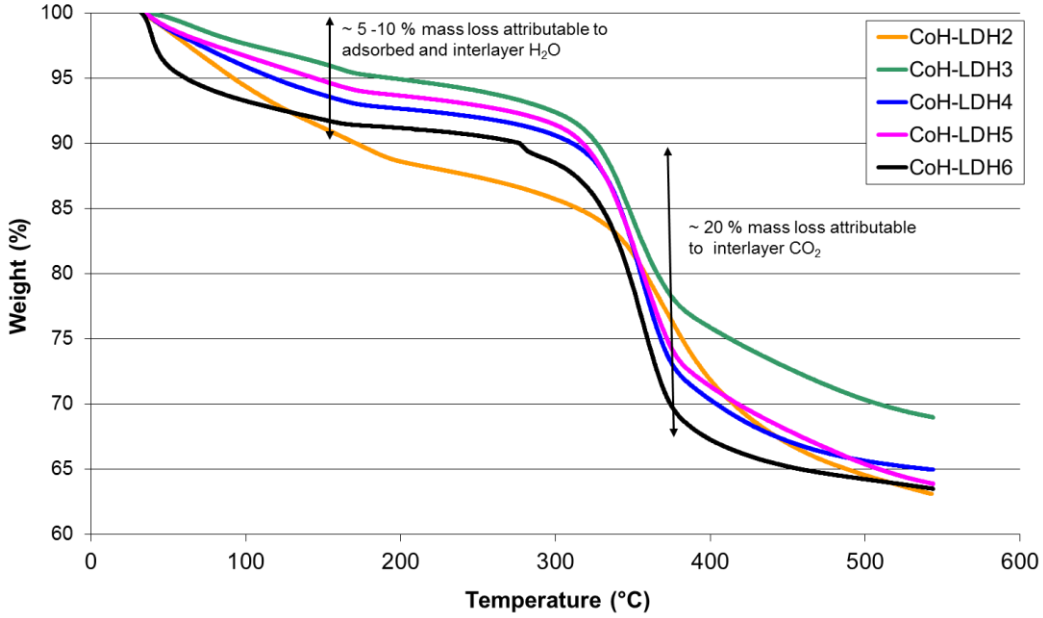

Figure 3.10 Thermogravimetric analyses of CoH-LDH2 to CoH-LDH6.

3.4.2.2 Catalyst properties of the layered double hydroxides

Nitrogen adsorption/desorption isotherms for the co-hydrated LDHs are shown in Figure 3.11a. All samples tested exhibit type IV isotherms, characteristic of mesoporous materials.[143, 200] In each case, the hysteresis loop is narrow, with almost parallel adsorption and desorption branches, indicative of pores with regular geometry, while the steep desorption behaviour indicates that the pore size distribution is narrow (Figure 3.11b).

The measured surface area for CoH-LDH2 was 33 m^2/g, considerably lower than that measured for CoP-LDH2 (91 m^2/g). The CoH-LDH3 to CoH-LDH6 samples all possess very similar surface areas, between 42-46 m^2/g, which, unlike their analogues prepared via co-precipitation, show little variation as a function of R-value. All samples have surface areas within

the range typically cited for LDHs.[122, 193] The average pore size distribution was highest for CoH-LDH5 (13.3 nm) and lowest for CoH-LDH2 (9.7 nm). Pore volume was greatest for CoH-LDH3 at 0.1 cm^3/g and lowest for CoH-LDH2 at 0.05 cm^3/g. The average pore widths were found to generally increase with increasing Mg:Al ratio, over the range ~8.5 to ~11-13 nm, similar to that of the CoP-LDHs, however over a much narrower range (*cf.* 3 - 22 nm). The pore volume was greatest for CoH-LDH1 at 0.20 cm^3/g, however this is not deemed to be an LDH since it only contains aluminium. CoH-LDH2 to CoH-LDH6 all exhibit similar pore volumes of between 0.05 to 0.10 cm^3/g, with the average pore width increasing from CoH-LDH2 to CoH-LDH3 and then being very similar up to CoH-LDH6.

Table 3.10 Analytical data and possible calculated chemical formulae for co-hydrated LDHs. Analytical data: [a] from TGA analysis; [b] from elemental analysis. Adip = adipic acid

Sample	H_2O (%)	C (%)	H (%)
CoH-LDH1 - analytical data	n.d.	5.57[b]	2.08[b]
Not deemed an LDH by PXRD	-	-	-
CoH-LDH2 - analytical data	11.07[a]	8.39[b]	3.64[b]
$[Mg_{1.3}Al(OH)_{4.6}](CO_3)_{0.31}Adip_{0.19}.1.26H_2O$	11.07	8.39	4.23
$[Mg_{1.3}Al(OH)_{4.6}](OH)_{0.53}Adip_{0.24}.1.24H_2O$	11.07	8.39	4.74
$[Mg_{1.3}Al(OH)_{4.6}](CO_3)_{0.34}Adip_{0.16}.0.45H_2O$	4.32	8.39	3.64
CoH-LDH3 - analytical data	4.68[a]	5.73[b]	3.45[b]
$[Mg_{2.3}Al(OH)_{6.6}](CO_3)_{0.36}Adip_{0.14}.0.65H_2O$	4.68	5.73	3.65
$[Mg_{2.3}Al(OH)_{6.6}](OH)_{0.61}Adip_{0.19}.0.64H_2O$	4.68	5.73	3.45
$[Mg_{2.3}Al(OH)_{6.6}](CO_3)_{0.37}Adip_{0.13}.0.32H_2O$	2.36	5.73	3.45
CoH-LDH4 - analytical data	7.02[a]	3.19[b]	2.89[b]
$[Mg_{3.7}Al(OH)_{9.4}](CO_3)_{0.42}Adip_{0.08}.1.31H_2O$	7.02	3.19	3.79
$[Mg_{3.7}Al(OH)_{9.4}](OH)_{0.70}Adip_{0.15}.1.30H_2O$	7.02	3.19	4.20
CoH-LDH5 - analytical data	5.88[a]	3.61[b]	3.45[b]
$[Mg_{3.2}Al(OH)_{8.4}](CO_3)_{0.42}Adip_{0.08}.0.99H_2O$	5.88	3.61	3.68
$[Mg_{3.2}Al(OH)_{8.4}](OH)_{0.70}Adip_{0.15}.0.98H_2O$	5.88	3.61	4.13
$[Mg_{3.2}Al(OH)_{8.4}](CO_3)_{0.42}Adip_{0.08}.0.51H_2O$	3.15	3.61	3.45
$[Mg_{3.2}Al(OH)_{8.4}](OH)_{0.21}Adip_{0.14}.0.94H_2O$	5.88	3.61	4.06
CoH-LDH6 - analytical data	4.41[a]	3.48[b]	3.50[b]
$[Mg_{5.0}Al(OH)12_{.0}](CO_3)_{0.36}Adip_{0.14}.1.01H_2O$	4.41	3.48	3.70
$[Mg_{5.0}Al(OH)_{12.0}](OH)_{0.60}Adip_{0.20}.1.00H_2O$	4.41	3.48	3.99
$[Mg_{5.0}Al(OH)12_{.0}](CO_3)_{0.37}Adip_{0.13}.0.44H_2O$	1.98	3.48	3.50

As discussed previously (Section 3.4.1.2), LDHs are microporous solids with interlayer spacings typically in the 1 -2 nm range,[194] again far smaller than the average pore sizes established here, which are considered mesoporous.[143] The average pore size distributions for the co-hydrated LDHs are, similar to the co-precipitated LDHs, presumably due to inter-particle voids rather than internal porosity of the interlayer nanostructure, since only the external surface is probed;[137] consequently interpretation of the adsorption isotherms need to be treated with care. The surface areas for the co-hydrated LDHs all appear very similar, in contradiction to that of the co-precipitated LDHs. A possible reason for this is that the very controlled particle size dispersion in the CP5 alumina reactant for the co-hydration reaction leads to a more consistent particle size in the final LDH product.

Measurement of Hammett basicity for the various co-hydrated materials gave a basicity for CoH-LDH1 to CoH-LDH4 of between pK_a 6.0-7.6, which is lower than that determined for CoP-LDH5 to CoP-LDH6, lying in the 7.6-9.0 range. Evidently, the basicity of the various CoP-LDH and CoH-LDH materials varies not only as a function of R-value, but also with the method used for their preparation.[201] The weaker basicity of the co-hydrated sample prepared in this thesis may be a reflection that adipate is the interlayer anion, rather than carbonate. The use of an organic acid is believed to be necessary, however, in order to peptise the alumina and enable reactivity and, though this allows near neutral pH synthesis with no carbonate contamination, as well as control of morphology, it may also result in sample with only weakly basic sites. The CoH-LDHs are also more rich in Al (along with brucite and MgO co-phases), which will also result in lower basicity.

In summary, adipate-containing LDHs have been prepared by co-hydration of a 1 % w/w slurry of alumina and MgO, in the presence of a di-carboxylic acid at moderate temperature, without the presence of alkali base or inert atmosphere. Various parameters relating to the crystal structures of the various LDH materials, including cell parameters and possible chemical compositions, have been elucidated as well as properties relating to the bulk materials such as

surface area and external maximum basicity estimations. The co-hydrated LDHs appear to be weakly basic, and control of magnesium hydroxide phase growth seems inexorable at Mg:Al > 2.

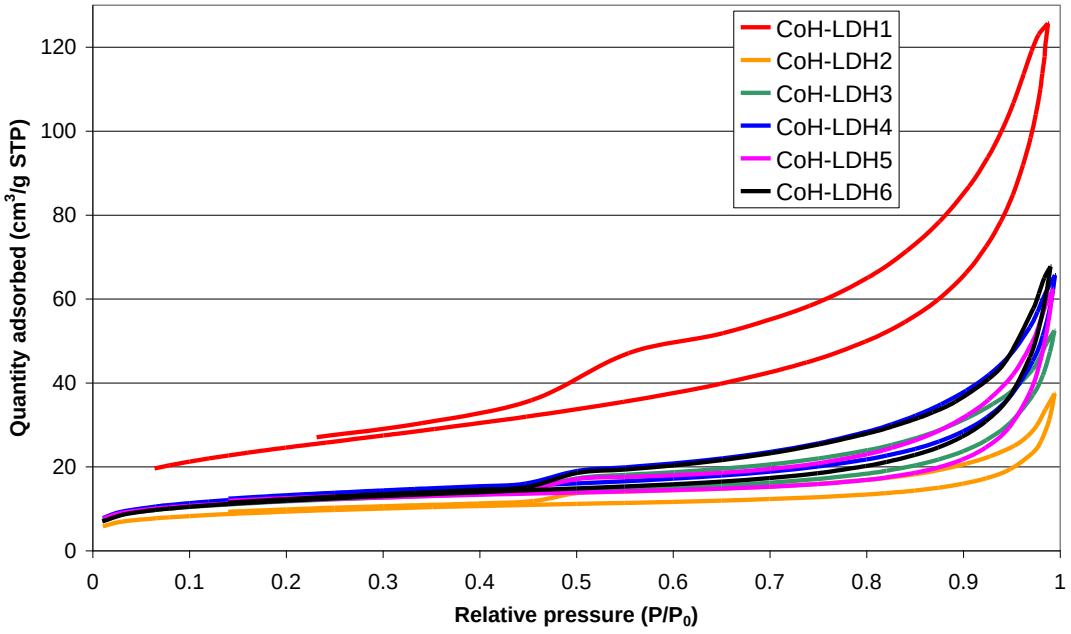

a)

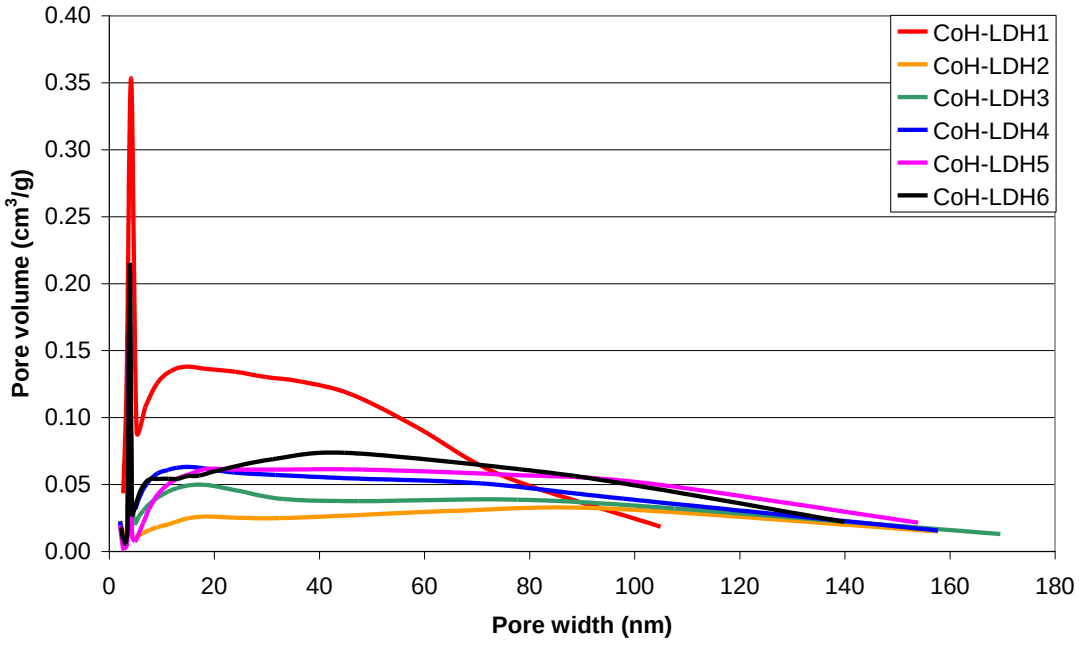

b)

Figure 3.11 a) Nitrogen adsorption/desorption plots showing typical hysteresis behaviour of type IV mesoporous solids and b) associated pore width distributions for CoH-LDH1-6

Table 3.11 Nitrogen adsorption analysis and Hammett basicity data for CoH-LDH1 to CoH-LDH6. Surface area standard deviations show in brackets.

Sample	surface area (m^2/g)	pore volume (cm^3/g)	average pore size (nm)	Hammett basicity range (pK_a)
CoH-LDH1	88.2032 (0.4370)	0.20	8.5	6.0-7.6
CoH-LDH2	32.9947 (0.2055)	0.05	9.7	6.0-7.6
CoH-LDH3	41.6270 (0.3200)	0.08	10.2	6.0-7.6
CoH-LDH4	46.1677 (0.2774)	0.10	10.8	6.0-7.6
CoH-LDH5	41.9519 (0.3527)	0.09	13.3	7.6-9.0
CoH-LDH6	42.6305 (0.2595)	0.10	11.1	7.6-9.0

3.4.3 Comparison of layered double hydroxides prepared by co-precipitation with layered double hydroxides prepared by co-hydration

In terms of producing phase pure LDH products, the CoP-LDHs generally (with the exception of CoP-LDH6) appear to be impurity free by both X-ray diffraction analysis and SEM-EDS, whereas the CoH-LDH show a degree of increasing impurity from CoH-LDH2 to CoH-LDH6, which may be attributed to brucite ($Mg(OH)_2$) and MgO.[123] Similar preparations to the co-hydration by Kelkar and Schutz,[202] using pseudoboehmite and acetate anions along with MgO, have similarly resulted in PXRDs with weak LDH reflections and a MgO byproduct , which increases with time until the reaction is complete.

When comparing the LDHs formed by the different synthesis methods, for CoH-LDH2 and CoH-LDH3, expanded and collapsed phases due to the different orientations of the adipate dianion within the interlayer are present. As expected the gallery heights are larger for the CoH-LDHs intercalated with adipate, but are also of a more consistent value in comparison to the CoP-LDHs which vary over a larger range.

Other than CoP-LDH4, which had an unusually low Mg:Al ratio of 3.3, all of the co-precipitated LDHs showed higher incorporation of Mg towards the desired initial reactant ratio (i.e. R-value), than the co-hydrated LDHs did. SEM-EDX data for the CoP-LDHs showed similar Mg:Al ratios of around 3.10, suggesting a degree of heterogeneity when compared to the ICP-OES bulk values, whereas the CoH-LDHs of the same R-value ratios tended to increase in line with the

desired ratio. Areas of varying Mg:Al ratios were also found for the CoP-LDHs, but not the CoH-LDHs.

All the CoH-LDHs, except CoH-LDH1, have a narrower range of surface areas, measured pore volumes and pore size distribution compared to their CoP-LDH analogues, suggesting CoH-LDH are a more homogeneous set of materials. However, the CoH-LDHs are generally of lower surface area, average pore size and pore volume than the CoP-LDHs.

The CoP-LDHs generally exhibit sites of higher basicity than the CoH-LDHs. For both LDH sets of materials, basicity increases with R-value. The CoH-LDHs may exhibit lower basicity since they are richer in Al as evidenced by their ICP-OES Mg:Al ratios. The lower basicity may also be a consequence of differing morphologies between the synthesised LDHs, that impact directly on the extents of surface edge/layer edges, which in turn alters the accessibility of surface sites with different basicity.

3.4.4 Thermal treatment of co-precipitation layered double hydroxides to form mixed metal oxides

3.4.4.1 Structure of the mixed metal oxides

MMOs were prepared by calcination of 1g of the parent CoP-LDHs, using the method outlined in Section 3.3. Initially during calcination, adsorbed and interlayer water are removed up to around 250 °C. According to Kustrowski *et al.*, calcination of LDHs at up to 500 °C results in dehydroxylation of the LDH hydroxide layer but without further modifying the structure to a spinel-like phase ($MgAl_2O_4$), which then occurs at excessive temperatures significantly above this.[203] Furthermore, it is known that upon calcination to 500 °C around 20 % of the octahedrally coordinated Al^{3+} within an MgAl LDH transform into tetrahedrally coordinated Al^{3+}.[204, 205] However, Reichle *et al.*,[205] propose that surface Al^{3+} remains unaffected by this. During LDH

thermal decomposition, it has been shown that PXRD reflections for an MgO-like material are first observed in the range 300-400 °C.[80]

The PXRD patterns of the CoP-MMOs attained by calcination of the CoP-LDH are shown in Figure 3.12, and highlight the distinct structural changes resulting from decomposition of the LDH materials.[203] The characteristic 00*l*, 10*l* and 11*l* peaks of an LDH structure are now absent and, instead, reflections ascribed to MgO are present.[206] The PXRD pattern peaks are broad, owing to the material containing very small crystallites and having high lattice strain. The CoP-MMO structures show some evidence of rehydration prior to analysis for R-values of 4 and 5, since nascent low angle peaks are once again observed. Also, the reflections in the PXRD arising from the CoP-MMO materials are progressively sharper as the R-value increases, correlating with the presence of increased amounts of brucite in the original CoP-LDH material (see Section 3.4.1.1).

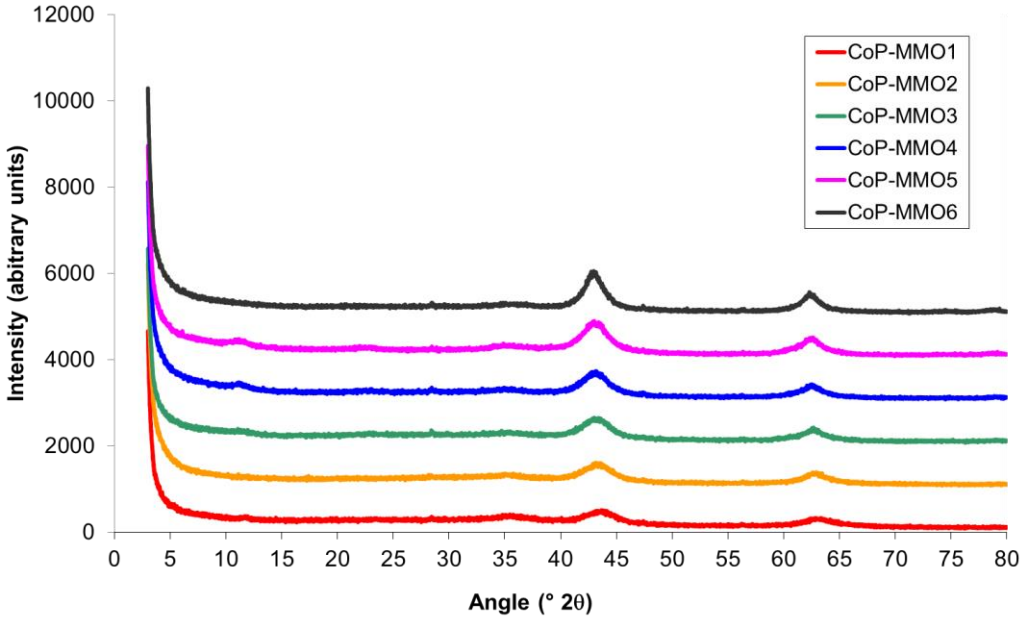

Figure 3.12 PXRD patterns for MMOs prepared from co-precipitated LDHs. When compared with the LDHs (Figure 3.3) it can be seen that the main LDH reflections have disappeared.

As would be expected, for the CoP-MMOs generated by calcination of the corresponding CoP-LDH materials, IR spectroscopy confirmed the absence of both hydroxyl and carbonate stretches owing to loss of carbonate and structural hydroxide.[207] SEM images were not acquired for the CoP-MMO compounds, however from the literature it is known that these materials show similar morphology to their uncalcined precursors.[207, 208]

3.4.4.2 Catalyst properties of the mixed metal oxides

By nitrogen adsorption measurements, all samples exhibit, similar to their LDH parents, type IV isotherms (Figure 3.13) characteristic of mesoporous materials. The results of BET surface area analysis are shown in Table 3.12. The corresponding CoP-LDH precursor data is also shown in parentheses, to facilitate comparison. It can be seen that for all calcined CoP-LDH samples, the formation of CoP-MMO materials resulted in an increase in surface area along with a commensurate increase in total pore volume. CoP-MMO1 exhibited the largest surface area (229 m^2/g), twice that of its uncalcined CoP-LDH1 precursor, something similar to the observations of Reichle *et al*. for calcined LDH materials.[205] The CoP-MMO surface area values are within agreement with those found in the literature.[122]

In a similar fashion, the pore volumes increased for all CoP-MMOs into the range 0.40-0.61 cm^3/g post-calcination. The average pore size for CoP-MMO1 to CoP-MMO3 increased, similarly in line with Li *et al.*,[204] whereas for CoP-MMO4 to CoP-MMO6 the average pore size decreases. According to Reichle *et al.*, numerous fine pores in the 2-4 nm region form during calcination of LDHs, which if the case, would lead to a decrease in the average pore size compared to the CoP-LDH precursors. Nevertheless, the average pore size distribution for the COP-MMOs (6.2 – 14.7 nm) is considerably narrower than that for the corresponding CoP-LDHs (3.1-22.3 nm), with both sets of materials being classified as being mesoporous. The associated increase in surface area and pore volume is believed to occur due to fine pores forming perpendicular to the crystal surface during calcination, through which gases formed from the dehydroxylation decomposition leave the crystal structure.[204, 205, 209]

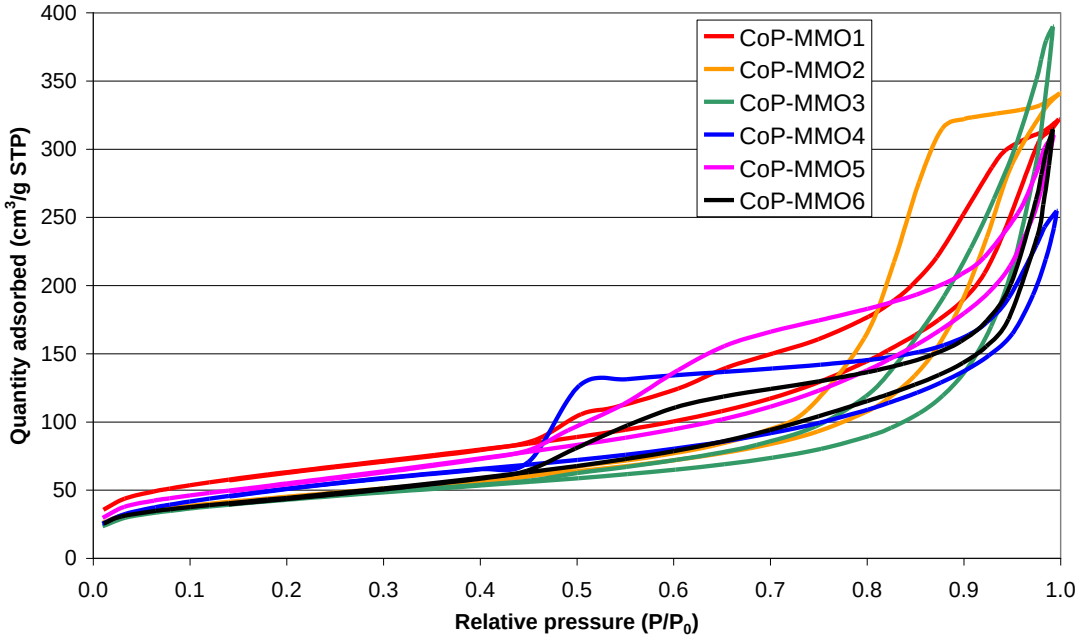

a)

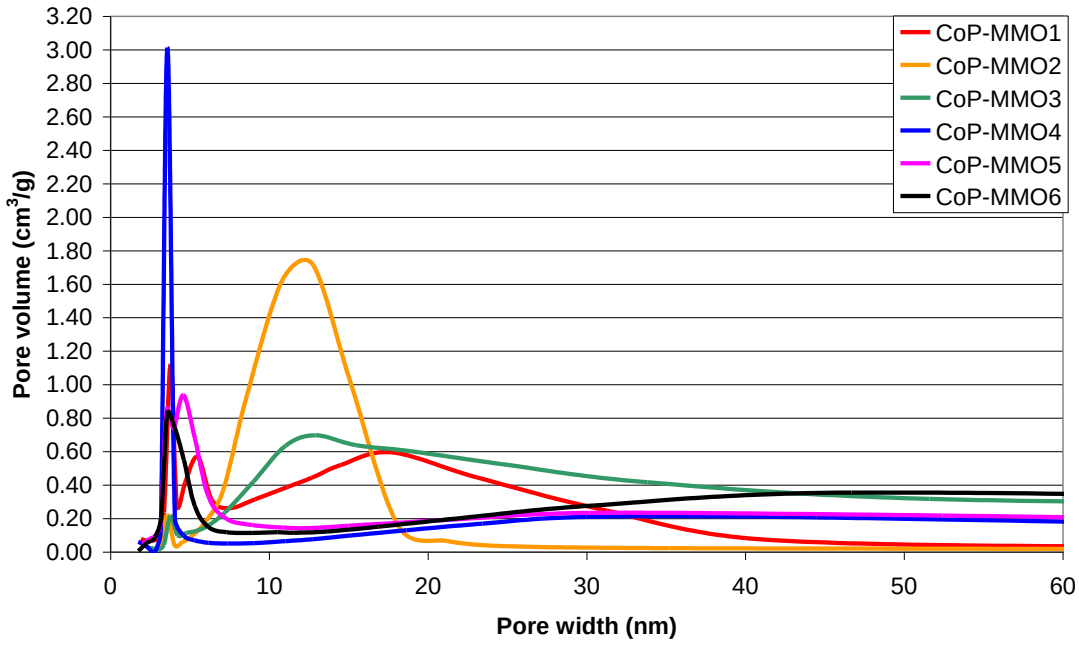

b)

Figure 3.13 a) Nitrogen adsorption/desorption isotherms showing typical hysteresis behaviour of type IV mesoporous solids and b) pore width distributions for CoP-MMO1 to CoP-MMO6

Table 3.12 Nitrogen adsorption analysis and Hammett basicity data for CoP-MMO1 to CoP-MMO6, with the corresponding CoP-LDH1 to CoP-LDH6 data shown in parentheses, for ease of comparison.

Sample	surface area (m^2/g)	pore volume (cm^3/g)	average pore size (nm)	Hammett Basicity (pK_a)
CoP-MMO1	229 (115)	0.51 (0.25)	7.8 (3.1)	7.6-9.0 (7.6-9.0)
CoP-MMO2	163 (91)	0.53 (0.32)	10.4 (8.7)	7.6-9.0 (9.0-10.0)
CoP-MMO3	155 (82)	0.61 (0.42)	14.7 (14.4)	7.6-9.0 (7.6-9.0)
CoP-MMO4	190 (17)	0.40 (0.12)	6.2 (20.5)	9.0-10.0 (9.0-10.0)
CoP-MMO5	199 (24)	0.49 (0.17)	7.2 (20.2)	9.0-10.0 (9.0-10.0)
CoP-MMO6	160 (39)	0.49 (0,25)	9.2 (22.3)	7.6-9.0 (9.0-10.0)

Following calcination to the CoP-MMOs, a semi-quantitative assessment of the basicity of these new materials using Hammett basicity indicators (Table 3.12) was undertaken. This study showed that the pK_a of CoP-MMO1 and CoP-MMO3 to CoP-MMO5 all lie in the range as those of the parent CoP-LDH materials. In contrast, the basicity decreased for CoP-MMO2 and CoP-MMO6 from pK_a 9.0–10.0 to pK_a 7.6-9.0, relative to their corresponding CoP-LDH precursors.

Corma *et al.* devised a novel way of distinguishing the distribution of base strength for MgAl/CO_3-derived MMOs. The materials were used as catalysts for Knoevenagel reactions with reactants of different pK_a. Here, catalysis can only occur if sites of greater pK_a than those of the substrate are present on the catalyst. Using this method, in the prior study, found that MMOs were made up of sites mainly in the range $10.7 \leq pK_a \leq 13.3$ along with few in the range $13.3 \leq pK_a \leq 16.5$. Also as R-value increased the number of basic sites was found to increase, however the number of stronger basic sites overall decreased.

This is the opposite case to that observed here where CoP-MMO4 and CoP-MMO5 were both found to exhibit the highest basicity (9.0-10.0), however these values did not change from their uncalcined precursors. A possible reason for the results observed here remaining largely unchanged from CoP-LDHs to CoP-MMOs is that even though the samples were calcined then stored in a desiccator, rehydration may have occurred prior to analysis. Also the samples were analysed for basicity in methanol, which is known to be hygroscopic, so may have resulted in rehydration towards the parent LDH structure via the memory effect.[180] Alternatively, the solvent may be interacting with the LDH and then the indicators.

Constantino and Pinnavaia studied the base-catalysed disproportionation of 2-methyl-3butyn-2-ol (MBOH) and found that the uncalcined MgAl LDH precursors were superior, as solid base catalysts, to the calcined MMO derivatives.[187] They ascertain this result to the involvement of basic interlayer anions in the catalytic reaction at external edge and basal surfaces of the LDHs, which correlates with the results reported here when comparing carbonate and adipate LDHs (Section 3.4.3). Post-calcination, medium-strong Lewis basic O^{2-}-M^{n+} pairs remain along with

strong basic sites relating to secluded O^{2-} ions.[122] These active basic sites are also joined by OH^- weakly basic groups remaining from calcination. As mentioned, an increase in calcination temperature generally leads to an increase in basicity and the amount of strong basic sites. However a degree of Lewis acidity is also found due to surface Al^{3+} sites being present.[210]

3.4.5 Thermal treatment of co-hydration layered double hydroxides to form mixed metal oxides

3.4.5.1 Structure of the mixed metal oxides

MMOs were prepared by calcination of 1g of the parent CoH-LDHs, using the method outlined in Section 3.3, which has been shown to result in dehydroxylation, but without further modifying the structure to a spinel-like phase ($MgAl_2O_4$) at excessive temperatures significantly above 500 °C.[203] The PXRD patterns of the CoH-MMO materials obtained by calcination of the CoH-LDH are shown in Figure 3.14. these show the distinct structural changes resulting from the decomposition of LDH materials as previously described in the last section,[203] with the exception of CoH-MMO1 that is not deemed an MMO since SEM-EDX of the parent material showed it was made up of principally of alumina.

For the series of materials from CoH-MMO2 to CoH-MMO6 the characteristic 00*l*, 10*l* and 11*l* peaks are now absent and, instead, MgO reflections are present.[206] For each material, very sharp peaks are observed consistent with the presence of moderately crystalline MgO-like material as seen by Chmielarz *et al*..[206] The CoH-MMO peaks are clearly much sharper than in the corresponding CoP-MMO patterns, indicating the presence of increased amounts of brucite and MgO in the original CoH-LDH material (vide supra). However, particularly in CoH-MMO4, an additional peak that may indicate possible spinel-type phase formation is observed at 37° 2θ. Nascent peaks in this region are also observed for the remaining CoH-MMO. Impurity peaks in the

CoH-LDH4 material at high angle (75-80° 2θ), have further increased post-calcination. Similar peaks can be seen in the remaining CoH-MMOs.

As with the CoP-MMOs, IR spectroscopy confirmed the loss of both hydroxyl and carbonyl stretches as the layer hydroxides decompose and carbonate is lost as carbon dioxide.[207]

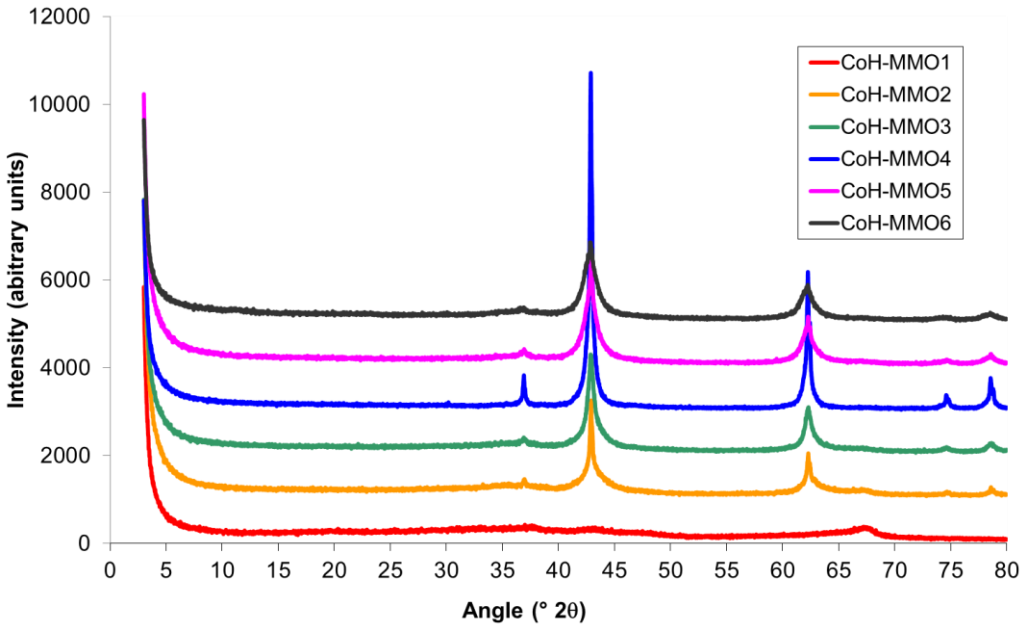

Figure 3.14 PXRD patterns for MMOs prepared from co-hydrated LDHs. When compared with the LDHs (Figure 3.8) it can be seen that the main LDH reflections have disappeared.

3.4.5.2 Catalyst properties of the mixed metal oxides

The results of BET surface area analyses for CoH-MMO1-6 are shown in Table 3.13 and Figure 3.15. The corresponding CoH-LDH precursor data is also shown in parentheses, to facilitate comparison. It can be seen that for calcined CoH-LDH samples, the formation of CoH-MMO materials resulted in an increase in surface area along with a commensurate increase in total pore volume. Interestingly, though CoH-MMO1 was not an MMO, confirmed *via* PXRD analysis, it has a very high surface area of 240 m^2/g. Disregarding this material, CoH-MMO2 exhibited the largest surface area (231 m^2/g), significantly higher than that of its uncalcined CoH-LDH2 precursor (33 m^2/g). CoP-LDH3 and COP-LDH6 surface areas increased similarly from 42-46 m^2/g to 153-213 m^2/g upon calcination. These values indicate a slight decrease in surface area with decreasing R-

value, with all the CoH-MMO surface areas agreeing well with those found in the literature for MMOs.[196, 203]

In comparison with the analogous R-value CoP-MMOs, the surface areas were similar or higher for the corresponding CoH-MMOs. The pore volumes increased similarly for all CoH-MMOs into the region 0.32-0.40 cm^3/g following calcination, again in line with the CoP-MMOs, but to a slightly lower volume (*cf.* 0.40-0.61 m^2/g) and over a narrower range. The average pore size was seen to decrease to a range of 4.8-7.5 nm comparable to that for CoP-MMO4 to CoP-MMO6, and hence all these materials may be classified in the mesoporous range. The average pore width decreases, according to Reichle *et al,* as numerous fine pores in the 2-4 nm region form during calcination.[205] As discussed in the last section, these pores are thought to form perpendicular to the crystal surface during calcination, as gases formed from the dehydroxylation process are lost from the crystal structure.[204, 205, 209] All samples exhibit type IV isotherms (Figure 3.15) characteristic of mesoporous materials in BET surface area analysis. For each sample, the hysteresis loop is narrow, with almost parallel adsorption and desorption branches, something that is indicative of pores with regular geometry, while the steep desorption behaviour indicates that the pore size distribution is narrow.[143]

Following calcination to the CoH-MMOs, a semi-quantitative assessment of the basicity of these new materials using Hammett basicity indicators (Figure 3.15) was undertaken. This study showed that the pK_a's of CoH-MMO2 to CoH-MMO6 all lie in the same range of 7.6-9.0. The basicities of CoH-MMO5 and CoH-MMO6 remain unchanged from their LDH precursors, however CoH-MMO2 to CoH-MMO4 have all increased in basicity. This supports the earlier assertion that this is due to the fact that the CoH-LDHs are more acidic since they contain interlayer adipate anions. Post-calcination, basicity is generally seen to increase as medium-strong Lewis basic O^{2-}-M^{n+} pairs remain along with strong basic sites relating to secluded O^{2-} ions.[122]

Table 3.13 Nitrogen adsorption analysis and Hammett basicity data for CoH-MMO2 to CoP-MMO6, with the corresponding CoH-LDH1 to CoH-LDH6 data shown in parentheses, to facilitate comparison.

Sample	surface area (m^2/g)	pore volume (cm^3/g)	average pore size (nm)	Hammett Basicity (pK_a)
CoH-MMO1	240 (88)	0.40 (0.20)	6.0 (8.5)	7.6-9.0 (6.0-7.6)
CoH-MMO2	231 (33)	0.32 (0.05)	4.8 (9.7)	7.6-9.0 (6.0-7.6)
CoH-MMO3	213 (42)	0.39 (0.08)	5.9 (10.2)	7.6-9.0 (6.0-7.6)
CoH-MMO4	184 (46)	0.37 (0.10)	6.4 (10.8)	7.6-9.0 (6.0-7.6)
CoH-MMO5	153 (42)	0.37 (0.09)	7.5 (13.3)	7.6-9.0 (7.6-9.0)
CoH-MMO6	198 (43)	0.39 (0.10)	5.8 (11.1)	7.6-9.0 (7.6-9.0)

Interestingly, even though CoH-MMO1 is not deemed an MMO (and CoH-LDH1 not an LDH), the basicity increased in a similar fashion to that observed for CoH-MMO2, CoH-MMO3 and CoH-MMO4 post-calcination. Corma *et al.*, stated that as R-value increased the number of basic sites was found to increase, however the number of stronger basic sites overall decreased.[196] In this study all basicities lie in the same range as that for the majority of the CoP-MMOs. Again, a possible reason for the CoH-MMOs described here not showing such enhanced basicity relative to the study by Corma *et al.*,[196] is that partial reconstruction might occur prior to analysis. The samples were analysed for basicity in methanol which is hygroscopic and may have resulted in rehydration towards the parent LDH structure *via* the memory effect,[180] though adipate anions would not have been present for complete restructuring.

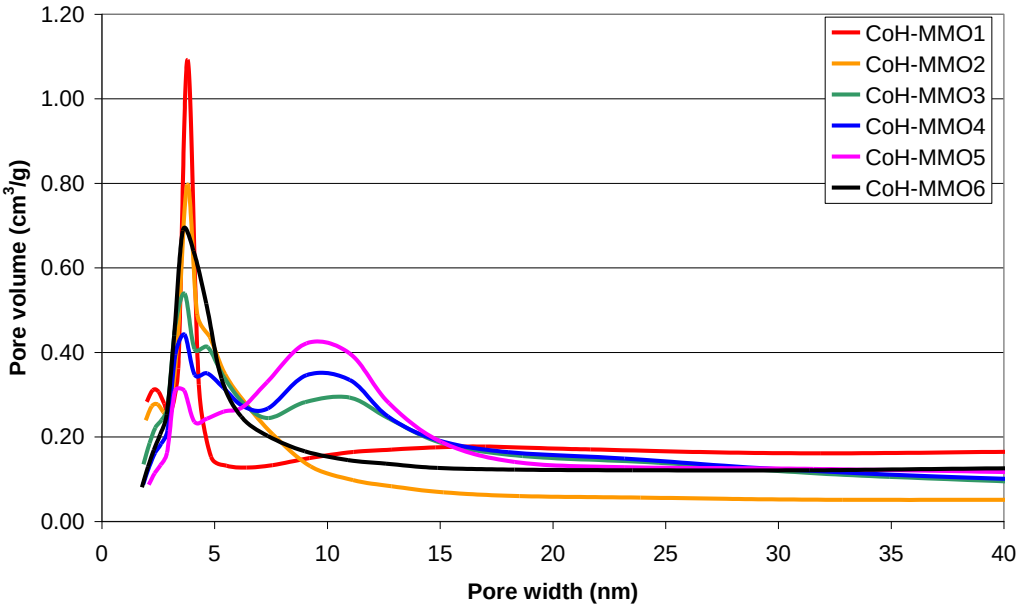

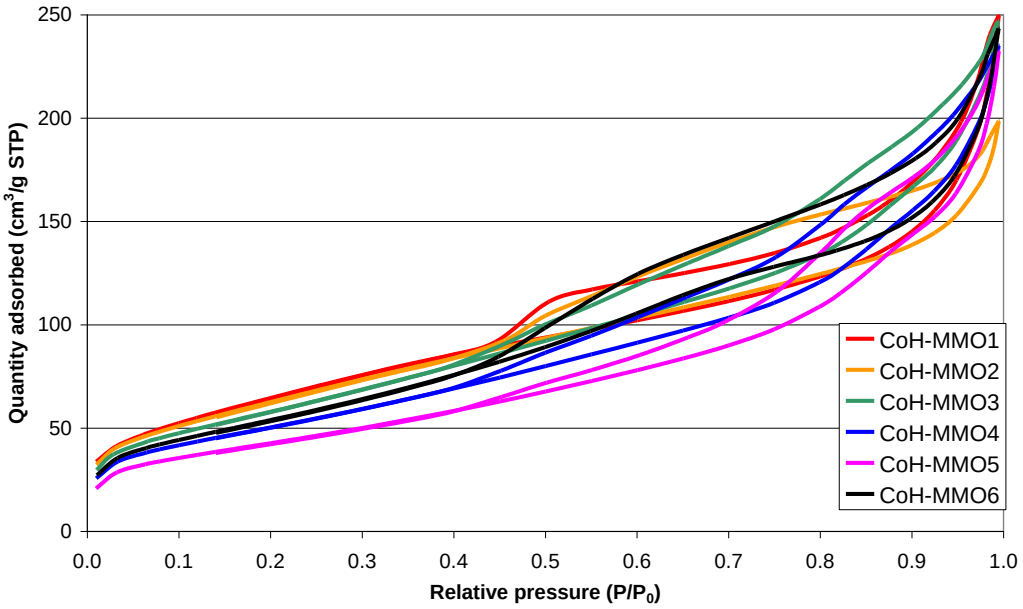

Figure 3.15 a) Nitrogen adsorption/desorption plots showing typical hysteresis behaviour of type IV mesoporous solids and b) pore width distributions for CoH-MMO1-6

3.4.6 Sequential thermogravimetric analyses of a calcined-rehydrated layered double hydroxide

As part of the work for this thesis a study was performed on CoP-LDH1 in order to probe the effects of calcination and subsequent rehydration for LDHs upon exposure to atmospheric conditions. CoP-LDH1 was initially calcined at a rate of 5 °C/min up to 500 °C in a TGA instrument (Figure 3.16). This showed a characteristic mass loss of around 15 % water up to 175 °C, followed by a further 29 % mass loss up to 500 °C, attributable to interlayer anions and dehydroxylation. The sample was then left to rehydrate under atmospheric conditions for 1 day, followed by a second calcination, which resulted in a 16 % mass loss, similar to the mass lost for water in the first calcination. This sample was again then left to rehydrate under atmospheric conditions for a further 1 day, followed by a third calcination which resulted in a 14 % mass loss, similar to the 15 % water loss in the first calcination.

It has been shown that for an LDH sample which has been calcined and left exposed to air/moisture for 24 h the sample regains a mass similar to that lost during the first stage of calcination. A recent study found that LDHs can exchange interlayer carbonate with atmospheric

carbon dioxide, however this was severely hindered by high relative humidity where 50 % exchange occurred in one week.[211] The authors propose that in low-humidity atmospheres there are vacancies in the interlayer into which CO_2 may enter and exchange with existing interlayer carbonate through reaction with water, however in high-humidity atmospheres the interlayer is fully occupied by water and vacancies do not exist for CO_2 to enter the system. Hence a similar system may be occurring here where the interlayer becomes saturated with water and as the kinetics of CO_2 adsorption are slower than that of H_2O adsorption, the adsorption of CO_2 is not observed to occur in the relatively short timeframe of 24 hours, resulting in the initial formation of a meixnerite-type structure ($[Mg_6Al_2(OH)_{16}].(OH)_2.4(H_2O)$), where the interlayer anion is now hydroxide.

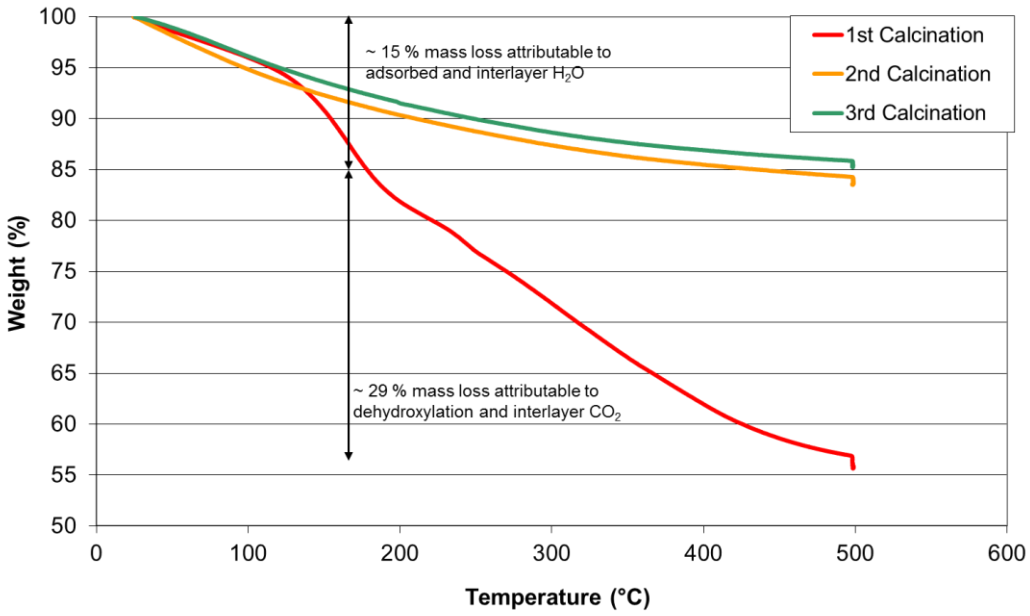

Figure 3.16 Thermogravimetric analyses of CoP-LDH1, showing an initial calcination, followed by a 2nd calcination after 1 day of atmospheric exposure, then a 3rd calcination after a further 1 day of atmospheric exposure. The red line shows that, upon initial heating to 500 °C, there is a 15 % mass loss, which is attributed to loss of water and 29 % mass loss attributed to loss of interlayer CO_2 and dehydroxylation. Following exposure to atmospheric conditions for 24 h, upon heating to 500 °C (yellow line) results in a 15 % mass loss, which is attributed to loss of H_2O which had readsorbed and reacted to form a meixnerite-type structure during exposure to atmospheric conditions. Following exposure to atmospheric conditions again for 24 h, similarly, 15 % mass loss occurred upon heating to 500 °C (green line), attributed to loss of H_2O, again which had readsorbed and reacted to form a meixnerite-type structure

This short study illustrates the rehydration and restructuring process of highly disordered MMO materials towards their parent LDHs, dubbed the memory effect.[164] As a result, over time the desired MMO properties, such as basicity and large surface area will gradually decrease to that

of an LDH material. It should be noted though, within the timeframe involved here the sample did not completely regain the masses lost in the initial calcination. From this it can be concluded that it is important to calcine LDH materials, to produce MMOs, only immediately prior to their subsequent use as catalysts or for their analysis, otherwise LDHs structures will inherently start to reform upon exposure to air and moisture and the inherent MMO properties will be lost.

3.5 Summary and conclusions

On the basis of the results from PXRD, TGA, and SEM analyses, the samples prepared via co-precipitation, namely CoP-LDH1 to CoP-LDH6, and those from co-hydration, CoH-LDH2 to COH-LDH6, have structures/compositions typical of LDH materials. Secondary phases are found to be present, in many cases, especially in the CoH-LDHs, which may be attributable to brucite and unreacted MgO.

The Mg:Al ratio determined by ICP-OES of the CoP-LDHs followed the expected Mg:Al ratio more closely than the same analysis of the CoH-LDH counterparts. SEM-EDX results showed that the CoP-LDHs all demonstrated Mg:Al ratios at the micro-scale of around 3.10, whereas the Mg:Al ratios for the analogous CoH-LDHs increased in line with the expected ratio on the basis of R-value. Areas of varying Mg:Al ratios were also found for the CoP-LDHs, but not the CoH-LDHs, indicating that sample heterogeneity at a microscale needs ascertaining. The importance of washing co-precipitated materials was illustrated following analysis of an unwashed CoP-LDH1 sample, which showed the presence of sodium in the bulk sample. Similarly no LDH resulted from the co-hydration performed at an R-value of 1, possibly due to the larger particle size of the alumina used as a reactant, than that used by Greenwell *et al.*[123]

Pore volume and pore size distribution were greatest for the CoP-LDH materials, but as has been discussed, the average pore size results for the LDHs are presumably due to inter-particle voids rather than internal porosity of the interlayer nanostructure.

The CoP-LDHs were found to be more basic than the CoH-LDHs, owing to the former containing basic carbonate groups in the interlayer, whereas the latter contain acidic interlayer groups. The CoH-LDHs are also richer in Al (along with brucite and MgO co-phases), which results in lower basicity. For both CoP-LDHs and CoH-LDHs, basicity was found to increase slightly with R-value.

For all of the LDH materials synthesised here, calcination results in loss of the typical layered LDH structure, affording a low order mixed metal oxide phase, as evidenced by loss of the low angle basal reflections in the PXRD patterns (Figure 3.12 and Figure 3.14). The surface areas and pore volumes of the various materials increased greatly on calcining from LDH to MMO, with all surface areas being greater than 153 m^2/g. The average pore widths were found to increase for CoP-MMO1 to CoP-MMO3, however CoP-MMO4 to CoP-MMO6 and all CoH-MMO samples were found to decrease in pore volume compared to their LDH precursors, although remained in the mesoporous range.

The CoP-MMOs and CoH-MMOs were found to be of similar basicity, being generally in the $7.6 \leq pK_a \leq 9.0$, with the exception of CoP-MMO5 and CoP-MMO6 being slightly higher at $9.0 \leq pK_a \leq 10.0$. (unchanged from their LDH precursors). It appears there was a reduction in basicity following the calcination of the co-precipitated sample and an increase in basicity for the calcination of the co-hydrated samples. This may be the result of the loss of basic and acidic interlayer anions, respectively. MMOs are generally seen as being more basic than their uncalcined counterparts,[122] however observed basicity can be reaction-specific with the methods used to assess them over/under estimating basicity due to various effects such as accessibility to active sites. For example, some studies have shown LDHs to have superior basicity to MMOs[187] and others have shown the contrary.[154]

The importance of only calcining LDHs to produce MMOs immediately prior to their further use or analysis has been outlined in section 3.4.6, otherwise they will begin to rehydrate and reconstruct into LDHs under atmospheric conditions. Since the basicity measurements in this study

were carried out in methanol, which is hygroscopic, this may have resulted in partial or full rehydration and reconstruction of MMOs to their LDH structures, misrepresenting the obtained results.

4 Direct decarboxylation of stearic acid over a supported Pd/C catalyst

4.1 Introduction to decarboxylation of fatty acids

Crude oil is not a sustainable source of energy and attempts are being made to extend the shelf life of infrastructure which depends on it by producing alternative bio-based fuels.[212] Typical bio-derived oils can be extracted from feedstocks such as algae, plants and seeds, with the main non-polar components being made up of triglycerides. Present, oxygen-rich biofuels, produced from vegetable oils *via* processes such as *trans*-esterification, are of low energy density and not entirely suited to crude oil based fuel engines. If deoxygenated biofuels can be produced then these could be used as a direct replacement for petroleum sourced hydrocarbons.[212, 213]

Triglycerides are essentially glycerol tri-esters of saturated or unsaturated carboxylic acids (see Figure 1.5).[214] Hydrolysis of triglycerides leads to free fatty acids (FFAs) and glycerol ($C_2H_5(OH)_3$),[215] the latter usually a by-product of biofuel production,[216] but also a fuel in its own right.[217] FFAs are currently one of the many possible sources of current advanced drop-in biofuels and chemicals,[218] but are also believed to have played a role in crude oil formation.[88] The catalysis of the decarboxylation of carboxylic acids has ranged from early studies on petroleum geology,[90] to more recent attempts at chemical upgrading of bio-oils for fuel-grade use.[2] Hydrocarbons, found in crude oil, were formed by thermal maturation in conjunction with catalytic action of formation rocks (containing natural clay mineral catalysts) over millions of years on settled and sedimented lipids and fatty acids from marine organisms.[88] Almon and Johns, from experimental evidence, postulated that this occurred *via* a radical mechanism.[219] However, in more recent work, Geatches *et al*., who employed computational studies, believe this to be due to the substitutions in the clay sheet, which attract a counter-ion that may donate an electron to the reactant-clay system,[91] with fatty acid decarboxylation proceeding by means of an alcohol intermediate to the alkane (see Figure 4.1).[220] Alcohol intermediates have previously been shown to be involved in the production of alkanes from carboxylic acids.[221]

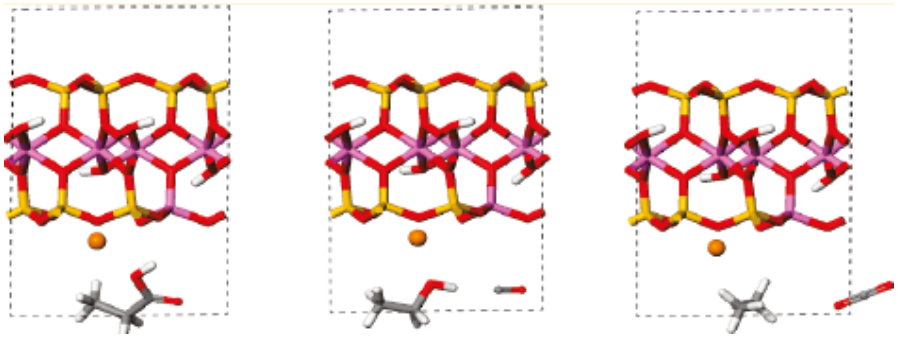

Figure 4.1 Proposed decarboxylation route of a model fatty acid *via* an alcohol intermediate by Geatches *et al.*, involving a clay sheet and counter-ion. On going from left to right the starting carboxylic acid, clay sheet and associated sodium cation are shown (left), followed by the alcohol and CO intermediates obtained from density functional theory (middle) and finally the resulting alkane and CO_2 products (right) from decarboxylation. Colour scheme: oxygen, red; hydrogen, white; aluminium, pink; carbon, grey; silicon, yellow. Taken from Geatches *et al.*[220]

Within this chapter, attempts are described which replicate decarboxylation reactions from the literature, to produce alkanes from fatty acids. The catalysts previously employed in prior work in the literature tend to be of 3 types: transition metal mediated; metal oxides and mixed metal oxides and, finally, aluminosilicate clay-type compounds. Several mechanisms have been proposed for the decarboxylation reactions of fatty acids, depending on the type of catalyst used. A brief review of the literature in this respect is given in the following section, prior to describing the experiments and results from decarboxylation reactions carried out for this thesis.

4.1.1 Transition metal-mediated decarboxylation– a review of the literature

The first recorded direct decarboxylation reaction was carried out in 1936, when Bertram published work using a homogeneous catalyst over selenium to decarboxylate stearic acid to heptadecane with 50 % yield.[94] Since then, a range of transition metal-mediated decarboxylation reactions have been undertaken, as reviewed below.

4.1.1.1 Decarboxylation reactions using Pd/C catalysts

Recently, Murzin *et al*. have shown that Pd/C is an effective catalyst with respect to decarboxylation reactions of compounds representing model vegetable oils, leading to long-chain hydrocarbons.[2] These studies include the decarboxylation of stearic acid ($C_{17}H_{35}COOH$), ethyl stearate ($C_{17}H_{35}COOC_2H_5$) and tristearin ($C_3H_5(C_{18}H_{35}O_2)_3$) at high pressure (17-40 bar),[2] stearic acid at lower pressure (6 bar),[96] kinetics of ethyl stearate reactions,[95] oleic acid ($C_{17}H_{33}COOH$), linoleic acid ($C_{17}H_{31}COOH$) and methyl oleate reactions ($C_{17}H_{33}COOCH_3$)[97] and the decarboxylation of stearic acid using palladium supported on synthetic carbon Sibunit (a porous carbon-carbon composite material with a high mesopore volume).[98] An organic solvent is used in these reactions, typically dodecane ($C_{12}H_{26}$).

With a commercial activated carbon supported catalyst, *n*-heptadecane ($C_{17}H_{36}$) was found to be the main product when the model compounds stearic acid, ethyl stearate and tristearin were deoxygenated.[2] The decarboxylation of stearic acid resulted in production of heptadecenes ($C_{17}H_{34}$), the concentration of which decreased over time, suggesting that they were intermediates in the process. In a further described study stearic acid was decarboxylated using 5 % Pd/C in dodecane solvent, at 300 °C in 17 bar He atmosphere.[2] This led to 41 % conversion after 300 mins, with over 90 % selectivity to *n*-heptadecane (Figure 4.2). Other minor products included C_{17} olefins and C_{17} aromatics (undecylbenzenes, $C_6H_5C_{11}H_{23}$).

At 300 °C and at a pressure of 17 bar, stearic acid was found to have a higher overall conversion to *n*-heptadecane when in a reaction atmosphere of 5 % hydrogen and 95 % argon v/v than compared to reaction atmospheres of 100 % helium and 100 % hydrogen v/v, as shown in Figure 4.3, indicating that in the presence of hydrogen, hydro-decarboxylation was favoured.[2] Selectivity to unsaturated C_{17} products decreased over time for all atmosphere types. Ethyl stearate was first found to convert into stearic acid before decarboxylating to *n*-heptadecane, similarly, with a higher turnover frequency in a reaction atmosphere of 5 % hydrogen and 95 % argon v/v (64×10^3

s^{-1}) than 100 % helium (32 x 10^3 s^{-1}). Selectivity to *n*-heptadecane decreased on going from 300 °C to 360 °C when the yield of aromatics, which are undesirable in diesel-type fuels, increased 9-fold.

The reaction kinetics for ethyl stearate and stearic acid decarboxylation over Pd/C catalyst have been studied.[95] Using ethyl stearate the rate of reaction increased on going from 300 °C to 360 °C, having an activation energy of 57.3 kJ/mol from first order kinetics (K = 6.27×10^{-12} min^{-1} at 300 °C). The major intermediate product, being stearic acid, results in a reaction order of almost zero, with the Pd/C catalyst being deactivated at high concentrations of stearic acid.

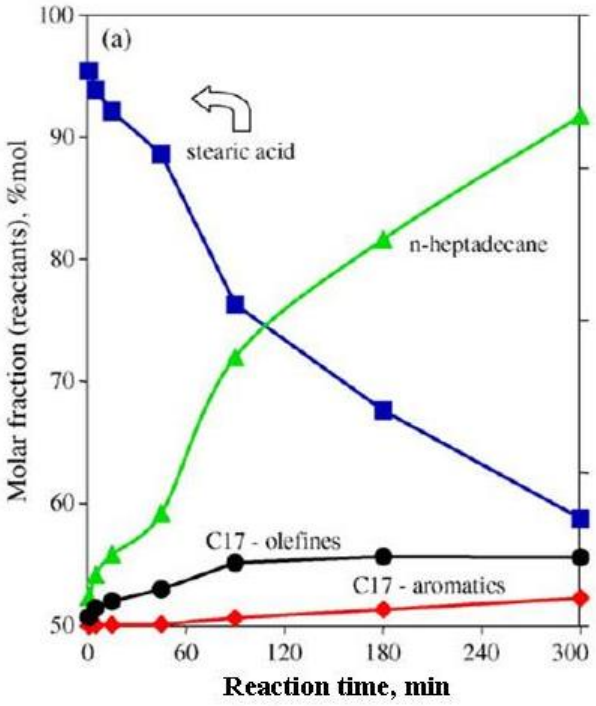

Figure 4.2 Conversion of stearic acid using 5 % Pd/C in He atmosphere at 300 °C and 17 bar pressure. In the reaction, stearic acid converts mainly into *n*-heptadecane through decarboxylation, and this is confirmed in the study by the evolution of CO_2 (not shown). In addition, minor conversion to C_{17} alkene and C_{17} aromatic groups is observed. Taken from Kubickova *et al.*[2]

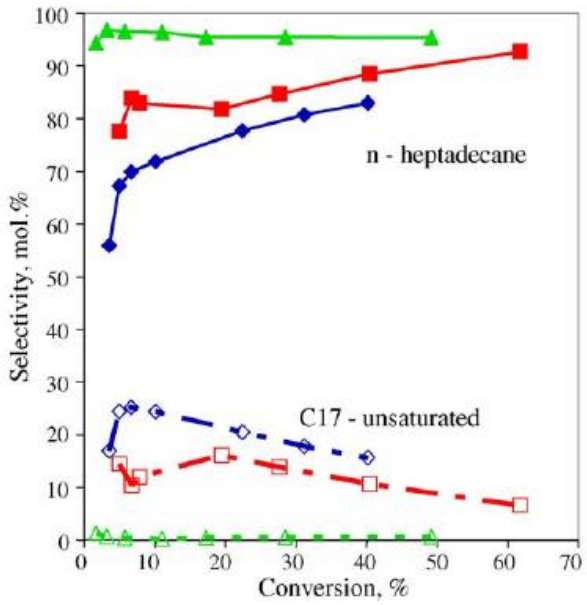

Figure 4.3 Conversions of stearic acid and selectivities to the major reaction products using 5 wt % Pd/C after 6 hours at 300 °C, 17 bar in different reaction atmospheres. Atmosphere colour scheme: blue, 100 % He; red 5 % H_2, 95 % Ar; green 100 % H_2. Taken from Kubickova *et al.*[2]

Interestingly, 1 % and 10 % loadings of commercial Pd/C catalyst have exhibited lower selectivity to n-heptadecane (52 and 60 % respectively) than 5 % loading Pd/C (95 %), possibly due to the former two leading to formation of unsaturated products, which then cause catalyst coking (Figure 4.4).[96] Further to this initial study, 10 % Pd/C catalyst was found to be slightly acidic whereas 1 % and 5 % Pd/C were found to be alkaline. Additional semi-batch process work with palladium supported on Sibunit as a catalyst, in dodecane, at a pressure of 17 bar helium was carried out.[98] Using 4 % wt catalyst, stearic acid was deoxygenated with increasing initial reaction rate and a decreasing time for 100 % conversion as temperature was increased from 270 °C to 300 °C to 330 °C. At 270 °C it was found that the there was a lag time of around 60 mins before stearic acid conversion progressed. However, as well as the *n*-heptadecane produced using activated Pd/C, *n*-pentadecane was produced with analogous selectivity, demonstrating that the support structure can also play a vital role in catalyst selectivity.[98]

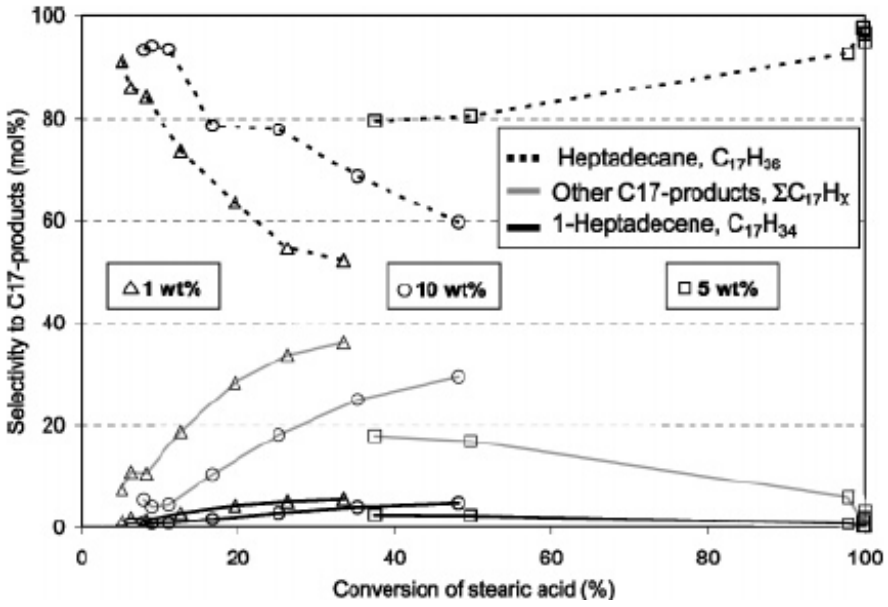

Figure 4.4 Pd/C wt % loading and effect on selectivities, with 1 g catalyst at 300 °C and 6 bar in H_2 atmosphere. Taken from Snare *et al*.[96]

Further studies into heterogeneous decarboxylation were carried out, with the uncatalysed reaction only leading to < 5 % conversion.[96] Using direct current plasma atomic emission spectroscopy (DCP-AES) with Pd/C catalyst it was confirmed that the reaction was indeed heterogeneous and not homogeneous due to catalyst leaching into solution. Pd/C at 250 °C under hydrothermal conditions has been reported to decarboxylate 2-(4-hydroxyphenyl)-propanoic acid (C_6H_4OH-C_3H_4OOH) at 89 % conversion.[222] These conditions were also found to effectively decarbonylate aromatic aldehydes and further remove aromatic amide groups.

The most probable role of Pd in decarboxylation has been suggested to be *via* the scission of the O-H bond from the RCOOH acid group, to form RCOO, followed by scission of the R-C bond, releasing CO_2.[223] Though, it has been noted that, in these experiments decarbonylation could also be occurring where OH is removed and the reaction proceeds by RCO.[223]

4.1.1.2 Decarboxylation catalysis studies using other metals

A range of catalysts were tested in a study by Snare *et al*., supported on carbon and metal oxides (Ir, Mo, Ni, Os Pd, Pt, Rh and Ru) as well as a Raney nickel catalyst, with the results shown in Table

4.1.[96] Generally, side reactions were observed over 6 h reaction time (300 °C, 6 bar, helium) such as isomerisation, dehydrogenation, aromatic production and shorter hydrocarbons production *via* cracking. The initial reaction rate was greatest for 5 % Pd/C (1.9 mmol/s/g_{met}) with carbon supported catalysts in general leading to higher rates, possibly due to enhanced surface area of the support structure and metal dispersion. It was found that some side products, produced using Ru/C and Rh/C catalysts, were selective towards unsaturated by-products, which could have led to catalyst deactivation. When using Ru/MgO, stearone ($(C_{17}H_{35})_2CO$) was formed with > 99 % selectivity, suggesting that ketonic decarboxylation may be preferred here. 5 % Pd/C was found to be the preferred catalyst for decarboxylation of stearic acid (100 % conversion, 95 % selectivity, greater than when at 17 bar)[2], with Pt/C giving best performance for decarbonylation, followed by Ni, Rh, Ir, Ru and Os.

Similar reactions have also been used by Masende to decarboxylate the dicarboxylic acid malonic acid using a Pt/graphite catalyst leading to CO_2 and acetic acid with over 80 % conversion,

Table 4.1 Catalyst performance for the deoxygenation of stearic acid, with 1 g catalyst at 300 °C and 6 bar. Taken from Snare *et al.*[96]

		deoxygenation selectivity, S^a (%)				side product selectivity, S^a (%)				
catalyst	conversion, X^a (%)	S_{n-C17}	S_{1-C17}	$S_{\sum C17}$	Total S_{C17}	S_{C18}	S_{C35}	$S_{crack}{}^b$	$S_{heavy}{}^c$	$S_{other}{}^d$
81% Raney-Ni	14.0	30	13	7	50	<0.5		17	32	
16% Ni/Al_2O_3	17.8	29	12	4	46	<0.5	12	13	29	
60% Ni/SiO_2	18.1	19	30	10	58	1		20	21	
50% Ni/Cr_2O_3	12.3	48	8	3	60			17	24	
3%,9% $NiMo/Al_2O_3$	8.6	15	4	3	23			3	74	
5% Ru/SiO_2	7.2	6	14	4	23		60	7	11	
5% Ru/MgO	96.2						99	–	1	
5% Ru/C	13.2	24	27	14	65	<0.5	8	11	15	
5% Pd/Al_2O_3	23.7	20	7	15	42		48	1	9	
1% Pd/C	33.4	52	6	36	94	1		1	2	2
10% Pd/C	48.1	60	5	29	94	<0.5	3	1		2
5% Pd/C	100.0	95	0	3	99			1		<0.5
8%,2% PdPt/C	61.6	73	7	15	96	<0.5		3	1	<0.5
5% Pt/Al_2O_3	19.9	18	17	11	46	<0.5	37	2	14	<0.5
5% Pt/C	86.0	87	1	7	95	<0.5		4	<0.5	<0.5
2% Ir/Al_2O_3	17.2	1	1		2		85		12	
1% Ir/SiO_2	4.6	14	29	26	69			2	29	
5% Os/C	6.9	29	15	9	53		17	7	22	
3% Rh/SiO_2	15.7	7	9	7	23		56	3	18	
1% Rh/C	17.9	18	13	53	85	<0.5	4	4	7	<0.5

[a] Conversion of stearic acid and selectivities toward products after 6 h of reaction. [b] Crack denotes cracking products consisted of shorter fatty acids, C10−C17 acids ,and shorter hydrocarbons, C13−C16 hydrocarbons. [c] Heavy denotes dimeric products formed via unsaturated acids and olefins. [d] Other denotes unidentified products.

compared to less than 30 % for the uncatalysed reaction).[224] The reaction was carried out at 18 bar with temperatures of 120-160 °C in a flow of oxygen, but it was unknown whether it was the platinum metal, graphite or both that were responsible for catalysis. Do *et al*.,[225] found 1 % Pt/Al_2O_3 to be effective in the conversion of methyl octanoate and methyl stearate to straight chain hydrocarbons through decarboxylation with a hydrogen atmosphere. However in the absence of hydrogen, ketonic decarboxylation to form ketones occurred.

Ascorbic acid and 1 mmol copper sulphate has also been found to catalyse the decarboxylation of benzoic acid to benzene, in food products where these naturally occurring acids are found.[226] This was found to proceed by a free radical mechanism in that hydrogen peroxide is formed *in situ* when an oxygen molecule is broken down and subsequent peroxide formation *via* interactions with the ascorbic acid and the copper oxidation state.

In order to improve the selectivity of reactions, promoter molecules have also been studied, for example, Cu catalysts with bipyridine promoters have been utilized as catalysts for decarboxylation of aromatic acids > 95 % at 250 °C. However the same catalysts were found to be ineffective with acids of natural origin,[227] stated as being due to unsaturated rings acting as H-donors and deactivating catalysts.

4.1.2 Metal oxides and complex catalysts for deoxygenation

Sulphided $NiMo/\gamma\text{-}Al_2O_3$ has been used to catalyse the hydrodeoxygenation of the methyl esters methyl heptanoate ($C_7H_{15}COOCH_3$) and methyl hexanoate ($C_6H_{13}COOCH_3$) at 15 Bar pressure (hydrogen), leading to 100 % conversion to alkanes at 275 °C.[221] The catalysts were reportedly not stable and product distributions were observed to change over time. Three reaction pathways were proposed, one being the simultaneous loss of methane and decarboxylation (Figure 4.5). In this reaction water was found to hinder the decarboxylation reaction and suppressed oxygen removal by the catalyst.[228] H_2S was added to compensate this but the product distribution also changed slightly towards C_6 hydrocarbons. This catalyst system has also been used to hydrotreat vegetable oils and

vegetable oil-heavy vacuum oil (HVO) mixtures into liquid alkanes, using an existing process.[229] The mixture led to greater conversion into alkanes than pure sunflower oil with 87 % conversion to C_{15}-C_{18} alkanes.

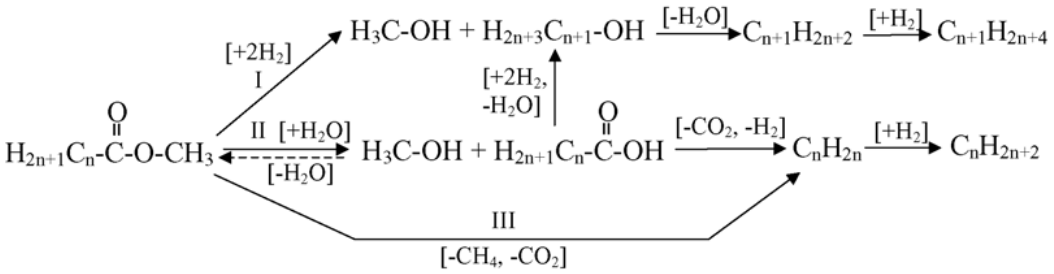

Figure 4.5 Reaction scheme for hydrodeoxygenation of aliphatic methyl esters (n = 6 for methyl heptanoate and n = 5 for methyl hexanoate). Taken from Senol *et al*.[221]

Zeolite HZSM-5 catalyst has been used for the decarboxylation of esters and acids.[230] Work by More *et al*. has used zinc oxide, alumina and the zeolite ZSM-5 to decarboxylate carboxylic acids.[231] At longer reaction times C_8-C_{10} alkanes are produced. A hydroxyl group (-OH), formed by a concerted deprotonation of an acid group, on the MgO surface, [99] could be acting as an acid site which helps the breaking of the C-C bond during decarboxylation, in a concerted pathway (Figure 4.6). In comparison, acidic solids such as zeolites could be performing in a similar manner to these protonated MgO surfaces. Zeolite HZSM-5 catalyst was found to catalyse the conversion of carboxylic acids through decarboxylation, ketonic decarboxylation, cracking, dehydration, aromatisation and polymerisation reaction pathways.[230]

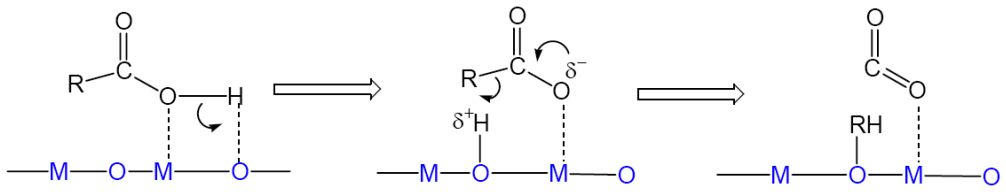

Figure 4.6 Theoretical decarboxylation pathway via an anionic and/or concerted pathway. Taken from Zhang *et al*. [232]

It has been shown that MgO catalysts can lead to ketonic decarboxylation where two carboxylic acid molecules lead to one ketone, one water and one CO_2 molecule,[112] with up to 96%

conversion.[109] This has also been confirmed by Zhang [99] which could explain the lower CO_2 yields found for MgO catalysis. The salt, Mg-$(RCOO)_2$, was found to be one of the products, which could be a catalyst for ketonic decarboxylation.

MgO has been shown to catalyse the removal of naphthenic acid and, in fact, many other organic acids, successfully irrespective of their structure compared to other transition metal oxides with a reaction temperature of 150-300 °C.[233] This suggests the possibility of lower ketonic decarboxylation reaction temperatures. MgO clearly demonstrated enhanced conversion compared to other alkaline earth metal oxides when measured with respect to $CO_{2(g)}$ production, although not as much $CO_{2(g)}$ was released compared to acid conversion (Figure 4.7). This was attributed by the authors to being possibly because: a) strong interactions with the metal oxide leads to carbonate production; b) cracking and neutralization reactions; c) ketonic decarboxylation may occur. Regardless of the carboxylic acid used, the MgO catalyst led to decarboxylation of high yield, which was further enhanced with the presence of Ni and Cu. MgO was also unaffected by sulphur-poisoning.[232] Compared to MgO, calcium oxide (CaO) led to greater acid conversion but the corresponding CO_2 production is lacking for decarboxylation. $CO_{2(g)}$ yield and acid conversion against reaction temperature and catalyst loading for MgO have also been studied (Figure 4.8), with encouraging conversions at 250 °C and 20 wt% MgO loading.

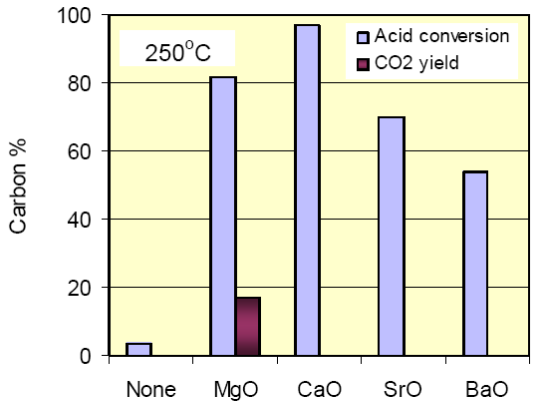

Figure 4.7 Naphthenic acid conversion and $CO_{2(g)}$ yield for various metal oxide catalysts. Taken from Zhang *et al.* [99]

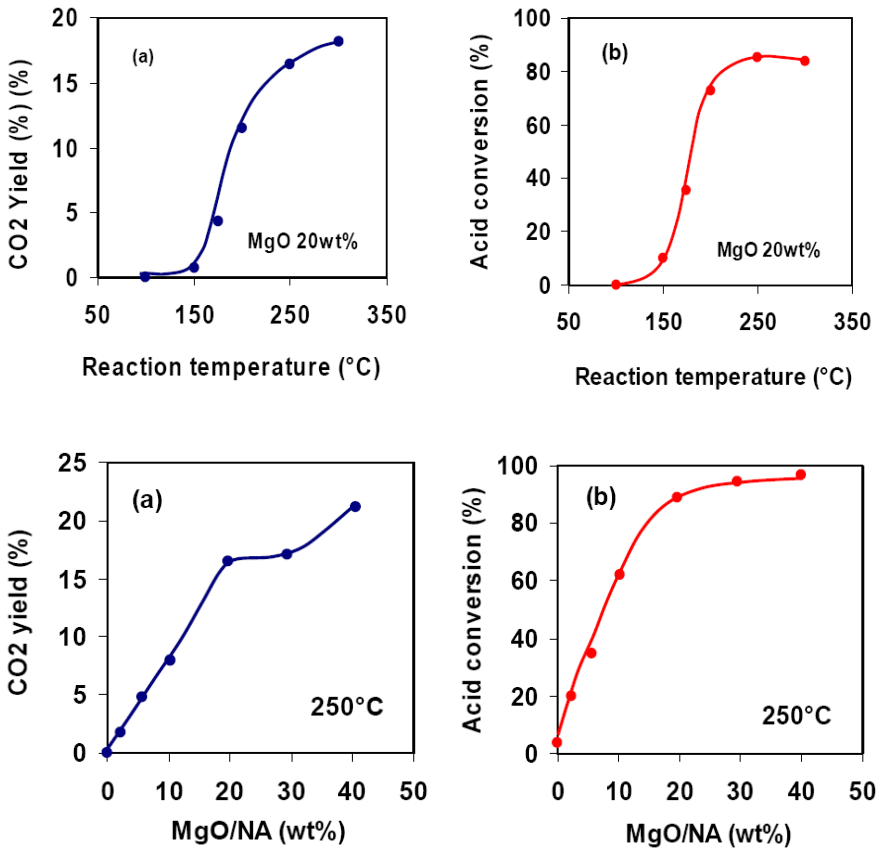

Figure 4.8 $CO_{2(g)}$ and naphthenic acid conversion at various reaction temperatures and catalyst loadings for magnesium oxide. Taken from Zhang *et al*.[99]

The product of decarbonylation, CO, is nucleophilic, whereas triglycerides are electrophilic, thus solid base catalysts will absorb triglycerides strongly and allow reactions to be carried out at lower temperatures and hydrogen partial pressures, with limited deactivation caused by coking.[234]

It has been suggested that active catalysts require acidic and basic sites and the alkali exchanged zeolite CsNaX contains both of these; the alkali cation has Lewis acidity and the oxygen which bridges the Si and Al has basicity.[234] This is similar to peptide formation mechanisms using clay catalysts where carbonyl oxygen groups can interact with electrophilic alumina.[235] CsNaX was used for the conversion of methyl octanoate in the presence of nonane and methanol. When nonane was used as the solvent and co-reactant, initial conversion was at 90 %, but this reportedly decreased rapidly over 350 mins to less than 10 % conversion, at 425 °C. The initial major products were heptenes and octenes, along with an increasing amount of pentadecanone, after which the ketone peaked at 23 % yield after 125 mins and subsequently all yields began to decline.

It was suggested that the catalyst was deactivated because the methyl octanoate was adsorbed strongly onto the base-exchanged zeolite. Once adsorbed, the methyl-octanoate formed high molecular weight 8-pentadecanone ($(C_7H_{15})CO$), via ketonic decarboxylation reactions, which subsequently blocked the pores of the catalyst.

In contrast, when methanol was used as a solvent and co-reactant it was believed that its decomposition products, formate and carbonate species, could be competitively adsorbed, preventing the self-condensation of methyl octanoate ($C_8H_{17}COOCH_3$). This reaction was reported to mainly have led to heptenes (19.3 %), hexenes (26.1 %) and octenes (6.7 %), with only 0.9 % yield of pentadecanone. The proposed mechanism for the overall conversion of methyl octanoate to the major products heptene and hexane in this reaction is shown in Figure 4.9. When methanol was employed as a co-reactant it readily decomposed on the surface of the CsNaX zeolite leading to formate species (as shown by NMR) and hydrogen (Figure 4.10). This led towards octene production *via* hydrogenation reactions.

Coupled with a recent patent application for converting glycerol (the byproduct of biodiesel production) into methanol,[236] this CsNaX conversion process could be used to produce octane from biological sources. Other catalysts used for comparison included NaX zeolite, which led to undesirable products such as substituted aromatics and dimethyl ether from methanol conversion, due to its weak acidic sites and reduced basicity. However as the acid sites became deactivated by coking, decarbonylation continued to occur, deactivating at a much lower rate.

Of relevance to the work described later on in this thesis, a MgO catalyst was found to give a maximum conversion less than 10 % at 425 °C in methanol, lower than that for CsNaX, ascertained due to the lack of a highly polar environment being important, as well as basicity.[234] In the MgO reaction hexenes, pentadecanone and oxygenates were the main products, as opposed to heptenes, hexenes and octenes for CsNaX.

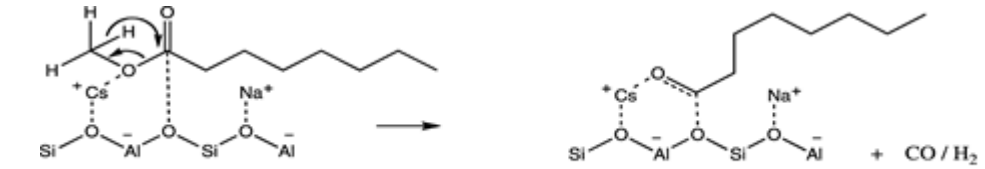

(a)

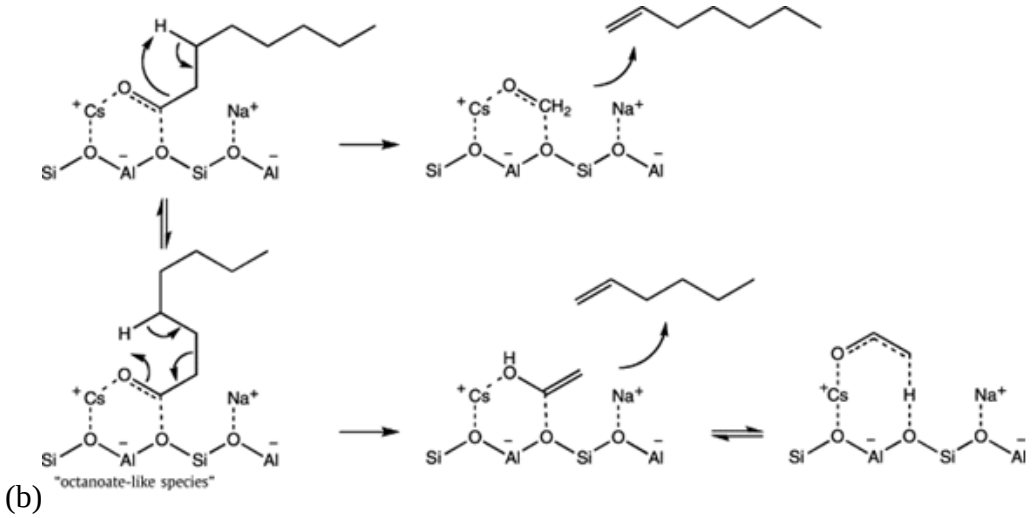

(b)

Figure 4.9 (a) Decarbonylation to octanoate-like species; and (b) subsequent decomposition to hexene and heptene like species. Taken from Sooknoi *et al*.[234]

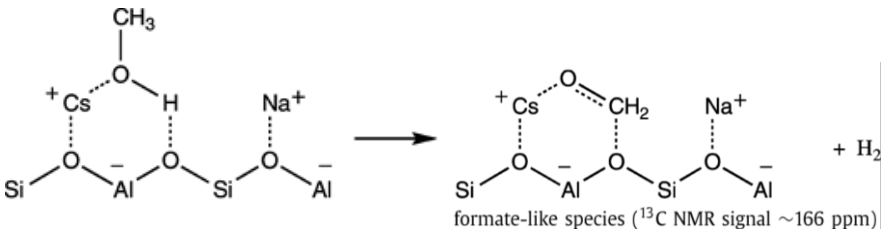

Figure 4.10 Decomposition of methanol to formate-like species as shown by 13C NMR. Taken from Sooknoi *et al*.[234]

Supercritical water and zirconia catalysts were also shown to decarboxylate acetic acid, although more desirable methane was formed without the catalyst, whereas with the catalyst acetone tended to form.[237] When KOH was employed this led to ketonic decarboxylation (Figure 4.11).

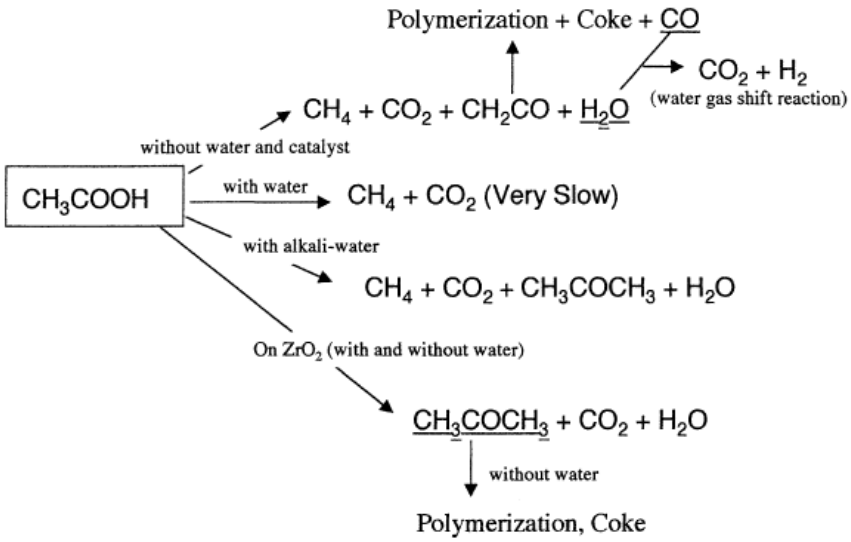

Figure 4.11 Schematic showing the decarboxylation and ketonic decarboxylation pathways for acetic acid in various reactions involving supercritical water, zirconia and KOH alkali base. Taken from Watanabe *et al.*[237]

Mo_8O_{23} has been used to successfully catalyse the deoxygenation of benzoic acid in the presence of hydrogen, leading to benzene, benzaldehyde and toluene.[238] This reaction did not occur in the presence of propylene, although the deoxygenation of benzoic acid has been coupled with the oxidation of propylene using a Co-molybdate catalyst.[239]

Using computational simulations, coupled with experimental methods, the use of Lewis acid catalysis in the removal of naphthenic acids from high total acid number (TAN) crude oil has been studied. Crude oils high in petroleum acid content sell for around $10 a barrel less than sweet crude oil, and, as such, reducing TAN in oil is an area of considerable interest.[240] Lewis acids have empty orbitals, which can interact with the negative charges on the carboxyl groups in the petroleum acids and are thus postulated as ideal candidates, as shown in Figure 4.12 where the carboxyl group of benzoic acid is interacting with the Al centre of the alumina-silicate. Following this interaction, the hydrogen atom then approaches the α-carbon to the carboxyl group and eventually separates from the carboxyl group. In comparison, the thermal decarboxylation reaction on quartz sand lowered the acidic content by 40 %, as compared to 84 % for catalytic decarboxylation over Lewis acidic γ-Al_2O_3 in a fixed bed reactor.

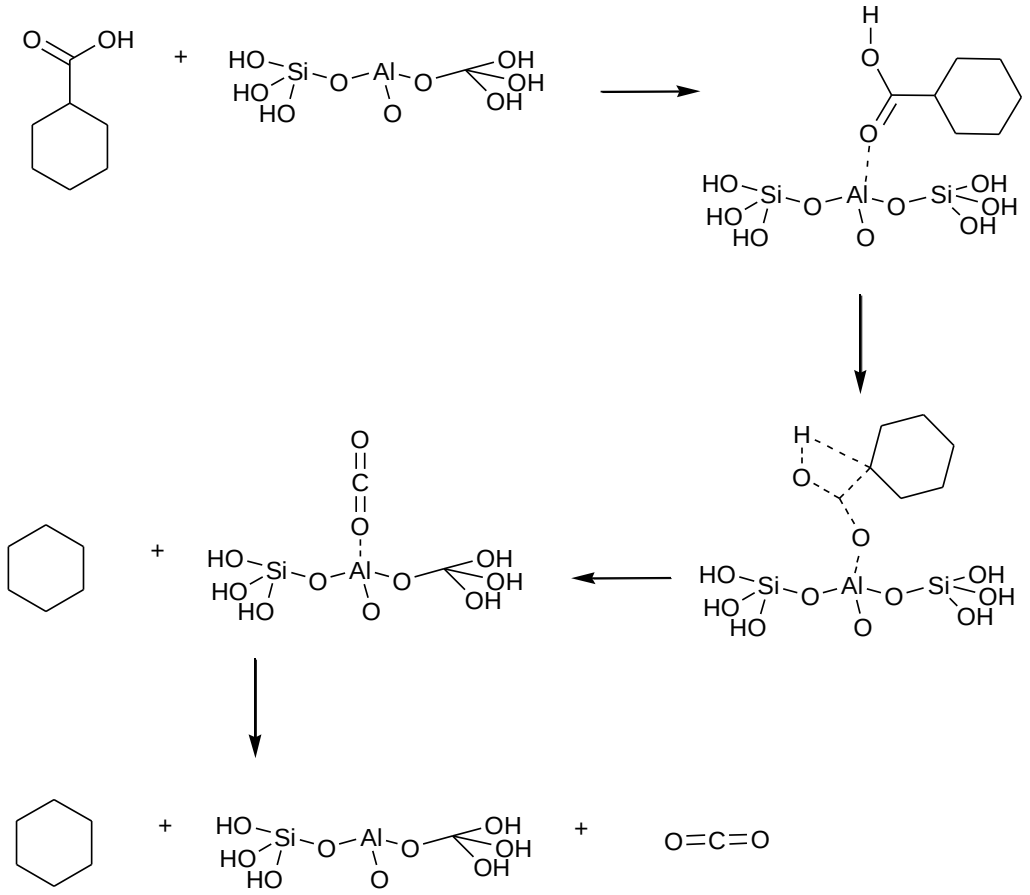

Figure 4.12 Proposed mechanism of catalytic decarboxylation by Lewis acids. Taken from Fu *et al.*[241]

4.1.3 Review of role of natural and synthetic layered clay mineral catalysts in decarboxylation reactions

In efforts to better constrain the formation conditions for crude oil production in nature, theories have been developed to explain crude oil forming reactions, whereby clay minerals were involved as natural catalysts for the conversion of organic matter into petroleum feedstocks.[219]

In early work investigating petroleum formation in source rocks, Almon and Johns used Ca-montmorillonite to decarboxylate *n*-docosanoic acid ($C_{21}H_{43}COOH$).[90] The ratio of branched alkanes:linear alkanes was 1:10 in the presence of water, whereas it was 9:2 in the anhydrous system. This reaction was seen to proceed by a free-radical mechanism, since it was enhanced in the presence of hydrogen peroxide, which generates free radicals. The reaction mechanism was believed to involve the interlayer surface of the clay mineral, as well as octahedrally co-ordinated aluminium ions at the clay crystallite edges.

In decarboxylation reactions of stearic acid carried out in a flow reactor, clays with their octahedral sheets populated by more basic Mg and Li cations, more readily decarboxylated stearic acid than those clays with only Fe and Al ions, suggesting the reaction proceeds at edge surfaces, which are the sites in the layered structure where these cations would be exposed to be involved in chemical reactions.[242] Mg or Li rich surfaces led to increased decarboxylation whereas Al-rich surfaces were found to stabilise COOH. In this study contrasting results were found to Almon and Johns [243] work where gibbsite-type minerals led to the greatest decarboxylation, but this may be due to the fact that: a) closed reaction systems behave differently to open ones and; b) Almon and Johns used the disappearance of the reactant stearic acid as a measure of the decarboxylation rate, rather than analysing the products and polymerization/ketonic decarboxylation may have occurred without loss of CO_2.

Ni/Zr-laponite synthetic clay minerals have been used for the deoxygenation of stearic acid.[244] The clays were calcined before use at 500 °C and found to have a large surface area and pore size, desirable for catalytic activity, with 8 % Ni/Zr-laponite having the largest surface area (265 m^2g^{-1}), and pore volume (9.04 cm^3 g^{-1}) compared to 4 % Ni/Zr-laponite. However, smaller pore size effected selectivity with 4 % Ni/Zr-laponite yielding more desirable linear alkanes (dimethyldecane and dodecane), rather than cyclic alkanes (as in 8% Ni/Zr-laponite) after the 3 hour reaction time.

In a study looking into radiation-induced catalysis of carboxylic acids adsorbed in clays, gamma radiation has been used to decarboxylate various carboxylic acids in Na-montmorillonite clay, with the main products being methane, carbon monoxide and carbon dioxide, when acetic acid (CH_3COOH) was the reactant. More than twenty-fold CO_2 was produced in the system with clay, than without clay. It has been postulated that radiation produces surface defects on the clay, plus interacts with trapped non-equilibrium charge carriers,[245] with light induced decomposition of acetic acid in the presence of an iron oxide/clay catalyst having been observed.[246] The mechanism involves the acetate anion, leading to CH_3 production which either then reacts with adsorbed

hydrogen or with protonated and/or neutral surface hydroxyl groups leading to methane production, as well as CO and CO_2. In the absence of clay, dimerisation reactions of acetic acid occurred.

As mentioned previously in the introduction on decarboxylation, Geatches *et al*., *via* computational studies postulate that a substitution in the clay sheet attracts a counter-ion which then donates an electron to the reactant-clay system,[91] proceeding by means of an alcohol intermediate to the alkane (Figure 4.1).[220] This has been seen experimentally since alcohol intermediates have previously been shown to be involved in the production of alkanes from carboxylic acids.[221]

4.2 Assessment of decarboxylation reactions of stearic acid over Pd/C catalyst

4.2.1 Rationale

There are clearly many types of catalyst systems that have been used for the deoxygenation of carboxylic acids and associated compounds. A review of the literature reveals a body of recent work on decarboxylation has been carried out by Murzin and co-workers[2, 95-98, 247] The feedstock generally used by these authors is stearic acid (Figure 4.13) although ethyl stearate, lauric acid and tristearin have also been used. In the patent US2006/0161032, assigned by Neste Oil Oyj,[248] the conditions used include temperatures of between 200-400 °C and pressures from 1 bar to 150 bar. Typically, reactions in the literature carried out by this group described conditions of 17 bar and 270-300 °C.[98]

Typically all of these reactions are carried out in the presence of H_2, however in one study stearic acid was decarboxylated using 5 % Pd/C in dodecane solvent, at 300 °C in 17 bar He atmosphere.[2] This led to 41 % conversion after 300 mins, with over 90 % selectivity to *n*-heptadecane (Figure 4.2). Other minor products included C_{17} olefins and C_{17} aromatics (undecylbenzenes).

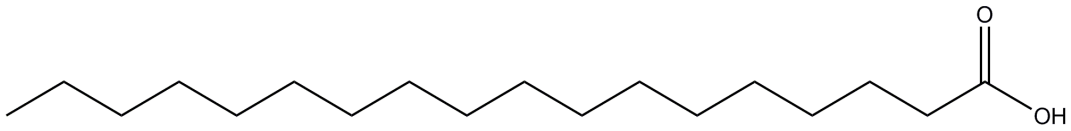

Figure 4.13 Schematic showing the structure of stearic acid ($C_{17}H_{35}COOH$), used as a model biomass reactant in this thesis.

In the remainder of this chapter this particular decarboxylation experiment is adapted, with stearic acid being used as the reactant (Figure 4.13), which represents one of the compounds that can be extracted from triglyceride oils. In this present work hydrogenation is avoided as the industrial partner, KiOR Inc., advised against this, since it is already a readily available commercialised process and alternative mechanisms for decarboxylation were investigated, with only the loss of $CO_{2(g)}$ being involved in the decarboxylation reaction, i.e. direct decarboxylation. To set a benchmark for decarboxylation reactions, a similar set of conditions and reactor vessels to the original experiment by Kubickova *et al.*[2] will be used, however as the overriding purpose is to understand how effective the reaction is for direct decarboxylation without involvement of H_2, Pd/C was not activated with H_2 in this study as the industrial partner involved was seeking alternative biomass upgrading mechanisms to hydro-decarboxylation. The reaction temperatures for the studies carried out in this thesis were also reduced from the 300 °C of the prior work, to 230 °C owing to reactor constraints, and to probe the effect of temperature on direct decarboxylation.

4.2.2 Experimental method

The reactions within this thesis were all performed in the purpose-built Durham University High Pressure Facility, where reactions could be started and controlled remotely to the reactor cells. Reagents were used as supplied: stearic acid (97 %, Acros organics); dodecane (98 %, Sigma-Aldrich), activated carbon supported palladium (5 wt.%, Aldrich). Stearic acid (4.5g, 15.8 mmol)_ was placed in 86 g (64.5 ml) dodecane solvent with 1 g of 5 % Pd/C catalyst in a stirred 600 ml Parr autoclave. The autoclave was pump-purged ten times with $N_{2(g)}$ and then pressurised to 10 bar at room temperature with $N_{2(g)}$. The stirrer was initiated, at 500 rpm, and the reaction heated to an

internal temperature of 230 °C over 30 minutes, achieving a final internal pressure of 17 Bar, and was left for 6-48 hours (depending on experiment, see Table 4.3). Following this, the reactor was cooled to room temperature over 3 hours, under continuous stirring, depressurised to atmospheric pressure and subsequently filtered at room temperature using a sintered glass filter Büchner ring and Büchner flask, under vacuum to remove the Pd/C catalyst. The resulting catalyst remained as a black powder on the filter, and the filtrate was almost colourless. Five decarboxylation replication experiments (D1-D5) were performed, with time varying from 6-48 h. Following the decarboxylation reactions described above, the liquid products were analysed quantitatively using a similar methodology as described by Snare *et al*.[96]

The liquid products obtained after filtration were analysed by gas chromatography (HP 5890 Series II) equipped with a nonpolar column (VF-5MS, with dimensions 30 m x 0.25 mm x 0.25 μl) and a flame ionisation (FID) detector. The injector and detector temperatures were 250 and 275 °C respectively. To analyse stearic acid, the sample must first be derivatised by silylation to make the compound more volatile, less polar and more thermally stable. This is where the acidic proton is replaced with a trimethyl-silyl group (Me_3Si). To do this, following each experiment, 1 ml of reaction mixture was removed (containing maximum 0.0677 g of unreacted 97 % stearic acid, 0.00024 moles, assuming zero conversion) and was silylated using 100 mol% excess N,O-bis(trimethyl)trifluoroacetamide (BSTFA, 0.00048 moles, 0.1225 g) and dissolved in 30 mol% pyridine (0.00007 moles, 0.0056g). 0.002 ml of 0.1 M standard eicosane in dodecane was then added as an analytical standard, and the sample was left for 12 hours to completely silylate. Following this, a 5 μl aliquot was then injected into the GC with helium as the carrier gas at pressure of 2.07 bar. The GC was kept at 200 °C throughout the whole run.

4.2.2.1 Gas chromatography calibration curves

In order to analyse pre- and post-reaction samples by gas chromatography, calibration curves were first prepared for all the required materials. Chemical standards of *n*-heptadecane (Acros, 99 %),

eicosane (Acros, 99 %), stearic acid (Acros, 97 %) (including the silylating agents pyridine and BSTFA), C_8-C_{20} alkane GC standard solution (Fluka) and the solvent dodecane (Sigma-Aldrich, 98 %) were purchased. Quantitative calculations were performed using the internal standard (eicosane) method to produce calibration curves for the reactants stearic acid and the product *n*-heptadecane. Data analysis and peak integration were performed using the Clarity software.[159] The samples for the calibration curves were prepared in vials using the following quantities and made up to 5 ml with dodecane:

Solution S: 0.1 M Silylated Stearic acid in dodecane

0.1422 g Stearic acid

0.264 ml N,O-Bis(trimethylsilyl)trifluoroacetamide (BSTFA) (Acros Organics, 98+%) (100% wt excess)

0.0436ml pyridine (Acros Organics) (30% wt)

The solution was made up to 5 ml with dodecane (Aldrich, 98+%) and left to silylate for 12 hours.

Solution H: 0.1 M *n*-Heptadecane in dodecane

0.155ml n-heptadecane (Acros, 99%)

The solution was made up to 5 ml with dodecane.

Solution E: 0.1 M Eicosane in dodecane

0.141 g eicosane (Acros, 99%)

The solution was made up to 5 ml with dodecane.

These three standard stock solutions were then made up into calibration standard mixtures as shown in Table 4.2.

Table 4.2 Reference samples prepared for calibration of stearic acid, and n-heptadecane.

Reference Name	Silylated stearic Acid (µl)	Heptadecane (µl)	Eicosane (µl)
9S1H5E	900	100	500
7S3H5E	700	300	500
5S5H5E	500	500	500
3S7H5E	300	700	500
1S9S5E	100	900	500
10S0H5E	1000	0	500
0S10H5E	0	1000	500

The samples were each injected into the GC machine 3 times and averages were obtained for peak integrations. A typical chromatogram is shown in Figure 4.14.

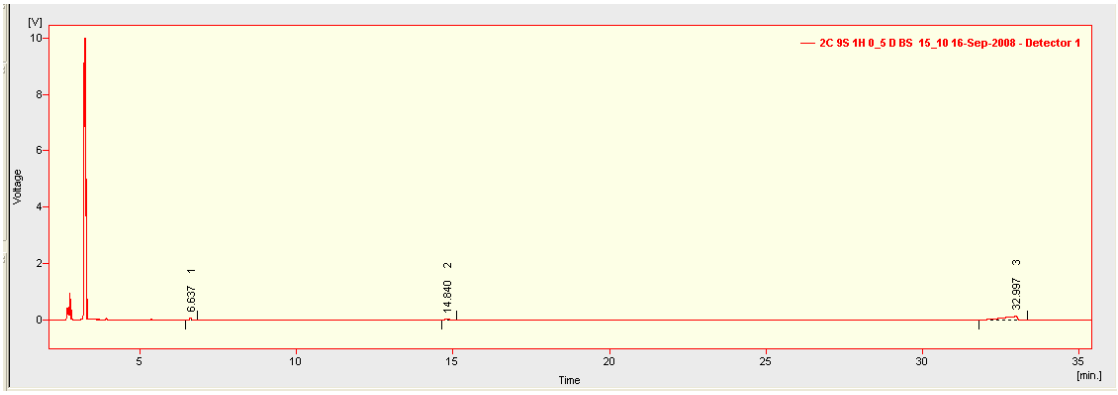

Figure 4.14 A typical GC chromatogram for silylated stearic acid (32.997 min.) and *n*-heptadecane (6.637min.) with the internal standard eicosane (14.840 min.) in the solvent dodecane (~2min.).

Using the internal standard eicosane ($C_{20}H_{42}$), the observed and expected number of moles were calculated and calibration curves were obtained for stearic acid and *n*-heptadecane (Figure 4.15).

Using these calibration curves quantitative experiments were performed on the liquid portions of stearic acid reaction mixtures enabling percentage conversions and percentage yields for the reactions to be calculated.

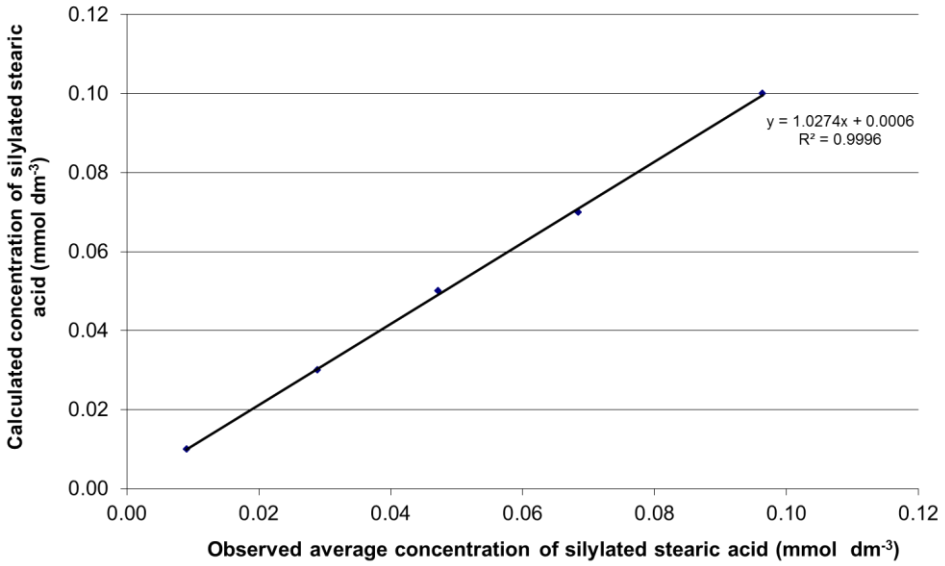

(a)

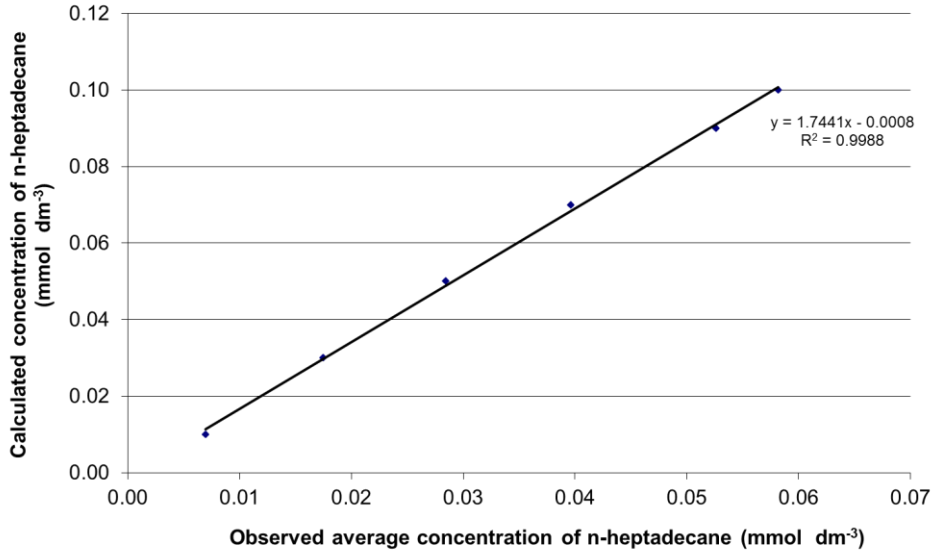

(b)

Figure 4.15 Calibration curves obtained by GC for: (a) silylated stearic acid and (b) n-heptadecane in dodecane

4.2.3 Results and discussion

Five decarboxylation replication experiments (D1-D5) were performed following the same reaction conditions as described in section 4.2.2, whilst varying reaction time. The results are shown in Table 4.3.

Decarboxylation reaction 1 (D1) was carried out over a period of 6 hours at a reaction temperature of 230 °C to facilitate a direct comparison with the previous literature by Kubickova *et al.*[2] Upon workup and analysis, however, no conversion of stearic acid was observed to occur. It is

interesting to note that stearic acid is present at 97 %, which is coincidentally its purity value, hence the 3 % unidentified products are most probably attributed to impurities. Kubickova *et al*., noted that there was a 1 h lag time at 270 °C before stearic acid conversion progressed. The uncatalysed control reaction studied by Kubickova *et al*., was found to give < 5 % conversion at 300 °C within 6 hours, so combined with lower temperature and longer lag time for an unactivated Pd/C catalyst, a similar situation may be occurring here, since, as a general rule, reaction rates double for every 10 °C increase in temperature.[249]

Table 4.3 Liquid product percentages from decarboxylation experiments D1-D5. * = unidentified product. Reaction conditions, 230 °C, 20 wt% catalyst (with respect to stearic acid), 100 % N_2 atmosphere at 17 bar. Errors shown in parentheses.

Reaction:	Reaction time (h)	*n*-heptadecane (%)	Stearic acid (%)	Other (%) *
D1	6	0 (0.15)	97 (2.66)	3
D2	24	58 (0.87)	42 (1.15)	0
D3	24	43 (0.65)	57 (1.56)	0
D4	48	13 (0.20)	87 (2.39)	0
D5	48	36 (0.54)	35 (0.96)	29

For reaction D2, the reaction time was increased further, up to 24 hours and it was observed that 58 % of stearic acid was converted to *n*-heptadecane. In a replication reaction of D2, denoted D3, 43 % of stearic acid was decarboxylated to *n*-heptadecane, with 50 % being the average conversion of D2 and D3. This shows the difficulty of replicating reactions with unactivated Pd/C. This conversion is comparable to the study of Snare *et al*., where it was shown that when 10 % of Pd/C was used as a catalyst for 6 hours reaction time, in 6 bar H_2 atmosphere, resulting in 48 % conversion, however with only 60 % selectivity to *n*-heptadecane, the rest being mainly C_{17} isomers, with a little C_{35} stearone byproduct.[96]

Reactions D4 and D5 further extended the reaction time to 48 hours, with more variable results. In reaction D4 there was a great deal of unreacted stearic acid present, 87 %, with only 13 % conversion to *n*-heptadecane. In reaction D5 only 35 % of unreacted stearic acid remained (lowest of all reactions), leading to 36 % *n*-heptadecane in solution, along with 29 % of remaining unidentified conversion products at low retention time (Figure 4.16). Attempts were made to

identify these products as alkanes in the range C_8-C_{20} using GC standard solutions but this proved unsuccessful.

Snare noted that when Ni catalysts were used in decarboxylation studies, cracking reactions occurred to produce shorter chain acids.[96] Furthermore, when Snare investigated 5 % Pd supported on alumina as a catalyst, this led to ~ 24 % conversion resulting in amounts of dimerised heavy products of unsaturated acids and hydrocarbons as well as 48 % selectivity to C_{35} stearone, compared to only 20 % selectivity to *n*-heptadecane.[96] Further reaction products may also be appearing in the reactions trialled in this thesis, with the longer reaction times employed (6-24 h).

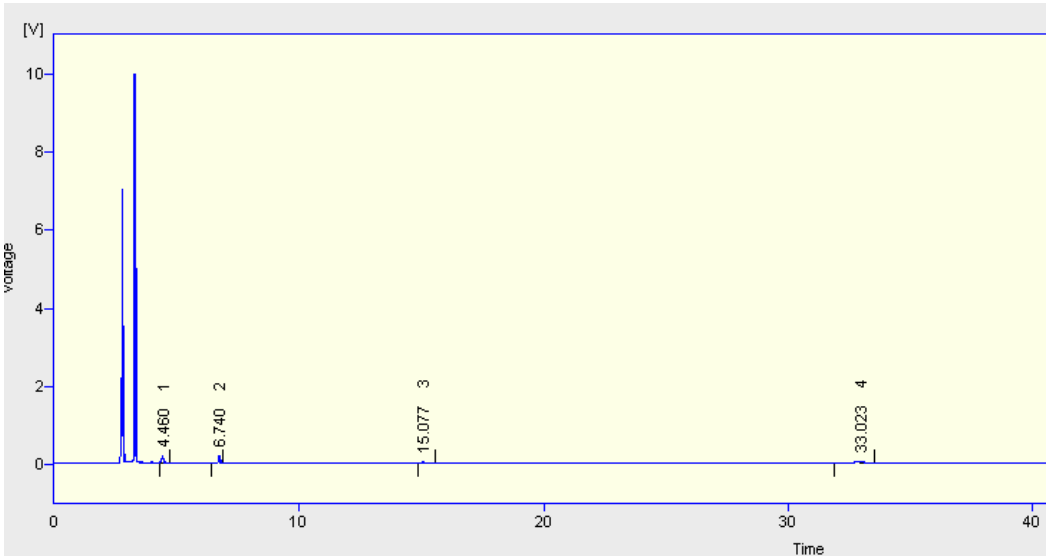

Figure 4.16 Gas chromatography trace of reaction D5, with unidentified product at 4.5 mins, along with heptadecane product (6.7 mins), eicosane standard (15.1 mins) and stearic acid reactant (33 mins).

Another reason that this set of reactions may show such dramatic variation (especially D4) is possibly due to the Pd/C catalyst decomposing to produce a precipitate of elemental palladium, a reaction which is known in the literature,[250] which is indistinguishable visually from the initial Pd/C catalyst.

The purpose of this study was to evaluate the efficiency of 5 % Pd/C for direct decarboxylation. The catalyst was not activated with $H_{2(g)}$ prior to reaction in this study due to the industrial partner seeking alternative mechanisms for upgrading biomass without the use of $H_{2(g)}$. The impacts of not activating Pd/C are potentially significant since this will change the catalyst

surface properties from being in a reduced state to an oxidised one, affecting reactant adsorption rates, kinetics, reaction types and selectivities. It is anticipated that if the catalysts were activated with $H_{2(g)}$ then similar results to Kubickova *et al*. would have been obtained, however one of the aims of this project was to not involve the use of $H_{2(g)}$ in the upgrading process and the experiments D1-D5 set a benchmark for other catalyst tests, described in subsequent chapters.

4.3 Conclusions

In this study, benchmarks for direct decarboxylation using H_2-free conditions were established by repeating recent decarboxylation reactions found in the literature, but with no use of H_2 for either catalyst activation or for hydro-decarboxylation. It was anticipated that decarboxylation would still occur in the absence of H_2 and at lower reaction temperatures than those used by Kubickova *et al*.[2] However, the 5 % Pd/C catalyst appeared to be unstable in this present study and the rate of stearic acid conversion *via* decarboxylation to *n*-heptadecane was not as favourable at 230 °C (maximum conversion 58 % after 24 h) compared to the much shorter reaction time at 300 °C reaction of Kubickova *et al*. (maximum conversion 41 % after 6 h). A further challenge was noted in that some material, believed to be stearic acid, was still present in the solid form in the end reaction mixture, and so a method will need to be developed for future work to allow the determination of the amount of stearic acid and other products present in filtered reaction solids.

5 Ketonic decarboxylation using MgAl layered double hydroxide catalysts

5.1 Introduction & Rationale

In Chapter 4, Pd/C was used as a catalyst to decarboxylate stearic acid, leading to the straight chain alkane, *n*-heptadecane, through loss of CO_2. However, issues with the stability of the Pd/C were encountered at the desired reaction temperatures leading to variability in the conversions recorded. Furthermore, the use of precious metals such as Pd, which typically require activation with $H_{2(g)}$, is undesirable if safer, cheaper and more environmentally-sustainable alternatives can be identified. Based on work by Zhang *et al*. on reduction of total acid number (TAN) in crude oils using simple oxides, [99] reviewed in section 4.1.2, in this and the next chapters of this thesis, the use of layered double hydroxide (LDH) and mixed metal oxide (MMO) materials will be investigated, respectively, as potential catalysts, which can be synthesised from relatively-cheap, readily available starting materials.

5.1.1 Layered double hydroxides as catalysts

One of the main, large-scale applications of LDHs is as catalyst pre-cursors.[196] Their calcined derivatives, MMOs,[251] are of high basicity, and along with rehydrated MMOs,[252] these are more often used in catalysis studies, rather than the direct use of LDHs. Yet, LDHs have been employed as catalysts for a variety of reactions, as now reviewed here.

LDHs have been reported as being used as heterogeneous catalysts for a wide range of applications including Knoevenagel condensation, Claisen-Schmidt condensation, self-condensation, cross-Aldol condensation of aldehydes and ketones and Michael additions.[165, 253] These mainly utilise the LDH as a solid base material, with basicity varying with cation composition. For instance NiAl and ZnAl LDHs are often proposed to be less basic than MgAl LDHs.[80] The magnitude of the R-value also has a significant role since, as this increases for

calcined MgAl LDHs, there is an increase in the number of basic sites in the range $9.0 \leq pK_a \leq 13.3$.[196] But, in addition, as R-value increases, the sites which can catalyse Michael addition and Aldol condensation reactions in the basicity range $13.3 \leq pK_a \leq 16.5$ decrease in number. Indeed the strength of basic sites is greater for LDHs than even calcined MgO, although the total number of sites are less numerous.[122] Calcination of LDHs results in materials with sites of weak (OH^-), medium-strong (O^{2-}-M^{n+} pairs) and strong (isolated O^{2-} ions) basicity.[122] The strength of basic O^{2-} ions depends on their coordination environment, with ions located at crystal corners exhibiting stronger basicity than those located on crystal surfaces and edges. From this it follows that the number of strong O^{2-} increases as crystallite size decreases and it has been shown that larger crystallite sizes have led to lower activity per surface area.[254]

MgAl-CO_3 LDHs have been used in epoxidation reactions at 40 °C to activate hydrogen peroxide via removal of protons.[255] The MgAl-CO_3 LDHs were found to lead to 97 % conversion and 95 % selectivity of isophorone to epoxyketone, with superior conversion when compared to their calcined MMO counterparts, calcined MgO, NaOH, Na_2O_3 and various other catalysts (Table 5.1). The LDHs were superior to the MMOs, which the authors attributed to the latter having basicity, but also enhanced acidity due to the Al coordinated to oxygen having a δ^+ charge (Figure 5.1), which led to alternative acid catalysed side products.[255] In the study, PXRD also revealed that the MMOs were actually partially rehydrated in the aqueous hydrogen peroxide media. An increase in the Mg:Al ratio (R-value), and so basicity, was observed to lead to an increase in reactivity for both LDHs (97 % conversion for R-value 5, compared to 77 % conversion for R-value 3) and MMOs (88 % conversion for R-value 5, compared to 69 % conversion for R-value 3). The LDHs were thought to be consequently effective, not just because of their basicity (calcined MgO exhibits high basicity), but due to the hydroxyl groups reacting with hydrogen peroxide to form a perhydroxyl anion and water. The authors postulated the perhydroxyl anion then reacts with a quaternary ammonium ion and is transported into the organic phase, where it reacts producing a quaternary ammonium hydroxide, which then further regenerates the LDH structure (Figure 5.2).[255]

Table 5.1 Isophorone epoxidation reactions catalysed by various bases. Taken from Yamaguchi *et al.*.[255]

entry	catalyst	convn of isophorone (%)	yield of epoxyketone[b] (%)	heat of adsorption[c] (J g^{-1})
1	$Mg_{10}Al_2(OH)_{24}CO_3$	97	95	14.2
2[d]	$Mg_{10}Al_2(OH)_{24}CO_3$	88	84	20.2
3	$Mg_6Al_2(OH)_{16}CO_3$	77	73	6.3
4[d]	$Mg_6Al_2(OH)_{16}CO_3$	69	62	16.9
5	$Mg_6Al_2(OH)_{16}SO_4$	61	61	5.1
6[e]	MgO	51	40	8.4
7	$Mg(OH)_2$	60	60	6.4
8	$Al(OH)_3$	8	7	1.8
9[f]	NaOH	81	70[g]	
10[f]	Na_2CO_3	53	47	
11	without	<1	<1	

[a] Reaction conditions: isophorone (2 mmol), catalyst (0.15 g), *n*-heptane (5 mL), DTHMAB (0.3 mmol), water (3 mL), 30% aq H_2O_2 (0.9 mL, 8 mmol), 40 °C, 24 h. [b] Yields of the epoxide were determined by GC. [c] See ref 4d. [d] Catalysts calcined at 400 °C were used. [e] MgO calcined at 400 °C was used. [f] 0.2 mmol. [g] 3,3-Dimethyl-5-oxohexanoic acid was also formed as a byproduct.

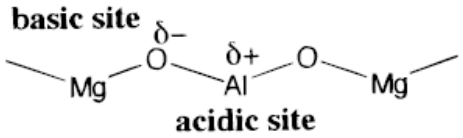

Figure 5.1 Basic and acidic sites found in MMOs. Taken from Yamaguchi et al.[256]

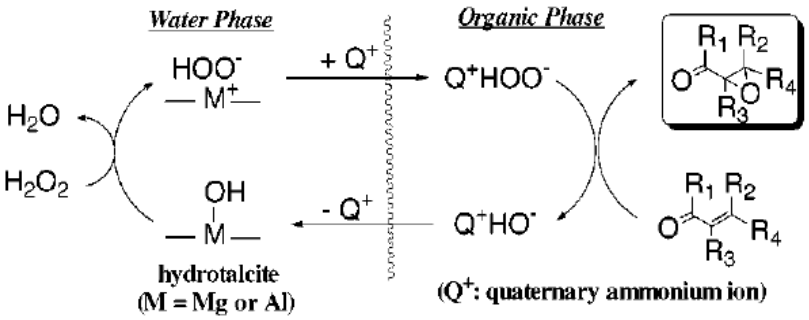

Figure 5.2 Proposed reaction mechanism for LDHs catalysing epoxidation reactions with H_2O_2. Taken from Yamaguchi *et al.*[255]

Similarly, oxidation reactions of benzonitrile involving peroxides and carbonate LDHs obtained significantly higher yields compared to calcined MgO, $Mg(OH)_2$ and the uncatalysed reaction.[257]

Constantino and Pinnavaia successfully used a range of MgAl LDHs of R value 2.49 to convert 2-methyl-3-butyn-2ol (MBOH) to acetylene and acetone.[187] These products were formed when using basic catalysts, whereas the use of acidic catalysts lead to 3-methyl-3-buten-1-yne and

amphoteric catalysts produce 3-methyl-3-buten-2-one and 3-hydroxy-3-methyl-2-butanone.[258] LDH intercalated with hydroxide was found to give 90.6 % conversion to the base-catalysed products, whereas carbonate-intercalated only converted MBOH to 22.4 % of the base-catalysed products. Both of these catalysts were more active than their respective calcined MMOs, with their basic interlayer anions being involved in reactions at basal and edge surfaces of the layer.

Cu-Cr LDHs have been used for alkylation reactions to produce glycolethers from butan-1-ol and ethylene oxide.[259] This reaction traditionally employs homogeneous catalysts with attendant separation and recycling issues.[260] Cu-Cr LDHs intercalated with Cl, CrO_4, Cr_2O_7, V_2O_7, $V_{10}O_{28}$ and Mo_7O_{24} anions were pre-treated at 100 °C to assess surface properties, however the authors treat this as calcination. Surface areas were in the range 26-43 m^2/g for the materials treated at 100 °C, with catalytic reactions carried out at 120 °C, however increases in surface area due to this higher experimental temperature were expected to be low. Cu-Cr-Cr_2O_7 LDH gave the largest conversion of 86 %, with respect to ethylene oxide after 7 hours, with 99.4 % selectivity to the desired product butyl-monoglycol ether. Cu-Cr-V_2O_7 LDH led to the lowest conversion at 30 % of ethylene oxide after 6 hours, but with 100 % selectivity to the major product butyl-monoglycol ether. The LDHs and were believed to be acting as dual acid-base catalysts, with Brønsted basic sites being present due to the OH^- components in the hydroxide layers and Lewis acid sites due to the interlayer transition metal complexes.

In summary, the variety of reactions outlined above all demonstrate that LDHs can behave as basic catalysts in their own right, rather than just be precursors to the highly basic calcined derivatives, MMOs, something, which will be examined in the following sections for fatty acid conversions. It should also be noted that the catalytic abilities of LDHs depend on the reaction types they are employed in.

5.2 Stearic acid ketonic decarboxylation experiments

Following on from the decarboxylation experiments using 5 % Pd/C a series of similar catalysed reactions were undertaken, using mineral based catalysts. These were layered double hydroxides prepared by two synthesis methods: co-precipitation[135] and co-hydration,[123] as described in Chapter 3. Catalyst properties relating to crystal structure, composition, surface area and relative basicity were also described and discussed in Chapter 3.

Similar reaction conditions were used to those described in chapter 4, except that the reactions were adjusted accordingly since they were carried out in an autoclave of different volume which was able to go to slightly higher reaction temperatures. All experiments were performed in the purpose-built Durham University High Pressure Facility (see Section 4.2.2).

5.2.1 Experimental

Reagents were used as supplied: stearic acid (97 %, Acros organics); dodecane (98 %, Sigma-Aldrich); magnesium oxide (Sigma-Aldrich, ACS 98 %); CP5 aluminium oxide (BASF); and CoP-LDH (see Section 3.2.2) and CoH-LDH (see Section 0) materials synthesised within this thesis. A 100 ml Parr autoclave was charged with stearic acid (0.1 g, 97 %, 0.3 mmol), dodecane solvent (10 ml), and catalyst (0.02 g), giving a catalyst loading of 20 wt% relative to the stearic acid. The vessel was sealed and subsequently pump-purged ten times with $N_{2(g)}$ and then pressurised to 9.7 bar at room temperature with $N_{2(g)}$. The stirrer was initiated, at 500 rpm, and the reaction heated to an internal temperature of 250 °C over 30 minutes, achieving a final internal pressure of 17 Bar. These reaction conditions were maintained for 24 h. The vessel was then allowed to cool under stirring over approximately 3 h, under continuous stirring, depressurised to atmospheric pressure and were subsequently filtered using a sintered glass filter Büchner ring and Büchner flask, under vacuum to remove the catalyst. The liquid fraction was retained for analysis (see section 5.2.2) and the solid/wax fraction was subjected to Soxhlet extraction. For this process, the solid/wax fraction

was placed in a cellulose Soxhlet extraction thimble within a Soxhlet chamber, ethanol (250 ml) was heated at reflux temperature for a period of 12 hours and continuously condensed, washing the solid/wax sample and removing any soluble reactants or wax products from the insoluble mineral catalyst into the still pot. The Soxhlet apparatus was then allowed to cool to room temperature over a period of 3 hours, following which, the ethanol solvent was removed using a rotary evaporator (50 mbar, 20 °C) to leave a solid residue, which was analysed as described in section 5.2.3. Validation of the Soxhlet extraction was carried out using known mixtures with various ratios of stearic acid and stearone to confirm that this extraction process was accurate (Section 5.2.5).

The catalysts used in these experiments were CoP-LDH1 to CoP-LDH6 and CoH-LDH1 to CoH-LDH6 (Table 5.2). For comparison, MgO and Al_2O_3 catalysts were also trialled, along with an uncatalysed control reaction for completeness.

Table 5.2 Layered double hydroxide materials employed as catalysts (20 wt% with respect to stearic acid) in the conversion of stearic acid at 250 °C, 17 bar $N2_{(g)}$, along with their method of synthesis and target structures.

Catalyst	Synthesis method	Target compound
CoP-LDH1	Co-precipitation	$([Mg_{0.5}Al_{0.5}(OH)_2](CO_3)_{0.25}.yH_2O$
CoP-LDH2	Co-precipitation	$([Mg_{0.66}Al_{0.33}(OH)_2](CO_3)_{0.165}.yH_2O$
CoP-LDH3	Co-precipitation	$([Mg_{0.75}Al_{0.25}(OH)_2](CO_3)_{0.125}.yH_2O$
CoP-LDH4	Co-precipitation	$([Mg_{0.8}Al_{0.2}(OH)_2](CO_3)_{0.1}.yH_2O$
CoP-LDH5	Co-precipitation	$([Mg_{0.83}Al_{0.17}(OH)_2](CO_3)_{0.09}.yH_2O$
CoP-LDH6	Co-precipitation	$([Mg_{0.86}Al_{0.14}(OH)_2](CO_3)_{0.07}.yH_2O$
CoH-LDH1	Co-hydration	$[Mg_{0.5}Al_{0.5}(OH)_2](OA)_{0.25}.yH_2O$
CoH-LDH2	Co-hydration	$[Mg_{0.66}Al_{0.33}(OH)_2](OA)_{0.165}.yH_2O$
CoH-LDH3	Co-hydration	$[Mg_{0.75}Al_{0.25}(OH)_2](OA)_{0.125}.yH_2O$
CoH-LDH4	Co-hydration	$[Mg_{0.8}Al_{0.2}(OH)_2](OA)_{0.1}.yH_2O$
CoH-LDH5	Co-hydration	$[Mg_{0.83}Al_{0.17}(OH)_2](OA)_{0.09}.yH_2O$
CoH-LDH6	Co-hydration	$[Mg_{0.86}Al_{0.14}(OH)_2](OA)_{0.07}.yH_2O$

5.2.2 Liquid product analysis

Chemical standards of the decarboxylation product *n*-heptadecane (Acros, 99 %), C_8-C_{20} alkane GC standard solution (Fluka), stearic acid (Acros, 97 %) (including the silylating agents pyridine (Acros) and BSTFA (Acros)), the ketonic decarboxylation product stearone (TCI, 95 %) eicosane (Acros, 99 %) and the solvent dodecane (Sigma-Aldrich, 98 %) were used as received. The liquid products obtained after filtration were analysed by gas chromatography (HP 5890 Series II) equipped with a nonpolar column (VF-5MS, with dimensions 30 m x 0.25 mm x 0.25 μl) and a flame ionisation (FID) detector. The injector and detector temperatures were 250 and 350 °C respectively. To analyse stearic acid, the sample must first be derivatised by silylation to make the compound more volatile, less polar and more thermally stable. This is where the acidic proton is replaced with a trimethyl-silyl group (Me_3Si). To do this, following each experiment, 1 ml of reaction mixture was removed (containing maximum 0.01 g of unreacted 97 % stearic acid, 0.34 mmol, assuming zero conversion) and was silylated using 100 mol% excess N,O-bis(trimethyl)trifluoroacetamide (BSTFA, 0.068 moles, 0.0176 g) and dissolved in 30 mol% pyridine (0.01 mmol, 0.0008g). 0.001 ml of 0.1 M standard eicosane in dodecane was then added as an analytical standard, and the sample was left for 12 hours to completely silylate. Following this, a 5 μl aliquot was then injected into the GC with helium as the carrier gas at pressure of 2.07 bar. The GC was held at 35 °C for 5 minutes then ramped up to 300 °C at 5 °C / min. Retention times were determined using standard materials and eicosane was used as an internal standard. Data analysis and peak integration were performed using Clarity software.[159] Calibration curves are shown in section 5.2.4.

5.2.3 Solid product analysis

Post-Soxhlet extracted wax solids were analysed using a Xevo QToF mass spectrometer (Waters Ltd, UK) equipped with an Agilent 7890 GC (Agilent Technologies UK Ltd, UK) and an atmospheric solids analysis probe (ASAP) solid handling sample introduction port for initial

identification. Solid samples were introduced into the spectrometer from a heated melting point tube (ramped from 100 °C to 600 °C over several minutes) previously dipped into neat sample. Mass spectrometry data was processed using MassLynx 4.1.[261] Exact mass measurements were recorded using a lock-mass correction to provide < 3 mDa precision.

Post-Soxhlet extracted wax solids were also dissolved in THF (0.1 mg in 1000 µl), silylated with 10 µl BSTFA and 10 µl pyridine. Following this the components were analysed quantitatively relative to each other using gas chromatography (HP 5890 Series 2) equipped with a TR-SD capillary column (length 10 m, ID 0.53 mm and film thickness 2.65 µm). The injector and detector temperatures were 250 and 350 °C respectively. 5 µl of sample was injected into the GC with helium as the carrier gas at pressure of 2.07 bar. The GC temperature program was based on ASTM D6584 10ae1 standard test method for determination of total monoglyceride, total diglyceride, total triglyceride, and free and total glycerin in B-100 biodiesel methyl esters by gas chromatography.[160] The GC was held at 50 °C for 1 min then ramped at 15 °C / min up to 180 °C, followed by ramping at 7 °C / min up to 230 °C then increasing up to 350 °C at 10 °C / min where it was held for 5 min. Retention times were corroborated using standard materials. The same chemical standards were used as with the liquid portion, as detailed in section 5.2.2. Data analysis and peak integration were performed using Clarity software.[159] Calibration curves are shown in the following section 5.2.4.

5.2.4 Gas chromatography calibration curves

In order to analyse pre- and post-reaction samples by gas chromatography, calibration curves were first prepared for all the required materials.

5.2.4.1 Liquid-phase calibration curves

Chemical standards of *n*-heptadecane (Acros, 99 %), eicosane (Acros, 99 %), stearic acid (Acros, 97 %) (including the silylating agents pyridine and BSTFA), C_8-C_{20} alkane GC standard solution

(Fluka) and the solvent dodecane (Sigma-Aldrich, 98 %) were purchased. Quantitative calculations were performed using the internal standard (eicosane) method to produce calibration curves for the reactants stearic acid and the product *n*-heptadecane using the GC method described in section 5.2.2. Data analysis and peak integration were performed using Clarity software.[159] The samples for the calibration curves were prepared in vials using the quantities shown in Section 4.2.2.1. Using the internal standard eicosane ($C_{20}H_{42}$), the observed and expected number of moles were calculated and calibration curves were obtained for stearic acid and *n*-heptadecane (Figure 4.15). Using these calibration curves quantitative experiments were performed on the liquid portions of stearic acid reaction mixtures enabling percentage conversions and percentage yields for the reactions to be calculated.

5.2.4.2 Solid-product calibration curves

Chemical standards of eicosane (Acros, 99 %), stearic acid (Acros, 97 %) (including the silylating agents pyridine and BSTFA), stearone (98.3 %) and the solvent THF (98 %) were purchased. Quantitative calibrations to produce calibration curves were performed using the methods described below. Data analysis and peak integration were performed using Clarity software.[159]

For the stearic acid calibration curve, samples were prepared in vials with the following quantities and made up to 10 ml with THF:

Solution Sc: 0.1 M Silylated Stearic acid in THF

0.2845 g Stearic acid

0.528 ml N,O-Bis(trimethylsilyl)trifluoroacetamide, BSTFA (Acros Organics, 98+%) (100% wt excess)

0.0872 ml pyridine (Acros Organics) (30% wt)

Made up to 10ml with THF (Fischer Scientific, 98+%).

The solution was left to silylate for 12 hours.

Solution E: 0.1 M Eicosane in THF

0.2820 g eicosane (Acros, 99%)

Made up to 10 ml with THF.

These solutions were made up into calibration standard mixtures as shown in Table 5.3.

Table 5.3 Reference samples prepared for calibration of stearic acid in THF.

Reference Name	Silylated Stearic Acid / µl	Eicosane / µl	THF / µl
9Sc5E1T	900	500	100
7S5E3T	700	500	300
5S5E5T	500	500	500
3S5E7T	300	500	700
1S5E9T	100	500	900
10S5E0T	1000	500	0
0S5E10T	0	500	1000

Using the internal standard eicosane ($C_{20}H_{42}$), the observed and expected number of moles were calculated and a calibration curve was obtained for stearic acid (Figure 5.3) using the GC method described above. The calibration curve obtained is not ideal since some points in the mid-section have a large offset from that of the obtained line of best-fit.

For the stearone calibration curve, samples were prepared in vials with the following quantities and made up to 10 ml with THF:

Solution Se: 0.1M Stearone in THF

0.0046 g Stearone

Made up to 10 ml with THF.

Solution E: 0.1 M Eicosane in THF

0.282 g eicosane (Acros, 99%)

Made up to 10 ml with THF.

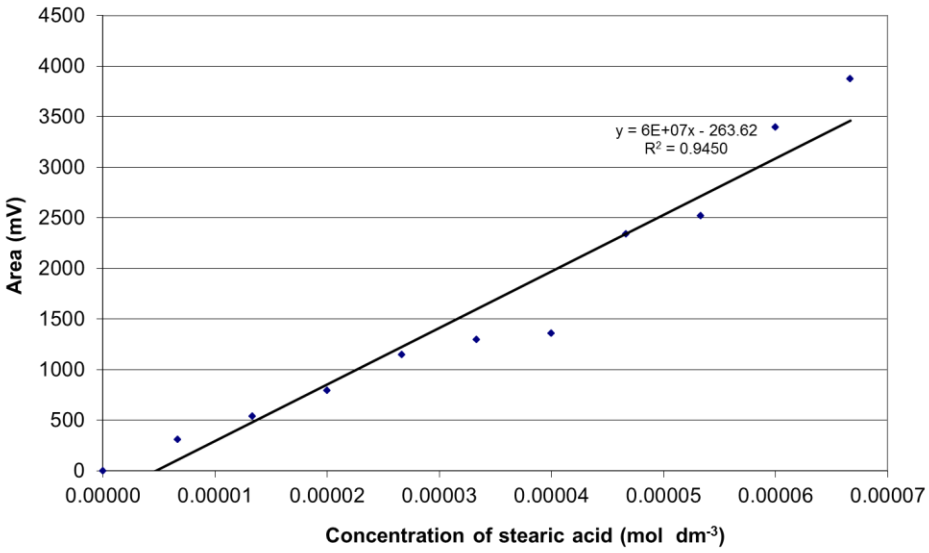

Figure 5.3 Calibration curve obtained by GC for silylated stearic acid in THF.

1000 µl solution Se was then added to 100 µl solution E, to produce a standard stock solution denoted SeE. The GC calibration for stearone was then performed by diluting this standard stock solution according to the values in Table 5.4 to produce the calibration curve for stearone shown in Figure 5.4 using the GC method described in section 5.2.3.

Table 5.4 Dilutions of the stock solution SeE used in stearone GC calibration.

Reference Name	SeE / µl	THF / µl
100 % SeE	1000	0
90 % SeE	900	100
80 % SeE	800	200
70 % SeE	700	300
60 % SeE	600	400
50 % SeE	500	500
25 % SeE	250	750
12.5 % SeE	125	875

In THF, the calibration curve for stearone has a higher coefficient of determination than that produced for the corresponding stearic acid calibration curve, being R^2 = 0.9979 and R^2 = 0.9450 respectively. Following this, to increase accuracy, the values for stearic acid in the following experiments were back-calculated from the values for the product stearone, as long as no other peaks were present.

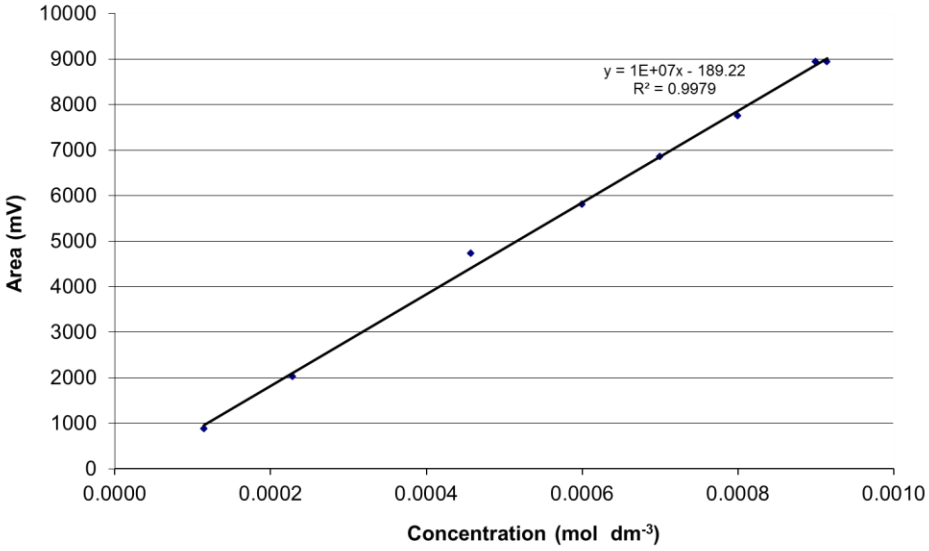

Figure 5.4 Calibration curve obtained by GC for stearone in THF.

5.2.5 Soxhlet extraction validation

An extraction validation process was carried out with various ratios of stearic acid and stearone to confirm the accuracy of this method, given that it incorporates the combined errors of both gas chromatography and Soxhlet extraction.

The masses of stearic acid and stearone stated in Table 5.5 were placed in a Soxhlet thimble and were extracted using ethanol (250 ml) at reflux for a period of 12 hours. The ethanol solvent was then removed using a rotary evaporator to leave a solid residue, which was analysed as described in section 5.2.3.

Table 5.5 Masses of stearic acid and stearone used in Soxhlet extraction samples 1 – 7, together with the expected and observed moles of each, post-extraction. Errors for observed moles shown in parentheses.

Sample	Mass / g		Moles / mmol			
	Stearic acid	Stearone	Expected stearic acid	Observed stearic acid	Expected stearone	Observed stearone
1	0.0500	0.0280	0.1758	0.2501 (0.069)	0.0553	0.0355 (0.0004)
2	0.0250	0.0890	0.0879	0.0627 (0.017)	0.1757	0.1467 (0.0018)
3	0.0750	0.0670	0.2636	0.3144 (0.086)	0.1322	0.1003 (0.0012)
4	0.0070	0.0500	0.0246	0.0212 (0.0006)	0.0987	0.0981 (0.0012)
5	0.0000	0.1000	0.0000	0.0000 (0.0012)	0.1974	0.1917 (0.0023)
6	0.1000	0.0000	0.3515	0.3303 (0.0091)	0.0000	0.0000 (0.0001)
7	0.0000	0.0100	0.0000	0.0000 (0.0012)	0.0197	0.0199 (0.0002)

The expected and observed moles of stearic acid and stearone were plotted as shown in Figure 5.5 and Figure 5.6. Analogous to the GC calibration curves for stearic acid and stearone, there is a great deal more variance on the stearic acid values than the stearone values, though both show increased error. This confirms that for ketonic decarboxylation reactions, conversions for stearic acid should be back calculated from the product, stearone, which has a higher coefficient of determination. The values obtained from the calibration curves will be used for comparisons between reactions in this thesis, however these must be treated with caution since the extraction process itself adds a degree of further error to this method.

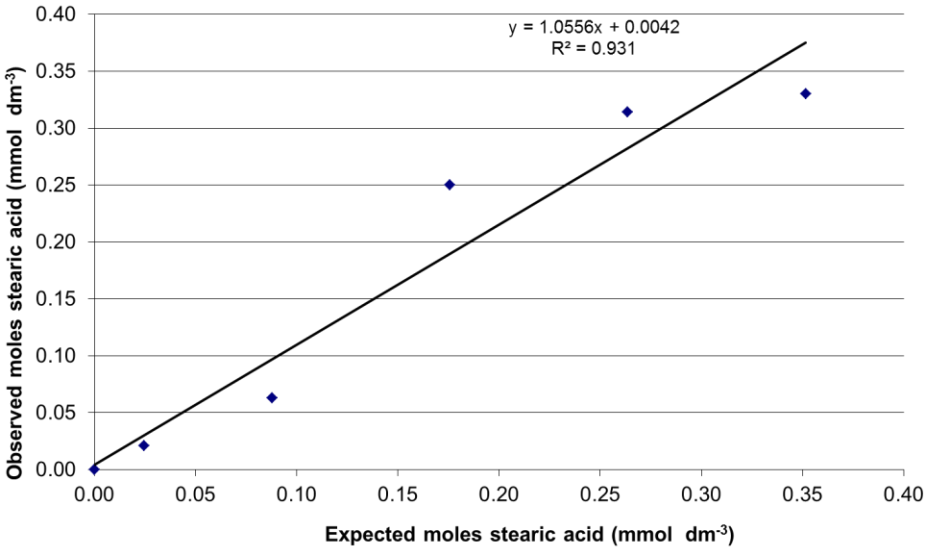

Figure 5.5 Expected and observed moles of stearic acid, post-extraction.

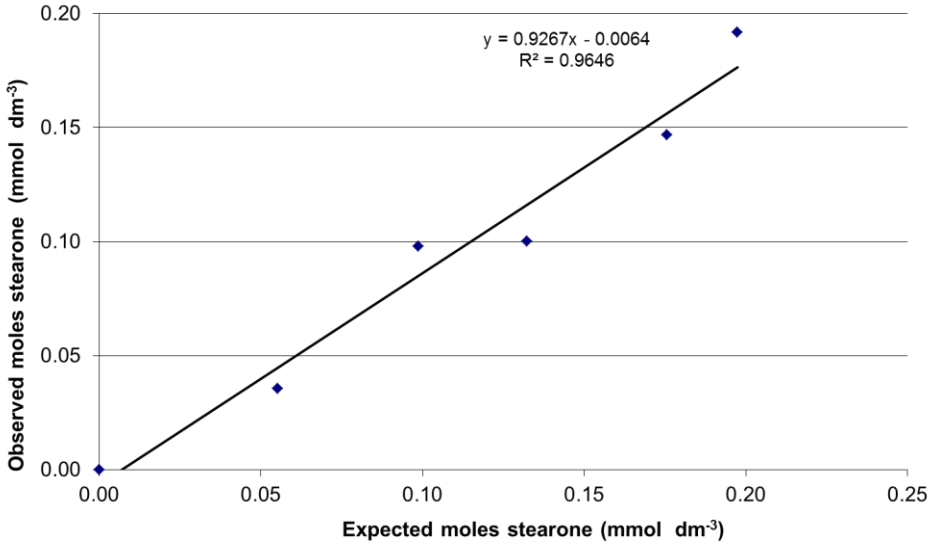

Figure 5.6 Expected and observed moles of stearone, post-extraction.

5.1 Results and discussion of decarboxylation reactions

The following sections will assess and discuss the decarboxylation experiments. Initially, the co-precipitated LDHs and co-hydrated LDHs are discussed individually, in section 5.1.1 and 5.1.2, respectively. Finally, a comparison of the two catalyst types is undertaken in section 5.1.3.

5.1.1 Reactions using co-precipitated layered double hydroxide catalysts

Following the experimental procedure outlined above, for the CoP-LDH catalysed reactions, liquid phases were extracted and analysed by GC. For all reactions, analysis showed that the decarboxylation product, *n*-heptadecane, was not formed from stearic acid. The control reaction did not lead to any conversion of stearic acid, with it remaining 100 % present at the end of the reaction, giving a good baseline to compare catalysts against, suggesting there is no thermal reaction at this reaction temperature. For all other reactions, except CoP-LDH1, stearic acid was still present, but at a reduced level showing that some conversion had occurred (0.1222-0.0113 mmoles), as given in Table 5.6. To account for the loss of stearic acid reactant, the reaction mixture was carefully analysed.

A waxy residue was noted within the end-point reaction mixture. Similarly, in prior studies using LDH catalysts, waxy compounds have been assigned as saponified compounds, though without conclusive analysis[262] Another option is that ketonic decarboxylation has occurred, whereby two stearic acid molecules react to form a long-chain waxy ketone, with loss of CO_2 and water (Figure 5.7). Ketone formation has been observed by Zhang *et al.*[99] when using MgO catalysts, where reactant acid was converted, but there was less CO_2 produced than that which would theoretically evolve from decarboxylation of each acid molecule.

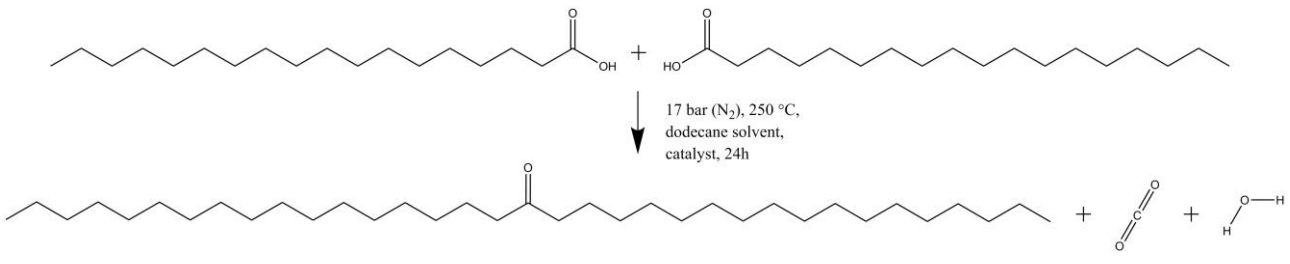

Figure 5.7 Conversion of stearic acid to stearone, carbon dioxide and water in presence of a catalyst.

To establish the identity of the waxy material, the solid phases produced in the present reactions were extracted using a Soxhlet apparatus (as described in Section 5.2.3) and analysed by

GC (as described in Section 5.2.3) and compared to purchased standards for stearic acid and stearone, with the results given in Table 5.6. No other principle products were observed in the CG trace.

Table 5.6 Moles of unreacted stearic acid, stearone product and conversion of steric acid for the uncatalysed reaction and employing catalysts CoP-LDH1 to CoP-LDH6. . Reaction conditions, 250 °C, 20 wt% catalyst (with respect to stearic acid), 100 % N_2 atmosphere at 17 bar, t =24 hours. Errors shown in parentheses,

Catalyst	Stearic acid (moles x 10^{-3})	Stearone (moles x 10^{-3})	Conversion of stearic acid (%)
Uncatalysed	0.3515 (0.0246)	0.0000 (0.0001)	0.0 (2.5)
CoP-LDH1	0.3515 (0.0246)	0.0000 (0.0001)	0.0 (2.5)
CoP-LDH2	0.1222 (0.0086)	0.1146 (0.0052)	65.2 (2.9)
CoP-LDH3	0.0168 (0.0012)	0.1673 (0.0075)	95.2 (4.3)
CoP-LDH4	0.0113 (0.0008)	0.1701 (0.0077)	96.8 (4.4)
CoP-LDH5	0.0407 (0.0029)	0.1554 (0.0029)	88.4 (4.0)
CoP-LDH6	0.0139 (0.0010)	0.1687 (0.0076)	96.0 (4.3)

5.1.1.1 Effect of R-value in co-precipitated layered double hydroxide catalysed reactions

CoP-LDH1 did not lead to any conversion of stearic acid, similar to the uncatalysed reaction. As described in Section 3.4.1.1, characterisation of this catalyst showed that it was made up of a variety of phases according to SEM-EDX measurements, ranging from an R-value of 0.32-3.00, along with MgO and Al_2O_3 phases. CoP-LDH2 was observed to catalyse the reaction moderately with 65.2 % conversion of stearic acid to stearone. With the higher R-values of CoP-LDH3 to CoP-LDH6 conversion of stearic acid to stearone significantly increased to between 88-96 %. Generally, for an LDH, as R-value increases, basicity increases as the composition tends towards the highly basic $Mg(OH)_2$.[196] Hammett basicity measurements (Section 3.4.1) showed that CoP-LDH2 and CoP-LDH4 to CoP-LDH6 were in the range $9.0 \leq pK_a \leq 10.0$ with CoP-LDH1 and CoP-LDH3 being lower at $7.6 \leq pK_a \leq 9.0$. However, for these reactions, the slight differences in measured Hammett basicity do not appear to indicate any influence on catalysis to produce stearone. Though, clearly for R-values of 3 – 6 a greater degree of catalysis occurs than for 1 – 2,

shown in Figure 5.8. This is most likely owing to the lower R-values having more acidic character, with the reaction here being base-catalysed.

Although these LDH reactions have been ranked according to the stearone calibration curve, it must be noted that this ranking is likely to have been affected by the extraction process (thus increasing the margin of error, see Section 5.2.5) with the values overlapping each other with respect to the errors associated with extraction and subsequent GC analysis.

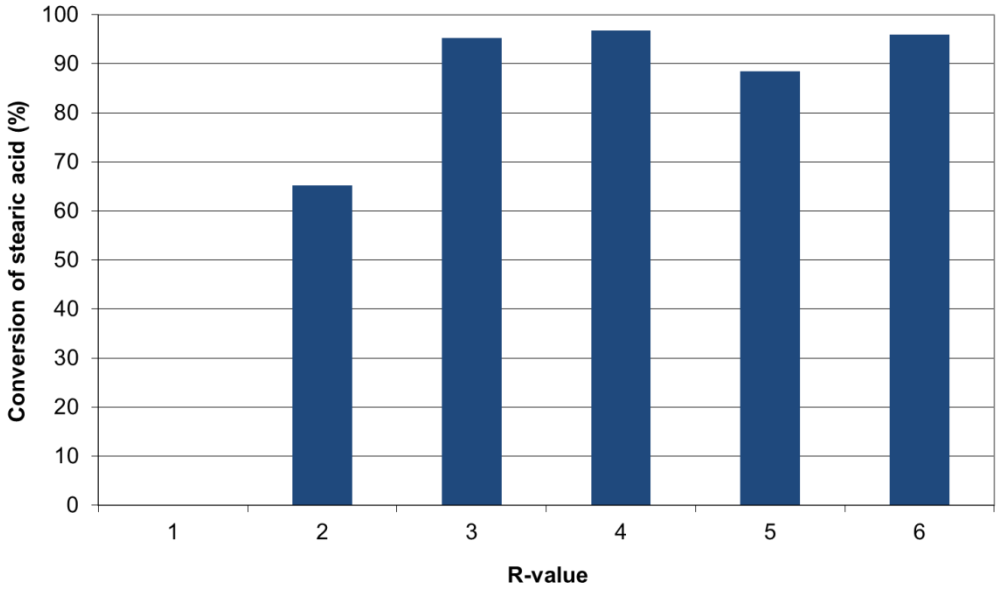

Figure 5.8 Bar chart of conversion of stearic acid *vs.* R-value for the catalysts CoP-LDH1 to CoP-LDH6.

5.1.1.2 Effect of average pore size in co-precipitated layered double hydroxide catalysed reactions

The average pore sizes for the CoP-LDHs, along with their conversions of stearic acid, are shown in Table 5.7 and graphically in Figure 5.9.

In comparison with the other COP-LDH samples, CoP-LDH1 had a very narrow average pore size of 3.1 nm, increasing up to 8.7 nm for CoP-LDH2, 14.4 nm for CoP-LDH3 and 20.2 nm-22.3 nm for CoP-LDH4 to CoP-LDH6. In Figure 5.9 it can be seen that there is a relationship between average pore size and conversion of stearic acid to stearone. Converting two molecules of stearic acid, with an 18-carbon backbone chain, into stearone, with a 35-carbon backbone chain

may be sterically hindered in the catalysts which exhibit small pore size. For 14.4 nm and above average pore size, conversion to stearone was between 88-97 %, suggesting there is both a minimum and lowest optimum pore size for this reaction. As the 3.1 nm pore size of CoP-LDH1 led to zero conversion of stearic acid, this suggests that the composition of the LDH materials is important. Acetic acid has been converted to acetone by calcined LDHs of pore size 4.2-7.0 nm previously but at 100 °C higher temperatures than those employed here.[115] However this 2-carbon chain length is not a representative compound of fatty acids found in biomass, which the present study is targeting.

Table 5.7 Average pore sizes and conversion of stearic acid, in ascending conversion values for the catalysts CoP-LDH1 to CoP-LDH6. Reaction conditions, 250 °C, 20 wt% catalyst (with respect to stearic acid), 100 % N_2 atmosphere at 17 bar, t =24 hours. Errors shown in parentheses.

Catalyst	Average pore size (nm)	Conversion of stearic acid (%)
CoP-LDH1	3.1	0.0 (2.5)
CoP-LDH2	8.7	65.2 (2.9)
CoP-LDH5	20.2	88.4 (4.0)
CoP-LDH3	14.4	95.2 (4.3)
CoP-LDH6	22.3	96.0 (4.3)
CoP-LDH4	20.5	96.8 (4.4)

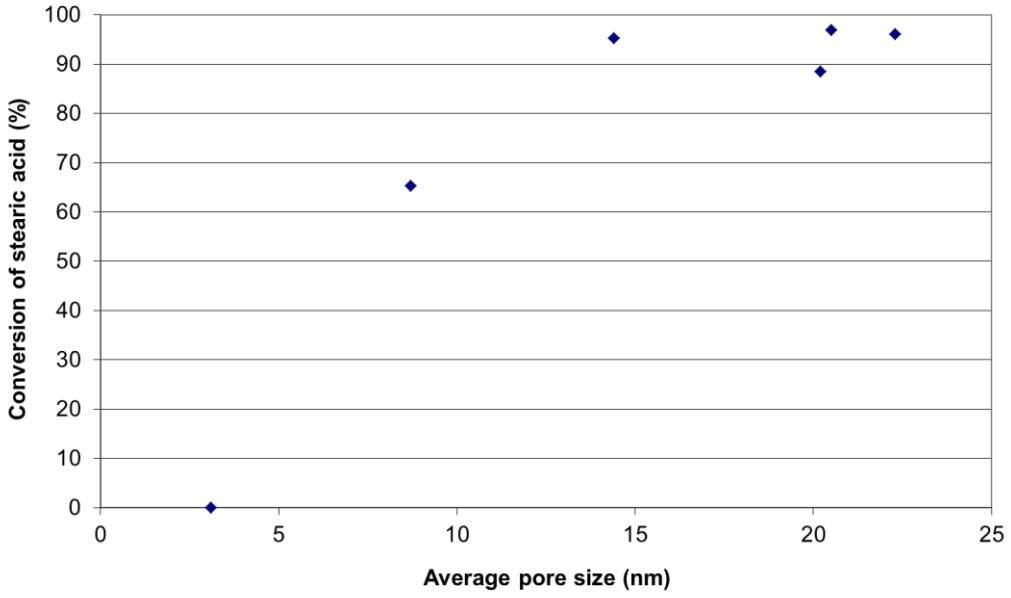

Figure 5.9 Conversion of stearic acid to stearone *vs.* average pore size for the catalysts CoP-LDH1 to CoP-LDH6.

5.1.1.3 Comparison of decarboxylation reactions undertaken using MgO and Al_2O_3 with reactions using MgAl Layered double hydroxides

Uncalcined MgO and uncalcined Al_2O_3 were also assessed as control catalysts for the conversion of stearic acid at 250 °C, with the results shown in Table 5.8.

Uncalcined MgO was found to only lead to 0.5 % conversion of stearic acid to stearone, suggesting that the high basicity of this material is not the only factor in stearic acid conversion. Although it could have potentially led to surface Mg-stearate product,[262] which can block catalytic sites on the surface and finally be removed during the Soxhlet extraction procedure. In comparison, a reaction from the literature using lauric acid ($C_{11}H_{23}COOH$) led to 97 % conversion to form laurone ($(C_{10}H_{11})_2CO$) at 400 °C with MgO, but this may be related to an *in situ* activation of the catalyst at this temperature, or the kinetics may be enhanced. Uncalcined Al_2O_3 led to no conversion of stearic acid, illustrating that the reaction is not acid catalysed at this reaction temperature. Between 300 °C – 400 °C this reaction has been recorded to have occurred in the presence of Al_2O_3,[114] though this may be due to pyrolytic reactions at these temperatures.[99]

Table 5.8 Moles of unreacted stearic acid, stearone product and conversion of stearic acid for the reaction employing catalysts uncalcined MgO and uncalcined Al_2O_3. Reaction conditions, 250 °C, 20 wt% catalyst (with respect to stearic acid), 100 % N_2 atmosphere at 17 bar, t =24 hours. Errors shown in parentheses.

Catalyst	Stearic acid (moles x 10^{-3})	Stearone (moles x 10^{-3})	Conversion of stearic acid (%)
Uncalcined MgO	0.3499 (0.0245)	0.0009 (0.0001)	0.5 (2.5)
Uncalcined Al_2O_3	0.3515 (0.0246)	0.0000 (0.0001)	0.0 (2.5)

5.1.1.4 Mechanistic insights from co-precipitated layered double hydroxide catalysed decarboxylation reactions

Based on the results shown in sections 5.1.1, it is clear that, under the reaction conditions used (250 °C, 20 wt% catalyst with respect to stearic acid, 100 % N_2 atmosphere at 17 bar, t =24 hours) stearic acid is preferentially converted *via* ketonic decarboxylation to form stearone. The

results suggest that the mechanism of stearic acid conversion to stearone entails a surface mediated phenomenon for the CoP-LDHs as the thermal reaction, with no mineral control or catalyst, yielded no conversion. As Al_2O_3 did not work, though LDHs did, it can be hypothesised that the reaction involves catalysis *via* medium strength basic OH^- sites and possibly CO_3^{2-} interlayer anions at basal and edge surfaces of the layer. A strong correlation was observed between pore size and the degree of catalysis, with no thermal decarboxylation occurring at these temperatures (250 °C). Murzin *et al*. observed < 5 % conversion for thermal decarboxylation under hotter and reducing conditions after 6 hours, giving 1-heptadecene and heptadecane at 300 °C in 100 % H_2 atmosphere at 6 bar.[96] A similar reaction utilising oleic acid was found to have < 10 % conversion at 300 °C, along with 29 % at 350 °C and 84 % at 400 °C, leading to pyrolysis products.[262]

CoP-LDH1, according to the cation avoidance rule,[169] cannot be prepared by co-precipitation and gave zero conversion of stearic acid, however this material also had the smallest average pore size (3.1 nm). CoP-LDH1, being an R-value of 1, is rich in Al (Table 3.5), and it was shown that Al_2O_3 did not lead to any catalysis for this reaction, due to its acidity.

For CoP-LDH2, with an R-value of 2, moderate conversion of stearic acid to stearone of 65 % was observed, however CoP-LDH2 is also of larger average pore size than CoP-LDH1, being 8.7 nm. The Hammett basicity of CoP-LDH2 was found to be greater than that for CoP-LDH1 ($9.0 \leq pK_a \leq 10.0$ and $7.6 \leq pK_a \leq 9.0$, respectively), which may also indicate that the strength of accessible basic sites plays a role. As R-value is increased, up to CoP-LDH3, again the conversion of stearic acid to stearone increased, up to 95.2 %. As the measured Hammett basicity for CoP-LDH3 is lower than that of CoP-LDH2. ($7.6 \leq pK_a \leq 9.0$ and $9.0 \leq pK_a \leq 10.0$, respectively), it suggests that the accessibility of basic sites is not as significant in determining yield, however the enhanced average pore size (14.4 nm) indicates that this parameter is dominant. On moving to R-values 4 – 6 there is only a minor difference in conversion of stearic acid to stearone (88 – 97 %), however CoP-LDH5 yields a lower conversion. Again, the average pore size is high at 20.2-22.3

nm, with CoP-LDH4-CoP-LDH6 catalysts having a similar Hammett basicity, being in the range $9.0 \leq pK_a \leq 10.0$.

In summary, using LDH catalysts at 250 °C and 17 Bar pressure for 24 h, ketonic decarboxylation occurs. From the results reported here, it can be concluded that the conversion of stearic acid to stearone exhibits some correlation with R-value, with CoP-LDH3 to CoP-LDH6 leading to highest conversions, but there is also a relationship between the average size of the LDH pores and their corresponding activity in the ketonic decarboxylation reaction. With the reaction converting two long chain fatty acid molecules into similarly long chain ketone product molecules, accessibility to catalytic sites may be sterically hindered by the small average pore size of CoP-LDH1 (2 nm). Pores of medium average size (8.7 nm, CoP-LDH2) may still be accessible to a degree, but for 14.4 nm and above (CoP-LDH3 to CoP-LDH6) the reaction can proceed unhindered.

5.1.2 Reactions using co-hydrated layered double hydroxide catalysts

Following the experimental procedure outlined above (Section 5.2.1), for the CoH-LDH reactions, liquid and solid phases were extracted and analysed by GC (Sections 5.2.2 and 5.2.3), with the results given in Table 5.9.

Table 5.9 Moles of unreacted stearic acid, stearone product and conversion of stearic acid for the uncatalysed reaction and also employing catalysts: CoH-LDH1 to CoH-LDH6; uncalcined MgO and uncalcined Al_2O_3. Reaction conditions, 250 °C, 20 wt% catalyst (with respect to stearic acid), 100 % N_2 atmosphere at 17 bar, t =24 hours. Errors shown in parentheses.

Catalyst	Stearic acid (moles x 10^{-3})	Stearone (moles x 10^{-3})	Conversion of stearic acid (%)
Uncatalysed	0.3515 (0.0246)	0.0000 (0.0001)	0.0 (2.5)
CoH-LDH1	0.3515 (0.0246)	0.0000 (0.0001)	0.0 (2.5)
CoH-LDH2	0.0368 (0.0026)	0.1573 (0.0071)	89.5 (4.0)
CoH-LDH3	0.0499 (0.0035)	0.1508 (0.0035)	85.8 (3.9)
CoH-LDH4	0.0101 (0.0007)	0.1707 (0.0077)	97.1 (4.4)
CoH-LDH5	0.0425 (0.0030)	0.1545 (0.0070)	87.9 (4.0)
CoH-LDH6	0.0383 (0.0027)	0.1566 (0.0070)	89.1 (4.0)
Uncalcined MgO	0.3499 (0.0245)	0.009 (0.0001)	0.5 (2.5)
Uncalcined Al_2O_3	0.3515 (0.0246)	0.0000 (0.0001)	0.0 (2.5)

Similar to the CoP-LDHs, decarboxylation of stearic acid to give the *n*-heptadecane alkane product, with the loss of CO_2, was not observed in any CoH-LDH sample. Again, a long chain ketone, stearone was formed *via* ketonic decarboxylation.

The uncatalysed reaction is repeated here as an *aide memoire*, indicating that thermal decarboxylation did not occur at 250 °C under reaction conditions. Similarly, the results for uncalcined MgO and uncalcined Al_2O_3 are repeated for comparison.

5.1.2.1 Effect of R-value in co-hydrated layered double hydroxide catalysed reactions

CoH-LDH1 was not deemed an LDH by PXRD and was assumed to be an alumina compound. For completeness it was included in the catalytic testing. It, similarly to Al_2O_3, did not convert stearic acid, due to its acidic nature.[119]

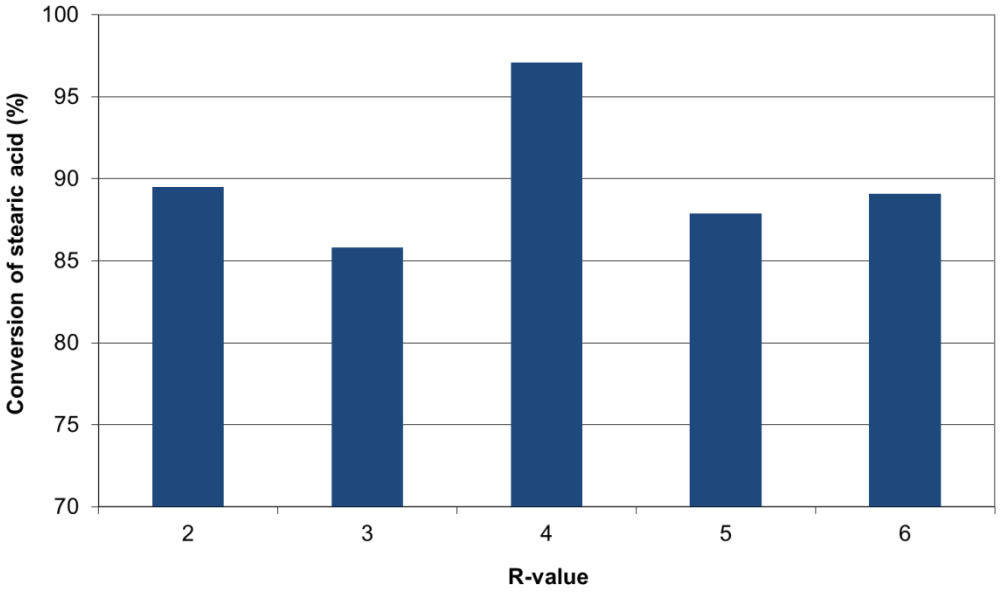

Figure 5.10 Conversion of stearic acid *vs.* R-value for the catalysts CoH-LDH2 to CoH-LDH6.

CoH-LDH2 to CoH-LDH6 all showed high conversion of stearic acid to stearone, between 85.8 % - 97.1 %, with no observable trends occurring due to increasing R-value (Figure 5.10). R-value 4 yielded the highest amount of conversion (97.1 %). However, variability and errors

associated with the Soxhlet extraction (see Section 5.2.5) has shown that there may be additional inaccuracies within these values, with the ranking of catalysts not being so clear at these high conversion levels.

5.1.2.2 Effect of average pore size in co-hydrated layered double hydroxide catalysed reactions

The average pore sizes for the CoH-LDHs, along with their conversion of stearic acid to stearone, are shown in Table 5.10, and graphically in Figure 5.11.

Table 5.10 Surface areas, average pore sizes and conversion of stearic acid, in ascending conversion values for the catalysts: CoH-LDH2 to CoH-LDH6. Reaction conditions, 250 °C, 20 wt% catalyst (with respect to stearic acid), 100 % N_2 atmosphere at 17 bar, t =24 hours. Errors shown in parentheses.

Catalyst	Average pore size (nm)	Conversion of stearic acid (%)
CoH-LDH3	10.2	85.8 (3.9)
CoH-LDH5	13.3	87.9 (4.0)
CoH-LDH6	11.1	89.1 (4.0)
CoH-LDH2	9.7	89.5 (4.0)
CoH-LDH4	10.8	97.1 (4.4)

In Figure 5.11 it can be seen that for average pore sizes between 9.7 nm and 13.3 nm there is no discernable correlation with conversion of stearic acid to stearone, since all catalysts behave in the same way. This suggests that, when compared to the co-precipitated LDH catalysts, the average pore size in the co-hydrated materials is large enough for the conversion of stearic acid to stearone, without hindrance.

5.1.2.3 Mechanistic insights from co-hydrated layered double hydroxide catalysed decarboxylation reactions

With respect to R-value and average pore size, no discernable correlations with conversion are observed for the CoH-LDHs, except that all materials catalysed the reaction to a similar degree,

with no restrictions due to average pore size and given the narrow pore size distribution of these LDHs.

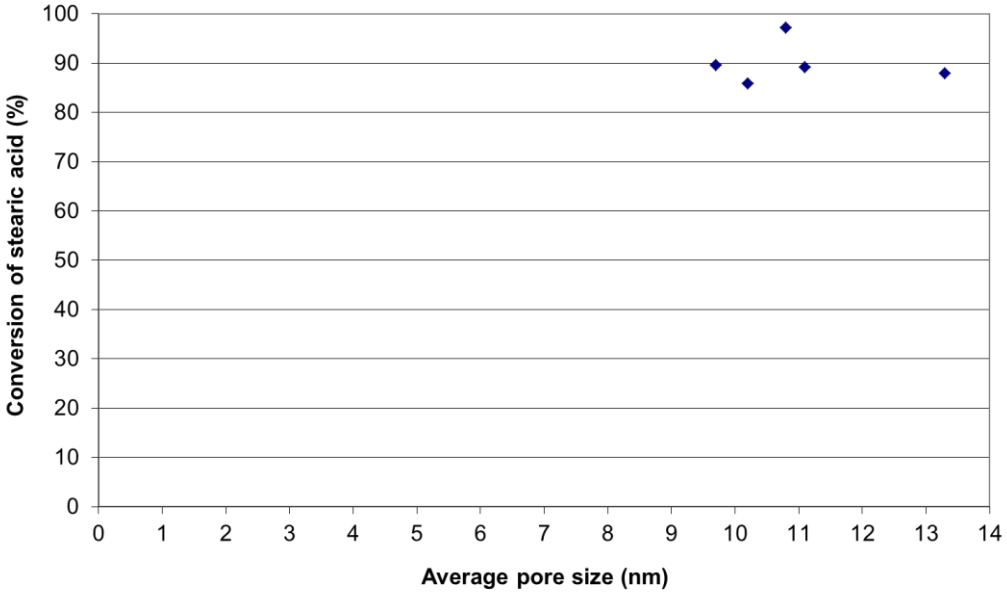

Figure 5.11 Conversion of stearic acid *vs.* average pore size for the catalysts CoH-LDH2 to CoH-LDH6.

The measured Hammett basicities of CoH-LDH2 to CoH-LDH4 were in the range $6.0 \leq pK_a \leq 7.6$ and for CoH-LDH5 to CoH-LDH6, $7.6 \leq pK_a \leq 9.0$, and, again, no correlation is apparent between the observed % conversion and the Hammett basicity.

CoH-LDH4 yielded the highest conversion (97.1 %) and it was noted that this LDH contained a well-crystallised MgO co-phase, as identified by PXRD, to a greater extent than all of the other LDHs. The peak heights at 43 ° 2θ, attributed to MgO impurity have been plotted against conversion of stearic acid to stearone for CoH-LDH2 to CoH-LDH6 and are shown in Figure 5.12. According to the trend observed, as the MgO peak height increases, the conversion of stearic acid to stearone also increases. From the intercept of the equation for the trend line it follows that at zero MgO co-phase, 85.5 % conversion of stearic acid to stearone would theoretically occur *via* the LDH catalytic sites. There may be a synergistic effect occurring with the LDH and MgO phases catalysing the reaction together since MgO itself only led to 0.5 % conversion of stearic acid to stearone, yet its presence appears to lead to enhanced conversion of stearic acid in the CoH-LDH

catalysts. A possible explanation is that the MgO formed in the LDH reaction mixture has smaller crystal size than the MgO control. Although a trend is observed, it does lie within the errors of the experiment and so further replicates would be needed to confirm this trend.

In comparison, similar plots of full-width half-maximum (FWHM) and crystal size for CoH-LDH2 to CoH-LDH6 (calculated using the Scherrer equation **(5)**) did not show any correlation with conversion of stearic acid to stearone (Figure 5.13).

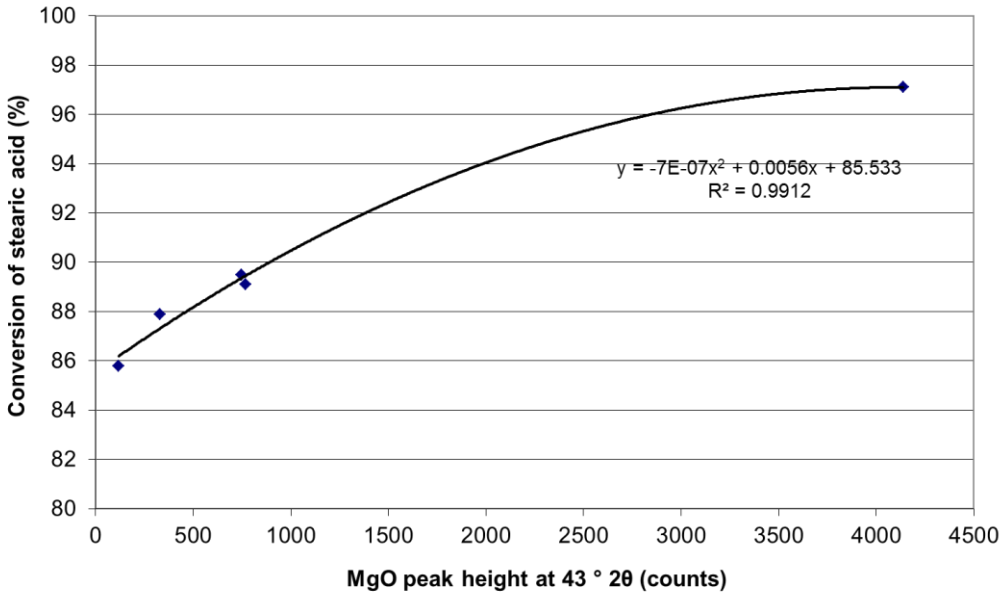

Figure 5.12 Graph to illustrate the relationship between conversion of stearic acid and MgO-co phase peak height in CoH-LDH2 to CoH-LDH6.

The apparent enhanced catalysis with an MgO-like co-phase suggests that the reaction is occurring *via* a base catalysed mechanism, since LDHs also contain weak to medium strength basic sites, with OH^- on their surfaces.

Ketonic decarboxylation of acetic acid using MgO catalyst, with its inherent high basicity and low lattice energy, is known to produce bulk acetates, followed by thermal decomposition, whereas catalysts of high lattice energy involve surface-mediated catalysis.[263] As discussed earlier, 0.5 % of stearic acid was converted to stearone with MgO, with potentially, in addition, saponified Mg-stearate ($(C_{17}H_{37}COO)_2Mg$) product being formed on the catalyst surface, blocking active sites.[262]

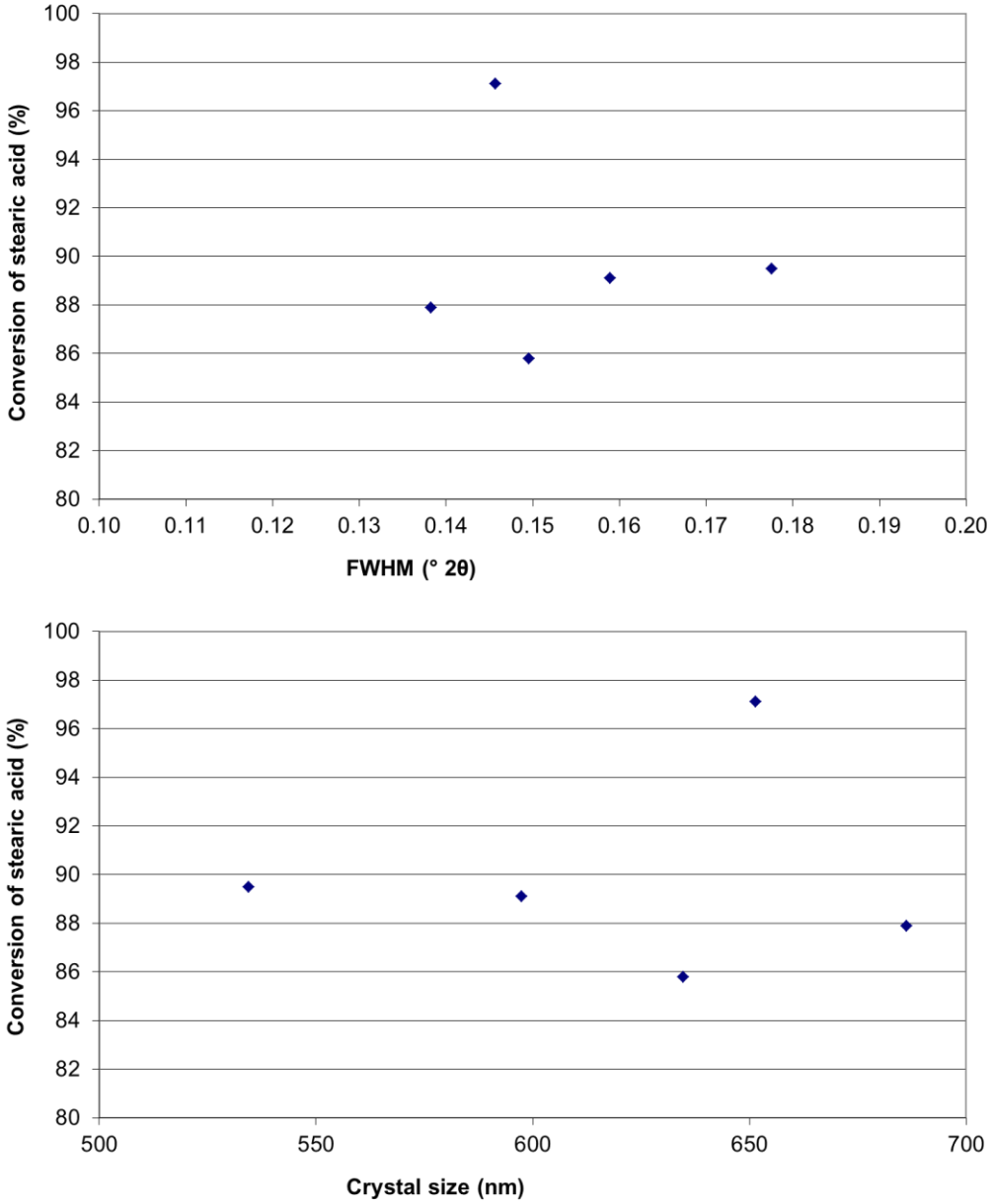

Figure 5.13 Graphs to illustrate the relationship between conversion of stearic acid and MgO-co phase FWHM (top) / crystal size (bottom) in CoH-LDH2 to CoH-LDH6.

When looking at TAN reduction of crude oils, Zhang *et al*. noted that when using MgO catalyst (20 wt%), over 80 % conversion of naphthoic acid occurred at 250 °C, greater than at 300 °C.[99] The authors proposed that the ketonic decarboxylation reaction was initiated by the adsorption of an acid molecule onto the MgO through loss of the acidic proton. This results in a weakening and lengthening of the bond between the α- and β-carbons, as shown in Figure 5.14. Following this weakening and lengthening of the bond, a second free acid molecule interacts with this adsorbate and reacts in a six-membered transition state, leading to the formation of a ketone,

CO_2 and water. Through density functional theory studies (DFT), it was shown that this transition state was the most favourable for MgO catalysis of the ketonic decarboxylation reaction, with larger transition state barriers being found for both the uncatalysed reaction mechanism and also for the reaction mechanism involving carboxylate salts, which requires much higher temperatures to decompose through pyrolytic processes.[232]

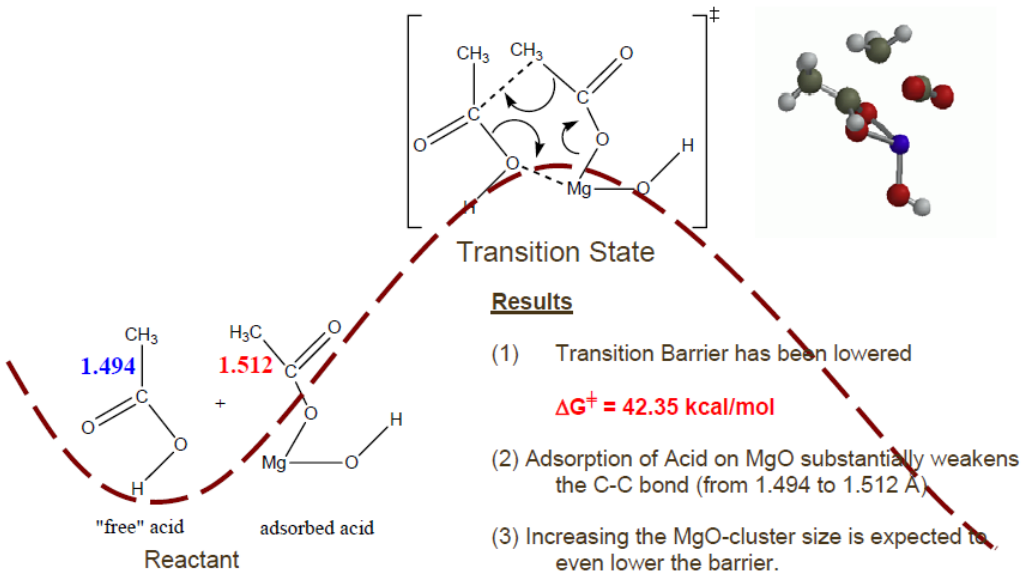

Figure 5.14 Proposed pathway and transition state for ketonic decarboxylation. Image and annotations taken from Zhang et al.[99]

The ketonic decarboxylation reactions involving CoH-LDH2 to CoH-LDH6, which are of weak to medium basicity, were carried out at similar temperatures of 250 °C. As the reaction temperature for the CoH-LDHs is at 250 °C, it must be noted that a partial calcination of the LDH may occur in the reaction resulting in removal of water and CO_2. Further, if any metal salts are formed from the reaction of stearic acid and metal cations composing the LDH structure, then these may also be constantly decomposing back to an anhydrous LDH material at this temperature, rather than contributing to any catalyst poisoning effects.[106, 264]

5.1.3 Comparison of co-precipitated and co-hydrated layered double hydroxide catalysts in decarboxylation reactions

The CoP-LDHs and CoH-LDHs were found to catalyse the conversion of stearic acid to stearone through a ketonic decarboxylation reaction, and a comparison of the relative performance of the two sets of materials is discussed in the following sections.

5.1.3.1 Comparison of the effect of R-value for ketonic decarboxylation reactions of co-hydrated versus co-precipitated layered double hydroxides

As R-value increased from CoP-LDH1 to CoP-LDH3, the degree of conversion increased and then stayed approximately constant up to CoP-LDH6. This suggests that a more $Mg(OH)_2$-like structure favours catalysis, correlating with greater R-values having increased basicity according to Corma *et al.*[196] However, in the present investigation uncalcined MgO was only found to lead to 0.5 % conversion of stearic acid, with potentially, in addition, saponified Mg-stearate ($(C_{17}H_{37}COO)_2Mg$) product being formed on the catalyst surface, blocking active sites.[262]

There was no corresponding effect of R-value observed for the CoH-LDHs, with all R-values leading to similar degrees of catalysis.

An overall graph, plotting R-value versus stearic acid conversion, for both the CoP-LDHs and CoH-LDHs is shown in Figure 5.15. CoP-LDH1 does not lead to any conversion, due to its acidic nature, whereas for R-values 2 to 6 they all lead to moderate to high conversions, with no discernable differences. For both LDH preparation types, an R-value of 4 gave the highest conversion. Note that the smallest variation is observed for the CoH-LDH samples.

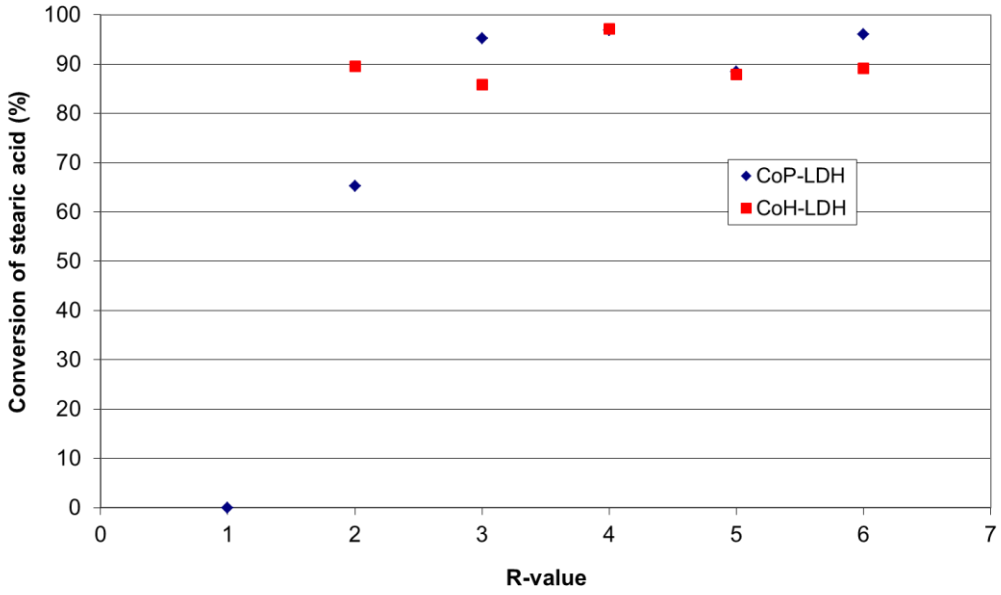

Figure 5.15 Stearic acid conversion *vs.* R-value for CoP-LDH1 to CoP-LDH6 and CoH-LDH2 to CoH-LDH6.

5.1.3.2 Effect of average pore size for the layered double hydroxides

The average pore sizes for CoP-LDH1 to CoP-LDH6 and CoH-LDH1 to CoH-LDH6 as well as the respective conversions of stearic acid to stearone are shown in Table 5.11 and Figure 5.16.

Table 5.11 Average pore size and conversion of stearic acid, in ascending conversion values for the catalysts: CoP-LDH1 to CoP-LDH6 and CoH-LDH2 to CoH-LDH6. Reaction conditions, 250 °C, 20 wt% catalyst (with respect to stearic acid), 100 % N_2 atmosphere at 17 bar, t =24 hours. Errors shown in parentheses.

Catalyst	Average pore size (nm)	Conversion of stearic acid(%)
CoP-LDH1	3.1	0.0 (2.5)
CoP-LDH2	8.7	65.2 (2.9)
CoH-LDH3	10.2	85.8 (3.9)
CoH-LDH5	13.3	87.9 (4.0)
CoP-LDH5	20.2	88.4 (4.0)
CoH-LDH6	11.1	89.1 (4.0)
CoH-LDH2	9.7	89.5 (4.0)
CoP-LDH3	14.4	95.2 (4.3)
CoP-LDH6	22.3	96.0 (4.3)
CoP-LDH4	20.5	96.8 (4.4)
CoH-LDH4	10.8	97.1 (4.4)

Figure 5.16 suggests that there is a minimum average pore size required for this reaction, with zero reaction for CoP-LDH1 at 3.1 nm average pore size, which increases to 65.2 %

conversion for CoP-LDH2 with an average pore size of 8.7 nm and no discernable difference for average pore sizes of 9.7 nm (CoH-LDH2) and above. This suggests the reaction may be sterically hindered in pores of smaller average size, due to the bulky reactant and product molecules and their required alignment for ketonic decarboxylation.

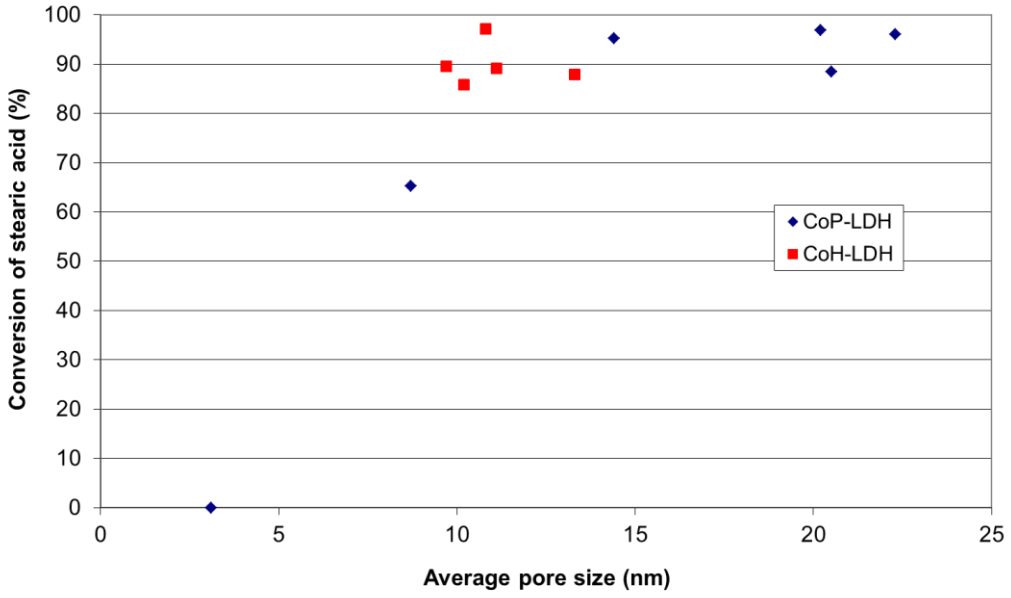

Figure 5.16 Conversion of stearic acid *vs.* average pore size for the catalysts CoP-LDH1 to CoH-LDH6 and CoH-LDH2 to CoH-LDH6.

5.1.3.3 Mechanistic insights for the layered double hydroxides

R-value was found to show a trend with conversion to stearone for the CoP-LDHs, but not the CoH-LDHs which all catalysed the reaction to the same degree. Thus, it can be stated that preparation procedure has an effect on the reaction outcome. CoH-LDH4 and CoP-LDH4 led to the two highest conversions, only differing by 0.3 %, suggesting R-value 4 is optimal for the ketonic decarboxylation reaction of stearic acid under the conditions used, however this may be a coincidence of the results with the additional errors involved from the extraction process.

A correlation is suggested between average pore size and the degree of conversion of stearic acid to stearone, with these both being bulky molecules. In comparison, the smaller acid, acetic

acid has been converted by calcined LDHs of pore size 4.2-7.0 nm previously, but at 100 °C higher temperatures.[115]

As discussed, Zhang et al., looking at methods to upgrade low-quality oil through reduction of acid content, studied the use of calcined MgO catalyst at 250 °C, finding this to yield over 80 % acid conversion.[99] Similarly, the reactions carried out here with LDHs are at 250 °C and a partial calcination of the catalysts may be occurring *in situ*. This leads to an anhydrous LDH of increased Lewis basicity and acidity, as studied by Constantino and Pinnavaia, which was found to be more reactive in base catalysis than LDHs calcined at higher temperatures.[122, 264]

Zhang *et al*., proposed initiation of the ketonic decarboxylation reaction through the abstraction of a proton on one acid molecule by Mg-O Lewis basic sites, through studying the reactions with electronic structure computer simulations. This was followed by carboxylate adsorption, with a second acid molecule then reacting in a six-membered transition state of lower energy barrier compared to the uncatalysed and metal-salt mediated reactions.[99] Analogously, for the LDH reactions studied here, it is believed catalysis occurs in the present reactions *via* a surface mediated mechanism involving LDH weakly basic OH^- groups and medium-strong Mg^{2+}-O^{2-} Lewis basic sites at basal edges and surfaces. These interact with the carboxylic acid molecules, abstracting protons and initiating ketonic decarboxylation.

In an attempt to understand the surface mediated ketonic decarboxylation mechanism, Pulido *et al*. employed a combination of quantum mechanical computation chemistry using density functional theory (DFT) and experimental studies for m-ZrO_2.[265] Two proposed mechanisms were considered, one using a beta-keto acid and the other involving a concerted mechanism (Figure 5.17). It was found that the beta-keto acid mechanism was kinetically favoured in the DFT calculations and this was complemented by experimental studies for monocarboxylic acids, with the removal of an α-proton initiating the reaction.

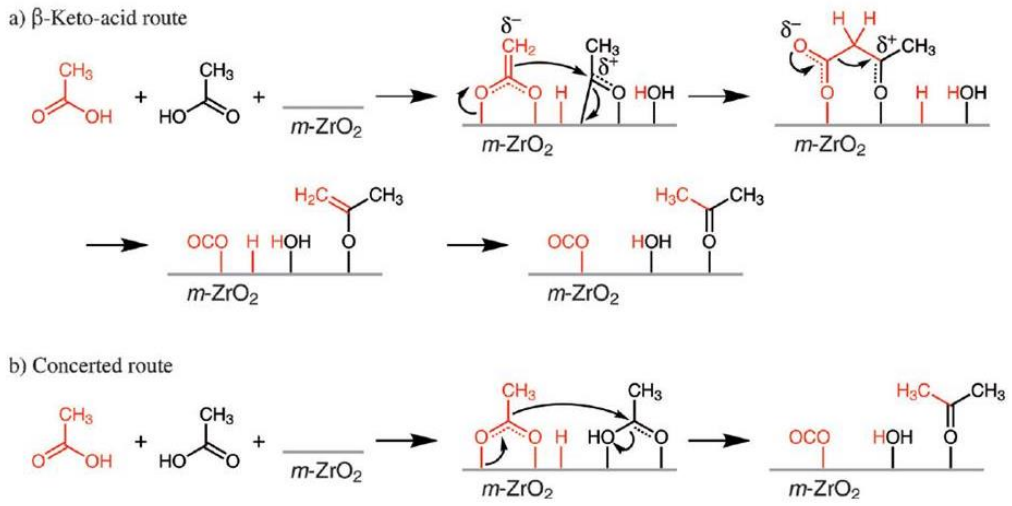

Figure 5.17 Ketonic decarboxylation reaction mechanism a) involving a beta-keto acid and b) through a concerted route. Taken from Pulido *et al.*[265]

Uncalcined MgO catalyst in the present study, with its proposed inherent strong basicity, was not observed to catalyse the ketonic decarboxylation reaction a great deal, possibly because of production of surface magnesium carboxylate.[262] With the CoH-LDHs all having an LDH structure along with an MgO co-phase, it is possible that there may be more than one reaction type occurring, whereby both bulk magnesium stearate formation resulting from the MgO phase and surface mediated catalysis resulting from the LDH phase are simultaneously occurring, enhanced by a potential synergistic effect of the two reaction types/phases. The CoP-LDHs did not exhibit a similar corresponding MgO co-phase by PXRD, however the effect of a partial calcination may generate an MgO-like structure *in situ*, enhancing catalysis. In addition, the interlayer anions and water may be participating in the reaction.

Hammett basicity, which measures the strength of basic surface sites, was not observed to have any effect on the degree of catalysis, however the catalyst structures may have changed within the reaction vessel at 250 °C and the basicity was quantified at lower temperature and pressure.

5.2 Conclusions and summary

Stearic acid was not found to convert to *n*-heptadecane *via* decarboxylation at 250 °C with either CoP-LDHs or CoH-LDHs, but instead underwent ketonic decarboxylation, where two molecules of stearic acid lead to one molecule of stearone, water and CO_2, respectively. Currently ketone production is carried out industrially by means of oxidation of fossil-based hydrocarbons.[107] Ketones that are produced from the ketonic decarboxylation of free fatty acids provides a bio-based route to these desirable compounds.

In summary, the main findings of the present study to examine two different synthesis methods and six different compositions of MgAl LDH upon the conversion of stearic acid at 250 °C and 17 bar pressure were:

- No thermal reaction was observed to occur at 250 °C.
- CoH-LDH4 (97.1 %) and CoP-LDH4 (96.8 %) led to the two highest acid conversions, being 0.3 % different, suggesting R-value 4 is optimal, with no differences resulting from synthesis method.
- For CoH-LDH2 to CoH-LDH6 the reaction is catalysed to a similar degree, whereas similar catalysis only occurs for CoP-LDH3 to CoP-LDH6.
- With R-value 1, the acidic nature of the catalyst dominates, resulting in little or no reaction, similar to that of Al_2O_3.
- A link between average pore size and the degree of ketonic decarboxylation is observed, with the bulky reactant FFA molecule head to head alignment to produce the bulky product molecule being hindered in smaller pores.
- The reaction involves surface mediated catalysis, external of the interlayer, by means of weakly basic LDH OH^- sites and medium Mg-O sites, possibly modified by a partial *in situ* calcination.

- Non-activated MgO yielded a very low amount of stearone, with possibly surface magnesium stearate being formed instead.
- Conversely, MgO co-phases in the CoH-LDHs may have enhanced the conversion of stearic acid to stearone.
- Interlayer anions and water may be participating in the reaction.

6 Ketonic decarboxylation experiments using mixed metal oxides

6.1 Introduction

6.1.1 Rationale for use of mixed metal oxides for decarboxylation reactions

In chapter 5, layered double hydroxides (LDHs) synthesised *via* two different methods, co-precipitation[135] and co-hydration,[123] and with 6 different Mg:Al ratios (1-6), were assessed as catalysts for decarboxylation reactions of stearic acid at 250 °C and 17 bar. Though direct decarboxylation to form *n*-heptadecane was not observed, the catalysts were found to efficiently convert stearic acid to stearone through ketonic decarboxylation. The LDHs were of medium basicity, with other studies also having looked at using weak bases such as ZrO_2.[237] To see if an increase of basicity could result in direct decarboxylation, the use of the calcined derivatives of LDHs, mixed metal oxides (MMOs), of strong basicity (as determined in Section 3.4.4.2), will be examined as potential catalysts for the conversion of stearic acid.

6.1.2 Review of mixed metal oxide preparation and uses in catalysis

MMOs are prepared from the calcination of LDHs, with structural changes as the temperature increases corresponding to: [137-139]

a) Loss of adsorbed surface water up to 100 °C;

b) Loss of interlayer water between 100 °C and 250 °C;

c) Decomposition of organic interlayer species and CO_2 evolution above 250 °C;

d) M^{2+}/M^{3+} layer dehydroxylation between 400 and 600 °C.

It should be noted that the latter two steps often overlap.[138] Calcination of an LDH at 500 °C results in a collapse of the layered structure affording a highly disordered mixed metal oxide. MMOs contain medium-strong Lewis basic O^{2-}-M^{n+} pairs and strong O^{2-} basic sites relating to secluded oxygen ions.[210] Some weakly basic OH^- sites also remain post-calcination. There is also a

degree of Lewis acidity attributed to Al-O-Mg in the structure, with octahedral Al^{3+}.[266] For MMOs, an increase in calcination temperature generally leads to an increase in basicity and the amount of strong basic sites, though an amount of Lewis acidity is also found due to surface Al^{3+} sites being present.[210]

Often, carbonate containing LDHs are prepared as precursors to MMOs since they do not require an inert atmosphere for their synthesis. $MgAlCO_3$-derived MMOs have been found to comprise of mainly basic sites in the range $10.7 \leq pK_a \leq 13.3$ along with limited sites in the range $13.3 \leq pK_a \leq 16.5$.[196] With increasing R-value the number of basic sites has been found to increase, however the overall number of stronger basic sites decreases.[196]

Upon calcination the surface areas of mixed metal oxides increase, for example in a study by Constantino and Pinnavaia,[187] surface area increased from 89 $m^2\ g^{-1}$ to 180 $m^2\ g^{-1}$ on going from 150 °C to 450 °C. Also, Reichle *et al.* stated that numerous fine pores between 2-4 nm form during calcination,[205] which leads to a decrease in the average pore size from that of the parent LDH.

MMOs have been used for a range of acid and base catalysis applications including Aldol condensation, Claisen-Schmidt condensations, Knoevenagel condensation, alkylation and acylation.[253] MMOs contain both acidic and basic sites, though either type of site can predominate in certain reactions, for example in the conversion of 2-methyl-3-butyn-2-ol (MBOH), only the products due to base catalysis formed, rather those due to acidic or amphoteric sites.[267]

With respect to biomass, MMOs have been used for the base catalysed *trans*-esterification of triglycerides, found in vegetable oils, into fatty acid methyl esters (FAMEs). Using glyceryl tributyrate as a model compound and Mg-Al MMOs as catalysts, Cantrell *et al*. observed that the degree of activity increased with increasing R-value (Mg content).[63] The MMO with a measured R-value of 2.93 led to the highest conversion with ten times more activity than MgO, ascribed to be due to the lower porosity and so reduced accessibility to basic sites. Al_2O_3 was found to be completely inactive for *trans*-esterification. Water has been found to increase the rate of conversion in *trans*-esterification, but also inhibits this reaction since it hydrolyses the ester producing acid

groups, which react with basic sites.[268] Parida and Das have also investigated the use of MMOs for the ketonic decarboxylation of acetic acid as a model free fatty acid.[115, 116]

6.2 Stearic acid ketonic decarboxylation experiments

Following on from the ketonic decarboxylation experiments using layered double hydroxides (Chapter 5), a series of similar catalysed reactions were undertaken, using mineral based catalysts. These were MMOs calcined from LDH precursors prepared by two synthesis methods: co-precipitation and co-hydration; as described in Chapter 3. Catalyst properties relating to crystal structure, composition, surface area and relative basicity are also described and discussed in this section. For the reactions involving ketonic decarboxylation of stearic acid, identical conditions were used to those described in Chapter 5.

6.2.1 Experimental

Reagents were used as supplied: stearic acid (97 %, Acros organics); dodecane (98 %, Sigma-Aldrich); magnesium oxide (Sigma-Aldrich, ACS 98 %); CP5 aluminium oxide (BASF); and CoP-MMO (see Section 3.4.1) and CoH-MMO (see Section 3.4.2) materials synthesised within this thesis. A 100 ml Parr autoclave was charged with stearic acid (0.1 g, 97 %, 0.3 mmol), dodecane solvent (10 ml), and catalyst (0.02 g), giving a catalyst loading of 20 wt% relative to the stearic acid. The vessel was sealed and subsequently pump-purged ten times with $N_{2(g)}$ and then pressurised to 9.7 bar at room temperature with $N_{2(g)}$. The stirrer was initiated, at 500 rpm, and the reaction heated to an internal temperature of 250 °C over 30 minutes, achieving a final internal pressure of 17 Bar. These reaction conditions were maintained for 24 h. The vessel was then allowed to cool under stirring over approximately 3 h, under continuous stirring and depressurised to atmospheric pressure. The endpoint reaction mixture, containing the solid catalyst and wax residues, was filtered at room temperature through a sintered glass filter Büchner ring and Büchner

flask, under vacuum. The liquid fraction was retained for analysis (see section 6.2.2) and the solid/wax fraction was subjected to Soxhlet extraction. For this process, the solid/wax fraction was placed in a cellulose Soxhlet extraction thimble within a Soxhlet chamber, ethanol (250 ml) was heated at reflux temperature for a period of 12 hours and continuously condensed, washing the solid/wax sample and removing any soluble reactants or wax products from the insoluble mineral catalyst into the still pot. The Soxhlet apparatus was then allowed to cool to room temperature over a period of 3 hours, following which, the ethanol solvent was removed using a rotary evaporator (50 mbar, 20 °C) to leave a solid residue, which was analysed as described in section 6.2.3. Validation of the Soxhlet extraction was carried out using known mixtures with various ratios of stearic acid and stearone to confirm that this extraction process was accurate (Section 5.2.5).

Table 6.1 Mixed metal oxide materials employed as catalysts (20 wt% with respect to stearic acid) in the conversion of stearic acid at 250 °C, 17 bar $N2_{(g)}$, along with their method of synthesis and target structures.

Catalyst	Synthesis method	Target compound
CoP-MMO-1	Co-precipitation, calcination	$[Mg_{0.5}Al_{0.5}O_{1.25}]$
CoP-MMO-2	Co-precipitation, calcination	$[Mg_{0.66}Al_{0.33}O_{1.17}]$
CoP-MMO-3	Co-precipitation, calcination	$[Mg_{0.75}Al_{0.25}O_{1.13}]$
CoP-MMO-4	Co-precipitation, calcination	$[Mg_{0.8}Al_{0.2}O_{1.1}]$
CoP-MMO-5	Co-precipitation, calcination	$[Mg_{0.8}Al_{0.17}O_{1.08}]$
CoP-MMO-6	Co-precipitation, calcination	$[Mg_{0.86}Al_{0.14}O_{1.07}]$
CoH-MMO-1	Co-hydration, calcination	$[Mg_{0.5}Al_{0.5}O_{1.25}]$
CoH-MMO-2	Co-hydration, calcination	$[Mg_{0.66}Al_{0.33}O_{1.17}]$
CoH-MMO-3	Co-hydration, calcination	$[Mg_{0.75}Al_{0.25}O_{1.13}]$
CoH-MMO-4	Co-hydration, calcination	$[Mg_{0.8}Al_{0.2}O_{1.1}]$
CoH-MMO-5	Co-hydration, calcination	$[Mg_{0.8}Al_{0.17}O_{1.08}]$
CoH-MMO-6	Co-hydration, calcination	$[Mg_{0.86}Al_{0.14}O_{1.07}]$

The catalysts used in these experiments were CoP-MMO1 to CoP-MMO6 and CoH-MMO1 to CoH-MMO6 (Table 6.1). For comparison, MgO and Al_2O_3 catalysts were also trialled, along with an uncatalysed control reaction for completeness.

6.2.2 Liquid product analysis

Chemical standards of the decarboxylation product *n*-heptadecane (Acros, 99 %), C_8-C_{20} alkane GC standard solution (Fluka), stearic acid (Acros, 97 %) (including the silylating agents pyridine (Acros) and BSTFA (Acros)), the ketonic decarboxylation product stearone (TCI, 95 %) eicosane (Acros, 99 %) and the solvent dodecane (Sigma-Aldrich, 98 %) were used as received. The liquid products obtained after filtration were analysed by gas chromatography (HP 5890 Series II) equipped with a nonpolar column (VF-5MS, with dimensions 30 m x 0.25 mm x 0.25 μl) and a flame ionisation (FID) detector. The injector and detector temperatures were 250 and 350 °C respectively. To analyse stearic acid, the sample must first be derivatised by silylation to make the compound more volatile, less polar and more thermally stable. This is where the acidic proton is replaced with a trimethyl-silyl group (Me_3Si). To do this, following each experiment, 1 ml of reaction mixture was removed (containing maximum 0.01 g of unreacted 97 % stearic acid, 0.34 mmol, assuming zero conversion) and was silylated using 100 mol% excess N,O-bis(trimethyl)trifluoroacetamide (BSTFA, 0.068 moles, 0.0176 g) and dissolved in 30 mol% pyridine (0.01 mmol, 0.0008g). 0.001 ml of 0.1 M standard eicosane in dodecane was then added as an analytical standard, and the sample was left for 12 hours to completely silylate. Following this, a 5 μl aliquot was then injected into the GC with helium as the carrier gas at pressure of 2.07 bar. The GC was held at 35 °C for 5 minutes then ramped up to 300 °C at 5 °C / min. Retention times were determined using standard materials and eicosane was used as an internal standard. Data analysis and peak integration were performed using Clarity software.[159] Calibration curves are shown in section 5.2.4.

6.2.3 Solid product analysis

Post-Soxhlet extracted wax solids were analysed using a Xevo QToF mass spectrometer (Waters Ltd, UK) equipped with an Agilent 7890 GC (Agilent Technologies UK Ltd, UK) and an atmospheric solids analysis probe (ASAP) solid handling sample introduction port for initial identification. Solid samples were introduced into the spectrometer from a heated melting point tube (ramped from 100 °C to 600 °C over several minutes) previously dipped into neat sample. Mass spectrometry data was processed using MassLynx 4.1.[261] Exact mass measurements were recorded using a lock-mass correction to provide < 3 mDa precision.

Post-Soxhlet extracted wax solids were also dissolved in THF (0.1 mg in 1000 µl), silylated with 10 µl BSTFA and 10 µl pyridine. Following this the components were analysed quantitatively relative to each other using gas chromatography (HP 5890 Series 2) equipped with a TR-SD capillary column (length 10 m, ID 0.53 mm and film thickness 2.65 µm). The injector and detector temperatures were 250 and 350 °C respectively. 5 µl of sample was injected into the GC with helium as the carrier gas at pressure of 2.07 bar. The GC temperature program was based on ASTM D6584 10ae1 standard test method for determination of total monoglyceride, total diglyceride, total triglyceride, and free and total glycerin in B-100 biodiesel methyl esters by gas chromatography.[160] The GC was held at 50 °C for 1 min then ramped at 15 °C / min up to 180 °C, followed by ramping at 7 °C / min up to 230 °C then increasing up to 350 °C at 10 °C / min where it was held for 5 min. Retention times were corroborated using standard materials. The same chemical standards were used as with the liquid portion, as detailed in section 6.2.2. Data analysis and peak integration were performed using Clarity software.[159] Calibration curves are shown in section 5.2.4.

6.3 Results and discussion of decarboxylation reactions

In Section 6.3.1, the catalytic results will be examined for MMOs prepared from co-precipitated LDHs. Following this, the catalytic results for the MMOs prepared from co-hydrated LDHs will be discussed in Section 6.3.2. Finally, a comparison of the two MMO catalyst types is made in Section 6.3.3.

6.3.1 Reactions using mixed metal oxide catalysts prepared from co-precipitated layered double hydroxides

Following the experimental procedure for the CoP-MMO outlined above, in Section 6.2.1, MMO catalysed decarboxylation reactions were undertaken. The liquid and solid phases from the endpoint reaction mixture were extracted, separated further by Soxhlet reaction (Section 6.2.1) and analysed by GC using the protocol described in Sections 6.2.2 and 6.2.3, with the results given in Table 6.2. As a control, the thermal reaction (i.e. with no MMO or other mineral catalyst present) is repeated here from chapter 5, and further control reactions with individual calcined alumina and magnesium oxide (prepared using the calcination procedure outlined in Section 3.3) are also undertaken to check on the effect these impurities may have and on the reaction yield.

Table 6.2 Moles of unreacted stearic acid, stearone product and conversion of stearic acid for the uncatalysed reaction and employing catalysts: CoP-MMO1 to CoP-MMO6. Reaction conditions, 250 °C, 20 wt% (with respect to stearic acid) catalyst, 100 % N_2 atmosphere at 17 bar, t =24 hours. Errors shown in parentheses.

Catalyst	Stearic acid (moles x 10^{-3})	Stearone (moles x 10^{-3})	Conversion of stearic acid (%)
Uncatalysed	0.3515 (0.0246)	0.0000 (0.0001)	0.0 (2.5)
CoP-MMO1	0.3515 (0.0246)	0.0000 (0.0001)	0.0 (2.5)
CoP-MMO2	0.0496 (0.0035)	0.1510 (0.0068)	85.9 (3.9)
CoP-MMO3	0.0411 (0.0029)	0.1552 (0.0070)	88.3 (3.8)
CoP-MMO4	0.0599 (0.0042)	0.1459 (0.0066)	83.0 (3.7)
CoP-MMO5	0.0242 (0.0017)	0.1636 (0.0074)	93.1 (4.2)
CoP-MMO6	0.0288 (0.0020)	0.1613 (0.0073)	91.8 (4.1)

Upon work up, the thermal (no catalyst) reaction was found to contain no noticeable decrease in stearic acid content, indicating that thermal decarboxylation did not occur at 250 °C under reaction conditions (17 bar N_2, 24 h, stirred). Analysis of the endpoint reaction mixtures showed that, as with the LDHs, for the CoP-MMOs, direct decarboxylation of stearic acid to yield *n*-heptadecane and CO_2 did not occur. Instead, a waxy solid was once again produced, which, upon extraction and analysis, was found to be stearone, formed *via* ketonic decarboxylation (Figure 5.7). No other products were evident within the GC trace. This result is similar to studies by Na *et al*.,[262] who, using MMO catalysts calcined at 550 °C for 3 hours, did not observe direct decarboxylation to occur below 400 °C. At 300 °C a great deal of unreacted oleic acid remained, however at 350 °C a wax residue was obtained which was attributed to in the study by the authors as a saponified Mg-oleate. However, no direct analysis was provided and, on the basis of this present study it seems Na *et al*., may also have formed the ketone product. The following section will look at the effect of R-value on conversion.

6.3.1.1 Effect of R-value in co-precipitated mixed metal oxide catalysed reactions

CoP-MMO1 did not lead to conversion of stearic acid, whereas CoP-MMO2 to CoP-MMO6 all led to more comparable conversions to stearone, between 83.0 and 93.1 %, though the actual values may lie within error of each other. A plot of R-value against stearic acid conversion to stearone is show in Figure 6.1.

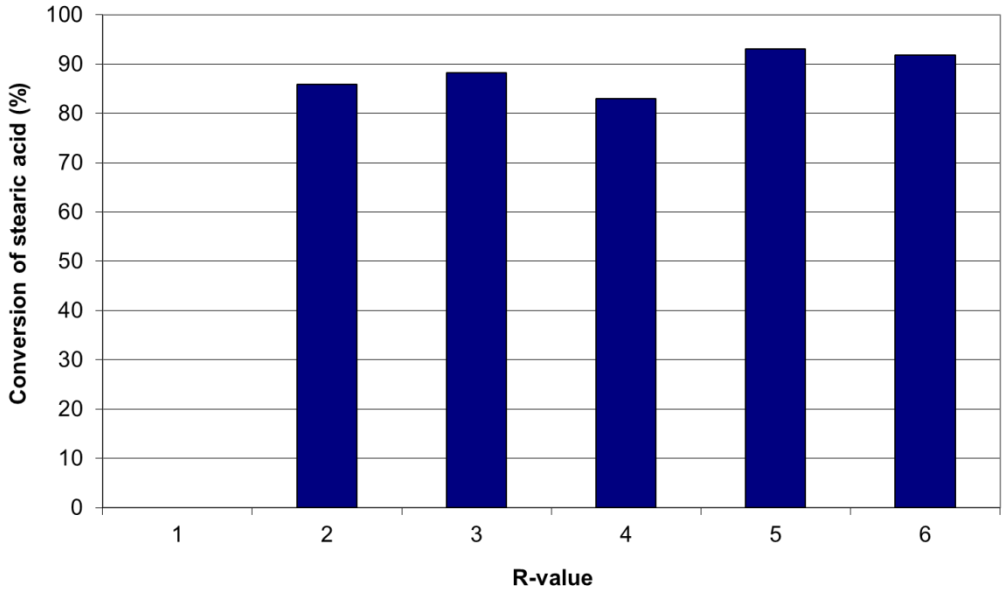

Figure 6.1 Conversion of stearic acid vs. R-value for the catalysts CoP-MMO1 to CoP-MMO6.

It has previously been shown that as the R-value increases, the basicity of MMOs tends to increase.[196] CoP-MMO1 to CoP-MMO3 and CoP-MMO6 had a measured Hammett basicity of 7.6 $\leq pK_a \leq$ 9.0, whereas CoP-MMO4 and CoP-MMO5 were in the range 9.0 $\leq pK_a \leq$ 10.0, however, there seems to be no evident correlation from the data between the measured basicity and the effect of R-value upon the conversion observed. CoP-MMO1, relatively rich in Al^{3+}, would be expected to exhibit the lowest basicity, being quite acidic in nature, and this correlates with the observed lack of reaction for this catalyst, with 0 % conversion of stearic acid recorded. The high yields evidenced by GC for CoP-MMO2 to CoP-MMO6 (83.0-93.1 % conversion of stearic acid), being of increased basicity owing to Lewis base O^{2-}-M^{n+} pairs and strong O^{2-} basic sites, indicate that this is a base catalysed reaction, with a minimum threshold of pKa 7.6-9.0, according to the Hammett indicator tests. The high surface areas of CoP-MMO2-CoP-MMO6 (155-199 m^2/g) all being much greater and more homogeneous than their parent CoP-LDH2-CoP-LDH6 materials (17-91 m^2/g) may be a reason as to why there is much less variation in the conversion of stearic acid with the CoP-MMOs (83.0-93.1 %) than the CoP-LDHs (65.2-96.8 %).

6.3.1.2 Effect of average pore size in co-precipitated mixed metal oxide catalysed reactions

The average pore sizes for the prepared CoP-MMOs, along with the GC measured conversions of stearic acid to stearone, are shown in Table 6.3 and graphically in Figure 6.2.

Table 6.3 Average pore sizes and conversion of stearic acid, in ascending conversion values for the catalysts: CoP-MMO1 to CoP-MMO6. Reaction conditions, 250 °C, 20 wt% catalyst (with respect to stearic acid), 100 % N_2 atmosphere at 17 bar, t =24 hours. Errors shown in parentheses.

Catalyst	Average pore size (nm)	Conversion of stearic acid (%)
CoP-MMO1	7.8	0.0 (2.5)
CoP-MMO4	6.2	83.0 (3.7)
CoP-MMO2	10.4	85.9 (3.9)
CoP-MMO3	14.7	88.3 (4.0)
CoP-MMO6	9.2	91.8 (4.1)
CoP-MMO5	7.2	93.1 (4.2)

All the CoP-MMOs lie in the average pore size range 6.2 to 14.7 nm. Aside from CoP-MMO1, which owing to its high acidic nature may not be leading to conversion of stearic acid, these materials all yielded stearone at high conversions. A comparison with the CoP-LDH average pore sizes is given in Section 6.3.1.4.

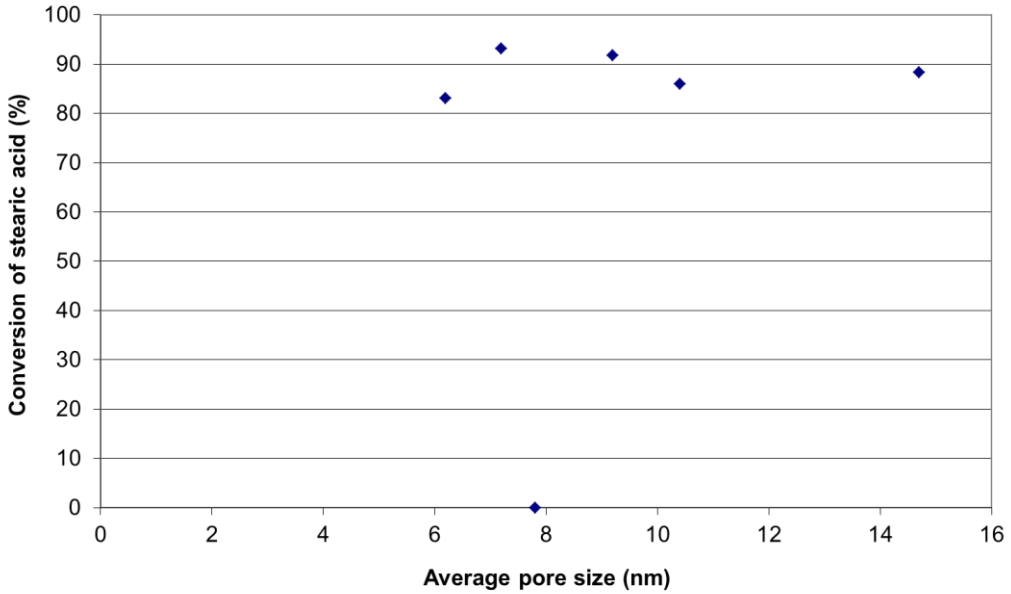

Figure 6.2 Conversion of stearic acid *vs.* average pore size for the catalysts CoP-MMO1 to CoP-MMO6.

6.3.1.3 Comparison of decarboxylation reactions undertaken using calcined MgO and calcined Al_2O_3 with reactions using MgAl mixed metal oxides

Calcined MgO and calcined (CP5) Al_2O_3 were also assessed as control catalysts for the conversion of stearic acid at 250 °C, with the results shown in Table 6.4. Calcined Al_2O_3 did not lead to any conversion of stearic acid, being attributed to the acidic nature of the catalyst, with similarly uncalcined Al_2O_3 also exhibiting zero conversion (Chapter 5). This indicates that no catalytic activation occurs upon calcination for Al_2O_3 and correlates well with the lack of activity identified for the Al rich phase present in CoP-MMO1.

Table 6.4 Moles of unreacted stearic acid, stearone product and conversion of stearic acid for the reaction employing catalysts calcined MgO and calcined Al_2O_3. Reaction conditions, 250 °C, 20 wt% catalyst (with respect to stearic acid), 100 % N_2 atmosphere at 17 bar, t =24 hours. Errors shown in parentheses.

Catalyst	Stearic acid (moles x 10^{-3})	Stearone (moles x 10^{-3})	Conversion of stearic acid(%)
Calcined MgO	0.0352 (0.0025)	0.1582 (0.0071)	90.0 (4.1)
Calcined Al2O3	0.3515 (0.0246)	0.0000 (0.0001)	0.0 (2.5)

In contrast to the lack of reactivity found in (CP5) Al_2O_3, 90 % of stearic acid was converted to stearone with calcined MgO, whereas with uncalcined MgO only 0.5 % of stearic acid was converted to stearone. In the previous chapter this was attributed to the uncalcined MgO potentially creating saponified Mg-stearate product,[262] with some stearone produced as a by-product. In a study using lauric acid by Corma et al.,[109] 97 % conversion to laurone is seen at 400 °C with MgO, but this may be related to an *in situ* activation of the catalyst at this temperature or the kinetics may be enhanced.

Through *in situ* diffuse reflectance infrared Fourier transform spectroscopy (DRIFTS) studies the calcination of MgO has been followed.[269] Bound H_2O was shown to be present on the MgO surface in abundance along with basic OH groups but on calcination up to 500 °C the adsorbed water disappeared and the basic OH groups increased in intensity (Figure 6.3). These basic OH groups were detected at an OH frequency known not to form hydrogen bonds to the

surface of the sample. Thus, in this present study, the conversion of stearic acid to stearone by MgO may be attributable to weakly basic OH^- groups on the catalyst surface.

As Calcined MgO is an effective catalyst for the ketonic decarboxylation reaction itself then this material may be preferentially employed due to it not requiring a preparative method, as is the case with the LDHs and MMOs studied here.

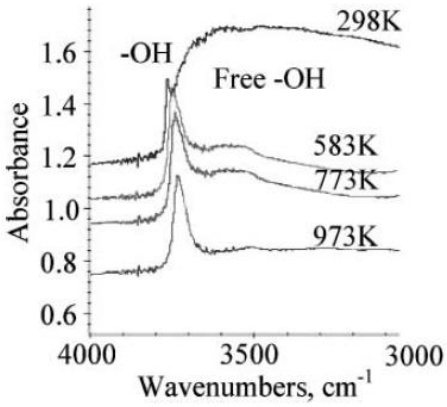

Figure 6.3 Fourier transform-Infrared spectra of MgO in the region 4000–3000 cm^{-1}, illustrating the disappearance of free OH groups associated with water and increase of weakly basic OH groups on going from 25 ° to 700 °C. Taken from Corma *et al*.[269]

In the context of the current study, it is interesting that MgO is activated by calcination, leading to a high conversion of stearic acid to stearone, over the uncalcined precursor as it might be expected that the MMOs with high Mg content would behave more akin to the MgO phase, which, as discussed is known to be active in these reactions. It is then pertinent to note that the $Mg(OH)_2$ phase was not active, while the uncalcined LDH materials were, suggesting that the interlayer anions and bound water may potentially have a role in the catalysis for the LDH material, as these would not be present in the $Mg(OH)_2$.

6.3.1.4 Comparison of co-precipitated mixed metal oxides and co-precipitated layered double hydroxide catalysts in decarboxylation reactions

For both the CoP-MMOs and CoP-LDHs a plot of R-value against stearic acid conversion to stearone is show in Figure 6.4. It has been found in this thesis that zero conversion of stearic acid

occurs with catalysts of high acidity, with both CoP-MMO 1 and CoP-LDH1 behaving similarly due to their high Al^{3+} content, and control reactions with acidic alumina also yielding no conversion.

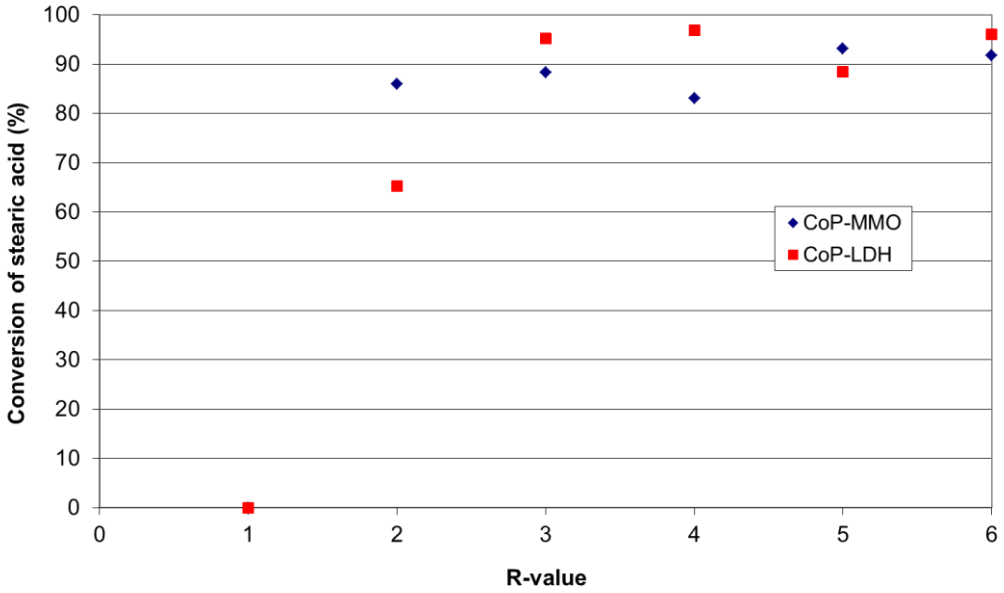

Figure 6.4 Conversion of stearic acid *vs.* R-value for the catalysts CoP-MMO1 to CoP-MMO6 and CoP-LDH1 to CoP-LDH6.

The yield of stearone is 20.7 % higher for CoP-MMO2 than that for CoP-LDH2 resulting from increased Lewis acid and basic sites post-calcination.[196, 266] However, Hammett basicity indicated that CoP-MMO2 was less basic (pK_a 7.6-9.0) than CoP-LDH2 (pK_a 9.0-10.0). CoP-LDH3 gave a high conversion of 95.2 % stearic acid to stearone, slightly higher than that of CoP-MMO3. For R-value 4 the LDH yielded a higher conversion of stearic acid to stearone than the MMO, but for R-values 5 and 6 there is not a great difference between the LDHs and MMOs, though these results may all be similar, within error of the reaction extraction (± 3.5 %) and GC analysis calibration curves (± 1 %).

From the plot in Figure 6.4 the observed conversions suggests that at low R-value, where basicity is expected to be the least,[196] calcination increases the amount of basic sites,[122] whereas at higher R-values the basicity is such that calcination does not lead to such a large effect.

Comparing the average pore sizes of the CoP-LDHs and CoP-MMOs (Figure 6.5), the latter have a much narrower average pore size range, mainly between 6.2 and 10.4 nm, whereas for the former, average pore sizes are much larger. It was suggested that small average pore size may be hindering the conversion of stearic acid with the LDHs in chapter 5, however with the smaller average pore sizes observed here for the CoP-MMOs there does not appear to be a similar effect. The average pore size increased upon calcination for R-values 1-3, whereas it decreased for R-values 4-6.

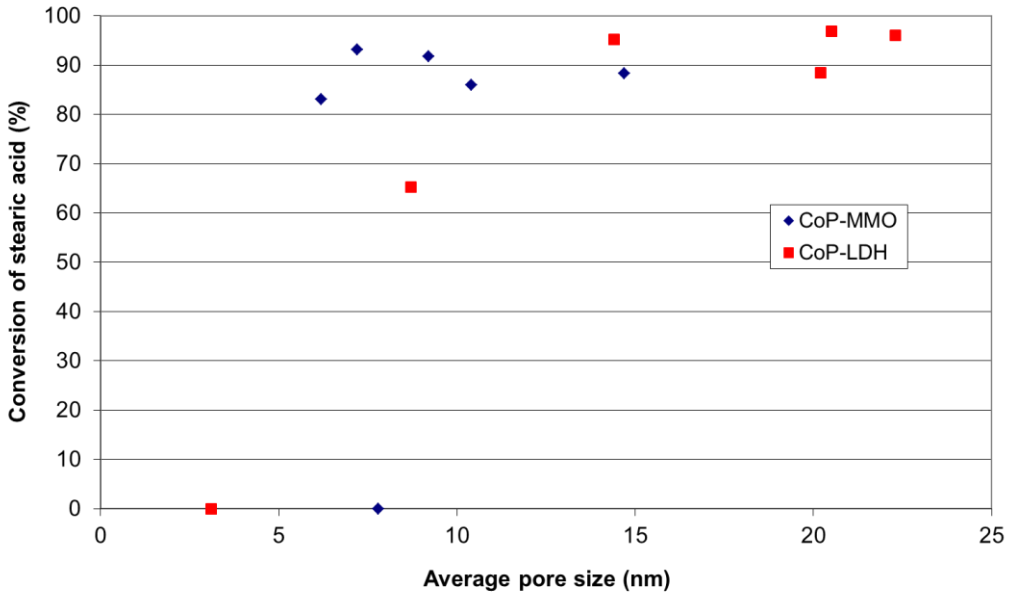

Figure 6.5 Conversion of stearic acid to stearone vs. average pore size for the catalysts CoP-LDH1 to CoP-LDH6 and CoP-MMO1 to CoP-MMO6.

It may be possible, owing to CO_2 and water being produced in the ketonic decarboxylation reaction, see Figure 5.7, that as the reaction proceeds in the presence of the MMOs, the MMO catalysts may begin to partially reconstruct into an LDH using the evolved water to rehydroxylate. Similarly, for LDHs, since the reaction is at 250 °C this may lead to an *in situ* partial calcination of the catalysts to an anhydrous LDH, which is known to start to occur at 200 °C,[138] increasing the Lewis acid and basic site content of the material.

6.3.1.5 Mechanistic insights from co-precipitated mixed metal oxide catalysed decarboxylation reactions

he CoP-MMOs, aside from CoP-MMO1 (for the reasons highlighted above), were all found to give a good, to high, conversion of stearic acid to stearone (between 83 – 93.1 %). MMOs are known to have a larger number of basic sites (as well as Lewis acidity) than their LDH precursors, though, within the error associated with extraction and calibration of analysis, there is no discernable difference differences between the R-values (2, 3, 4, 5, 6), and no correlation seems to exist for these samples in terms of surface areas (155-199 m^2/g) or average pore sizes (6.2-14.7 nm) and their degree of conversion of stearic acid (~83 %-93 %).

The reaction clearly requires a hydroxide or oxide surface, as the thermal reaction yields negligible conversion (state). In line with the mechanism proposed by Zhang *et al*.[232] the ketonic decarboxylation reaction also requires basic sites since the CoP-MMO1, with its inherent acidity, led to no discernible conversion of stearic acid. Prior studies in the literature have suggested ketonic decarboxylation proceeds *via* a beta keto-acid intermediate, which requires the presence of basic sites on the catalyst surface.[265] This is owing to the need to initially remove the acidic proton from a carboxylic acid molecule, anchoring it in position on the catalyst surface, and then remove an α-proton, producing a vinyl acid, which attacks a second carboxylic acid molecule and leads to the beta-keto acid intermediate, with finally, loss of CO_2 producing the ketone (Figure 5.17).[265]

Ketonic decarboxylation has been the subject of a number of studies including the use of calcined MgAl-LDHs. In a study by Parida and Das,[115] acetic acid was used as the model fatty acid and the LDHs were calcined at 400 °C to yield MMOs. Catalysis was then carried out with acetic acid vapour in a nitrogen stream, where conversion with R values in the range 2 – 4 began at 300 °C. R-values of 5 and 7 required further elevated temperatures of 325-350 °C. At 350 °C the MgAl-MMO with R-value 4 gave the highest overall conversion of acetic acid, of 86.5 %. This material also had the greatest surface area for all the Mg-Al MMOs studied. It is believed that a surface interaction was occurring, showing that as the gas hourly space velocity was increased, and

thus surfaces became saturated, the conversion decreased, requiring higher temperatures for comparable conversions.

It is proposed that the reactions in the current study presented here, being a batch process, had increased contact time and yielded higher corresponding reactivity at lower temperatures. The surface area does not have such a large impact in the current study, with CoP-MMO surface areas between 160 – 199 m^2/g all leading to similar conversions of stearic acid. When using ZnAl-MMOs, Das and Parida found the material with R-value 3 led to the highest yield of acetone (> 89 %) but at much higher temperatures of 425 °C.[116] This material was also found to have the highest surface area (103.5 m^2/g), which is still low in comparison to the smallest surface area measured for the CoP-MMOs used here (155 m^2/g for CoP-MMO3). Other oxides, such as ceria, have been used as catalysts in ketonic decarboxylation reactions. Nagashima *et al*. found CeO_2–Mn_2O_3 to lead to 73.9 % conversion of propanoic acid to propanone with 97.4 % selectivity at 350 °C, whereas CeO_2-MgO has a lower (66.8 %) conversion but with similarly high selectivity.[118] The authors speculated the reaction mechanism involved adsorption of carboxylates, followed by abstraction of an α-proton to create a radical which formed a beta-keto acid with a second carboxylate, followed by decarboxylation to the ketone. When using mixed acid feedstocks with ceria-zirconia catalysts, the cross-ketonic decarboxylation was found to proceed at a faster rate than homo-ketonic decarboxylation.[270] However, such a redox driven process is not feasible in our MgAl systems.

In order to account for the similar performance of the LDH and MMO species, as well as the differences observed compared to $Mg(OH)_2$ and MgO control reactions, it is plausible that for all the active CoP-MMOs, the actual material performing catalysis in the reactor vessels, and under reaction conditions, may be a partially reconstructed LDH as described in Section 6.3.1.4.

It was postulated in the previous chapter that the variance in LDH catalysis was possibly due to an effect of suitable average pore size, allowing accessibility of reactant and product molecules, and surface area for reaction to occur. The calcined derivatives used in reactions here exhibit lower average pore size and increased surface area, however, based on the data from the CoP-MMOs, it

can be concluded that average pore size appears to be less of a controlling factor for ketonic decarboxylation.

6.3.2 Reactions using mixed metal oxide catalysts prepared from co-hydrated layered double hydroxides

Following the experimental procedure outlined in Section 6.2.1, CoH-MMO catalysed decarboxylation reactions were undertaken. The liquid and solid phases from the final reaction mixture were extracted, further separated by Soxhlet reaction (Section 6.2.1) and analysed by gas chromatography using the procedures described in Sections 6.2.2 and 6.2.3, with the results given in Table 6.5. The thermal reaction (i.e. with no MMO or other mineral catalyst present) is repeated here from chapter 5, as a control, with individual calcined alumina and magnesium oxide (prepared using the calcination procedure outlined in Section 3.3) as further control reactions, undertaken to check on the effect these impurities may have and on the reaction yield.

Table 6.5 Moles of unreacted stearic acid, stearone product and conversion of stearic acid for the uncatalysed reaction and also employing catalysts: CoH-MMO1 to CoH-MMO6. Reaction conditions, 250 °C, 20 wt% catalyst (with respect to stearic acid), 100 % N_2 atmosphere at 17 bar, t =24 hours. Errors shown in parentheses.

Catalyst	Stearic acid (moles x 10^{-3})	Stearone (moles x 10^{-3})	Conversion of stearic acid (%)
Uncatalysed	0.3515 (0.0246)	0.0000 (0.0001)	0.0 (2.5)
CoH-MMO1	0.3515 (0.0246)	0.0000 (0.0001)	0.0 (2.5)
CoH-MMO2	0.0225 (0.0016)	0.1645 (0.0074)	93.6 (4.2)
CoH-MMO3	0.0411 (0.0028)	0.1557 (0.0070)	88.6 (4.0)
CoH-MMO4	0.0161 (0.0011)	0.1677 (0.0075)	95.4 (4.3)
CoH-MMO5	0.0357 (0.0025)	0.1578 (0.0071)	89.8 (4.0)
CoH-MMO6	0.0097 (0.0007)	0.1708 (0.0077)	97.2 (4.4)

Upon extraction and analysis, the thermal (no catalyst) reaction was found to contain no detectable decrease in stearic acid content, indicating that thermal decarboxylation did not occur at 250 °C under reaction conditions (17 bar N_2, 24 h, stirred). Analysis of the CoH-MMO endpoint reaction mixtures showed that, as with the LDHs and CoP-MMOs, direct decarboxylation of stearic acid to yield *n*-heptadecane and CO_2 did not occur. Alternatively, a waxy solid was again

produced, which, was found to be stearone, upon extraction and analysis, formed *via* ketonic decarboxylation (Figure 5.7). No further products were evidenced within the GC trace.

6.3.2.1 Effect of R-value in co-hydrated mixed metal oxide catalysed reactions

CoH-MMO1 did not lead to conversion of stearic acid, whereas CoH-MMO2 to CoH-MMO6 all gave a high conversion of stearic acid (between 88.6 and 97.2 %) to stearone. As with the CoP-MMOs, the variation as a function of R-value is slight, approximately +/- 5%, and this falls within the error present within the extraction process (see Section 5.2.5) and, to a lesser extent, the calibration curves of the GC for each pure standard (as shown in Section 5.2.4). A plot of R-value against stearic acid conversion to stearone is show in Figure 6.6

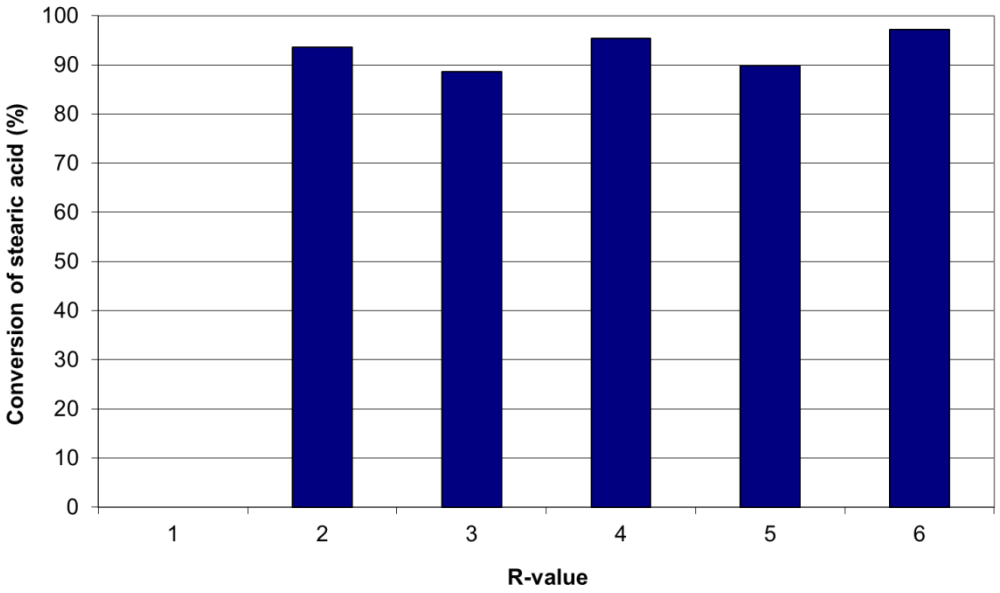

Figure 6.6 Conversion of stearic acid *vs*. R-value for the catalysts CoH-MMO1 to CoH-MMO6

CoH-MMO1 and its precursor CoH-LDH1 are believed to be alumina compounds by PXRD, and so, similar to the calcined Al_2O_3 (*vide supra*), the lack of activity is due to the acidic nature of these catalysts, and in this thesis, it has already been established a basic catalyst material is required (see Section 5.1). It has previously been reported that the basicity of MMOs tends to increase as R-value increases,[196] however all of the CoH-MMOs here had a measured Hammett

basicity of $6.0 \leq pK_a \leq 7.6$. In a sense, this is unsurprising as Greenwell *et al.*[123] showed that in the co-hydration reaction variation in product Mg:Al ratio is small, irrespective of R-value, with, instead, LDH phases of similar R-value forming with varying degree of $Mg(OH)_2$ impurity. In the conversion of stearic acid *via* ketonic decarboxylation, CoH-MMO2 to CoH-MMO6, all exhibit sufficient base catalytic sites, with no discernable differences between them.

6.3.2.2 Effect of average pore size in co-hydrated mixed metal oxide catalysed reactions

The average pore sizes for the CoH-MMOs, along with their conversions of stearic acid to stearone, are shown in Table 6.6 and graphically in Figure 6.7.

It is interesting that all the CoH-MMOs lie within a narrow average pore size range of 4.8 to 7.5 nm. For the active catalysts there is no discernable trend with average pore size since they all convert stearic acid to a similar high degree, within the error of the extraction process.

Table 6.6 Average pore sizes and conversion of stearic acid, in ascending conversion values for the catalysts: CoH-MMO1 to CoH-MMO6. Reaction conditions, 250 °C, 20 wt% catalyst (with respect to stearic acid), 100 % N_2 atmosphere at 17 bar, t =24 hours. Errors shown in parentheses.

Catalyst	Average pore size (nm)	Conversion of stearic acid (%)
CoH-MMO1	6.0	0.0 (2.5)
CoH-MMO3	5.9	88.6 (4.0)
CoH-MMO5	7.5	89.8 (4.0)
CoH-MMO2	4.8	93.6 (4.2)
CoH-MMO4	6.4	95.4 (4.3)
CoH-MMO6	5.8	97.2 (4.4)

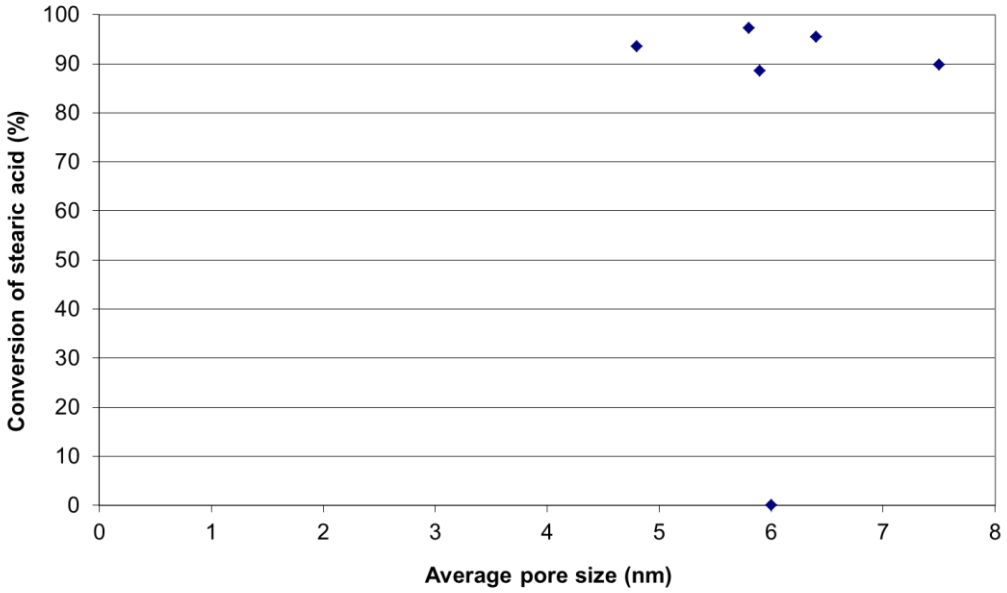

Figure 6.7 Conversion of stearic acid *vs.* average pore size for the catalysts CoH-MMO1 to CoH-MMO6.

6.3.2.3 Comparison of co-hydrated mixed metal oxides and co-hydrated layered double hydroxide catalysts in decarboxylation reactions

For both the CoH-MMOs and CoH-LDHs a plot of R-value against stearic acid conversion to stearone is show in Figure 6.8 indicating that there is very little difference between the activity of the CoH-LDHs and CoH-MMOs. The values reported here use the figures obtained from the stearone calibration curve, whereas the extraction process incorporates further error onto this evaluation, so the performance of all the active CoH-LDHs and CoH-MMOs are assumed to be the same within this error. The CoH-LDHs all contain an $Mg(OH)_2$ co-phase of varying degrees, (see Chapter 3, Figure 3.8 for PXRD patterns of the prepared LDHs), which are still present in the calcined CoH-MMOs as MgO, but are overlapped with the broader MgO-like MMO peaks (see Chapter 3, Figure 3.14 for PXRD patterns of the prepared MMOs). As MgO was activated by calcination for ketonic decarboxylation catalysis, the MgO co-phases would be expected to behave analogously, however no further enhancement (or hindrance) of the reaction is observed over that of the CoH-LDHs, and it is possible the MgO accounts for the slightly higher conversion in the CoH-MMO than the CoP-MMO.

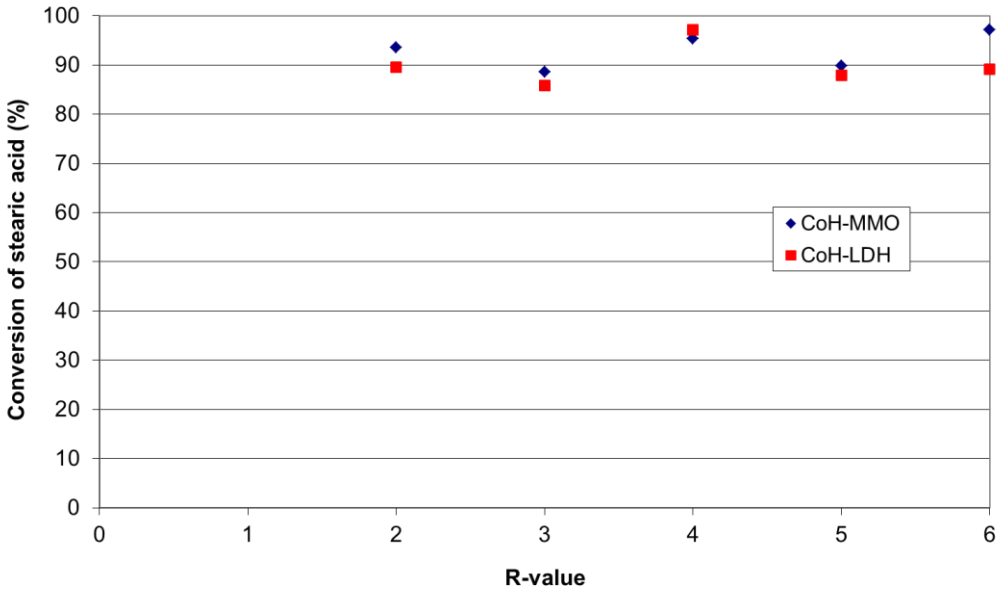

Figure 6.8 Conversion of stearic acid *vs.* R-value for the catalysts CoH-MMO2 to CoH-MMO6 and CoH-LDH2 to CoH-LDH6.

A plot for average pore size against conversion of stearic acid to stearone (Figure 6.9) shows that the average pore size is smaller for the MMOs, as expected, but the extent of catalysis is very similar. Compared to the LDHs (Chapter 5), there is less correlation evident for the MMOs with respect to average pore size and conversion of stearic acid. The much larger surface areas attributed to the CoH-MMOs (153-231 m^2/g) do not affect the degree of catalysis in comparison to the CoH-LDHs (33-46 m^2/g).). This suggests for the given batch reaction time, the reactions are not limited by diffusion of the reactant molecules to surfaces, though a time series analysis of products would be required to establish whether there are any kinetic constraints on the reactions.

From Figure 6.8 it is evident that the CoH-LDHs and CoH-MMOs led to comparable conversions of stearic acid to stearone (~ 89-97 %) and this may be because, as described in Section 6.3.1.4, the MMOs partially reconstruct to an LDH within the reaction vessel under the conditions used, owing to production of water in the reaction. If the need for pre-calcination is not required to produce an active catalyst for the ketonic decarboxylation of FFAs, then this will be of economic benefit to the process.

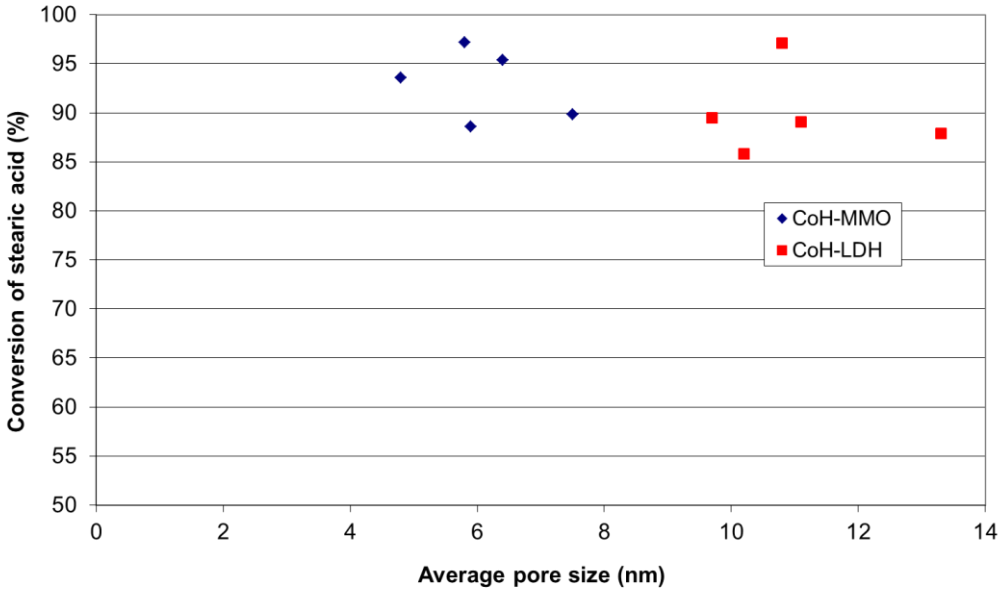

Figure 6.9 Conversion of stearic acid *vs.* average pore size for the catalysts CoH-MMO2 to CoH-MMO6 and CoH-LDH2 to CoH-LDH6.

6.3.2.4 Mechanistic insights from co-hydrated mixed metal oxide catalysed decarboxylation reactions

The CoH-MMOs behave very similarly to the CoH-LDHs suggesting that when the reaction is underway, both sets of materials undergo a transformation into a partially hydroxylated MMO with weak-medium strength basic sites. The ketonic decarboxylation reaction requires the presence of a base, since acidic calcined Al_2O_3 does not convert any of the reactant under the same reaction conditions (250 °C, 17 bar, 24 h).

In the present work, similar to results attained by Zhang *et al*., over 80 % conversion of acid was observed at 250 °C.[99] Zhang *et al*., attributed the reaction of MgO to be due to the adsorption of the carboxylate molecules, which then react in a six-membered transition state to form a ketone (Section 5.1.2.3). Other studies in the literature have suggested that ketonic decarboxylation possibly occurs *via* a beta keto-acid intermediate (*vide infra*).

From the data obtained here for the CoH-MMOs, target R-value and average pore size do not correlate with any observed effects relating to catalysis in comparison to the LDHs studied in Chapter 5.

6.3.3 Comparison of co-precipitated and co-hydrated mixed metal oxide catalysts

In the following sections, relative reactivity of the mixed metal oxides prepared *via* calcination of co-precipitated and co-hydrated LDH precursors for ketonic decarboxylation of stearic acid will be described, and the reasons for any differences discussed.

6.3.3.1 Effect of R-value for the mixed metal oxide catalysis reactions

A plot of R-value against stearic acid conversion to stearone is show in Figure 6.10. For the active catalysts (R = 2 – 6), generally, it seemed that the CoH-MMOs yielded a higher conversion of stearic acid to stearone than the CoP-MMOs, however this difference may well fall within the range of assessed errors in the extraction process (Section 5.2.5). All the materials (excepting R =1) showed conversion of stearic acid as being above 80 %, suggesting they behave similarly under these reaction conditions.

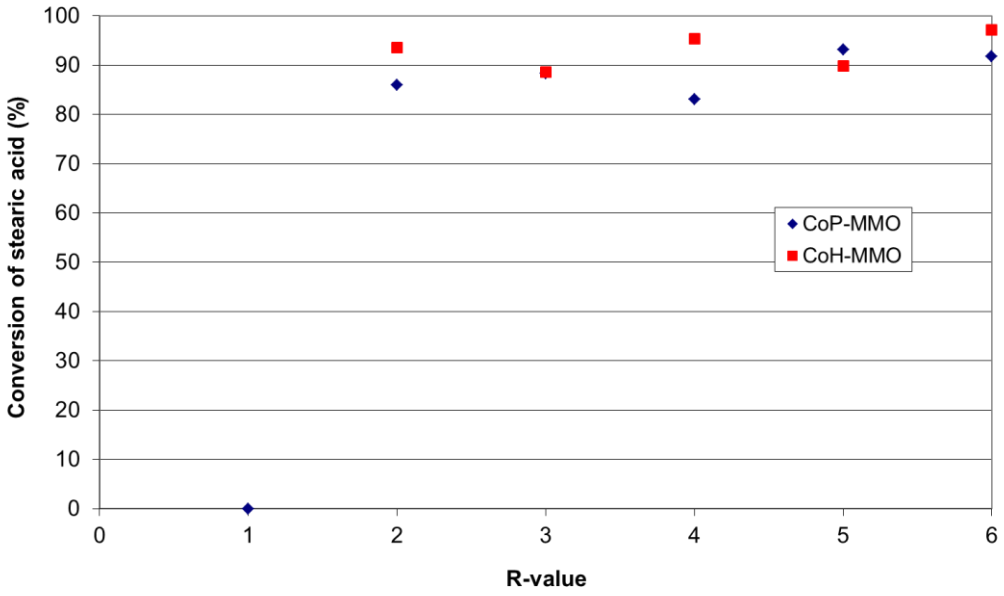

Figure 6.10 Conversion of stearic acid *vs.* R-value for the catalysts CoP-MMO1 to CoP-MMO6 and CoH-MMO2 to CoH-MMO6.

6.3.3.2 Effect of average pore size for the mixed metal oxides

The average pore sizes for the CoH-MMOs, along with their conversions of stearic acid to stearone, are shown in Figure 6.11.

For the active MMO catalysts, the CoH-MMOs have a smaller average pore size range than the CoP-MMOs, with conversion of stearic acid to stearone possibly decreasing with increasing average pore size, though this is a very weak trend and lies within the error of the extraction process (Section 5.2.5). Hence average pore size does appear to be affecting the reaction for the MMOs.

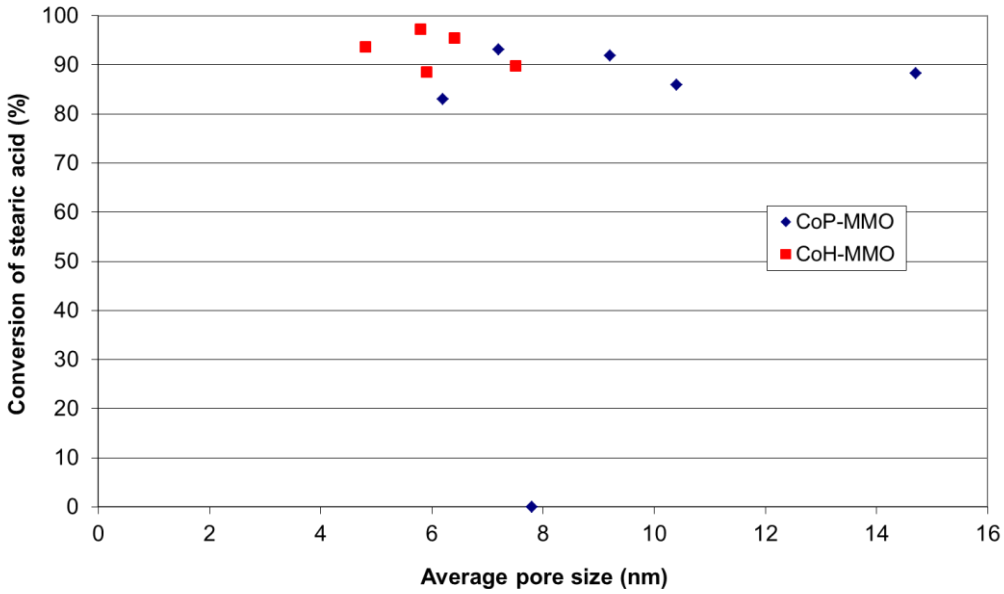

Figure 6.11 Conversion of stearic acid *vs.* Average pore size for the catalysts CoP-MMO1 to CoP-MMO6 and CoH-MMO2 to CoH-MMO6.

6.3.3.3 Mechanistic insights from co-precipitated and co-hydrated mixed metal oxide catalysed decarboxylation reactions

The CoP-MMOs behave very similarly to the CoH-MMOs, with similar degrees of conversion, suggesting either that the ketonic decarboxylation reaction does not have a strong dependency on the synthetic method or differences within the composition, pore structure or surface area of the MMOs. Neither the R-value nor average pore size can explain any observed effects relating to

catalysis, with the basicity of all MMOs being sufficient to catalyse the conversion of stearic acid to stearone. CoP-MMO1 with its inherent acidity does not lead to catalysis.

The CoH-MMOs were noted to have very sharp peaks corresponding to MgO co-phases, resulting from their CoH-LDH precursor materials, which were not observed to lead to any strong effects on the degree of conversion of stearic acid, as measured by GC. These sharp peaks are overlapped with the much broader MgO-like peak attributed to the decomposition of the LDH structures. However, the CoP-MMOs with their broad MgO-like peaks are equally as active (within experimental error) as the CoH-MMOs, for the catalysis of stearic acid to stearone.

Previous studies have shown that ketonic decarboxylation has occurred with MgO catalysts at 250 °C, through an adsorption mechanism with a six-membered transition state.[99] Neunhoeffer and Paschke were the first to suggest the ketonic decarboxylation mechanism occurs through the abstraction of an α-proton and a β-keto acid intermediate (Figure 6.12)[271] and this mechanism has since been confirmed using DFT studies.[265] Further to this Pham et al. have proposed that Lewis acid and Brønsted basic sites are required for ketonic decarboxylation on oxides.[263] The Brønsted base sites are required to dissociate carboxylic acids, producing carboxylates and abstract the α-proton. Lewis acidic sites then stabilise and activate a second carboxylic acid group which then leads to the coupling reaction. With both Lewis acid and basic sites being present in MMOs,[266] the ketonic decarboxylation observed here is likely to proceed through a similar mechanism.

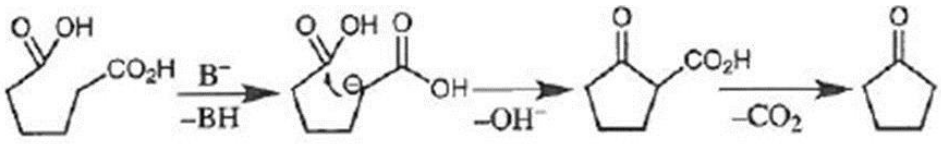

Figure 6.12 Ketonic decarboxylation reaction mechanism for the dicarboxylic acid, adipic acid, proposed by Neunhoeffer and Paschke involving a beta-keto acid. Taken from Pulido *et al.*[265]

6.4 Conclusions and summary

Stearic acid was not found to convert to *n*-heptadecane *via* direct decarboxylation at 250 °C and 17 bar with either CoP-MMOs or CoH-MMOs, but, similarly to their precursor LDHs, stearic acid

underwent ketonic decarboxylation, where two molecules of stearic acid lead to one molecule of stearone, water and CO_2, respectively, with > 80% yields after 24 h. This is an important reaction for bio-based materials, since the long chain ketones from FFAs may be used in lubricants, diesel fuels, surfactant precursors,[108] or they can be further upgraded into hydrocarbons and hydroxyalkylenes by cracking/hydrotreatment.

In conclusion, the main findings of this study on catalysis by the MMO material were:

- CoH-MMO2 (93.6 %), CoH-MMO4 (95.4 %) and CoH-MMO6 (97.2 %) gave the highest conversions of stearic acid to stearone for the MMOs, suggesting that co-hydration is the preferred synthesis method for MMO catalysts in this reaction.
- For the active MMO catalysts, average pore size, surface area and R-value were not observed to have any influence on activity, with all MMOs exhibiting sufficient basicity for the reaction to occur. Though the involvement of Lewis acid sites may be required for a β-keto acid intermediate reaction mechanism.[263]
- The CoH-MMOs and CoH-LDHs behave very similarly to one another as catalysts, as do CoP-MMOs and CoP-LDHs of R-value 5 and 6. This suggests that the catalysts are alike and that the LDHs may be partially calcined *in situ* at the 250 °C reaction temperature to form a partially hydrated MMO type structure, while the MMOs being partially reconstructed *in situ* to an LDH as the reaction proceeds, due to CO_2 and water being produced. The structural properties such as porosity, surface area and basicity will be modified, with the catalytic reaction occurring at basal and edge surfaces,[115, 272] external of the interlayer, *via* weak-medium basic OH^- and Mg-O^{2-} groups.
- The requirement of costly and energetic activations can be eliminated with the LDHs being nearly as effective at catalysis as the MMOs, over the 24 h reaction and under batch conditions, enhancing the green principles of the process.[273]
- MgO co-phases within the CoH-MMOs do not affect the degree of catalysis.

- Calcined Al_2O_3 exhibited no conversion of stearic acid, due to its acidic nature. Similarly, COH-MMO1 being an alumina compound and CoP-MMO1 being of high acidity, these too led to zero conversion.
- Calcined MgO led to 90 % conversion of stearic acid to stearone, whereas with uncalcined MgO only 0.5 % of stearic acid was converted to stearone. Thus it was proposed that the conversion with calcined MgO may be attributable to weakly basic OH^- groups created on the catalyst surface during activation.[269] Calcined MgO may be preferentially employed over the LDHs and MMOs studied here as a catalyst for the ketonic decarboxylation reaction since this material does not require a detailed preparative method.

7 Thesis summary

7.1 Introduction

The foundations of this thesis are in the upgrading of present day sustainably grown biomass into products that can replace those derived from fossil crude oil with it's associated release of entrapped carbon. Fossil-supplies will inevitably eventually expire,[4] but there is also a pressing need to recycle CO_2 in the Earths atmosphere rather than release it from a permanent energy store, a process driven by climate change policies.[18] Currently the major commercial use of biomass as a replacement for fossil-derived products is in the production of biofuels such as ethanol from sugars and biodiesel from triglycerides.[212] Recently, there has been interest in other, less studied. higher value materials being developed from biomass,[274, 275] and the concept of a biorefinery, where a whole range of products can be produced from the bioresource has become increasingly topical.[275]

Free fatty acids (FFAs) are a component of the lipid fraction found in biomass and can be directly obtained from the hydrolysis of triglycerides found in vegetable and algal oils. In this thesis the upgrading of FFAs to bio-products in the form of ketones has been studied using, initially, a supported transition metal catalyst, and subsequently with layered hydroxide materials and their calcined derivatives as catalysts.

7.2 Synthesis of layered double hydroxides and mixed metal oxides

7.2.1 Layered double hydroxides

Layered double hydroxides (LDHs) were synthesised *via* two methods, the previously extensively used co-precipitation (CoP) method and a more recently developed co-hydration (CoH) method. Co-precipitation is the most commonly encountered method for synthesising LDHs where a supersaturated solution of the appropriate metal salts is precipitated in the presence of a base such as $NaHCO_3$.[135] The use of an alkali-metal containing base to maintain the high pH necessary for the

LDH to precipitate can lead to the alkali-metal being entrained in the final product, influencing analytic and catalytic testing,[81] though attempts can be made to remove this through profuse washing with hot deionised water. Copious amounts of high pH supernatant, requiring disposal, are produced in co-precipitation through the use of these alkali-metal containing bases in the process, and this presents a good case to develop new synthetic approaches for these materials. As such, an alternative, co-hydration synthesis method, developed by Greenwell *et al*.,[123] utilises metal oxides and organic acids, which co-hydrate in solution to produce LDHs, without the need for additional base. This enhanced environmentally-friendly method of producing LDHs is preferred over the co-precipitation route according to the twelve principles of green chemisty.[273]

Within this thesis, both co-precipitated and co-hydrated LDHs have been synthesised, as described in Chapter 3, and characterised according to the analysis procedures described in Chapter 2. Powder X-ray diffraction (PXRD) was used to confirm the synthesis of LDH structures, with the CoP-LDHs being mainly single phase and the CoH-LDHs having co-phases attributed to brucite and crystalline MgO. The average crystal sizes were slightly greater for CoH-LDHs in the *a* direction and slightly greater for CoP-LDHs in the *c* direction (168-255 nm *c.f.* 289-387 in the *a* direction, 114-221 nm *c.f.* 102-189 in the *c* direction, respectively), showing only slight differences due to preparation method. ICP-OES was used to determine the bulk Mg:Al ratios, which were generally in line with target ratios of 2-6.

The CoP-LDHs had, in the main, a higher surface area (17-115 m^2/g *c.f.* 32-90 m^2/g), average pore size (3.1-22.3 nm *c.f.* 8.5-13.3 nm), pore volume (0.17-0.42 cm^3/g *c.f.* 0.05-0.20 cm^3/g) and Hammett basicity (7.6-9.0, 9.0-10.0 *c.f.* 6.0-7.6, 7.6-9.0) than the CoH-LDHs, though for both sets of LDH materials, basicity increased with R-value. CoH-LDH1 was found to be an alumina compound, being challenging to synthesise, according to the cation avoidance rule,[169] since it requires adjacent co-located Al^{3+}. However, this may also be a consequence of the alumina grade used in this study being of a larger particle size and requiring a longer hydration time to that used by Greenwell *et al.,* who successfully synthesised LDHs approaching R-value 1.[123]

7.2.2 Mixed metal oxides

Both co-precipitated and co-hydrated MMOs have been synthesised and characterised in Chapter 3. Upon calcination to 500 °C, in a non-inert atmosphere for 3 hours, the parent LDH structures break down through the loss of surface water, interlayer water, interlayer anions and dehydroxylation of the layers, as shown by the thermogravimetric analysis described in Section 3.4. This leads to a mixed metal oxide (MMO) with small crystallites and high lattice strain, consisting of medium-strong Lewis basic O^{2-}-M^{n+} pairs, OH^- weakly basic groups and strong basic sites relating to secluded O^{2-} ions,[122] along with Lewis acidity due to incorporated Al^{3+}. Post-calcination, the characteristic LDH reflections are lost in the PXRD pattern spectra and, instead, broad MgO-like reflections are observed (see Figure 3.12 and Figure 3.14). The CoH-MMOs also contained an overlapping sharp MgO peak resulting from the MgO co-phase and decomposition of the $Mg(OH)_2$ co-phase present in the CoH-LDH precursors.

For both the CoP-MMOs and CoH-MMOs there was a 2-8 fold increase in specific surface area from the parent LDHs (153-231 m^2/g *c.f.* 17-115 m^2/g). CoP-MMO4 to CoP-MMO6 and all the CoH-MMOs decreased in average pore volume upon calcination of their LDH precursors, however CoP-MMO1 to CoP-MMO3 saw an increase in average pore size. The Hammett basicity increased upon calcination of parent-LDHs for CoH-MMO1 to CoH-MMO4, however decreased for CoP-MMO2 and CoP-MMO6 (possibly due to accessibility of basic sites), with all other MMOs remaining unchanged. The importance of avoiding MMO exposure to humidity and atmospheric conditions was further illustrated when three sequential thermogravimetric analyses were performed, illustrating the reconstruction of the MMO to a meixnerite-type structure within a short time period.[211]

7.3 Synthesis of n-heptadecane via decarboxylation reactions involving Pd/C

FFAs have been demonstrated in the literature to undergo decarboxylation reactions whereby they lose CO_2 and form straight-chain hydrocarbon molecules that can be used as direct fossil replacements.[96] In a representative study, 5 % Pd/C, activated with H_2, was employed under an inert atmosphere for the conversion of stearic acid to *n*-heptadecane at 300 °C.[2] As a comparator to the work on the LDH and MMO catalyst systems, this reaction was adapted and carried out here at lower reaction temperature, however the 5 % Pd/C was not activated by being reduced using $H_{2(g)}$ as the industrial partner involved in this study was seeking alternative upgrading methods avoiding the use of $H_{2(g)}$. Stearic acid was decarboxylated to *n*-heptadecane using this catalyst, however the reaction was not found to be as favourable at 230 °C (58 % conversion of stearic acid to *n*-heptadecane in 24 hours) and the Pd/C was found to be unstable, possibly decomposing *in situ*.[250]

7.4 Ketonic decarboxylation reactions of layered double hydroxides and mixed metal oxides

Following on from the decarboxylation experiments using 5 % Pd/C a series of similar catalysed reactions were undertaken at 250 °C, but now using mineral based catalysts. The rationale for this was to increase stability of the catalyst during the reaction, a failing of the supported Pd system trialled, and also reduce the cost associated with using a precious metal catalyst. Inspired by the work of Zhang *et al*.,[232] where simple metal oxides were used to reduce the total acid number (TAN) in crude oils through decarboxylation reactions, the use of Mg/Al LDH and MMO mineral based materials was explored. The prepared catalysts were co-precipitated LDHs (CoP-LDHs), co-hydrated (CoH-LDHs), and their corresponding mixed metal oxides (i.e. CoP-MMOs and CoH-MMOs), as well as calcined and uncalcined Al_2O_3 and MgO as the end members of the Mg/Al LDH series, and a control reaction with no mineral phase present. Initial studies were carried out to

examine catalysis of the decarboxylation reaction trialled with the Pd/C system, however no decarboxylated product formed, despite conversion of the stearic acid reactant being observed. Instead, a waxy product was produced, similar to other studies in the literature which attributed this, without full analysis, to be a saponified product.[262] A great deal of time was expended in developing a suitable extraction and analysis process to separate the resulting waxy solid residue from the catalyst, to yield reactant and products for analysis. As such, ketonic decarboxylation was found to occur in these reactions, **(13)**, converting stearic acid to stearone, carbon dioxide and water in presence of a catalyst, creating high value ketones.

$$2\ C_{17}H_{35}COOH_{(s)} \xrightarrow[250\ °C,\ 17\ bar,\ 24\ h]{Catalyst} C_{17}H_{35}COC_{17}H_{35(s)} + CO_{2(g)} + H_2O_{(l)} \quad \textbf{(13)}$$

7.4.1 Catalysis using layered double hydroxides

No reaction occurred for either CoP-LDH1 or CoH-LDH1, which was ascribed to the relatively acidic nature of the materials, as Al_2O_3 rich phases were formed rather than LDH phases. CoP-LDH3 to CoP-LDH6 all had greater conversions of stearic acid to stearone (88.4 - 96.8 %) than CoP-LDH2 (65.2 %), with the former materials being more basic in character and having larger average pore sizes. Similarly the CoH-LDHs all led to 85.8 – 97.1 % conversion of stearic acid to stearone, having greater average pore sizes than CoP-LDH2, suggesting average pore size may affect the degree of catalysis with these bulky reactant and product molecules, though the inherent errors associated with analysis must be taken into consideration. Ketonic decarboxylation has previously been shown to involve Lewis acid and Brønsted basic sites on metal oxides,[263] with a possible similar mechanism occurring here involving abstraction of an α-proton and a β–keto acid intermediate. Thus average pore size may be inhibiting the alignment of the required activated adjacent carboxylic acid molecule for a surface mediated process involving weak-medium basic

OH^- sites. The activity of the CoH-LDHs was also found to follow a trend with the height of the peak in the PXRD spectra corresponding to an MgO co-phase, suggesting this may have increased catalytic reactivity, though this may be an artificial artefact within the errors involved in the extraction and analysis process. R-value 4 was found to give the highest catalytic activity for both CoP- and CoH-LDHs, with little difference being attributed to whether the more sustainable co-hydration- or the traditional co-precipitation- synthesis method was employed.

7.4.2 Catalysis using mixed metal oxides

The highest three conversions of stearic acid to stearone were for CoH-MMO2 (93.6 %), CoH-MMO4 (95.4 %) and CoH-MMO6 (97.2 %), suggesting CoH-MMOs are more active for this reaction. However these values are all within error of each other when taking into consideration the margins involved with the product extraction process. Despite the MMOs having lower average pore sizes than the LDHs, this did not hinder the reaction in a similar manner to that observed for the LDHs. CoP-MMO1, similar to its uncalcined precursor did not convert stearic acid, due to its large inherent acidity. CoH-MMO1 was also determined to be an aluminium oxide rich phase, and analogously yielded zero conversion.

When the catalysis of each was compared, the MMOs and LDHs studied here behave very similarly. This may be because the LDHs are partially calcined at 250 °C, within the reaction vessel, while the MMOs gradually reconstruct to an LDH as the reaction proceeds, due to the water and CO_2 formed from ketonic decarboxylation. Thus the presence of dual acid-base sites on these structurally similar catalyst surfaces may lead to ketonic decarboxylation through a β–keto acid mechanism or six-membered transition state as proposed in the literature.[99, 265]

7.4.3 Insight gained through control reactions

No observable conversion occurred for the thermal reaction at 250 °C, which is in line with literature studies.[96] With both calcined and uncalcined Al_2O_3 no reaction occurred, assumed due to

the acidic nature of the catalysts. Uncalcined MgO yielded 0.5 % conversion of stearic acid to stearone, with possibly surface magnesium stearate being formed instead, blocking catalytic sites, whereas calcined MgO led to 90 % conversion. It has been proposed that the enhanced conversion with calcined MgO may be owing to the creation of weakly basic surface OH^- groups during activation.[269] Similar yields of acid conversion through ketonic decarboxylation using 20 wt% MgO at 250 °C have been observed previously.[99] As calcined MgO was found to be an effective catalyst for the ketonic decarboxylation reaction itself then this material may be preferentially employed over the LDHs and MMOs studied here due to it not requiring a multi-step preparative method.

7.5 Summary of mixed metal oxide and layered double hydroxide catalysts tested for deoxygenation reactions

In this study a range of heterogeneous hydroxide and oxide catalysts have been examined for the ketonic decarboxylation of free fatty acids to high value ketones. In the scientific literature, oxides have been studied frequently,[99, 109, 265] but hydroxides less so.[115, 116, 262] With this being a process producing sustainable ketones, as suitable replacements for fossil-derived sources, it is important to also use a process for the method of manufacture which is inherently sustainable.

In the present study, very little difference could be attributed to the activity of the catalysts synthesised using the methods of co-precipitation and co-hydration (despite their MgO co-phases), however the best CoP-MMOs were lower performing than the best CoP-LDH, CoH-LDH and CoH-MMOs. With the co-hydration method being a more environmentally friendly procedure, avoiding the production of highly basic supernatants,[123] this synthesis method would be preferred to enhance the sustainability of the overall process, without the need for economically and energetically undesirable calcinations.

With calcination comes the requirement for minimising exposure to air to prevent the subsequent regeneration to an LDH precursor. However, it has been shown that uncalcined LDHs are as effective as MMOs and this present study suggests the actual catalysis is performed by an

LDH-MMO intermediate at 250 °C. CoH-LDH4 was the most effective co-hydrated LDH catalyst with a conversion to stearone of 97.1 %, and for future commercial application possibilities this catalyst should be further studied. If this catalyst requires regeneration by calcination to produce CoH-MMO4 then this gives a comparable conversion to stearone (95.4 %).

Interestingly, MgO is activated by calcination, leading to a significantly higher conversion of stearic acid to stearone, compared to the uncalcined precursor. From this it might be expected that the MMOs, with their inherently high Mg content would behave more analogously to the MgO phase, which, as discussed is known to be active in these reactions. In comparison, the $Mg(OH)_2$ phase was found to be inactive for the ketonic decarboxylation reaction, while the uncalcined LDH materials were active, indicating that the interlayer anions and bound water of the LDH may play a potential role in the catalysis, since these would not be present in the $Mg(OH)_2$. Furthermore, if the catalyst activation step can be omitted and LDHs utilised, rather than MMOs, then this will be of economic and energetic benefit to commercial processes.

7.6 Further work

There are a number of areas from the work presented in this thesis, which raise questions for further study. Following the research carried out here, a MSc research project was developed and assisted with, looking into the optimisation of time, temperature and reaction pressure for ketonic decarboxylation using LDHs/MMOs, but employing a shorter chain FFA, decanoic acid. The use of stearic acid was challenging in this present study, due to it's ketonic decarboxylation product having a high molecular weight, leading to a complex extraction procedure, combined with the GC analysis, and so other model compounds may be more tractable. However the aspects of catalysis may vary with acid chain length due to the possible effect of average pore size observed with the LDHs studied here. Furthermore, stearic acid is the second most abundant acid in nature, below that of palmitic acid,[52] so its study is of high relevance as a model compound.

Future studies into the re-usability of the catalysts investigated here, as well as their stability, are of importance. After numerous experiments, calcinations may be required to regenerate the

catalyst, however the corresponding MMOs have been found to be just as effective in ketonic decarboxylation catalysis, so the recycling of catalysts should be straightforward. Based on a cost and energy analysis, it may be deemed more suitable to re-synthesise further LDH material, though disposal of used resources must be a last resort. However, this should also be studied in comparison to the control reaction involving calcined MgO, since this catalyst does not require any multi-step preparations other than calcination.

The composition of the used catalyst requires further study to determine its properties before, during and after calcination. It was noted that the LDH materials potentially catalyse the conversion of stearic acid through involvement of their interlayer anions and intercalated water, hence studies of various LDH compositions can be studied to determine and confirm this effect and the properties influencing this phenomenon. The use of hydrocarbon solvents in this process is undesirable, even though they are recoverable, unless they can be provided through decarboxylation of biomass, creating an integrated sustainable route. As an alternative, studies can be undertaken to identify if the FFAs alone can be used in catalysis reactions with LDHs and MMOs, enhancing the process through green chemical principles.[273]

Mixed feedstocks of biomass origin require study to determine the suitability of the catalysts employed here in true bio-based ketonic decarboxylation reactions. Klimkiewicz *et al*.,[110, 111] have used an interesting methodology to convert methyl esters found in rape oil to ketones, with metal oxide catalysts and sources of methanol, at 385-390 °C. Hence, the co-feeding of alcohols, along with FFAs, yields a further extension to this process whereby vegetable/algal oils may be upgraded to ketones directly, avoiding the use of additional *trans*-esterification and hydrolysis reactions.

7.7 Concluding remarks

A number of milestones have been achieved within this body of work:

- The reactions were the first to undertake fatty acid ketonic decarboxylation using MMO catalysts to produce high-value ketone bio-products;
- The LDH precursors were shown to be as effective at ketonic decarboxylation as the MMOs, eliminating the requirement of costly and energetic activations;
- Catalysts synthesised *via* a more environmentally-friendly co-hydration route are as effective as their co-precipitated counterparts, enhancing the green credibility of this process and ruling out homogenous catalysis by base used in the preparation.[273] The presence of MgO co-phases in CoH materials does not pose any issues with catalysis;
- The MMO catalysts behave akin to the calcined MgO material in the ketonic decarboxylation of stearic acid, whereas the catalytic reactions involving LDH catalysts potentially involve the interlayer anions and cations as they are far more effective than $Mg(OH)_2$.
- There is some indication of catalytic dependence on average pore size within the catalysts, resulting from the bulk size and required head alignment of the long-chain fatty acid molecules;
- Calcined MgO was found to be almost as effective at catalysis as the LDHs and MMOs, however having the advantage of it not requiring up-front preparative methods.
- These reactions have set a boundary for decarboxylation *vs.* ketonic decarboxylation pathways.

This study, along with many other emerging green technologies and chemical processes, allows us to consider pathways to selectively eliminate fossil-derived chemical feedstocks and processes,

replacing them with a more sustainable and integrated bio-based economy, until, for future generations dependency on fossil fuels will be dramatically reduced, if not eliminated altogether.

Appendix 1

PXRD indexing file for CoP-LDH2

Measurement Conditions: (Bookmark 1)

Dataset Name	PL2
File name	C:\Documents and Settings\dch3bs\My Documents\Chemistry\3rd Year\expts\Cambridge PXRD 2010\hcg21\PL2\PL2.rd
Comment	Configuration=Flat Bracket, Owner=cma35, Goniometer=PW3050/60 (Theta/2Theta); Min
Measurement Date / Time	10/11/2010 10:35:00
Raw Data Origin	PHILIPS-binary (scan) (.RD)
Scan Axis	Gonio
Start Position [°2Th.]	3.0084
End Position [°2Th.]	79.9504
Step Size [°2Th.]	0.0170
Scan Step Time [s]	23.9101
Scan Type	Continuous
Offset [°2Th.]	0.0000
Divergence Slit Type	Fixed
Divergence Slit Size [°]	0.5000
Specimen Length [mm]	10.00
Receiving Slit Size [mm]	12.7500
Measurement Temperature [°C]	-273.15
Anode Material	Cu
K-Alpha1 [Å]	1.54060
K-Alpha2 [Å]	1.54443
K-Beta [Å]	1.39225
K-A2 / K-A1 Ratio	0.50000
Generator Settings	40 mA, 40 kV
Diffractometer Type	XPert MPD
Diffractometer Number	1
Goniometer Radius [mm]	200.00
Dist. Focus-Diverg. Slit [mm]	91.00
Incident Beam Monochromator	No
Spinning	No

Main Graphics, Analyze View: (Bookmark 2)

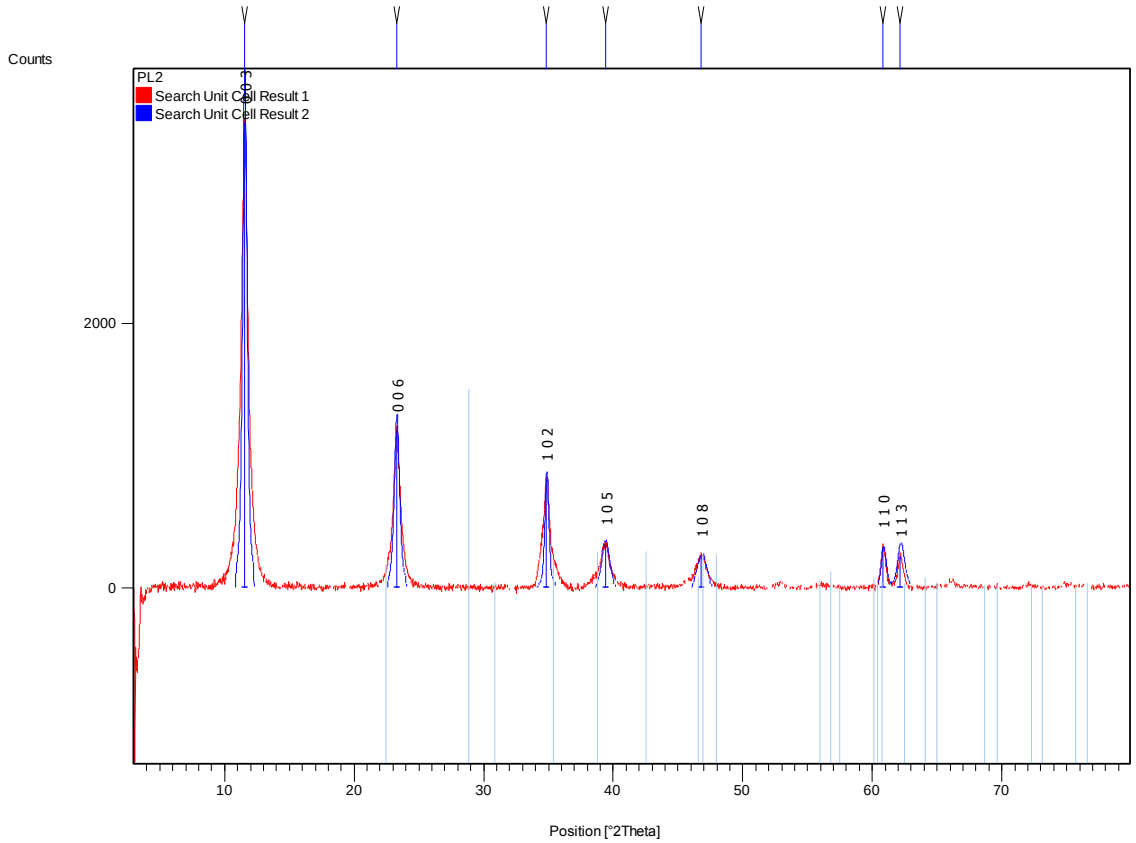

Peak List: (Bookmark 3)

Pos. [°2Th.]	Height [cts]	FWHM [°2Th.]	d-spacing [Å]	Rel. Int. [%]
11.5604	3522.96	0.4015	7.65485	100.00
23.2843	1186.72	0.4684	3.82033	33.69
34.8504	821.27	0.3346	2.57442	23.31
39.3769	326.86	0.6691	2.28829	9.28
46.8070	241.01	0.8029	1.94091	6.84
60.8320	309.52	0.4015	1.52276	8.79
62.1608	240.74	0.5712	1.49213	6.83

Pattern List: ***(Bookmark 4)***

Document History: (Bookmark 5)

Insert Measurement:
- File name = PL2.rd
- Modification time = "06/07/2013 19:03:29"
- Modification editor = "admin"

Interpolate Step Size:
- Step Size = "Derived"
- Modification time = "01/02/2006"
- Modification editor = "PANalytical"

Smooth:
- Type of smoothing = "Polynomial"
- Polynomial type = "Quintic"
- Convolution range = "7"

- Modification time = "19/05/2013 13:15:33"
- Modification editor = "admin"

Subtract Background:
- Correction method = "Automatic"
- Bending factor = "5"
- Use smoothed input data = "Yes"
- Granularity = "20"
- Add to net scan = "Nothing"
- Modification time = "18/06/2013 20:13:53"
- Modification editor = "admin"

Search Peaks:
- Minimum significance = "35.00"
- Minimum tip width = "0.01"
- Maximum tip width = "6.00"
- Peak base width = "7.00"
- Method = "Minimum 2nd derivative"
- Modification time = "06/07/2013 18:42:09"
- Modification editor = "admin"

Search & Match:
- Data source = "Profile and peak list"
- Restriction = "None"
- Scoring schema = "Multi phase"
- Auto residue = "Yes"
- Match intensity = "Yes"
- Demote unmatched strong = "Yes"
- Allow pattern shift = "Yes"
- Two theta shift = "0"
- Identify = "Yes"
- Max. no. of accepted patterns = "5"
- Minimum score = "50"
- Search depth = "10"
- Min. new lines / total lines = "60"
- Minimum new lines = "5"
- Minimum scale factor = "0.1"
- Modification time = "25/05/2013 16:14:40"
- Modification editor = "admin"

Cell Search:
- Indexing method = "McMaille"
- Calculation type = "Monte Carlo & Grid Search"
- Zero point = "0"
- Search cubic system = "False"
- Search hexagonal system = "True"
- Search tetragonal system = "False"
- Search orthorhombic system = "False"
- Search monoclinic system = "False"
- Search triclinic system = "False"
- Width of peaks = "-1"
- No. of unindexed lines = "6"
- Minimum cell parameter = "3"
- Maximum cell parameter = "25"
- Minimum cell volume = "200"
- Maximum cell volume = "1500"
- Minimum R profile = "0.1"

- Maximum R profile = "0.3"
- Grid search step cell parameter = "0.2"
- Grid search step cell angle = "0.2"
- No. of Monte Carlo tests = "20000"
- No. of Monte Carlo runs = "1"
- Search rhombohedral system = "True"
- Minimum cell a = "3"
- Maximum cell a = "15"
- Minimum cell b = "3"
- Maximum cell b = "15"
- Minimum cell c = "3"
- Maximum cell c = "15"
- Minimum cell alpha = "90"
- Maximum cell alpha = "90"
- Minimum cell beta = "90"
- Maximum cell beta = "90"
- Minimum cell gamma = "90"
- Maximum cell gamma = "90"
- Maximum R Refinement = "0.45"
- Modification time = "06/07/2013 19:04:22"
- Modification editor = "admin"

Cell Search:
- Indexing method = "Dicvol"
- Maximum beta = "130"
- Maximum axis = "25"
- Maximum volume = "1000"
- FOM better than = "12"
- Include monoclinic system = "False"
- Include triclinic system = "False"
- Test monoclinic super axis = "False"
- Minimum peak intensity = "0.1"
- Use first x peaks = "10"
- Modification time = "06/07/2013 19:05:25"
- Modification editor = "admin"

Unit Cell Refinement:
- No. of refined parameters = "2"
- Snyder's FOM = "11.4347400665283"
- Chi square = "3.0696162411914E-7"
- No. of not indexed lines = "0"
- No. of indexed lines = "7"
- H max. = "20"
- K max. = "20"
- L max. = "20"
- Use SVD = "True"
- Refinement mode = "Cell only"
- Weighting scheme = "Unit weights"
- Intensity min. = "0"
- 2Theta max. = "160"
- Delta 2Theta max. = "0.9"
- Use Included and Excluded = "False"
- Use only Single Indexed Lines = "False"
- Automatic Refinement = "True"
- Start with Cell = "True"
- Apply known offset = "False"
- Known offset = "0"

- Modification time = "06/07/2013 19:05:27"
- Modification editor = "admin"

Appendix 2

PXRD Indexing file for CoP-LDH4

Measurement Conditions: ***(Bookmark 1)***

Dataset Name	PL4
File name	C:\Documents and Settings\dch3bs\My Documents\Chemistry\3rd Year\expts\Cambridge PXRD 2010\hcg21\PL4\PL4.rd
Comment	Configuration=Flat Bracket, Owner=cma35, Goniometer=PW3050/60 (Theta/2Theta); Min
Measurement Date / Time	10/11/2010 12:14:00
Raw Data Origin	PHILIPS-binary (scan) (.RD)
Scan Axis	Gonio
Start Position [°2Th.]	3.0084
End Position [°2Th.]	79.9504
Step Size [°2Th.]	0.0170
Scan Step Time [s]	23.9101
Scan Type	Continuous
Offset [°2Th.]	0.0000
Divergence Slit Type	Fixed
Divergence Slit Size [°]	0.5000
Specimen Length [mm]	10.00
Receiving Slit Size [mm]	12.7500
Measurement Temperature [°C]	-273.15
Anode Material	Cu
K-Alpha1 [Å]	1.54060
K-Alpha2 [Å]	1.54443
K-Beta [Å]	1.39225
K-A2 / K-A1 Ratio	0.50000
Generator Settings	40 mA, 40 kV
Diffractometer Type	XPert MPD
Diffractometer Number	1
Goniometer Radius [mm]	200.00
Dist. Focus-Diverg. Slit [mm]	91.00
Incident Beam Monochromator	No
Spinning	No

Main Graphics, Analyze View: (Bookmark 2)

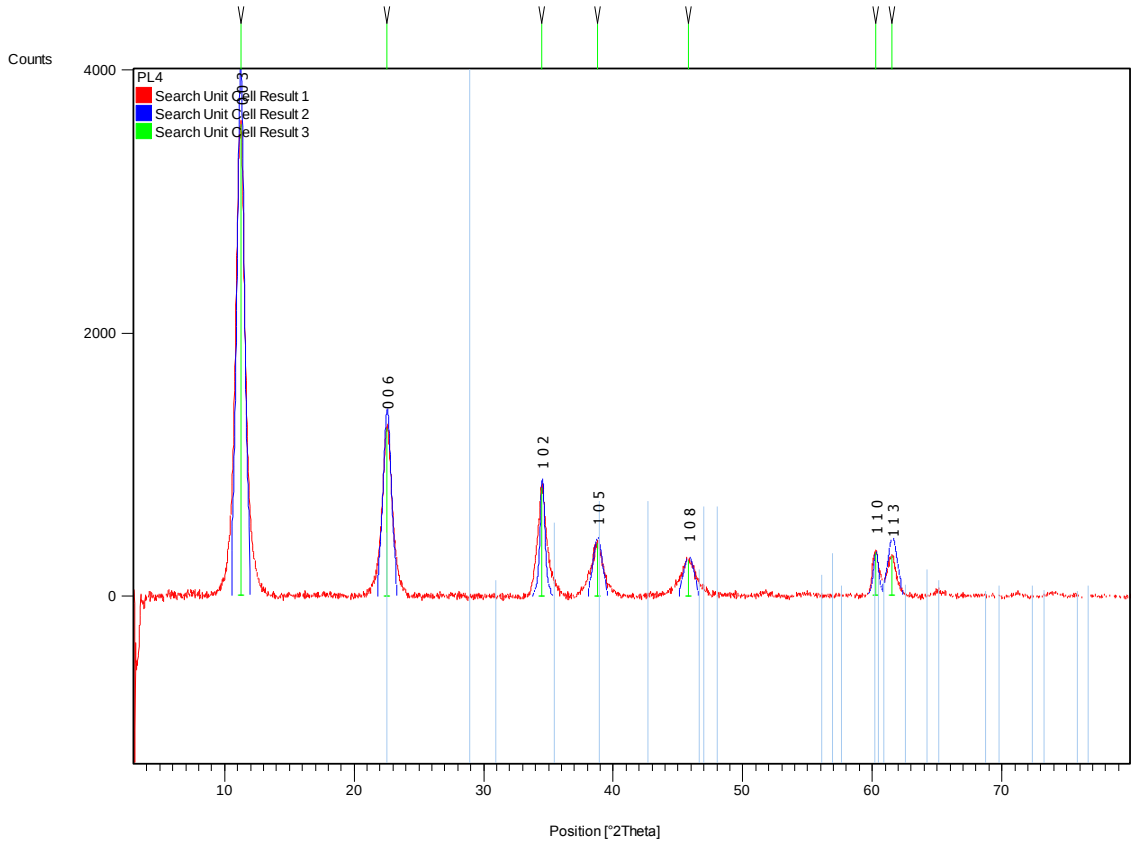

Peak List: (Bookmark 3)

Pos. [°2Th.]	Height [cts]	FWHM [°2Th.]	d-spacing [Å]	Rel. Int. [%]
11.2334	3584.38	0.6691	7.87695	100.00
22.5342	1277.33	0.7360	3.94577	35.64
34.5087	823.22	0.4015	2.59913	22.97
38.7633	401.67	0.8029	2.32309	11.21
45.7858	272.70	0.9368	1.98179	7.61
60.2310	332.03	0.4015	1.53651	9.26
61.4998	302.02	0.8160	1.50658	8.43

Pattern List: (Bookmark 4)

Document History: (Bookmark 5)

Insert Measurement:
- File name = PL4.rd
- Modification time = "06/07/2013 19:49:47"
- Modification editor = "admin"

Interpolate Step Size:
- Step Size = "Derived"
- Modification time = "01/02/2006"
- Modification editor = "PANalytical"

Smooth:
- Type of smoothing = "Polynomial"
- Polynomial type = "Quintic"
- Convolution range = "7"

- Modification time = "19/05/2013 13:15:33"
- Modification editor = "admin"

Subtract Background:
- Correction method = "Automatic"
- Bending factor = "5"
- Use smoothed input data = "Yes"
- Granularity = "20"
- Add to net scan = "Nothing"
- Modification time = "18/06/2013 20:13:53"
- Modification editor = "admin"

Search Peaks:
- Minimum significance = "35.00"
- Minimum tip width = "0.01"
- Maximum tip width = "6.00"
- Peak base width = "7.00"
- Method = "Minimum 2nd derivative"
- Modification time = "06/07/2013 18:42:09"
- Modification editor = "admin"

Search & Match:
- Data source = "Profile and peak list"
- Restriction = "None"
- Scoring schema = "Multi phase"
- Auto residue = "Yes"
- Match intensity = "Yes"
- Demote unmatched strong = "Yes"
- Allow pattern shift = "Yes"
- Two theta shift = "0"
- Identify = "Yes"
- Max. no. of accepted patterns = "5"
- Minimum score = "50"
- Search depth = "10"
- Min. new lines / total lines = "60"
- Minimum new lines = "5"
- Minimum scale factor = "0.1"
- Modification time = "25/05/2013 16:14:40"
- Modification editor = "admin"

Cell Search:
- Indexing method = "McMaille"
- Calculation type = "Monte Carlo & Grid Search"
- Zero point = "0"
- Search cubic system = "False"
- Search hexagonal system = "True"
- Search tetragonal system = "False"
- Search orthorhombic system = "False"
- Search monoclinic system = "False"
- Search triclinic system = "False"
- Width of peaks = "-1"
- No. of unindexed lines = "6"
- Minimum cell parameter = "3"
- Maximum cell parameter = "25"
- Minimum cell volume = "200"
- Maximum cell volume = "1500"
- Minimum R profile = "0.1"

- Maximum R profile = "0.3"
- Grid search step cell parameter = "0.2"
- Grid search step cell angle = "0.2"
- No. of Monte Carlo tests = "20000"
- No. of Monte Carlo runs = "1"
- Search rhombohedral system = "True"
- Minimum cell a = "3"
- Maximum cell a = "15"
- Minimum cell b = "3"
- Maximum cell b = "15"
- Minimum cell c = "3"
- Maximum cell c = "15"
- Minimum cell alpha = "90"
- Maximum cell alpha = "90"
- Minimum cell beta = "90"
- Maximum cell beta = "90"
- Minimum cell gamma = "90"
- Maximum cell gamma = "90"
- Maximum R Refinement = "0.45"
- Modification time = "06/07/2013 19:50:33"
- Modification editor = "admin"

Cell Search:
- Indexing method = "Dicvol"
- Maximum beta = "130"
- Maximum axis = "25"
- Maximum volume = "1000"
- FOM better than = "12"
- Include monoclinic system = "False"
- Include triclinic system = "False"
- Test monoclinic super axis = "False"
- Minimum peak intensity = "0.1"
- Use first x peaks = "10"
- Modification time = "06/07/2013 19:51:54"
- Modification editor = "admin"

Cell Search:
- Indexing method = "Dicvol04"
- Maximum beta = "130"
- Maximum axis = "25"
- Maximum volume = "1000"
- FOM better than = "12"
- Include monoclinic system = "False"
- Include triclinic system = "False"
- Test monoclinic super axis = "False"
- Minimum peak intensity = "0.1"
- Use first x peaks = "10"
- Modification time = "06/07/2013 19:53:17"
- Modification editor = "admin"

Unit Cell Refinement:
- No. of refined parameters = "2"
- Snyder's FOM = "7.15330982208252"
- Chi square = "3.85639424393958E-7"
- No. of not indexed lines = "0"
- No. of indexed lines = "7"
- H max. = "20"

- K max. = "20"
- L max. = "20"
- Use SVD = "True"
- Refinement mode = "Cell only"
- Weighting scheme = "Unit weights"
- Intensity min. = "0"
- 2Theta max. = "160"
- Delta 2Theta max. = "0.9"
- Use Included and Excluded = "False"
- Use only Single Indexed Lines = "False"
- Automatic Refinement = "True"
- Start with Cell = "True"
- Apply known offset = "False"
- Known offset = "0"
- Modification time = "06/07/2013 19:53:25"
- Modification editor = "admin"

Bibliography

1. Boultif, A., History of the dichotomy method for powder pattern indexing. *Powder Diffraction* **2005,** *20* (4), 284-287.
2. Kubickova, I.; Snare, M.; Eranen, K.; Maki-Arvela, P.; Murzin, D. Y., Hydrocarbons for diesel fuel via decarboxylation of vegetable oils. *Catalysis Today* **2005,** *106* (1-4), 197-200.
3. Terry, M. World has enough oil reserves, says BP boss. http://www.theguardian.com/business/2008/jun/11/commodities.bp (accessed 25/11/2013).
4. BP *BP Statistical Review of World Energy June 2012*; bp.com/statisticalreview, 2012; p 45.
5. Berry, D. A., Engineering organisms for industrial fuel production. *Bioengineered bugs* **2010,** *1* (5), 303-308.
6. Gonzalez, M. A.; Smith, R. L., A methodology to evaluate process sustainability. *Environmental Progress* **2003,** *22* (4), 269-276; Ohtake, H.; Yamashita, S.; Kato, J., Development of a new biotechnological basis for improving industrial sustainability in Japan. *Engineering in Life Sciences* **2006,** *6* (3), 278-284; Jayal, A. D.; Balaji, A. K.; Asme, On a process modeling framework for sustainable manufacturing: A machining perspective. *Proceedings of the Asme International Mechanical Engineering Congress and Exposition 2007, Vol 15: Sustainable Products and Processes* **2008**, 301-307.
7. Alvarez-Chavez, C. R.; Edwards, S.; Moure-Eraso, R.; Geiser, K., Sustainability of bio-based plastics: general comparative analysis and recommendations for improvement. *Journal of Cleaner Production* **2012,** *23* (1), 47-56.
8. Evans, J., Sustaining biofuels. *Biofuels Bioproducts & Biorefining-Biofpr* **2009,** *3* (6), 581-583.
9. Worldwatch Institute., *Biofuels for transport : global potential and implications for energy and agriculture*. Earthscan: London, 2007; p xxviii, 452 p.
10. Finlay, M. R., Old efforts at new uses: A brief history of chemurgy and the American search for biobased materials. *Journal of Industrial Ecology* **2003,** *7* (3-4).
11. Allen, M. R.; Frame, D. J.; Huntingford, C.; Jones, C. D.; Lowe, J. A.; Meinshausen, M.; Meinshausen, N., Warming caused by cumulative carbon emissions towards the trillionth tonne. *Nature* **2009,** *458* (7242); Cao, L.; Bala, G.; Caldeira, K.; Nemani, R.; Ban-Weiss, G., Importance of carbon dioxide physiological forcing to future climate change. *Proceedings of the National Academy of Sciences of the United States of America* **2010,** *107* (21).
12. Shein, K. A.; Waple, A. M.; Menne, M. J.; Christy, J. C.; Levinson, D. H.; Lawrimore, J. H.; Wuertz, D. B.; Xie, P.; Janowiak, J. E.; Robinson, D. A.; Schnell, R. C.; Elkins, J. W.; Dutton, G. S.; Levy, J. M.; Reynolds, R. W.; Johnson, G. C.; Lyman, J. M.; Willis, J. K.; Yu, L.; Weller, R. A.; Lumpkin, R.; Goni, G.; Baringer, M. O.; Meinen, C. S.; Merrifield, M. A.; Gill, S.; Mitchum, G. T.; Sabine, C. L.; Feely, R. A.; Wanninkhof, R.; Diamond, H. J.; Bell, G. D.; Halpert, M. S.; McPhaden, M. J.; Blake, E.; Mo, K. C.; Landsea, C. W.; Pasch, R.; Chelliah, M.; Goldenberg, S. B.; Bourassa, M. A.; Smith, S. R.; Hughes, P.; Rolph, J.; Camargo, S. J.; Gleason, K. L.; Salinger, M. J.; Watkins, A. B.; Burgess, S. M.; Richter-Menge, J.; Overland, J.; Proshutinsky, A.; Romanovsky, V.; Gascard, J. C.; Karcher, M.; Maslanik, J.; Perovich, D.; Shiklomanov, A.; Walker, D.; Box, J. E.; Oludhe, C.; Ambenje, P.; Ogallo, L.; Kabidi, K.; Thiaw, W. M.; Gill, T.; Landman, W. A.; Kocot, C.; Phillips, D.; Whitewood, R.; Vazquez, M. O.; Grover-Kopec, E. K.; Rusticuci, M.; Camacho, J. L.; Pabon, J. D.; Marengo, J. A.; Martinez, R.; Bidegain, M.; Bulygina, O. N.; Korshunova, N. N.; Razuvaev, V. N.; Ren, F.; Gao, G.; Rajeevan, M.; Kumar, K. R.; Rahimzadeh, F.; Khoshkam, M.; Kennedy, J. J.; Achberger, C.; Chen, D.; Trigo, R.; Garcia-Herrera, R.; Paredes, D.; Rachold, V.; Cappelen, J.; Heino, R.; Saku, S.; Parker, D.; Jonsson, T.; Walsh, J.; Bengtsson, L.; Maslowski, W.; Przybylak, R.; Forland, E.; Iden, K. A.; Groisman, P.; Zhang, H. M.; Angel, W. E.; Guttman, N.; Whitehurst, T.; Brown, W.; Stephens, S.; Gleason, B.; LeDuc, S.; Easterling, D.; Alexandersson, H., State of the climate in 2005. *Bulletin of the American Meteorological Society* **2006,** *87* (6), S6-S102.

13. Blunden, J., and D. S. Arndt,, State of the climate in 2011 Special Supplement to the Bulletin of the American Meteorological Society Vol. 93, No. 7, July 2012. *Bulletin of the American Meteorological Society* **2012,** *93* (7).
14. Stocker, T. F., D. Qin, G.-K. Plattner, M. Tignor, S.K. Allen, J. Boschung, A. Nauels, Y. Xia, V. Bex and P.M. Midgley *IPCC, 2013: Climate Change 2013: The Physical Science Basis. Contribution of Working Group I to the Fifth Assessment Report of the IntergovernmentalPanel on Climate Change*; 2013; pp 1-1535.
15. The drive for fuel. *Nature Geoscience* **2008,** *1* (5), 281-281.
16. Agarwal, A. K., Biofuels (alcohols and biodiesel) applications as fuels for internal combustion engines. *Progress in Energy and Combustion Science* **2007,** *33* (3), 233-271.
17. Searchinger, T.; Heimlich, R.; Houghton, R. A.; Dong, F. X.; Elobeid, A.; Fabiosa, J.; Tokgoz, S.; Hayes, D.; Yu, T. H., Use of US croplands for biofuels increases greenhouse gases through emissions from land-use change. *Science* **2008,** *319* (5867), 1238-1240.
18. Fargione, J.; Hill, J.; Tilman, D.; Polasky, S.; Hawthorne, P., Land clearing and the biofuel carbon debt. *Science* **2008,** *319* (5867), 1235-1238.
19. Tilman, D.; Hill, J.; Lehman, C., Carbon-negative biofuels from low-input high-diversity grassland biomass. *Science* **2006,** *314* (5805), 1598-1600.
20. Goldemberg, J., The challenge of biofuels. *Energy & Environmental Science* **2008,** *1* (5), 523-525.
21. Williams, P. J. L., Biofuel: microalgae cut the social and ecological costs. *Nature* **2007,** *450*, 478-478.
22. Yen, H. W.; Hu, I. C.; Chen, C. Y.; Ho, S. H.; Lee, D. J.; Chang, J. S., Microalgae-based biorefinery - From biofuels to natural products. *Bioresource Technology* **2013,** *135*, 166-174.
23. Directive 2003/30/EC of 8 May 2003 on the promotion of the use of biofuels or other renewable fuels for transport. In *OJ L 123, 17.5.2003*, 2003.
24. Biofuel statistics: Year 5 (2012 to 2013), report 5, Department for Transport. 2013.
25. Hammond, G. P.; Kallu, S.; McManus, M. C., Development of biofuels for the UK automotive market. *Applied Energy* **2008,** *85* (6), 506-515.
26. Our energy future – creating a low carbon economy, Cm 5761, February 2003, 5.1, Energy White Paper, DTI.
27. Fernando, S.; Adhikari, S.; Chandrapal, C.; Murali, N., Biorefineries: Current status, challenges, and future direction. *Energy & Fuels* **2006,** *20* (4), 1727-1737.
28. Slinn, M.; Kendall, K.; Mallon, C.; Andrews, J., Steam reforming of biodiesel by-product to make renewable hydrogen. *Bioresource Technology* **2008,** *99* (13), 5851-5858.
29. Valliyappan, T.; Bakhshi, N. N.; Dalai, A. K., Pyrolysis of glycerol for the production of hydrogen or syn gas. *Bioresource Technology* **2008,** *99* (10), 4476-4483.
30. Hirschmann, S.; Baganz, K.; Koschik, I.; Vorlop, K. D., Development of an integrated bioconversion process for the production of 1,3-propanediol from raw glycerol waters. *Landbauforschung Volkenrode* **2005,** *55* (4), 261-267.
31. Haveren, J. v.; Scott, E. L.; Sanders, J., - Bulk chemicals from biomass. **2008,** - *2* (- 1), - 57.
32. Savage, D. F.; Way, J.; Silver, P. A., Defossiling fuel: How synthetic biology can transform biofuel production. *Acs Chemical Biology* **2008,** *3* (1), 13-16.
33. Rudel, T. K., Food Versus Fuel: Extractive Industries, Insecure Land Tenure, and Gaps in World Food Production. *World Development* **2013,** *51*, 62-70.
34. FAO; WFP; IFAD, The State of Food Insecurity in the World 2012. Economic growth is necessary but not sufficient to accelerate reduction of hunger and malnutrition. *The State of Food Insecurity in the World 2012. Economic growth is necessary but not sufficient to accelerate reduction of hunger and malnutrition.* **2012**, Rome, FAO.
35. Hill, J.; Nelson, E.; Tilman, D.; Polasky, S.; Tiffany, D., Environmental, economic, and energetic costs and benefits of biodiesel and ethanol biofuels. *Proceedings of the National Academy of Sciences of the United States of America* **2006,** *103* (30), 11206-11210.

36. David, K.; Ragauskas, A. J., Switchgrass as an energy crop for biofuel production: A review of its ligno-cellulosic chemical properties. *Energy & Environmental Science* **2010,** *3* (9), 1182-1190.
37. Singh, R. N.; Vyas, D. K.; Srivastava, N. S. L.; Narra, M., SPRERI experience on holistic approach to utilize all parts of Jatropha curcas fruit for energy. *Renewable Energy* **2008,** *33* (8), 1868-1873.
38. Valentine, J.; Clifton-Brown, J.; Hastings, A.; Robson, P.; Allison, G.; Smith, P., Food vs. fuel: the use of land for lignocellulosic next generation' energy crops that minimize competition with primary food production. *Global Change Biology Bioenergy* **2012,** *4* (1), 1-19.
39. Slade, R.; Bauen, A., Micro-algae cultivation for biofuels: Cost, energy balance, environmental impacts and future prospects. *Biomass & Bioenergy* **2013,** *53*, 29-38.
40. Atsumi, S.; Hanai, T.; Liao, J. C., Non-fermentative pathways for synthesis of branched-chain higher alcohols as biofuels. *Nature* **2008,** *451*, 86-U13.
41. Marris, E., Drink the best and drive the rest. *Nature* **2006,** *444* (7120), 670-672.
42. Sanderson, K., A field in ferment. *Nature* **2006,** *444* (7120), 673-676.
43. King, C. W.; Holman, A. S.; Webber, M. E., Thirst for energy. *Nature Geoscience* **2008,** *1* (5), 283-286.
44. News, US universities promise to go carbon neutral. *Nature* **2007,** *447*, 897.
45. Kuesters, J.; Lammel, J., Investigations of the energy efficiency of the production of winter wheat and sugar beet in Europe. *European Journal of Agronomy* **1999,** *11* (1), 35-43.
46. Ruth, L., Bio or bust? The economic and ecological cost of biofuels. *Embo Reports* **2008,** *9* (2), 130-133.
47. Ramadhas, A. S.; Jayaraj, S.; Muraleedharan, C., Use of vegetable oils as IC engine fuels - A review. *Renewable Energy* **2004,** *29* (5), 727-742.
48. Ma, F. R.; Hanna, M. A., Biodiesel production: a review. *Bioresource Technology* **1999,** *70* (1), 1-15.
49. Chisti, Y., Biodiesel from microalgae. *Biotechnology Advances* **2007,** *25* (3), 294-306.
50. Chisti, Y., Biodiesel from microalgae beats bioethanol. *Trends in Biotechnology* **2008,** *26* (3), 126-131.
51. Greenwell, H. C.; Laurens, L. M. L.; Shields, R. J.; Lovitt, R. W.; Flynn, K. J., Placing microalgae on the biofuels priority list: a review of the technological challenges. *Journal of the Royal Society Interface* **2010,** *7* (46), 703-726.
52. Christie, W. W. AOCS Lipids library, Fatty acids: straight-chain saturated; structures, occurrence and biosynthesis. (accessed 25/11/2013).
53. Narasimharao, K.; Lee, A.; Wilson, K., Catalysts in production of biodiesel: A review. *Journal of Biobased Materials and Bioenergy* **2007,** *1*, 19-30.
54. Jesus Ramos, M.; Maria Fernandez, C.; Casas, A.; Rodriguez, L.; Perez, A., Influence of fatty acid composition of raw materials on biodiesel properties. *Bioresource Technology* **2009,** *100* (1), 261-268.
55. Zhao, Z., Comment on "Heterogeneous catalytic deoxygenation of stearic acid for production of biodiesel". *Industrial & Engineering Chemistry Research* **2006,** *45* (20), 6874-6874.
56. Snare, M.; Murzin, D. Y., Reply to "Comment on 'Heterogeneous catalytic deoxygenation of stearic acid for production of biodiesel'". *Industrial & Engineering Chemistry Research* **2006,** *45* (20), 6875-6875.
57. Institution of Chemical Engineers, E. C. T. S. G. c., *A biofuels compendium : making sense of the biofuels debate*. IChemE: Rugby, 2009; Mushrush, G. W.; Beal, E. J.; Hughes, J. M.; Wynne, J. H.; Sakran, J. V.; Hardy, D. R., Biodiesel fuels: Use of soy oil as a blending stock for middle distillate petroleum fuels. *Industrial & Engineering Chemistry Research* **2000,** *39* (10), 1-17; Ethanol, G. Material Safety Data Sheet: Greenfield Ethanol 2008, CDA 20 (200 Proof) Fuel Grade Alcohol (Denatured With Unleaded Gasoline). (accessed 12/01/13); Limited, S. U. O. P. Safety Data Sheet: Shell FuelSave Diesel version 2.1. (accessed 12/01/2013); Limited, S. U. O. P. Safety Data Sheet:Premium Unleaded Gasoline version 3.0. (accessed 12/01/2013).

58. Balat, M., Biodiesel fuel production from vegetable oils via supercritical ethonol transesterification. *Energy Sources Part a-Recovery Utilization and Environmental Effects* **2008,** *30* (5), 429-440.
59. West, A. H.; Posarac, D.; Ellis, N., Assessment of four biodiesel production processes using HYSYS. Plant. *Bioresource Technology* **2008,** *99* (14), 6587-6601.
60. Vicente, G.; Martinez, M.; Aracil, J., Integrated biodiesel production: a comparison of different homogeneous catalysts systems. *Bioresource Technology* **2004,** *92* (3), 297-305.
61. Miao, X. L.; Wu, Q. Y., Biodiesel production from heterotrophic microalgal oil. *Bioresource Technology* **2006,** *97* (6), 841-846.
62. Zafiropoulos, N. A.; Ngo, H. L.; Foglia, T. A.; Samulski, E. T.; Lin, W. B., Catalytic synthesis of biodiesel from high free fatty acid-containing feedstocks. *Chemical Communications* **2007**, 3670-3672.
63. Cantrell, D. G.; Gillie, L. J.; Lee, A. F.; Wilson, K., Structure-reactivity correlations in MgAl hydrotalcite catalysts for biodiesel synthesis. *Applied Catalysis a-General* **2005,** *287* (2), 183-190.
64. Macala, G. S.; Robertson, A. W.; Johnson, C. L.; Day, Z. B.; Lewis, R. S.; White, M. G.; Iretskii, A. V.; Ford, P. C., Transesterification catalysts from iron doped hydrotalcite-like precursors: Solid bases for biodiesel production. *Catalysis Letters* **2008,** *122* (3-4), 205-209.
65. Bo, X.; Xiao, G. M.; Cui, L. F.; Wei, R. P.; Gao, L. J., Transesterification of palm oil with methanol to biodiesel over a KF/Al2O3 heterogeneous base catalyst. *Energy & Fuels* **2007,** *21*, 3109-3112.
66. Li, X.; Lu, G. Z.; Guo, Y.; Wang, Y. Q.; Zhang, Z. G.; Liu, X. H.; Wang, Y. S., A novel solid superbase of Eu2O3/Al2O3 and its catalytic performance for the transesterification of soybean oil to biodiesel. *Catalysis Communications* **2007,** *8*, 1969-1972.
67. Bokade, V. V.; Yadav, G. D., Synthesis of Bio-diesel and Bio-lubricant by transesterification of vegetable oil with lower and higher alcohols over heteropolyacids supported by clay (K-10). *Process Safety and Environmental Protection* **2007,** *85* (B5), 372-377.
68. Azcan, N.; Danisman, A., Microwave assisted transesterification of rapeseed oil. *Fuel* **2008,** *87* (10-11), 1781-1788.
69. Barakos, N.; Pasias, S.; Papayannakos, N., Transesterification of triglycerides in high and low quality oil feeds over an HT2 hydrotalcite catalyst. *Bioresource Technology* **2008,** *99* (11), 5037-5042.
70. Kouzu, M.; Kasuno, T.; Tajika, M.; Yamanaka, S.; Hidaka, J., Active phase of calcium oxide used as solid base catalyst for transesterification of soybean oil with refluxing methanol. *Applied Catalysis A-General* **2008,** *334*, 357-365.
71. Garcia, C. M.; Teixeira, S.; Marciniuk, L. L.; Schuchardt, U., Transesterfication of soybean oil catalyzed by sulfated ziconia. *Bioresource Technology* **2008,** *99* (14), 6608-6613.
72. Saydut, A.; Duz, M. Z.; Kaya, C.; Kafadar, A. B.; Hamamci, C., Transesterified sesame (Sesamum indicum L.) seed oil as a biodiesel fuel. *Bioresour Technol* **2008,** *99* (14), 6656-60.
73. da Silva, R. B.; Neto, A. F. L.; dos Santos, L. S. S.; Lima, J. R. D.; Chaves, M. H.; dos Santos, J. R.; de Lima, G. M.; de Moura, E. M.; de Moura, C. V. R., Catalysts of Cu(II) and Co(II) ions adsorbed in chitosan used in transesterification of soy bean and babassu oils - A new route for biodiesel syntheses. *Bioresource Technology* **2008,** *99* (15), 6793-6798.
74. Leung, D. Y. C.; Guo, Y., Transesterification of neat and used frying oil: Optimization for biodiesel production. *Fuel Processing Technology* **2006,** *87* (10), 883-890.
75. Huber, G. W.; Iborra, S.; Corma, A., Synthesis of transportation fuels from biomass: Chemistry, catalysts, and engineering. *Chemical Reviews* **2006,** *106* (9), 4044-4098.
76. Canakci, M.; Sanli, H., Biodiesel production from various feedstocks and their effects on the fuel properties. *Journal of Industrial Microbiology & Biotechnology* **2008,** *35* (5), 431-441.
77. MJ, H.; S, B.; K, S. Process for the production of fatty acid alkyl esters US 6399800 B1. 2002.

78. Choudary, B. M.; Kantam, M. L.; Reddy, C. V.; Aranganathan, S.; Santhi, P. L.; Figueras, F., Mg-Al-O-t-Bu hydrotalcite: a new and efficient heterogeneous catalyst for transesterification. *Journal of Molecular Catalysis a-Chemical* **2000,** *159* (2), 411-416.
79. Corma, A.; Iborra, S.; Miquel, S.; Primo, J., Catalysts for the production of fine chemicals - Production of food emulsifiers, monoglycerides, by glycerolysis of fats with solid base catalysts. *Journal of Catalysis* **1998,** *173* (2), 315-321.
80. Cavani, F.; Trifirò, F.; Vaccari, A., Hydrotalcite-type anionic clays: Preparation, properties and applications. *Catalysis Today* **1991,** *11* (2), 173-301.
81. Cross, H. E.; Brown, D. R., Entrained sodium in mixed metal oxide catalysts derived from layered double hydroxides. *Catalysis Communications* **2010,** *12* (3), 243-245.
82. Hammett, L. P.; Deyrup, A. J., A series of simple basic indicators II Some applications to solutions in formic acid. *Journal of the American Chemical Society* **1932,** *54*, 4239-4247.
83. Hammett, L. P.; Deyrup, A. J., A series of simple basic indicators. I. The acidity functions of mixtures of sulfuric and perchloric acids with water. *Journal of the American Chemical Society* **1932,** *54*, 2721-2739.
84. Jacobson, K.; Gopinath, R.; Meher, L. C.; Dalai, A. K., Solid acid catalyzed biodiesel production from waste cooking oil. *Applied Catalysis B-Environmental* **2008,** *85* (1-2), 86-91.
85. Lou, W.-Y.; Zong, M.-H.; Duan, Z.-Q., Efficient production of biodiesel from high free fatty acid-containing waste oils using various carbohydrate-derived solid acid catalysts. *Bioresour Technol* **2008,** *99* (18), 8752-8.
86. EN 14214-Automotive fuels - Fatty acid methyl esters (FAME) for diesel engines - Requirements and test methods, 2003. .
87. Kulkarni, M. G.; Dalai, A. K., Waste cooking oil-an economical source for biodiesel: A review. *Industrial & Engineering Chemistry Research* **2006,** *45* (9), 2901-2913.
88. Smith, H., The hydrocarbon constituents of petroleum and some possible lipid precursors. *Journal of the American Oil Chemists' Society* **1967,** *44* (12), 680-690.
89. Kalnes, T.; Marker, T.; Shonnard, D. R., Green diesel: A second generation biofuel. *International Journal of Chemical Reactor Engineering* **2007,** *5*, A48.
90. Almon, W. R.; Johns, W. D., Petroleum forming reactions: the mechanism and rate of clay catalyzed fatty acid decarboxilation. In *7th International Meeting on Organic Geochemistry*, Wiley: Chichester, 1975; Vol. 7, pp 157-171.
91. Geatches, D. L.; Clark, S. J.; Greenwell, H. C., Role of Clay Minerals in Oil-Forming Reactions. *Journal of Physical Chemistry A* **2010,** *114* (10), 3569-3575.
92. Demirbas, A., The influence of temperature on the yields of compounds existing in bio-oils obtained from biomass samples via pyrolysis. *Fuel Processing Technology* **2007,** *88* (6), 591-597.
93. Demirbas, A., New liquid biofuels from vegetable oils via catalytic pyrolysis. *Energy Education Science and Technology* **2008,** *21* (1-2), 1-59.
94. Bertram, S. H., Organic. *Analyst* **1936,** *61* (729), 866-870.
95. Snare, M.; Kubickova, I.; Maki-Arvela, P.; Eranen, K.; Warna, J.; Murzin, D. Y., Production of diesel fuel from renewable feeds: Kinetics of ethyl stearate decarboxylation. *Chemical Engineering Journal* **2007,** *134*, 29-34.
96. Snare, M.; Kubickova, I.; Maki-Arvela, P.; Eranen, K.; Murzin, D. Y., Heterogeneous catalytic deoxygenation of stearic acid for production of biodiesel. *Industrial & Engineering Chemistry Research* **2006,** *45* (16), 5708-5715.
97. Snare, M.; Kubickova, I.; Maki-Arvela, P.; Chichova, D.; Eranen, K.; Murzin, D. Y., Catalytic deoxygenation of unsaturated renewable feedstocks for production of diesel fuel hydrocarbons. *Fuel* **2008,** *87* (6), 933-945.
98. Lestari, S.; Simakova, I.; Tokarev, A.; Maki-Arvela, P.; Eranen, K.; Murzin, D. Y., Synthesis of biodiesel via deoxygenation of stearic acid over supported Pd/C catalyst. *Catalysis Letters* **2008,** *122* (3-4), 247-251.
99. Zhang, A.; Ma, Q.; Wang, K.; Tang, Y.; Goddard, W. A. *Improved Processes to Remove Naphthenic Acids*; 2005; p Medium: ED.

100. Zaman, M.; Lee, J. H., Carbon capture from stationary power generation sources: A review of the current status of the technologies. *Korean Journal of Chemical Engineering* **2013,** *30* (8), 1497-1526.
101. Liu, Y.; Sotelo-Boyas, R.; Murata, K.; Minowa, T.; Sakanishi, K., Hydrotreatment of Jatropha Oil to Produce Green Diesel over Trifunctional Ni-Mo/SiO2-Al2O3 Catalyst. *Chemistry Letters* **2009,** *38* (6), 552-553.
102. Fu, J.; Lu, X.; Savage, P. E., Catalytic hydrothermal deoxygenation of palmitic acid. *Energy & Environmental Science* **2010,** *3* (3), 311-317.
103. Mikulec, J.; Cvengros, J.; Jorikova, L.; Banic, M.; Kleinova, A., Second generation diesel fuel from renewable sources. *Journal of Cleaner Production* **2010,** *18* (9), 917-926.
104. Morgan, T.; Santillan-Jimenez, E.; Harman-Ware, A. E.; Ji, Y.; Grubb, D.; Crocker, M., Catalytic deoxygenation of triglycerides to hydrocarbons over supported nickel catalysts. *Chemical Engineering Journal* **2012,** *189-190*.
105. Friedel, C., Ueber s. g. gemischte Acetone. *Justus Liebigs Annalen der Chemie* **1858,** *108* (1), 122-125.
106. Gaertner, C. A.; Serrano-Ruiz, J. C.; Braden, D. J.; Dumesic, J. A., Catalytic coupling of carboxylic acids by ketonization as a processing step in biomass conversion. *Journal of Catalysis* **2009,** *266* (1), 71-78.
107. Siegel, H.; Manfred, E., Ketones. *Ullmann's Encyclopedia of Industrial Chemistry* **2000**.
108. Hait, S. K.; Moulik, S. P., Gemini surfactants: A distinct class of self-assembling molecules. *Current Science* **2002,** *82* (9), 1101-1111.
109. Corma, A.; Renz, M.; Schaverien, C., Coupling Fatty Acids by Ketonic Decarboxylation Using Solid Catalysts for the Direct Production of Diesel, Lubricants, and Chemicals. *Chemsuschem* **2008,** *1* (8-9), 739-741.
110. Klimkiewicz, R.; Teterycz, H.; Grabowska, H.; Morawski, I.; Syper, L.; Licznerski, B. W., Ketonization of fatty methyl esters over Sn-Ce-Rh-O catalyst. *Journal of the American Oil Chemists Society* **2001,** *78* (5), 533-535.
111. Klimkiewicz, R.; Fabisz, E.; Morawski, I.; Grabowska, H.; Syper, L., Ketonization of long chain esters from transesterification of technical waste fats. *Journal of Chemical Technology and Biotechnology* **2001,** *76* (1), 35-38.
112. Renz, M., Ketonization of carboxylic acids by decarboxylation: Mechanism and scope. *European Journal of Organic Chemistry* **2005,** (6), 979-988.
113. Miller, A. L.; Cook, N. C.; Whitmore, F. C., The ketonic decarboxylation reaction - The ketonic decarboxylation of trimethylacetic acid and isobutyric acid. *Journal of the American Chemical Society* **1950,** *72* (6), 2732-2735.
114. Glinski, M.; Kijenski, J.; Jakubowski, A., Ketones from monocarboxylic acids - Catalytic ketonization over oxide systems. *Applied Catalysis a-General* **1995,** *128* (2), 209-217.
115. Parida, K.; Das, J., Mg/Al hydrotalcites: preparation, characterisation and ketonisation of acetic acid. *Journal of Molecular Catalysis a-Chemical* **2000,** *151* (1-2), 185-192.
116. Das, J.; Parida, K., Catalytic ketonization of acetic acid on Zn/Al layered double hydroxides. *Reaction Kinetics and Catalysis Letters* **2000,** *69* (2), 223-229.
117. Renz, M.; Corma, A., Ketonic decarboxylation catalysed by weak bases and its application to an optically pure substrate. *European Journal of Organic Chemistry* **2004,** (9), 2036-2039.
118. Nagashima, O.; Sato, S.; Takahashi, R.; Sodesawa, T., Ketonization of carboxylic acids over CeO2-based composite oxides. *Journal of Molecular Catalysis a-Chemical* **2005,** *227* (1-2), 231-239.
119. Deng, L.; Fu, Y.; Guo, Q.-X., Upgraded Acidic Components of Bio-oil through Catalytic Ketonic Condensation. *Energy & Fuels* **2009,** *23* (1), 564-568.
120. Rand, L.; Kovac, L. R.; Wagner, W.; Warner, P. O., Reactions catalyzed by potassium fluoride .2. Conversion of adipic acid to cyclopentanone. *Journal of Organic Chemistry* **1962,** *27* (3), 1034-1035.
121. Towards falling emissions. *Nature* **2008,** *451*, 499-499.

122. Debecker, D. P.; Gaigneaux, E. M.; Busca, G., Exploring, Tuning, and Exploiting the Basicity of Hydrotalcites for Applications in Heterogeneous Catalysis. *Chemistry-a European Journal* **2009,** *15* (16), 3920-3935.
123. Greenwell, H. C.; Marsden, C. C.; Jones, W., Synthesis of organo-layered double hydroxides by an environmentally friendly co-hydration route. *Green Chemistry* **2007,** *9*, 1299-1307.
124. Costantino, U.; Marmottini, F.; Nocchetti, M.; Vivani, R., New synthetic routes to hydrotalcite-like compounds - Characterisation and properties of the obtained materials. *European Journal of Inorganic Chemistry* **1998,** (10), 1439-1446.
125. Newman, S. P.; Jones, W.; O'Connor, P.; Stamires, D. N., Synthesis of the 3R(2) polytype of a hydrotalcite-like mineral. *Journal of Materials Chemistry* **2002,** *12* (2), 153-155.
126. Bookin, A. S.; Drits, V. A., Polytype diversity of the hydrotalcite-like materials .1. Possible polytypes and their diffraction features. *Clays and Clay Minerals* **1993,** *41* (5), 551-557.
127. Khan, A. I.; O'Hare, D., Intercalation chemistry of layered double hydroxides: recent developments and applications. *Journal of Materials Chemistry* **2002,** *12* (11), 3191-3198.
128. Kooli, F.; Chisem, I. C.; Vucelic, M.; Jones, W., Synthesis and properties of terephthalate and benzoate intercalates of Mg-Al layered double hydroxides possessing varying layer charge. *Chemistry of Materials* **1996,** *8* (8), 1969-1977.
129. Vaysse, C.; Guerlou-Demourgues, L.; Demourgues, A.; Lazartigues, F.; Fertier, D.; Delmas, C., New (Ni, Co)-based layered double hydroxides with intercalated oxometalate (Mo, W) species, obtained by chimie douce reactions. *Journal of Materials Chemistry* **2002,** *12* (4), 1035-1043.
130. Rietveld, H. M., A profile refinement method for nuclear and magnetic structures. *Journal of Applied Crystallography* **1969,** *2*, 65-&.
131. Wang, Y.; Chan, S.; Amal, R.; Shen, Y.; Kiatkittipong, K., XRD Anisotropic broadening of nano-crystallites. *Advances in X-Ray Analysis, Vol 54* **2011,** *54*, 92-100.
132. He, B.; Preckwinkel, U.; Smith, K., Comparison between conventional and two-dimensional XRD. *Advances in X-ray Analysis* **2003,** *46*, 37-42.
133. Allmann, R., The crystal structure of pyroaurite. *Acta Crystallographica Section B* **1968,** *24* (7), 972-977.
134. PANalytical; B.V. *X'Pert HighScore Plus*, 2006.
135. Kaneyoshi, M.; Jones, W., Formation of Mg-Al layered double hydroxides intercalated with nitrilotriacetate anions. *Journal of Materials Chemistry* **1999,** *9* (3), 805-811.
136. Thomas, G. S.; Kamath, P. V., Line broadening in the PXRD patterns of layered hydroxides: The relative effects of crystallite size and structural disorder. *Journal of Chemical Sciences* **2006,** *118* (1), 127-133.
137. Rives, V., *Layered Double Hydroxides: Present and Future*. Nova Science Publishers, Incorporated: 2001.
138. Mokhtar, M.; Inayat, A.; Ofili, J.; Schwieger, W., Thermal decomposition, gas phase hydration and liquid phase reconstruction in the system Mg/Al hydrotalcite/mixed oxide: A comparative study. *Applied Clay Science* **2010,** *50* (2), 176-181.
139. Valente, J. S.; Rodriguez-Gattorno, G.; Valle-Orta, M.; Torres-Garcia, E., Thermal decomposition kinetics of MgAl layered double hydroxides. *Materials Chemistry and Physics* **2012,** *133* (2-3), 621-629; Palmer, S. J.; Kristof, J.; Vagvolgyi, V.; Horvath, E.; Frost, R. L., Thermal decomposition of hydrotalcite with hexacyanoferrate(II) and hexacyanoferrate(III) anions in the interlayer a controlled rate thermal analysis study. *Journal of Thermal Analysis and Calorimetry* **2009,** *96* (2), 449-454; Palmer, S. J.; Frost, R. L.; Nguyen, T., Thermal decomposition of hydrotalcite with molybdate and vanadate anions in the interlayer. *Journal of Thermal Analysis and Calorimetry* **2008,** *92* (3), 879-886.
140. Sutton, M. A.; Li, N.; Joy, D. C.; Reynolds, A. P.; Li, X., Scanning electron microscopy for quantitative small and large deformation measurements part i: SEM imaging at magnifications from 200 to 10,000. *Experimental Mechanics* **2007,** *47* (6), 775-787.

141. Goodhew, P. J.; Humphreys, F. J., *Electron Microscopy and Analysis*. Taylor & Francis Group: 1988.
142. Brunauer, S.; Emmett, P. H.; Teller, E., Adsorption of gases in multimolecular layers. *Journal of the American Chemical Society* **1938,** *60*, 309-319.
143. Sing, K. S. W.; Everett, D. H.; Haul, R. A. W.; Moscou, L.; Pierotti, R. A.; Rouquerol, J.; Siemieniewska, T., Reporting physisorption data for gas solid systems with special reference to the determination of surface-area and porosity (recommendations 1984). *Pure and Applied Chemistry* **1985,** *57* (4), 603-619.
144. Dubinin, M. M., Physical Adsorption of Gases and Vapors in Micropores. In *Progress in Surface and Membrane Science*, D.A. Cadenhead, J. F. D. a. M. D. R., Ed. Elsevier: 1975; Vol. Volume 9, pp 1-70.
145. Gregg, S. J.; Sing, K. S. W., *Adsorption, surface area, and porosity*. Academic Press: 1991.
146. Wang, L. K.; Chen, J. P.; Hung, Y. T.; Shammas, N. K., *Membrane and Desalination Technologies*. Humana Press: 2010.
147. Barrett, E. P.; Joyner, L. G.; Halenda, P. P., The determination of pore volume and area distributions in porous substances .1. Computations from nitrogen isotherms. *Journal of the American Chemical Society* **1951,** *73* (1), 373-380.
148. Lowell, S., *Characterization of Porous Solids and Powders: Surface Area, Pore Size and Density*. Springer: 2004.
149. Xie, W. L.; Peng, H.; Chen, L. G., Calcined Mg-Al hydrotalcites as solid base catalysts for methanolysis of soybean oil. *Journal of Molecular Catalysis a-Chemical* **2006,** *246* (1-2), 24-32.
150. Jinesh, C. M.; Sen, A.; Ganguly, B.; Kannan, S., Microwave assisted isomerization of alkenyl aromatics over solid base catalysts: an understanding through theoretical study. *Rsc Advances* **2012,** *2* (17), 6871-6878.
151. Chisem, I. C.; Jones, W.; Martin, I.; Martin, C.; Rives, V., Probing the surface acidity of lithium aluminium and magnesium aluminium layered double hydroxides. *Journal of Materials Chemistry* **1998,** *8* (8), 1917-1925.
152. Navajas, A.; Campo, I.; Arzamendi, G.; Hernandez, W. Y.; Bobadilla, L. F.; Centeno, M. A.; Odriozola, J. A.; Gandia, L. M., Synthesis of biodiesel from the methanolysis of sunflower oil using PURAL (R) Mg-Al hydrotalcites as catalyst precursors. *Applied Catalysis B-Environmental* **2010,** *100* (1-2), 299-309.
153. de Jong, A. M.; Niemantsverdriet, J. W., Thermal desorption analysis: Comparative test of ten commonly applied procedures. *Surface Science* **1990,** *233* (3), 355-365.
154. Brito, A.; Borges, M. E.; Garin, M.; Hernandez, A., Biodiesel Production from Waste Oil Using Mg-Al Layered Double Hydroxide Catalysts. *Energy & Fuels* **2009,** *23*, 2952-2958.
155. Kloprogge, J. T.; Frost, R. L., Fourier transform infrared and Raman spectroscopic study of the local structure of Mg-, Ni-, and Co-hydrotalcites. *Journal of Solid State Chemistry* **1999,** *146* (2), 506-515.
156. Kanezaki, E., Intercalation of naphthalene-2,6-disulfonate between layers of Mg and Al double hydroxide: Preparation, powder X-ray diffraction, Fourier transform infrared spectra and X-ray photoelectron spectra. *Materials Research Bulletin* **1999,** *34* (9), 1435-1440; Kanezaki, E., Fourier transform infrared spectra of naphthalene disulfonates between layers of Mg and Al double hydroxide: Intercalation by means of coprecipitation and direct observation of coordination from the interlayer anion to the metal cation in the layer. *Journal of Inclusion Phenomena and Macrocyclic Chemistry* **2000,** *36* (4), 447-453.
157. Frost, R. L.; Kloprogge, J. T., Infrared emission spectroscopic study of brucite. *Spectrochimica Acta Part a-Molecular and Biomolecular Spectroscopy* **1999,** *55* (11), 2195-2205; Frost, R. L.; Kloprogge, J. T.; Russell, S. C.; Szetu, J. L., Vibrational spectroscopy and dehydroxylation of aluminum (oxo)hydroxides: Gibbsite. *Applied Spectroscopy* **1999,** *53* (4), 423-434.
158. Kagunya, W.; Baddour-Hadjean, R.; Kooli, F.; Jones, W., Vibrational modes in layered double hydroxides and their calcined derivatives. *Chemical Physics* **1998,** *236* (1-3), 225-234.

159. DataApex, Clarity Chromatography Station. *Clarity Chromatography Station version 2.4.1.57* **2003**, retrieved 9/2/2011.
160. International, A., ASTM D6584 - 10ae1 Standard Test Method for Determination of Total Monoglyceride, Total Diglyceride, Total Triglyceride, and Free and Total Glycerin in B-100 Biodiesel Methyl Esters by Gas Chromatography. ASTM International: 2010.
161. de Hoffmann, E.; Stroobant, V., *Mass Spectrometry: Principles and Applications*. Wiley: 2013.
162. Informatics, W. L. *MassLynx 4.1 Software*, 720001408EN.
163. Crepaldi, E. L.; Pavan, P. C.; Valim, J. B., Comparative study of the coprecipitation methods for the preparation of layered double hydroxides. *J. Braz. Chem. Soc.* **2000,** *11* (1), 64-70.
164. He, J.; Wei, M.; Li, B.; Kang, Y.; Evans, D. G.; Duan, X., Preparation of layered double hydroxides. *Layered Double Hydroxides* **2006,** *119*, 89-119.
165. Guida, A.; Lhouty, M. H.; Tichit, D.; Figueras, F.; Geneste, P., Hydrotalcites as base catalysts. Kinetics of Claisen-Schmidt condensation, intramolecular condensation of acetonylacetone and synthesis of chalcone. *Applied Catalysis a-General* **1997,** *164* (1-2), 251-264; Choudary, B. M.; Kantam, M. L.; Reddy, C. R. V.; Rao, K. K.; Figueras, F., The first example of Michael addition catalysed by modified Mg-Al hydrotalcite. *Journal of Molecular Catalysis a-Chemical* **1999,** *146* (1-2), 279-284.
166. Ostwald, W.; Bodenstein, M.; Clusius, K.; Bonhoeffer, K. F.; Falkenhagen, H., *Zeitschrift für physikalische Chemie*. Akademische Verlagsgesellschaft Geest & Portig: 1897.
167. Greenwell, H. C.; Bindley, L. A.; Unwin, P. R.; Holliman, P. J.; Jones, W.; Coveney, P. V.; Barnes, S. L., In situ monitoring of crystal growth and dissolution of oriented layered double-hydroxide crystals immobilized on silicon. *Journal of Crystal Growth* **2006,** *294* (1), 53-59.
168. Rivera, J. A.; Fetter, G.; Bosch, P., Microwave power effect on hydrotalcite synthesis. *Microporous and Mesoporous Materials* **2006,** *89* (1-3), 306-314.
169. Bourrie, G.; Trolard, F.; Refait, P.; Feder, F., A solid-solution model for Fe(II)-Fe(III)-Mg(II) green rusts and fougerite and estimation of their Gibbs free energies of formation. *Clays and Clay Minerals* **2004,** *52* (3), 382-394.
170. Evans, D. G.; Slade, R. C. T., Structural aspects of layered double hydroxides. *Structure and Bonding* **2006,** *119*, 1-87.
171. Zhao, Y.; Li, F.; Zhang, R.; Evans, D. G.; Duan, X., Preparation of layered double-hydroxide nanomaterials with a uniform crystallite size using a new method involving separate nucleation and aging steps. *Chemistry of Materials* **2002,** *14* (10), 4286-4291.
172. Ogawa, M.; Asai, S., Hydrothermal synthesis of layered double hydroxide-deoxycholate intercalation compounds. *Chemistry of Materials* **2000,** *12* (11), 3253-+.
173. Benito, P.; Herrero, M.; Barriga, C.; Labajos, F. M.; Rives, V., Microwave-assisted homogeneous precipitation of hydrotalcites by urea hydrolysis. *Inorganic Chemistry* **2008,** *47* (12), 5453-5463.
174. Greenwell, H. C.; Jones, W.; Rugen-Hankey, S. L.; Holliman, P. J.; Thompson, R. L., Efficient synthesis of ordered organo-layered double hydroxides. *Green Chemistry* **2010,** *12* (4), 688-695.
175. Morel-Desrosiers, N.; Pisson, J.; Israeli, Y.; Taviot-Gueho, C.; Besse, J. P.; Morel, J. P., Intercalation of dicarboxylate anions into a Zn-Al-Cl layered double hydroxide: microcalorimetric determination of the enthalpies of anion exchange. *Journal of Materials Chemistry* **2003,** *13* (10), 2582-2585; Israeli, Y.; Taviot-Gueho, T.; Beese, J. P.; Morel, J. P.; Morel-Desrosiers, N., Thermodynamics of anion exchange on a chloride-intercalated zinc-aluminum layered double hydroxide: a microcalorimetric study. *Journal of the Chemical Society-Dalton Transactions* **2000,** (5), 791-796.
176. Newman, S. P.; Jones, W., Synthesis, characterization and applications of layered double hydroxides containing organic guests. *New Journal of Chemistry* **1998,** *22* (2), 105-115.

177. Bubniak, G. A.; Schreiner, W. H.; Mattoso, N.; Wypych, F., Preparation of a new nanocomposite of $Al_{0.33}Mg_{0.67}(OH)_2(C_{12}H_{25}SO_4)_{0.33}$ and poly(ethylene oxide). *Langmuir* **2002,** *18* (16), 5967-5970.
178. Tseng, W. Y.; Lin, J. T.; Mou, C. Y.; Cheng, S. F.; Liu, S. B.; Chu, P. P.; Liu, H. W., Incorporation of C-60 in layered double hydroxide. *Journal of the American Chemical Society* **1996,** *118* (18), 4411-4418.
179. Vyalikh, A.; Massiot, D.; Scheler, U., Structural characterisation of aluminium layered double hydroxides by Al-27 solid-state NMR. *Solid State Nuclear Magnetic Resonance* **2009,** *36* (1), 19-23.
180. Erickson, K. L.; Bostrom, T. E.; Frost, R. L., A study of structural memory effects in synthetic hydrotalcites using environmental SEM. *Materials Letters* **2005,** *59* (2-3), 226-229.
181. Rocha, J.; del Arco, M.; Rives, V.; Ulibarri, M. A., Reconstruction of layered double hydroxides from calcined precursors: a powder XRD and Al-27 MAS NMR study. *Journal of Materials Chemistry* **1999,** *9* (10), 2499-2503.
182. Marchi, A. J.; Apesteguia, C. R., Impregnation-induced memory effect of thermally activated layered double hydroxides. *Applied Clay Science* **1998,** *13* (1), 35-48.
183. Nakayama, H.; Wada, N.; Tsuhako, M., Intercalation of amino acids and peptides into Mg-Al layered double hydroxide by reconstruction method. *International Journal of Pharmaceutics* **2004,** *269* (2), 469-478.
184. You, Y. W.; Zhao, H. T.; Vance, G. F., Hybrid organic-inorganic derivatives of layered double hydroxides and dodecylbenzenesulfonate: Preparation and adsorption characteristics. *Journal of Materials Chemistry* **2002,** *12* (4), 907-912.
185. Aloisi, G. G.; Costantino, U.; Elisei, F.; Latterini, L.; Natali, C.; Nocchetti, M., Preparation and photo-physical characterisation of nanocomposites obtained by intercalation and co-intercalation of organic chromophores into hydrotalcite-like compounds. *Journal of Materials Chemistry* **2002,** *12* (11), 3316-3323.
186. Donaldson, D.; Raahauge, B., *Essential Readings in Light Metals, Alumina and Bauxite*. Wiley: 2013.
187. Constantino, V. R. L.; Pinnavaia, T. J., Basic properties of $Mg_{1-X}^{2+}Al_X^{3+}$ layered double hydroxides intercalated by carbonate, hydroxide chloride and sulfate anions. *Inorganic Chemistry* **1995,** *34* (4), 883-892.
188. Botha, A.; Strydom, C. A., Preparation of a magnesium hydroxy carbonate from magnesium hydroxide. *Hydrometallurgy* **2001,** *62* (3), 175-183.
189. Allmann, R., *Neues Jb Mineralogie* **1969,** *1969*, 00544-00544.
190. Patterson, A. L., The Scherrer formula for x-ray particle size determination. *Physical Review* **1939,** *56* (10), 978-982.
191. Santhanalakshmi, J.; Raja, T., Selective N-methylation of aniline by calcined Mg-II-Al-III layered double hydroxides. *Applied Catalysis a-General* **1996,** *147* (1), 69-80.
192. Hudson, M. J.; Carlino, S.; Apperley, D. C., Thermal-conversion of a layered (Mg/Al) double hydroxide to the oxide. *Journal of Materials Chemistry* **1995,** *5* (2), 323-329.
193. Valente, J. S.; Sanchez-Cantu, M.; Lima, E.; Figueras, F., Method for Large-Scale Production of Multimetallic Layered Double Hydroxides: Formation Mechanism Discernment. *Chemistry of Materials* **2009,** *21* (24), 5809-5818.
194. Ma, R.; Liu, Z.; Li, L.; Iyi, N.; Sasaki, T., Exfoliating layered double hydroxides in formamide: a method to obtain positively charged nanosheets. *Journal of Materials Chemistry* **2006,** *16* (39), 3809-3813.
195. Zhao, Y.; He, J.; Jiao, Q. Z.; Evans, D. G.; Duan, X.; Lu, C. H.; Wang, Z. G., Selectivity of crystal growth direction and control of particle size in layered double hydroxides. *Chinese Journal of Inorganic Chemistry* **2001,** *17* (4), 573-579.
196. Corma, A.; Fornes, V.; Martinaranda, R. M.; Rey, F., Determination of base properties of hydrotalcites - condensation of benzaldehyde with ethyl acetoacetate. *Journal of Catalysis* **1992,** *134* (1), 58-65.

197. Farcasiu, D.; Ghenciu, A.; Marino, G.; Rose, K. D., Strength of solid acids and acids in solution. Enhancement of acidity of centers on solid surfaces by anion stabilizing solvents and its consequence for catalysis. *Journal of the American Chemical Society* **1997,** *119* (49), 11826-11831; Cheung, T. K.; Gates, B. C., Sulfated zirconia and iron- and manganese-promoted sulfated zirconia: do they protonate alkanes? *Topics in Catalysis* **1998,** *6* (1-4), 41-47.
198. Ramesh, T. N.; Jayashree, R. S.; Kamath, P. V., Disorder in layered hydroxides: DIFFaX simulation of the X-ray powder diffraction patterns of nickel hydroxide. *Clays and Clay Minerals* **2003,** *51* (5), 570-576.
199. Kiritsis, V.; Michaelides, A.; Skoulika, S.; Golhen, S.; Ouahab, L., Assembly of a porous three-dimensional coordination polymer: Crystal structure of { $La_2(adipate)_3(H_2O)_4 \cdot 6H_2O\}_{(n)}$. *Inorganic Chemistry* **1998,** *37* (13), 3407-+.
200. Kannan, S., Influence of synthesis methodology and post treatments on structural and textural variations in $MgAlCO_3$ hydrotalcite. *Journal of Materials Science* **2004,** *39* (21), 6591-6596.
201. Climent, M. J.; Corma, A.; Iborra, S.; Epping, K.; Velty, A., Increasing the basicity and catalytic activity of hydrotalcites by different synthesis procedures. *Journal of Catalysis* **2004,** *225* (2), 316-326.
202. Kelkar, C. P.; Schutz, A. A.; Cullo, L. A., Synthesis of hydrotalcite-like materials with a sheet-like morphology. *Synthesis of Porous Materials: Zeolites, Clays, and Nanostructures* **1997,** *69*, 691-703; Kelkar, C. P.; Schutz, A. A., Ni-, Mg- and Co-containing hydrotalcite-like materials with a sheet-like morphology: synthesis and characterization. *Microporous Materials* **1997,** *10* (4-6), 163-172.
203. Kustrowski, P.; Sulkowska, D.; Chmielarz, L.; Rafalska-Lasocha, A.; Dudek, B.; Dziembaj, R., Influence of thermal treatment conditions on the activity of hydrotalcite-derived Mg-Al oxides in the aldol condensation of acetone. *Microporous and Mesoporous Materials* **2005,** *78* (1), 11-22.
204. Li, F.; Jiang, X. R.; Evans, D. G.; Duan, X., Structure and basicity of mesoporous materials from Mg/Al/In layered double hydroxides prepared by separate nucleation and aging steps method. *Journal of Porous Materials* **2005,** *12* (1), 55-63.
205. Reichle, W. T.; Kang, S. Y.; Everhardt, D. S., The nature of the thermal-decomposition of a catalytically active anionic clay mineral. *Journal of Catalysis* **1986,** *101* (2), 352-359.
206. Chmielarz, L.; Kustrowski, P.; Rafalska-Lasocha, A.; Dziembaj, R., Influence of Cu, Co and Ni cations incorporated in brucite-type layers on thermal behaviour of hydrotalcites and reducibility of the derived mixed oxide systems. *Thermochimica Acta* **2003,** *395* (1-2), 225-236.
207. Sharma, S. K.; Parikh, P. A.; Jasra, R. V., Solvent free aldol condensation of propanal to 2-methylpentenal using solid base catalysts. *Journal of Molecular Catalysis a-Chemical* **2007,** *278* (1-2), 135-144.
208. Turco, M.; Bagnasco, G.; Costantino, U.; Marmottini, F.; Montanari, T.; Ramis, G.; Busca, G., Production of hydrogen from oxidative steam reforming of methanol - I. Preparation and characterization of $Cu/ZnO/Al_2O_3$ catalysts from a hydrotalcite-like LDH precursor. *Journal of Catalysis* **2004,** *228* (1), 43-55.
209. Velu, S.; Suzuki, K.; Okazaki, M.; Osaki, T.; Tomura, S.; Ohashi, F., Synthesis of new Sn-incorporated layered double hydroxides and their thermal evolution to mixed oxides. *Chemistry of Materials* **1999,** *11* (8), 2163-2172.
210. Prinetto, F.; Ghiotti, G.; Durand, R.; Tichit, D., Investigation of acid-base properties of catalysts obtained from layered double hydroxides. *Journal of Physical Chemistry B* **2000,** *104* (47), 11117-11126.
211. Ishihara, S.; Sahoo, P.; Deguchi, K.; Ohki, S.; Tansho, M.; Shimizu, T.; Labuta, J.; Hill, J. P.; Ariga, K.; Watanabe, K.; Yamauchi, Y.; Suehara, S.; Iyi, N., Dynamic Breathing of CO_2 by Hydrotalcite. *Journal of the American Chemical Society* **2013,** *135* (48), 18040-18043.
212. Smith, B.; Greenwell, H. C.; Whiting, A., Catalytic upgrading of tri-glycerides and fatty acids to transport biofuels. *Energy & Environmental Science* **2009,** *2* (3), 262-271.

213. Lestari, S.; Maki-Arvela, P.; Beltramini, J.; Lu, G. Q. M.; Murzin, D. Y., Transforming Triglycerides and Fatty Acids into Biofuels. *Chemsuschem* **2009,** *2* (12), 1109-1119.
214. Wahlen, B. D.; Barney, B. M.; Seefeldt, L. C., Synthesis of Biodiesel from Mixed Feedstocks and Longer Chain Alcohols Using an Acid-Catalyzed Method. *Energy & Fuels* **2008,** *22* (6), 4223-4228.
215. Wang, W. C.; Turner, T. L.; Stikeleather, L. F.; Roberts, W. L., Exploration of process parameters for continuous hydrolysis of canola oil, camelina oil and algal oil. *Chemical Engineering and Processing* **2012,** *57-58*, 51-58.
216. Tan, H. W.; Aziz, A. R. A.; Aroua, M. K., Glycerol production and its applications as a raw material: A review. *Renewable & Sustainable Energy Reviews* **2013,** *27*, 118-127.
217. McNeil, J.; Day, P.; Sirovski, F., Glycerine from biodiesel: The perfect diesel fuel. *Process Safety and Environmental Protection* **2012,** *90* (3), 180-188.
218. Carlos Serrano-Ruiz, J.; Pineda, A.; Mariana Balu, A.; Luque, R.; Manuel Campelo, J.; Angel Romero, A.; Manuel Ramos-Fernandez, J., Catalytic transformations of biomass-derived acids into advanced biofuels. *Catalysis Today* **2012,** *195* (1), 162-168.
219. Johns, W. D., Clay mineral catalysis and petroleum generation. *Annual Review of Earth and Planetary Sciences* **1979,** *7*, 183-198.
220. Geatches, D. L.; Greenwell, H. C.; Clark, S. J., Ab Initio Transition State Searching in Complex Systems: Fatty Acid Decarboxylation in Minerals. *Journal of Physical Chemistry A* **2011,** *115* (12), 2658-2667.
221. Senol, O. I.; Viljava, T. R.; Krause, A. O. I. In *Hydrodeoxygenation of methyl esters on sulphided NiMo/gamma-Al_2O_3 and CoMo/gamma-Al_2O_3 catalysts*, 11th Nordic Symposium on Catalysis, Oulu, Finland, May 23-25; Elsevier Science Bv: Oulu, Finland, 2004; pp 331-335.
222. Matsubara, S.; Yokota, Y.; Oshima, K., Palladium-catalyzed decarboxylation and decarbonylation under hydrothermal conditions: Decarboxylative deuteration. *Organic Letters* **2004,** *6* (12), 2071-2073.
223. Lu, J.; Behtash, S.; Heyden, A., Theoretical Investigation of the Reaction Mechanism of the Decarboxylation and Decarbonylation of Propanoic Acid on Pd(111) Model Surfaces. *Journal of Physical Chemistry C* **2012,** *116* (27), 14328-14341.
224. Masende, Z. P. G.; Kuster, B. F. M.; Ptasinski, K. J.; Janssen, F.; Katima, J. H. Y.; Schouten, J. C., Kinetics of malonic acid degradation in aqueous phase over Pt/graphite catalyst. *Applied Catalysis B-Environmental* **2005,** *56* (3), 189-199.
225. Do, P. T.; Chiappero, M.; Lobban, L. L.; Resasco, D. E., Catalytic Deoxygenation of Methyl-Octanoate and Methyl-Stearate on Pt/Al2O3. *Catalysis Letters* **2009,** *130* (1-2), 9-18.
226. Gardner, L. K.; Lawrence, G. D., Benzene production from decarboxylation of benzoic-acid in the presence of ascorbic-acid and a transition-metal catalyst. *Journal of Agricultural and Food Chemistry* **1993,** *41* (5), 693-695.
227. Lisitsyn, A. S., 2,2 '-Bipyridine and related N-chelants as very effective promoters for Cu catalysts in the decarboxylation. *Applied Catalysis A-General* **2007,** *332* (1), 166-170.
228. Senol, O. I.; Viljava, T. R.; Krause, A. O. I. In *Hydrodeoxygenation of aliphatic esters on sulphided NiMo/gamma-Al_2O_3 and CoMo/gamma-Al_2O_3 catalyst: The effect of water*, International Conference on Gas-Fuel 05, Brugge, Belgium, Nov 14-16; Brugge, Belgium, 2005; pp 186-189.
229. Huber, G. W.; O'Connor, P.; Corma, A., Processing biomass in conventional oil refineries: Production of high quality diesel by hydrotreating vegetable oils in heavy vacuum oil mixtures. *Applied Catalysis a-General* **2007,** *329*, 120-129.
230. Adjaye, J. D.; Bakhshi, N. N., Catalytic conversion of a biomass-derived oil to fuels and chemicals .1. Model compound studies and reaction pathways. *Biomass & Bioenergy* **1995,** *8* (3), 131-149.
231. More, A.; Schlup, J.; Hohn, K. In *Preliminary Investigations of the Catalytic Deoxygenation of Fatty Acids*, AIChE 2006 Annual Meeting, San Francisco, AIChE: San Francisco, 2006.
232. A, Z.; Q, M.; K, W.; Y, T.; WA, G. *Improved Processes to Remove Naphthenic Acids*; 2005; p OSTI ID: 825290.

233. Zhang, A. H.; Ma, Q. S.; Wang, K. S.; Liu, X. C.; Shuler, P.; Tang, Y. C., Naphthenic acid removal from crude oil through catalytic decarboxylation on magnesium oxide. *Applied Catalysis A-General* **2006,** *303* (1), 103-109.
234. Sooknoi, T.; Danuthai, T.; Lobban, L. L.; Mallinson, R. G.; Resasco, D. E., Deoxygenation of methylesters over CsNaX. *Journal of Catalysis* **2008,** *258* (1), 199-209.
235. Coveney, P. V.; Swadling, J. B.; Wattis, J. A. D.; Greenwell, H. C., Theory, modelling and simulation in origins of life studies. *Chemical Society Reviews* **2012,** *41* (16), 5430-5446.
236. Edman, T. S. C.; Owusu, O. W.; Redman, D. J. Methanol production process. WO2009130452 A1, 2009, 2009.
237. Watanabe, M.; Inomata, H.; Smith, R. L.; Arai, K., Catalytic decarboxylation of acetic acid with zirconia catalyst in supercritical water. *Applied Catalysis A-General* **2001,** *219* (1-2), 149-156.
238. Dury, F.; Clement, D.; Gaigneaux, E. A. In *The influence of the hydrogen origin at the surface of Mo suboxide during the deoxygenation of carboxylic acid*, 1st Conference of the European-Union-Coordination-Action -Coordination of Nanostructured Catalytic Oxides Research and Development in Europe, Louvain la Neuve, Belgium, Jan 26-28; Elsevier Science Bv: Louvain la Neuve, Belgium, 2005; pp 130-133.
239. Dury, F.; Meixner, S.; Clement, D.; Gaigneaux, E. M., Coupling the deoxygenation of benzoic acid with the oxidation of propylene on a Co molybdate catalyst. *Journal of Molecular Catalysis A-Chemical* **2005,** *237* (1-2), 9-16.
240. Fu, X. Q.; Dai, Z. Y.; Tian, S. B.; Hou, S.; Wang, X. Q., Molecular simulation of naphthenic acid removal on acidic catalyst - (I) Mechanism of catalytic decarboxylation. *China Petroleum Processing & Petrochemical Technology* **2008,** (1), 49-54.
241. Fu, X.; Dai, Z.; Tian, S.; Long, J.; Hou, S.; Wang, X., Catalytic decarboxylation of petroleum acids from high acid crude oils over solid acid catalysts. *Energy & Fuels* **2008,** *22* (3), 1923-1929.
242. Hellerkallai, L.; Aizenshtat, Z.; Miloslavski, I., The effect of various clay-minerals on the thermal-decomposition of stearic-acid under bulk flow conditions. *Clay Minerals* **1984,** *19* (5), 779-788.
243. R, A. W., Petroleum Forming Reactions: The mechanism and Rate of Clay Catalyzed Fatty Acid Decarboxylation. *Proc. Int. Meet. Org. Geochem.* **1977,** *7th*, 157-171.
244. Lestari, S.; Beltramini, J.; Lu, G. Q.; Ieee In *Preparation and characterization of mesoporous Ni/Zr-laponite for the catalytic deoxygenation of vegetable oils into liquid hydrocarbons*, International Conference on Nanoscience and Nanotechnology, Gwangju, South Korea, Dec 07-08; Ieee: Gwangju, South Korea, 2006; pp 395-398.
245. Negronmendoza, A.; Ramos, S.; Albarran, G., Enhance decarboxylation reaction of carboxylic-acids in clay-minerals. *Radiation Physics and Chemistry* **1995,** *46* (4-6), 565-568.
246. Miyoshi, H.; Mori, H.; Yoneyama, H., Light-induced decomposition of saturated carboxylic-acids on iron-oxide incorporated clay suspended in aqueous-solutions. *Langmuir* **1991,** *7* (3), 503-507.
247. Maki-Arvela, P.; Snare, M.; Eranen, K.; Myllyoja, J.; Murzin, D. Y., Continuous decarboxylation of lauric acid over Pd/C catalyst. *Fuel* **2008,** *87* (17-18), 3543-3549.
248. Kubickova, I.; Maki-Arvela, P.; Murzin, D. Y.; Myllyoja, J.; Snare, M. Method for the manufacture of hydrocarbons. US 2006/0161032, 2006.
249. Connors, K. A., *Chemical Kinetics: The Study of Reaction Rates in Solution*. VCH: 1990.
250. Iwasawa, T.; Tokunaga, M.; Obora, Y.; Tsuji, Y., Homogeneous palladium catalyst suppressing Pd black formation in air oxidation of alcohols. *Journal of the American Chemical Society* **2004,** *126* (21), 6554-6555.
251. Liu, Y.; Lotero, E.; Goodwin Jr, J. G.; Mo, X., Transesterification of poultry fat with methanol using Mg-Al hydrotalcite derived catalysts. *Applied Catalysis A: General* **2007,** *331*, 138-148.

252. Alvarez, M. G.; Chimentao, R. J.; Figueras, F.; Medina, F., Tunable basic and textural properties of hydrotalcite derived materials for transesterification of glycerol. *Applied Clay Science* **2012,** *58*, 16-24.
253. Sels, B. F.; De Vos, D. E.; Jacobs, P. A., Hydrotalcite-like anionic clays in catalytic organic reactions. *Catalysis Reviews-Science and Engineering* **2001,** *43* (4), 443-488.
254. Climent, M. J.; Corma, A.; Iborra, S.; Primo, J., Base catalysis for fine chemicals production - Claisen-Schmidt condensation on zeolites and hydrotalcites for the production of chalcones and flavanones of pharmaceutical interest. *Journal of Catalysis* **1995,** *151* (1), 60-66.
255. Yamaguchi, K.; Mori, K.; Mizugaki, T.; Ebitani, K.; Kaneda, K., Epoxidation of alpha,beta-unsaturated ketones using hydrogen peroxide in the presence of basic hydrotalcite catalysts. *Journal of Organic Chemistry* **2000,** *65* (21), 6897-6903.
256. Yamaguchi, K.; Ebitani, K.; Yoshida, T.; Yoshida, H.; Kaneda, K., Mg-Al mixed oxides as highly active acid-base catalysts for cycloaddition of carbon dioxide to epoxides. *Journal of the American Chemical Society* **1999,** *121* (18), 4526-4527.
257. Yamaguchi, K.; Mizugaki, T.; Ebitani, K.; Kaneda, K., Heterogeneous N-oxidation of pyridines using a combined oxidant of hydrogen peroxide and nitriles catalysed by basic hydrotalcites. *New Journal of Chemistry* **1999,** *23* (8), 799-801.
258. Lauronpernot, H.; Luck, F.; Popa, J. M., Methylbutynol - a new and simple diagnostic tool for acidic and basic sites of solids. *Applied Catalysis* **1991,** *78* (2), 213-225.
259. Malherbe, F.; Depege, C.; Forano, C.; Besse, J. P.; Atkins, M. P.; Sharma, B.; Wade, S. R., Alkoxylation reaction catalysed by layered double hydroxides. *Applied Clay Science* **1998,** *13* (5-6), 451-466.
260. Falgoux, D.; Simoulin, D.; Pascal-Mousselard, M. Catalytic etherification using triflate salt. 1985; Falgoux, D.; Joly, J.; Simoulin, D. Process for the preparation of addition products of epoxides and compounds containing an active hydrogen. 1986; Moody, K. Process for the alkoxylation of alcohols. 1981.
261. Waters *Mass Lynx 4.1*, 4.1.
262. Na, J. G.; Yi, B. E.; Kim, J. N.; Yi, K. B.; Park, S. Y.; Park, J. H.; Ko, C. H., Hydrocarbon production from decarboxylation of fatty acid without hydrogen. *Catalysis Today* **2010,** *156* (1-2), 44-48.
263. Pham, T. N.; Sooknoi, T.; Crossley, S. P.; Resasco, D. E., Ketonization of Carboxylic Acids: Mechanisms, Catalysts, and Implications for Biomass Conversion. *Acs Catalysis* **2013,** *3* (11), 2456-2473.
264. Constantino, V. R. L.; Pinnavaia, T. J., Structure-reactivity relationships for basic catalysts derived from a $Mg^{2+}Al^{3+}(CO_3^{2-})$ layered double hydroxide. *Catalysis Letters* **1994,** *23* (3-4), 361-367.
265. Pulido, A.; Oliver-Tomas, B.; Renz, M.; Boronat, M.; Corma, A., Ketonic Decarboxylation Reaction Mechanism: A Combined Experimental and DFT Study. *Chemsuschem* **2013,** *6* (1), 141-151.
266. Shen, J. Y.; Tu, M.; Hu, C., Structural and surface acid/base properties of hydrotalcite-derived MgAlO oxides calcined at varying temperatures. *Journal of Solid State Chemistry* **1998,** *137* (2), 295-301.
267. Kustrowski, P.; Chmielarz, L.; Bozek, E.; Sawalha, M.; Roessner, F., Acidity and basicity of hydrotalcite derived mixed Mg-Al oxides studied by test reaction of MBOH conversion and temperature programmed desorption of NH_3 and CO_2. *Materials Research Bulletin* **2004,** *39* (2), 263-281.
268. Xi, Y.; Davis, R. J., Influence of water on the activity and stability of activated Mg-Al hydrotalcites for the transesterification of tributyrin with methanol. *Journal of Catalysis* **2008,** *254* (2), 190-197.
269. Verziu, M.; Cojocaru, B.; Hu, J.; Richards, R.; Ciuculescu, C.; Filip, P.; Parvulescu, V. I., Sunflower and rapeseed oil transesterification to biodiesel over different nanocrystalline MgO catalysts. *Green Chemistry* **2008,** *10* (4), 373-381.

270. Gaertner, C. A.; Serrano-Ruiz, J. C.; Braden, D. J.; Dumesic, J. A., Ketonization Reactions of Carboxylic Acids and Esters over Ceria-Zirconia as Biomass-Upgrading Processes. *Industrial & Engineering Chemistry Research* **2010,** *49* (13), 6027-6033.
271. Neunhoeffer, O.; Paschke, P., The mechanism of ketone formation from carbonic acids. *Berichte Der Deutschen Chemischen Gesellschaft* **1939,** *72*, 919-929.
272. Roelofs, J.; van Dillen, A. J.; de Jong, K. P., Base-catalyzed condensation of citral and acetone at low temperature using modified hydrotalcite catalysts. *Catalysis Today* **2000,** *60* (3-4), 297-303.
273. Anastas, P.; JCA, W., *Green Chemistry: Theory and Practice*. Oxford University Press: 2000.
274. Bozell, J. J.; Petersen, G. R., Technology development for the production of biobased products from biorefinery carbohydrates-the US Department of Energy's "Top 10" revisited. *Green Chemistry* **2010,** *12* (4), 539-554; Clark, J. H.; Budarin, V.; Deswarte, F. E. I.; Hardy, J. J. E.; Kerton, F. M.; Hunt, A. J.; Luque, R.; Macquarrie, D. J.; Milkowski, K.; Rodriguez, A.; Samuel, O.; Tavener, S. J.; White, R. J.; Wilson, A. J., Green chemistry and the biorefinery: A partnership for a sustainable future. *Green Chemistry* **2006,** *8* (10), 853-860; Clark, J. H., Green chemistry for the second generation biorefinery - sustainable chemical manufacturing based on biomass. *Journal of Chemical Technology and Biotechnology* **2007,** *82* (7), 603-609.
275. Cherubini, F., The biorefinery concept: Using biomass instead of oil for producing energy and chemicals. *Energy Conversion and Management* **2010,** *51* (7), 1412-1421.